BioMed Research International

Molecular Imaging: From Bench to Clinic

Guest Editors: Yì-Xiáng J. Wáng, Yongdoo Choi, Zhiyi Chen, Sophie Laurent, and Summer L. Gibbs

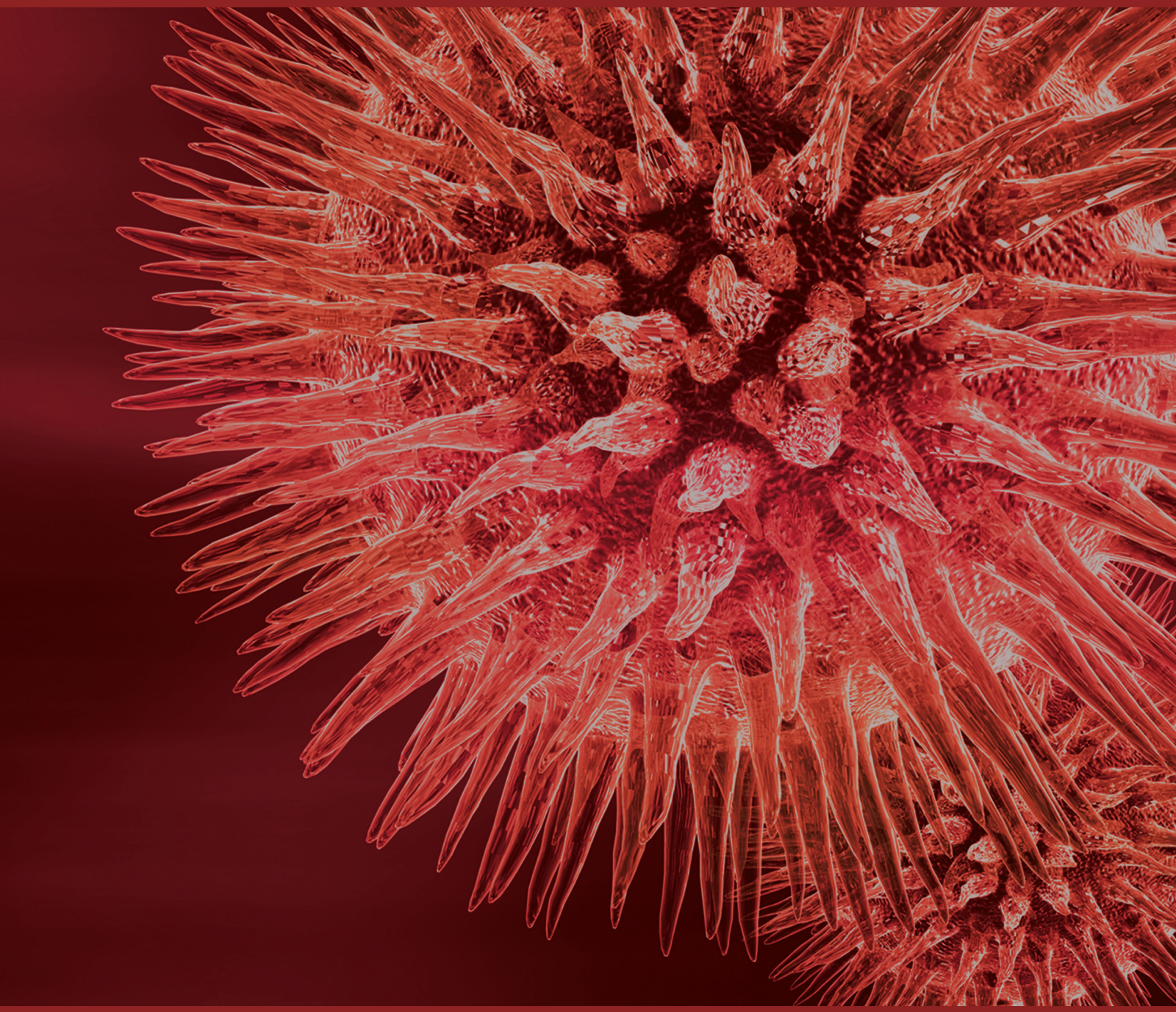

Molecular Imaging: From Bench to Clinic

BioMed Research International

Molecular Imaging: From Bench to Clinic

Guest Editors: Yì-Xiáng J. Wáng, Yongdoo Choi, Zhiyi Chen, Sophie Laurent, and Summer L. Gibbs

Contents

Hindawi Publishing Corporation
BioMed Research International
Volume 2014, Article ID 357258, 3 pages
http://dx.doi.org/10.1155/2014/357258

Editorial

Molecular Imaging: From Bench to Clinic

Yì-Xiáng J. Wáng,[1] Yongdoo Choi,[2] Zhiyi Chen,[3] Sophie Laurent,[4] and Summer L. Gibbs[5]

[1] *Department of Imaging and Interventional Radiology, Faculty of Medicine, The Chinese University of Hong Kong, Prince of Wales Hospital, Shatin, Hong Kong*
[2] *Molecular Imaging and Therapy Branch, National Cancer Center, 323 Ilsan-ro, Goyang-si, Gyeonggi-do 410-769, Republic of Korea*
[3] *Laboratory of Ultrasound Molecular Imaging, The Third Affiliated Hospital of Guangzhou Medical University, Guangzhou 510150, China*
[4] *NMR and Molecular Imaging Laboratory, Department of General, Organic and Biomedical Chemistry, Université de Mons, 7000 Mons, Belgium*
[5] *Department of Biomedical Engineering, Center for Spatial Systems Biomedicine, Knight Cancer Institute, Oregon Health and Science University, Portland, OR, USA*

Correspondence should be addressed to Yì-Xiáng J. Wáng; yixiang_wang@cuhk.edu.hk

Received 16 September 2014; Accepted 16 September 2014; Published 29 December 2014

Advances in molecular biology and new developments in imaging, engineering, and novel contrast agents position molecular imaging to play a major role in disease management. This current issue mainly covers ultrasound techniques and radionuclide imaging techniques, and both preclinical research on animal models and clinical studies on cancer patients are presented herein. Molecular imaging has demonstrated its potential in characterizing disease models in small animal preclinical studies. In the clinical setting, many patients have the potential to benefit from these new and quantitative imaging techniques providing improved disease characterization, therapeutic monitoring, and objective prognostic criteria. To realize the full potential of molecular imaging, chemists, molecular biologist, and biomedical engineers will need to work closely with clinicians to translate molecular imaging techniques into clinical applications, ultimately providing improved disease diagnosis, treatment monitoring, and noninvasive prognostic imaging for patients.

Advances in molecular biology and new developments in imaging, engineering, and novel contrast agents position molecular imaging to play a major role in disease management [1–16]. Ultrasound (US) imaging has great potential in molecular imaging because microbubble agents are nontoxic and can be used at very low dosages. US can reach both superficial and deep tissues depending on the frequency utilized for imaging. US contrast agents can also be targeted and used as carriers for local gene or drug delivery [5–7]. In addition, US is advantageous because it is of low cost and is widely available. Radionuclide imaging holds great promise due to its high sensitivity, with the small doses of radiotracer necessary and minimal background for imaging. Using appropriate tracer radionuclides, positron emission tomography (PET) and single photon emission computed tomography (SPECT), has demonstrated the capacity to image cellular and molecular targets [1, 2, 5, 16, 17]. However, production of radionuclide agents can be complex and expensive with low stability and limited availability. Optical imaging techniques (fluorescence and bioluminescence) are widely used in small animals, and clinical use is on the rise for imaging superficial tissues such as the breast. However, only fluorescence has clinical applicability, while bioluminescence remains a preclinical research tool because of the requirement of expression of luciferase by the genome. Optical imaging techniques are rapidly evolving, where their sensitivity is similar to radionuclide imaging in terms of detection of low concentrations of contrast agent and are advantageous because contrast agents are significantly more stable overtime. Two near-infrared imaging probes, methylene blue and indocyanine green, have been approved by the FDA for

clinical use [9]. The main drawback of optical imaging techniques are the high level of attenuation of signal with depth and the background signal due to autofluorescence, calling for new fluorophores to improve *in vivo* imaging [4, 9]. MRI is also a powerful method for molecular imaging, with novel techniques developing rapidly, including MR spectroscopy, chemical shift imaging, diffusion-weighted imaging, T1rho weighted imaging, chemical exchange saturation transfer, and targeted contrast agents [10–17].

There are currently three imaging strategies to noninvasively monitor and measure molecular events. They have been broadly defined as "direct," "biomarker," and "indirect" imaging [2, 3]. The "direct" molecular imaging motif builds on established chemistry and radiochemistry relationships. Bioconjugate chemistry can be used to link specific binding motifs and bioactive molecules to imaging agents, such as superparamagnetic particles for MRI or radionuclides for PET and SPECT imaging [5, 12]. However, a constraint limiting direct imaging strategy is the concentration of direct imaging targets necessary for imaging the individual target to enable visualization. Another constraint limiting direct imaging strategy is the necessity to develop a specific probe for each molecular target and then to validate the sensitivity, specificity, and safety of each probe for specific applications before their introduction into the clinic. A biomarker is a biological or biochemical change that is objectively measured as an indicator of biological processes or pharmacological responses to a therapeutic intervention. For "biomarker imaging," many existing imaging technologies are used for monitoring downstream changes of specific molecular/genetic pathways in diseases. Some biomarker probes could also be classified as direct imaging probes. For example, [^{18}F] 2-fluoro-2-deoxyglucose (FDG) can be considered a direct imaging substrate for visualizing hexokinase enzyme levels, as well as a biomarker for imaging, and is useful in a clinical setting for the identification of malignant lesions, for staging the extent of disease and, in some cases, to evaluate the treatment response, for example, in the case of gastrointestinal stromal tumour (GIST)-Gleevec ^{18}F-FDG [16–21]. However, biomarker imaging is likely to be less specific and more limited in measuring the activity of a particular "upstream" pathway. "Indirect" molecular (reporter gene) imaging studies will be more limited in patients compared with that in animals due to the necessity of transducing target tissue cells with a specific reporter construct or the production of transgenic animals bearing the reporter construct [2].

This current issue mainly covers ultrasound techniques and radionuclide imaging techniques, and both preclinical research on animal models and clinical studies on cancer patients are presented herein. Contrast-enhanced ultrasound (CEUS) and acoustic radiation force impulse elastography (ARFI) are evaluated in papers of this special issue. In a population of rectal carcinoma patients, Y. Wang et al. report a positive linear correlation between the CEUS enhanced intensity (EI) and microvessel density (MVD) evaluated by immunohistochemical staining of surgical specimens. Additionally, a significant difference for EI histological grading with EI decreased as T stage increased was found. The authors concluded that EI of endorectal CEUS provides noninvasive biomarker of tumor angiogenesis in rectal cancer. In another paper, J.-X. Zhang et al. showed CEUS was helpful in identifying BI-RADS category 3 or 4 small breast lesions and improved diagnostic sensitivity, reduced the negative likelihood ratio, and improved the negative predictive value for these lesions. X. Xu et al. evaluated ARFI for liver tumor radiofrequency ablation results assessment and determined that while CEUS accurately detected residual tumors, the ARFI technique has limited capacity to detect residual tumors; moreover, it was demonstrated that liver cirrhosis is associated with decreased chance of a complete ablation. In a review article, Y.-Y. Liao et al. discussed ultrasound targeted microbubble destruction (UTMD) as a gene delivery system, the combination of UTMD and gene therapy or stem cell therapy in angiogenesis research, and outlined the future challenges in the field.

Expression of multidrug pumps including P-glycoprotein (Pgp) in the plasma membrane of tumor cells often results in decreased intracellular accumulation of anticancer drugs causing serious impediment to successful chemotherapy. It has been shown earlier that combined treatment with UIC2 anti-Pgp monoclonal antibody and cyclosporine A is an effective way of blocking Pgp function. In this special issue, G. Trencsényi et al. investigated the suitability of four PET tumor diagnostic radiotracers, namely, ^{18}F-FDG, ^{11}C-methionine, 3′-deoxy-3′-[18F]-fluorothymidine (^{18}F-FLT), and [18F]-Fluoroazomycin-arabinofuranoside (^{18}FAZA) for *in vivo* follow-up of the efficacy of chemotherapy in both P-glycoprotein positive (Pgp+) and negative (Pgp−) human tumor xenograft pairs raised in CB-17 SCID mice. It was found that combined treatment resulted in a significant decrease of both the tumor size and the accumulation of the tumor diagnostic tracers in the Pgp+ tumors. These results demonstrated that ^{18}F-FDG, ^{18}F-FLT, ^{18}F-FAZA, and ^{11}C-methionine are suitable PET tracers for the diagnosis and *in vivo* follow-up of the efficacy of tumor chemotherapy both in Pgp+ and Pgp− human tumor xenografts by miniPET. In another experimental study, X. Bao et al. demonstrated that early treatment response of sunitinib was monitored in U87MG model mimicking glioblastoma multiforme by longitudinal ^{18}F-FLT microPET/CT imaging. In a study by W. Ma et al., a peptide containing Asn-Gly-Arg (NGR) sequence was synthesized and labeled with ^{99m}Tc, and its radiochemical characteristics, biodistribution, and SPECT imaging were evaluated in nude mice bearing human HepG2 hepatoma, demonstrating the potential of ^{99m}Tc-NGR for SPECT imaging agent of tumor. In the clinical study by K. Miwa et al., it was suggested that ^{11}C-methionine PET is a marker of the biological characteristics of glioblastoma multiforme and is useful for therapy planning of hypofractionated high-dose irradiation by intensity-modulated radiation. Studies by H. D. Zuo et al. report the effect of iRGD peptide (CRGDK/RGPD/EC) combined with SPIO on the labeling of pancreatic cancer cells. Their results describe a simple protocol to label panc-1 cells using SPIO in combination

with iRGD peptide and suggested a method to improve the sensitivity of pancreatic cancer imaging.

We hope readers find the progress on molecular imaging reported in this special issue interesting and stimulating. Molecular imaging has demonstrated its potential in characterizing disease models in small animal preclinical studies. In the clinical setting, many patients have the potential to benefit from these new and quantitative imaging techniques providing improved disease characterization, therapeutic monitoring, and objective prognostic criteria [3]. Current progress on clinical translation of targeted molecular imaging agents is less than initially anticipated. To realize the full potential of molecular imaging, chemists, molecular biologist, and biomedical engineers will need to work closely with clinicians to translate molecular imaging techniques into clinical applications, ultimately providing improved disease diagnosis, treatment monitoring, and noninvasive prognostic imaging for patients.

Yì-Xiáng J. Wáng
Yongdoo Choi
Zhiyi Chen
Sophie Laurent
Summer L. Gibbs

References

[1] R. Weissleder, "Molecular imaging: exploring the next frontier," *Radiology*, vol. 212, no. 3, pp. 609–614, 1999.

[2] N. Grenier and P. Brader, "Principles and basic concepts of molecular imaging," *Pediatric Radiology*, vol. 41, no. 2, pp. 144–160, 2011.

[3] Y. X. Wang and C. K. Ng, "The impact of quantitative imaging in medicine and surgery: charting our course for the future," *Quantitative Imaging in Medicine and Surgery*, vol. 1, no. 1, pp. 1–3, 2011.

[4] S. L. Gibbs, "Near infrared fluorescence for image-guided surgery," *Quantitative Imaging in Medicine and Surgery*, vol. 2, no. 3, pp. 177–187, 2012.

[5] M. L. James and S. S. Gambhir, "A molecular imaging primer: modalities, imaging agents, and applications," *Physiological Reviews*, vol. 92, no. 2, pp. 897–965, 2012.

[6] Z.-Y. Chen, Y.-X. Wang, Y. Lin et al., "Advance of molecular imaging technology and targeted imaging agent in imaging and therapy," *BioMed Research International*, vol. 2014, Article ID 819324, 12 pages, 2014.

[7] E. Unger, T. Porter, J. Lindner, and P. Grayburn, "Cardiovascular drug delivery with ultrasound and microbubbles," *Advanced Drug Delivery Reviews*, vol. 72, pp. 110–126, 2014.

[8] B. Jang, S. Park, S. H. Kang et al., "Gold nanorods for target selective SPECT/CT imaging and photothermal therapy in vivo," *Quantitative Imaging in Medicine and Surgery*, vol. 2, no. 1, pp. 1–11, 2012.

[9] J. H. Lee, G. Park, G. H. Hong, J. Choi, and H. S. Choi, "Design considerations for targeted optical contrast agents," *Quantitative Imaging in Medicine and Surgery*, vol. 2, no. 4, pp. 266–273, 2012.

[10] G. V. Velde, V. Baekelandt, T. Dresselaers, and U. Himmelreich, "Magnetic resonance imaging and spectroscopy methods for molecular imaging," *The Quarterly Journal of Nuclear Medicine and Molecular Imaging*, vol. 53, no. 6, pp. 565–585, 2009.

[11] S. Laurent, L. V. Elst, and R. N. Muller, "Lanthanide complexes for magnetic resonance and optical molecular imaging," *Quarterly Journal of Nuclear Medicine and Molecular Imaging*, vol. 53, no. 6, pp. 586–603, 2009.

[12] Y.-X. J. Wang, S. Xuan, M. Port, and J.-M. Idee, "Recent advances in superparamagnetic iron oxide nanoparticles for cellular imaging and targeted therapy research," *Current Pharmaceutical Design*, vol. 19, no. 37, pp. 6575–6593, 2013.

[13] D. L. Longo, P. Z. Sun, L. Consolino, F. C. Michelotti, F. Uggeri, and S. Aime, "A general MRI-CEST ratiometric approach for pH imaging: demonstration of in vivo pH mapping with iobitridol," *Journal of the American Chemical Society*, vol. 136, no. 41, pp. 14333–14336, 2014.

[14] Y.-X. J. Wang, J. Yuan, E. S. H. Chu et al., "T1ρ MR imaging is sensitive to evaluate liver fibrosis: an experimental study in a rat biliary duct ligation model," *Radiology*, vol. 259, no. 3, pp. 712–719, 2011.

[15] J. Yuan, J. Zhou, A. T. Ahuja, and Y.-X. J. Wang, "MR chemical exchange imaging with spin-lock technique (CESL): a theoretical analysis of the Z-spectrum using a two-pool $R_{1\rho}$ relaxation model beyond the fast-exchange limit," *Physics in Medicine and Biology*, vol. 57, no. 24, pp. 8185–8200, 2012.

[16] D. le Bihan, "Diffusion, confusion and functional MRI," *NeuroImage*, vol. 62, no. 2, pp. 1131–1136, 2012.

[17] K. H. Lee, J. M. Lee, J. H. Park et al., "MR imaging in patients with suspected liver metastases: value of liver-specific contrast agent gadoxetic acid," *Korean Journal of Radiology*, vol. 14, no. 6, pp. 894–904, 2013.

[18] A. Gallamini, C. Zwarthoed, and A. Borra, "Positron emission tomography (PET) in oncology," *Cancers*, vol. 6, no. 4, pp. 1821–1889, 2014.

[19] E. Valls-Ferrusola, J. R. García-Garzón, A. Ponce-López et al., "Patterns of extension of gastrointestinal stromal tumors (GIST) treated with imatinib (Gleevec) by ^{18}F-FDG PET/CT," *Revista Española de Enfermedades Digestivas*, vol. 104, no. 7, pp. 360–366, 2012.

[20] J.-L. Roh, J. P. Park, J. S. Kim et al., " ^{18}F fluorodeoxyglucose PET/CT in head and neck squamous cell carcinoma with negative neck palpation findings: a prospective study," *Radiology*, vol. 271, no. 1, pp. 153–161, 2014.

[21] M. S. Bolouri, S. G. Elias, D. J. Wisner et al., "Triple-negative and non-triple-negative invasive breast cancer: association between MR and fluorine 18 fluorodeoxyglucose PET imaging," *Radiology*, vol. 269, no. 2, pp. 354–361, 2013.

Hindawi Publishing Corporation
BioMed Research International
Volume 2014, Article ID 787365, 10 pages
http://dx.doi.org/10.1155/2014/787365

Research Article

^{18}FDG, [^{18}F]FLT, [^{18}F]FAZA, and ^{11}C-Methionine Are Suitable Tracers for the Diagnosis and *In Vivo* Follow-Up of the Efficacy of Chemotherapy by miniPET in Both Multidrug Resistant and Sensitive Human Gynecologic Tumor Xenografts

György Trencsényi,[1] Teréz Márián,[1] Imre Lajtos,[1] Zoltán Krasznai,[2] László Balkay,[1] Miklós Emri,[1] Pál Mikecz,[1] Katalin Goda,[2] Gábor Szalóki,[2] István Juhász,[3,4] Enikő Németh,[1] Tünde Miklovicz,[1] Gábor Szabó,[2] and Zoárd T. Krasznai[5]

[1] *Department of Nuclear Medicine, University of Debrecen, P.O. Box 63, Nagyerdei Körút 98, Debrecen 4012, Hungary*
[2] *Department of Biophysics and Cell Biology, University of Debrecen, Nagyerdei Körút 98, Debrecen 4012, Hungary*
[3] *Department of Dermatology, University of Debrecen, Nagyerdei Körút 98, Debrecen 4012, Hungary*
[4] *Department of Surgery and Operative Techniques, Faculty of Dentistry, University of Debrecen, Nagyerdei Körút 98, Debrecen 4012, Hungary*
[5] *Department of Obstetrics and Gynecology, University of Debrecen, Nagyerdei Körút 98, Debrecen 4012, Hungary*

Correspondence should be addressed to Teréz Márián; marian@pet.dote.hu

Received 16 January 2014; Revised 14 August 2014; Accepted 28 August 2014; Published 18 September 2014

Academic Editor: Yi-Xiang Wang

Expression of multidrug pumps including P-glycoprotein (MDR1, ABCB1) in the plasma membrane of tumor cells often results in decreased intracellular accumulation of anticancer drugs causing serious impediment to successful chemotherapy. It has been shown earlier that combined treatment with UIC2 anti-Pgp monoclonal antibody (mAb) and cyclosporine A (CSA) is an effective way of blocking Pgp function. In the present work we investigated the suitability of four PET tumor diagnostic radiotracers including 2-[^{18}F]fluoro-2-deoxy-D-glucose (^{18}FDG), ^{11}C-methionine, 3′-deoxy-3′-[^{18}F]fluorothymidine (^{18}F-FLT), and [^{18}F]fluoroazomycin-arabinofuranoside (^{18}FAZA) for *in vivo* follow-up of the efficacy of chemotherapy in both Pgp positive (Pgp^+) and negative (Pgp^-) human tumor xenograft pairs raised in CB-17 SCID mice. Pgp^+ and Pgp^- A2780AD/A2780 human ovarian carcinoma and KB-V1/KB-3-1 human epidermoid adenocarcinoma tumor xenografts were used to study the effect of the treatment with an anticancer drug doxorubicin combined with UIC2 and CSA. The combined treatment resulted in a significant decrease of both the tumor size and the accumulation of the tumor diagnostic tracers in the Pgp^+ tumors. Our results demonstrate that ^{18}FDG, ^{18}F-FLT, ^{18}FAZA, and ^{11}C-methionine are suitable PET tracers for the diagnosis and *in vivo* follow-up of the efficacy of tumor chemotherapy in both Pgp^+ and Pgp^- human tumor xenografts by miniPET.

1. Introduction

The miniPET technique is a well-established noninvasive method to detect tumors and follow up the effect of therapy of tumors, using PET tumor diagnostic tracers. The PET tumor diagnostic tracers, like ^{11}C-metionine, 2-[^{18}F]fluoro-2-deoxy-D-glucose (^{18}FDG), and (3′-deoxy-3′-[^{18}F]fluorothymidine) (^{18}F-FLT), are good candidates to measure the effect of the therapy. ^{18}FDG, an analog of glucose, the most commonly used PET radiotracer in clinical oncology, allows visualization of the changes in the glucose metabolic rate in tumors [1–3]. ^{18}FDG undergoes phosphorylation by hexokinase but can not pass through the rest of glycolysis, and it remains trapped in the cell. Increased cell proliferation is one of the main features of cancer cells. ^{18}F-FLT is used as a PET tracer for visualization of cell proliferation. The trapping of ^{18}F-FLT was demonstrated with the uptake of thymidine analogue after phosphorylation by thymidine kinase 1

(TK1) in the S phase of cell cycle [4, 5]. Another tumor diagnostic PET tracer is the ^{11}C labelled methionine applied for the follow-up of the amino acid transport and metabolism in the tumor [6]. Radiolabeled nitroimidazole derivatives (e.g., [^{18}F]fluoroazomycinarabinofuranoside (^{18}F-FAZA) and [^{18}F]-fluoromisonidazole (^{18}F-MISO)) validated markers to detect hypoxia in cancer cells. Nitroimidazoles labeled with ^{18}F isotope can undergo an oxygen-reversible single-electron reduction under hypoxic conditions, forming reactive oxygen radicals that subsequently bind covalently to macromolecular cellular components and are trapped in the intracellular space; consequently they are suitable tracers for *in vivo* detection of hypoxia in tumors. Hypoxia in tumor seems to be an important prognostic factor of chemotherapy response [7].

Multidrug resistance (MDR) seems to be the most widely observed mechanism in clinical cases of chemotherapy resistance. This phenomenon is often associated with the overexpression of certain ATP binding cassette transporters including P-glycoprotein (Pgp, coded by the MDR1 gene), which is an ATP dependent active efflux pump that is able to extrude a large variety of chemotherapeutic drugs from the cells [8, 9].

The conformation sensitive UIC2 mouse monoclonal antibody inhibits Pgp mediated substrate transport. However, this inhibition is usually partial and its extent is variable, since UIC2 binds only to 10–40% of all Pgp molecules present in the cell membrane [10, 11]. It has been shown earlier in *in vitro* and *ex vivo* experiments that the combined administration of UIC2 antibody and certain substrates or modulators used at low concentrations increases the antibody binding, leading to a near complete Pgp inhibition, thus providing a novel, specific, and effective way of blocking Pgp function [11, 12]. Krasznai et al. [12] also demonstrated that the combined treatment with UIC2 antibody and Pgp modulators effectively blocked the function of Pgp in ovarian carcinoma cells *in vitro* and the effect could be followed by using tumor diagnostic tracers, ^{99m}Tc-MIBI and ^{18}FDG.

Ovarian cancer is the second most common cancer of the female genital tract but accounts for over half of all deaths related to gynecologic neoplasms [13]. Anthracycline antibiotics have been used for more than 40 years in the treatment of gynecologic tumors in the first line in monotherapy or in combination with other drugs [14, 15].

In this paper using an animal model we demonstrate that the miniPET technique combined with tumor diagnostic radiopharmaceuticals is suitable for the detection of either Pgp expressing or Pgp nonexpressing tumors and it can be applied for *in vivo* monitoring of the effect of tumor therapy.

2. Materials and Methods

2.1. Cell Lines. Drug sensitive (Pgp$^+$) cell lines and their nonsensitive (Pgp$^-$) counterparts were used in the experiments. Human epidermoid (cervix) carcinoma cell lines—KB-V-1 (Pgp$^+$), KB-3-1 (Pgp$^-$)—and human ovarian carcinoma cell lines—A2780AD (Pgp$^+$), A2780 (Pgp$^-$)—were grown as monolayer cultures at 37°C in a 95% humidified air, 5% CO_2 atmosphere. The cell lines were maintained in 75 cm^2 flasks in Dulbecco's modified Eagle's medium (DMEM) containing 4.5 g/L glucose and supplemented with 10% heat-inactivated fetal bovine serum (FBS), 2 mM L-glutamine, and 25 μM/mL gentamicin. The KB-V-1 cells were cultured in the presence of 180 nM vinblastine and the A2780AD cells were cultured with 2 μM doxorubicin until use. The viability of the cells used in our experiments was always higher than 90%, as assessed by the trypan blue exclusion test.

2.2. Laboratory Animals. Twenty-four (10- to 12-week-old) pathogen-free B-17 severe combined immunodeficiency (SCID) female mice were used in this study. Animals were housed under pathogen-free conditions in air conditioned rooms at a temperature of 26 ± 2°C, with 50 ± 10% humidity and artificial lighting with a circadian cycle of 12 h. The diet and drinking water (sterilized by autoclaving) were available ad libitum to all the animals. The *Principles of Laboratory Animal Care* (National Institute of Health) were strictly followed, and the experimental protocol was approved by the Laboratory Animal Care and Use Committee of the University of Debrecen.

2.3. Animal Model and Study Design. SCID mice were injected subcutaneously (s.c.) with KB-3-1 (1.5×10^6 cells in 150 μL PBS) cells on the left and KB-V-1 (3×10^6 cells in 150 μL PBS) cells on the right side. Other groups of SCID mice were injected s.c. with A2780 (3×10^6 cells in 150 μL PBS) cells on the left and A2780AD (4.5×10^6 cells in 150 μL PBS) cells on the right side. On each side the animals received two injections of the same cell line, one in the shoulder and one in the thigh to double the tumor numbers per animal in order to limit the number of animals and to maximize the number of tumors imaged. Preliminary experiments showed that, in contrast to the Pgp$^-$ cells, the tumor formation from Pgp$^+$ cells has a slower kinetics. This difference was equalized by the injection of different cell numbers. Four days after the injection mice were treated with doxorubicin (DOX) (5 mg/kg) combined with UIC2 monoclonal antibody (5 mg/kg) and cyclosporine A (CSA) (10 mg/kg). Tumor growth was assessed by caliper measurements every two days by the same experienced researcher. The tumor size was calculated using the following formula: (largest diameter × smallest diameter^2)/2 [16].

2.4. Radiotracers. The glucose analog (^{18}FDG) was synthesized and labeled with the positron-decaying isotope ^{18}F according to Hamacher et al. [17]. The radiosynthesis of the thymidine analog (^{18}F-FLT) was performed according to the published method by Grierson and Shields [18]. ^{11}C-Methionine was synthesized as described by Mitterhauser et al. [19]. The ^{18}F-labeled nitroimidazole compound fluoroazomycin arabinoside (^{18}FAZA) was performed according to the published method by Piert et al. [7].

2.5. Small Animal PET Imaging Using Radiopharmaceuticals. After the implantation ^{18}FDG, ^{11}C-methionine, and ^{18}F-FLT scans were repeated at different time points. Prior to PET,

mice were fasted overnight. On the day of PET imaging mice were prewarmed to a body temperature of 37°C and this temperature was maintained throughout the uptake and scanning period to minimize the brown fat visualization. Mice were injected via the tail vein with 5.0 ± 0.2 MBq of ^{18}FDG, 8.1 ± 0.6 MBq of ^{11}C-methionine, 4.5±0.2 MBq of ^{18}F-FLT, or 5.5± 0.5 MBq of ^{18}FAZA. 20 min after ^{11}C-methionine or 40 min after ^{18}FDG or ^{18}F-FLT or 120 min after ^{18}FAZA tracer injection animals were anaesthetized by 3% isoflurane with a dedicated small animal anesthesia device. 20 min static single-frame PET scans were acquired using a small animal PET scanner (miniPET-II, Department of Nuclear Medicine, Debrecen) to visualize the tumors. On the same animal the ^{11}C-methionine and ^{18}FDG and ^{18}F-FLT scans were made within 4 days.

The miniPET-II scanner consists of 12 detector modules including LYSO scintillator crystal blocks and position sensitive PMTs [20]. Each crystal block comprises 35 × 35 pins of 1.27 × 1.27 × 12 mm size. Detector signals are processed by FPGA based digital signal processing boards with embedded Linux operating system. Data collection and image reconstruction are performed using a data acquisition module with Ethernet communication facility and a computer cluster of commercial PCs. Scanner normalization and random correction were applied on the data and the images were reconstructed with the standard EM iterative algorithm. The voxel size was 0.5 × 0.5 × 0.5 mm and the spatial resolution varies between 1.4 and 2.1 mm from central to 25 mm radial distances [20]. The system sensitivity is 11.4%.

2.6. PET Data Analysis. Radiotracer uptake was expressed in terms of standardized uptake values (SUVs) and tumor to muscle (T/M) ratios. Ellipsoidal 3-dimensional volume of interest (VOI) was manually drawn around the edge of the tumor xenografts activity by visual inspection using BrainCad software (http:/www.minipetct.hu/). The standardized uptake value (SUV) was calculated as follows: SUV = [VOI activity (Bq/mL)]/[injected activity (Bq)/animal weight (g)], assuming a density of 1 g/cm^3. The T/M ratios were computed as the ratio between the mean activity in the tumor VOI and in the background (muscle) VOI.

2.7. Whole-Body Autoradiography. For whole-body autoradiography the implantation of tumor cells was carried out as described above. On the 16th day after epidermoid carcinoma and on the 25th day after ovarian carcinoma cell implantation tumor-bearing mice were anaesthetized and the radioligands ^{18}F-FLT (4.5 ± 0.2 MBq in 150 μL saline) or ^{18}FDG (5.5 ± 0.2 MBq in 150 μL saline) or ^{18}FAZA (5.5 ± 0.5 MBq in 150 μL saline) were injected via the tail vein. Animals were euthanized 60 min after the administration of ^{18}FDG or ^{18}FLT and 120 min after ^{18}FAZA injection with 300 mg/kg pentobarbital (Nembutal). Each animal was embedded in 1% carboxymethylcellulose solution. After being frozen in liquid nitrogen, 60 μm thin cryostat sections (Leica CM 3600 cryomacrotome, Nussloch, Germany) were cut in the coronal plane. Sections were exposed to phosphorimaging plates (GE Healthcare, Piscataway, NJ, USA). For anatomic correspondence true color images of the sections were also obtained by a transparency scanner (Epson Perfection 1640, EPSON Deutschland GmbH, Meerbusch, Germany). Autoradiography and transmission images were overlaid to fuse the functional and anatomical information. For phosphorimage analysis of selected sections the ImageQuant 5.0 (GE Healthcare, Piscataway, NJ, USA) image analyzing software was used.

2.8. Tumor Sample Preparation. 16 days after epidermoid carcinoma and 25 days after ovarian carcinoma cell implantation mice were euthanized with an overdose of pentobarbital and tumors were dissected from the animals. Tumor samples were embedded in cryomatrix and snap-frozen in liquid nitrogen. Samples were stored at −80°C in an ultralow temperature freezer.

2.9. Immunohistochemistry. Immunohistochemistry was performed on 5 μm thick frozen tumor sections. Frozen sections were dried at room temperature and fixed in precooled acetone (−20°C) for 10 min. Sections were then washed and incubated with 0.3% H_2O_2 in methanol for 20 min to quench endogenous peroxidase activity. After blocking the nonspecific binding with 1% BSA for 20 minutes, sections were incubated for 60 min at room temperature with mouse anti-Pgp monoclonal antibody UIC2 (10 μg/mL). After two washes with PBS, anti-mouse EnVision Detection Systems DAB (Dako, Denmark) was used to visualize the primary antibodies and sections were counterstained with haematoxylin. Negative controls were obtained by omitting the primary antibody.

2.10. Flow Cytometric Measurements. Formaldehyde (1% in PBS) prefixed cells were centrifuged at 500 ×g for 5 min and washed twice with 1% PBS/BSA. To visualize the Pgp expression, cells (1×10^6 cells/mL) were incubated with 10 μg/mL of UIC2 mAb in PBS containing 1% BSA (PBS/BSA) at 37°C for 40 min. After two washes with ice-cold PBS, the cells were incubated with rabbit anti-mouse Alexa 488 secondary antibody (10 μg/mL A488-GaMIgG, Invitrogen, CA) at 4°C for 30 min. Negative controls were obtained by omitting the primary antibody. A Becton-Dickinson FACScan flow cytometer (Becton-Dickinson, Mountain View, CA) was used to determine fluorescence intensities. Emission was detected through a 540 nm broadband interference filter for Alexa 488. Cytofluorimetric data were analyzed by BDIS CELLQUEST (Becton-Dickinson) or FloWin (written by Drs. M. Emri and L. Balkay, Department of Nuclear Medicine, University of Debrecen) software.

2.11. Data Analysis. Data are presented as mean ± SEM of at least three independent experiments. The significance was calculated by Student's t-test (two-tailed). The level of significance was set at $P \leq 0.05$ unless otherwise indicated.

3. Results

3.1. Flow Cytometric Studies. Flow cytometric analyses showed a remarkably high expression of Pgp in the Pgp$^+$ cells.

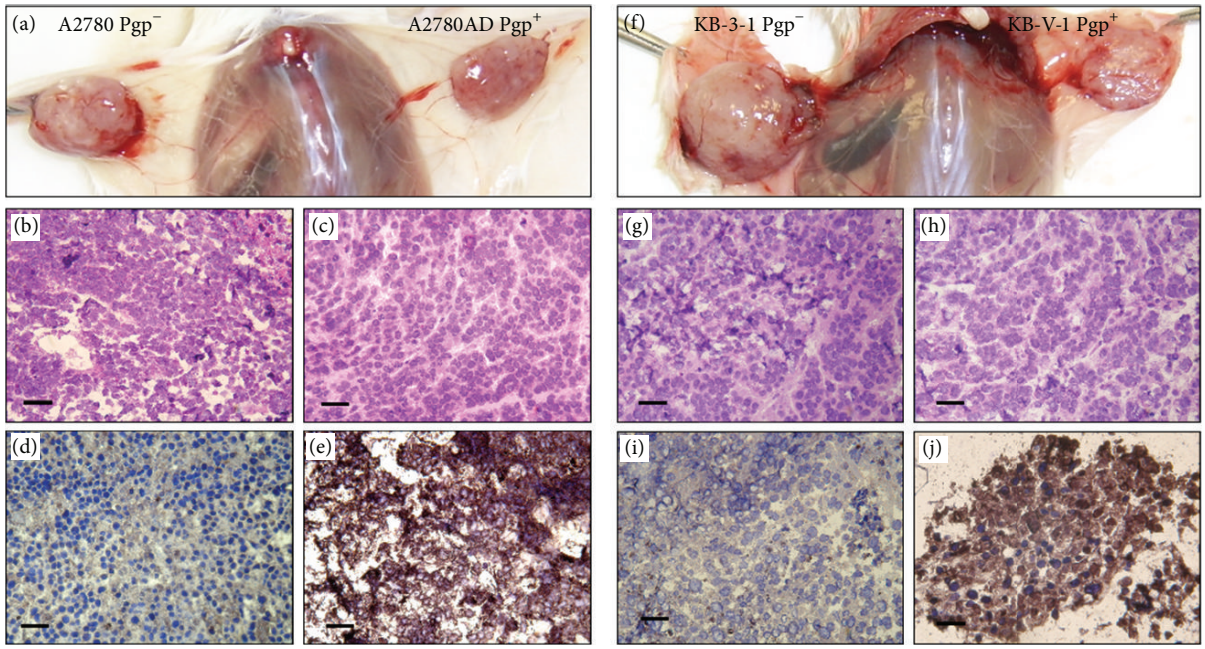

Figure 1: Histopathological analysis of tumor xenografts. Autopsy images show the human ovarian (a) and human epidermoid carcinoma (f) tumor xenografts 25 and 16 days after tumor cell implantation, respectively. Microscopic images of H&E staining ((b) A2780 Pgp^-, (c) A2780AD Pgp^+; (g) KB-3-1 Pgp^-, (h) KB-V-1 Pgp^+) and UIC2 mAb-DAB immunostaining ((d) A2780 Pgp^-, (e) A2780AD Pgp^+; (i) KB-3-1 Pgp^-, (j) KB-V-1 Pgp^+) of xenograft tumor sections. Bar: 50 μm; magnification ×200.

The ratio of the relative mean fluorescence intensities of the Pgp^+/Pgp^- ovarian carcinoma (A2780AD/A2780) and the epidermoid adenocarcinoma (KB-V-1/KB-3-1) cell line pairs was 12.7 ± 2.3 and 10.0 ± 1.8, respectively.

3.2. Histopathological Studies. SCID mice were injected in their left and right sides with Pgp^- (A2780, KB-3-1) and Pgp^+ (A2780AD, KB-V-1) cells, respectively. No morphological differences were seen between the congruous Pgp^- and Pgp^+ tumors upon histopathological analysis of harvested tumors by haematoxylin-eosin (H&E) staining (Figures 1(b), 1(c), 1(g), and 1(h)). Tumor cells implanted into the SCID mice retained their Pgp^+ or Pgp^- phenotype as proved by immunostaining of Pgp. Immunoperoxidase detection showed strong positive staining in Pgp^+ tumor cell membranes (Figures 1(e) and 1(j)); in contrast, no staining was visible in Pgp^- tumors (Figures 1(d) and 1(i)).

3.3. Impact of Combined Treatment on Tumor Volume. Four days after the s.c. injection of tumor cells mice were treated with a combination of UIC2 monoclonal antibody, DOX, and CSA. Other groups of animals (tumor-bearing control (untreated)) were injected with PBS. The growth rate of the ovarian carcinoma tumors (A2780 Pgp^- and A2780AD Pgp^+) was slower (doubling time: 4 days) than that of the epidermoid carcinoma tumors (KB-3-1 Pgp^- and KB-V-1 Pgp^+; doubling time: 3 days). The growth rates of the treated tumors were compared to that of the untreated tumors in both the cases of the Pgp^+ and the Pgp^- ones. In contrast to the control (untreated) tumors, where exponential growth was observed, the combined treatment inhibited the tumor growth (Figure 2). In case of the human ovarian carcinoma xenografts, from day 10 significant differences (on day 10: $P \leq 0.05$, on day 25: $P \leq 0.01$) were observed between the treated and untreated A2780AD and A2780 tumor volumes. These results were similar to the experiments with the human epidermoid carcinoma xenografts, where we found significant differences in the volume (from day 8: $P \leq 0.05$, from day 14: $P \leq 0.01$) of the control and treated tumors (Figure 2(b)).

3.4. miniPET Imaging of Combined Treated and Untreated Tumor Xenografts. For *in vivo* visualization of the effect of the combined treatment on tumors ^{18}FDG and ^{18}F-FLT miniPET scans were performed at different time points and SUVmean, SUVmax, T/Mmean, and T/Mmax ratios were calculated (Figure 3). Fifteen to twenty days after A2780 Pgp^- and A2780AD Pgp^+ cell implantation control (untreated) and combined treated tumor-bearing mice (6 mice, 24 tumors) received ^{18}FDG and ^{18}F-FLT. Control tumors demonstrated high ^{18}FDG and ^{18}F-FLT uptake (Figure 3(a), left). Quantitative image analysis showed significant differences ($P < 0.001$) between the ^{18}FDG avidity of treated Pgp^+ (SUVmean = 0.33 ± 0.03 and SUVmax = 0.54 ± 0.06) and untreated Pgp^+ (SUVmean = 1.62 ± 0.25 and SUVmax = 2.96 ± 0.6) tumors and also between the treated Pgp^- (SUVmean = 0.56 ± 0.03 and SUVmax = 0.94 ± 0.07) and untreated Pgp^- (SUVmean = 1.43 ± 0.17 and SUVmax = 2.51 ± 0.3) tumors. By taking the T/M ratios, the differences between the treated and untreated tumors were also significant ($P < 0.001$). The

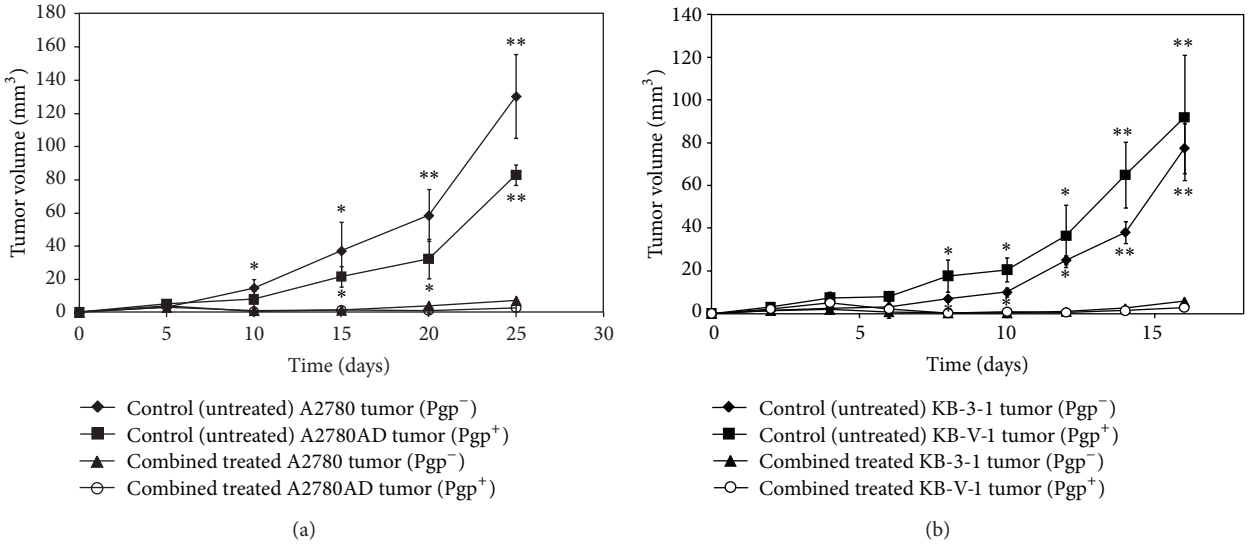

Figure 2: Impact of combined treatment on tumor growth. Pgp^+ and Pgp^- treated tumors' volumes were compared to Pgp^+ and Pgp^- control (untreated) tumors in tumor-bearing animals. Treatments began 4 days after tumor cell inoculations. (a) Impact of combined treatment on A2780AD Pgp^+ and A2780 Pgp^- (6 mice, 24 tumors). (b) Impact of combined treatment on KB-V-1 Pgp^+ and KB-3-1 Pgp^- tumors (6 mice, 24 tumors). Statistically significant changes in tumor volume compared to the tumor volume of untreated control are indicated ($^*P \leq 0.05$, $^{**}P \leq 0.01$).

uptake of ^{18}F-FLT was significantly increased at the control tumors compared with that at the combined treated tumors (Figure 3(b), left). The ^{18}F-FLT miniPET imaging and SUV values showed the efficiency of the combined treatment.

The biodistribution of ^{18}FDG and ^{18}F-FLT on days 10–15 following tumor inoculation in epidermoid carcinoma bearing mice is shown in Figure 3(a). The results of ^{18}FDG and ^{18}F-FLT miniPET scans showed significant accumulation in the untreated control tumors (Figure 3(a), right), in contrast to the combined treated KB-V-1 Pgp^+ and KB-3-1 Pgp^- tumors.

Overall, in the treated animals the T/M ratios showed no difference in the ^{18}FDG and ^{18}F-FLT uptake between the place of inoculation and its muscle environment, proving the lack of tumor cells. No significant differences were observed with these two radiopharmaceuticals in the SUV values between Pgp^+ and Pgp^- tumors.

Fifteen to twenty days after A2780 Pgp^- and A2780AD Pgp^+ cell implantation control (untreated) and treated tumor-bearing mice received ^{11}C-methionine. Control tumors showed high ^{11}C-methionine uptake (Figure 4(a)). Quantitative image analysis demonstrated that there were notable differences between the ^{11}C-methionine avidity of the treated Pgp^+ (SUVmean = 0.43 ± 0.02 and SUVmax = 0.83 ± 0.03) and untreated Pgp^+ (SUVmean = 1.35 ± 0.46 and SUVmax = 2.20 ± 0.6) tumors and also between the treated Pgp^- (SUVmean = 0.45 ± 0.03 and SUVmax = 0.84 ± 0.06) and untreated Pgp^- (SUVmean = 1.35 ± 0.8 and SUVmax = 2.40 ± 1.5) tumors.

The ^{11}C-methionine miniPET imaging (Figure 4(b)) and SUV values also showed the efficiency of the combined treatment in case of the epidermoid tumor xenografts. 10–15 days after KB-3-1 and KB-V-1 tumor cell implantation the quantitative image analysis showed notable differences between the ^{11}C-methionine uptake of the treated Pgp^+ (SUVmean = 0.49 ± 0.03 and SUVmax = 0.84 ± 0.02) and untreated Pgp^+ (SUVmean = 1.52 ± 0.43 and SUVmax = 2.43 ± 0.68) tumors and also between the treated Pgp^- (SUVmean = 0.49 ± 0.03 and SUVmax = 0.76 ± 0.05) and untreated Pgp^- (SUVmean = 1.48 ± 0.46 and SUVmax = 2.55 ± 1.0) tumors.

3.5. Assessment of Heterogeneity in Tumor Metabolism Using Radiopharmaceuticals. The metabolic heterogeneity of control tumors was investigated on the same animal by ^{18}FDG (22 days after tumor cell injection), ^{18}FAZA (23 days after tumor cell injection), and ^{18}F-FLT (24 days after tumor cell injection) using miniPET scanner and autoradiography techniques. Control tumors demonstrated heterogeneous ^{18}F-FLT uptake, with some areas of moderate uptake surrounded by areas of intense uptake, indicating the proliferation of tumor cells. We found that the ^{18}FDG positive tumor areas and the ^{18}F-FLT negative areas overlapped one another. The ^{18}FAZA uptake of these areas was high. After the quantitative analysis of the miniPET images the differences in the metabolic activity of the investigated tumors are shown on a representative figure (Figure 5). By taking the SUVmean values we found the following: ^{18}FDG avid areas: 1.20 ± 0.27, not ^{18}FDG avid areas: 0.79 ± 0.13; ^{18}F-FLT avid areas: 2.67 ± 0.35, not ^{18}F-FLT avid areas: 2.15 ± 0.19; ^{18}FAZA avid-hypoxic-areas: 0.70 ± 0.08, not ^{18}FAZA avid-not hypoxic-areas: 0.53 ± 0.07.

4. Discussion

Xenograft model and the miniPET technique are recently commonly used noninvasive methods in preclinical studies to

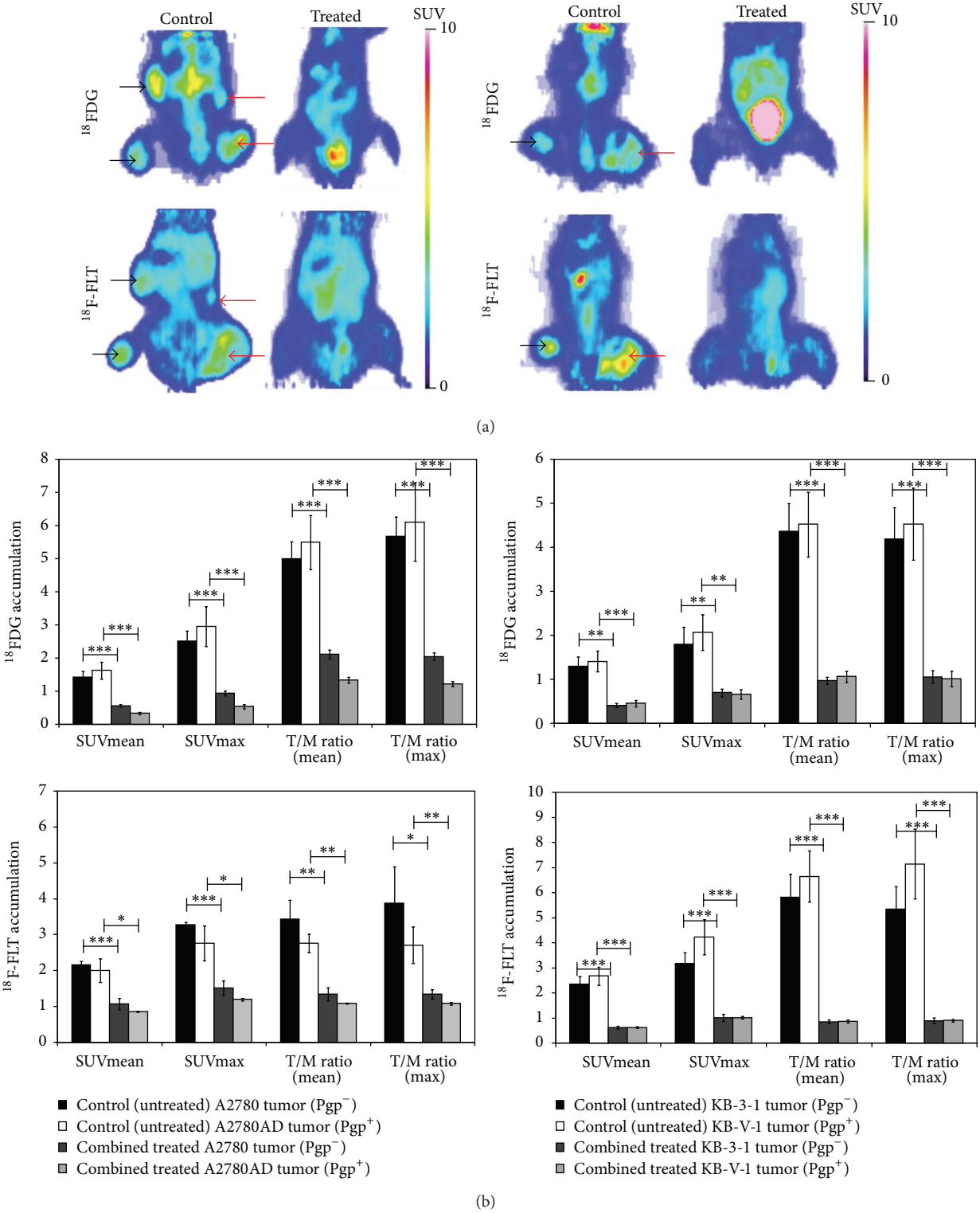

Figure 3: Effect of combined treatment on the ^{18}FDG and ^{18}F-FLT uptake of Pgp positive and negative human ovarian (left side) and epidermoid carcinoma (right side) tumors. (a) ^{18}FDG and ^{18}F-FLT miniPET images of control and combined treated Pgp$^-$ (left side, black arrows) and Pgp$^+$ (right side, red arrows) tumor-bearing mice (coronal sections). No tumors can be visualized in the treated animals. (b) The SUVmean and SUVmax and the mean and maximum T/M ratios are displayed (bars represent mean ± SEM). Statistically significant differences in comparison to combined treated tumors are indicated ($^*P \leq 0.05$, $^{**}P \leq 0.01$, and $^{***}P \leq 0.001$).

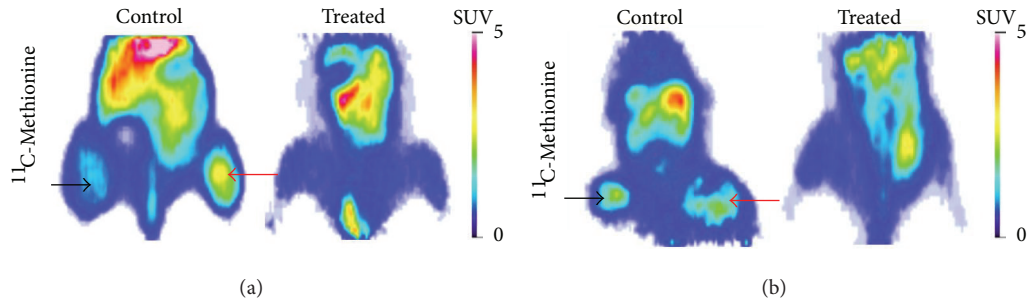

FIGURE 4: Effect of combined treatment on the ^{11}C-methionine uptake of Pgp positive and negative human ovarian (a) and epidermoid carcinoma (b) tumors. ^{11}C-Methionine miniPET images of control and treated Pgp$^-$ (left side, black arrows) and Pgp$^+$ (right side, red arrows) tumor-bearing mice (coronal sections). No tumors can be visualized in the treated animals.

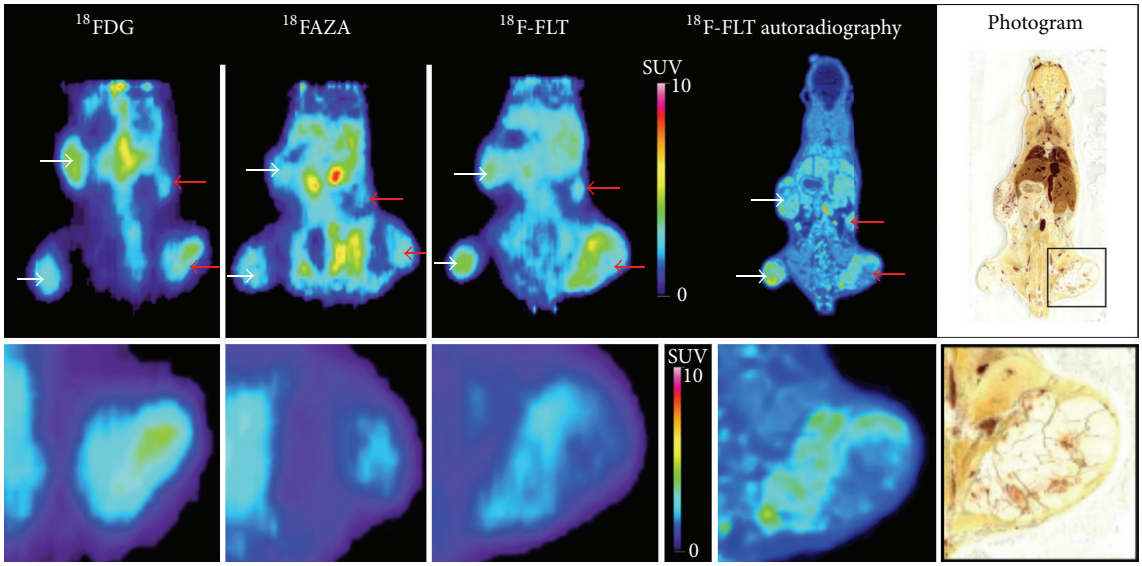

FIGURE 5: miniPET and whole-body autoradiography images from the same control tumor-bearing (ovarian carcinoma) SCID mouse (upper). Lower panels demonstrate the tumor heterogeneity using different radiopharmaceuticals on a representative Pgp$^+$ tumor. White arrows: Pgp$^-$ tumors; red arrows: Pgp$^+$ tumors. Color bars regard to the PET images only.

detect and follow up the effect of therapy of human tumors, using PET tumor diagnostic radiopharmaceuticals, like ^{18}FDG, ^{18}F-FLT, ^{18}FAZA, and ^{11}C-methionine.

It has been demonstrated earlier by Goda et al. [11], and Krasznai et al. [12] in their *in vitro* and *ex vivo* experiments that the combined application of the Pgp specific antibody UIC2 and cyclosporine A is a successful strategy to overcome Pgp-mediated multidrug resistance.

In our experiments we used similar treatment carried out on mouse xenografts. Our aim was to test the efficacy of the combined treatment on drug sensitive and resistant human ovary and cervix cancer xenograft models by using *in vivo* medical imaging technique (miniPET) and the most commonly applied tumor diagnostic radiopharmacons (^{18}FDG, ^{18}F-FLT, and ^{11}C-metionine) in the visualization of gynecological tumors.

The tumor cells were inoculated at four places in each animal in order to provide self-control experiment and reduce the necessary number of experimental animals. The presence of Pgp in the tumors was proved by immunohistochemistry (Figure 1).

The A2780 and A2780AD human ovarian tumors grew slower than the epidermoid adenocarcinoma tumors (KB-3-1, KB-V-1) (Figure 2). The treatment of the tumors started four days after the inoculation using a dose of 5 mg/kg doxorubicin. The size of the tumors was small (2–5 mm^3) but visually observable. Lee et al. [21] performed efficacy studies using BALB/c mice bearing C-26 colon carcinoma tumors. In their study they applied dendrimer-DOX in which the DOX was attached by means of a stable carbamate bond in an equivalent of 20 mg/kg doxorubicin in a single dose 8 days after tumor implantation, which caused complete tumor regression and 100% survival. Kratz et al. [22] published similar results: they observed in both male and female mice an LD50 of doxorubicin 12 mg/kg. Graf et al. [23] have shown that tumor growth was inhibited by a single dose of doxorubicin ranging from 25 μg to 200 μg in xenograft lymphoma tumors. Kim et al. [24] treated the human ovarian A2780/DOX carcinoma

xenografts with 10 mg/kg DOX three times at 3-day intervals without any effect of the MDR resistant tumor growth.

In our work we diagnosed the presence and followed the growth of multidrug sensitive and resistant tumors as well as the efficacy of the combined treatment with three tumor diagnostic tracers. The results show that the ^{18}FDG (a glucose metabolic tracer), ^{11}C-methionine (tracer for amino acid transport and protein synthesis), and the ^{18}F-FLT (a proliferation tracer) can be effectively used for monitoring both the Pgp$^+$ and the Pgp$^-$ tumors. The accumulation of the tracers could be followed by definite SUV values although the ^{18}F-FLT SUV values were higher than that of the ^{18}FDG (Figure 3) Ong et al. [25] called attention to the fact that the PET tracer accumulation can be different in *in vitro* experiments with tumor cells and in xenografts made from the same cells *in vivo*; therefore the pharmacon uptake should be tested. Xenografts *in vivo* can be less sensitive to PET tumor diagnostic tracers than cell lines *in vitro*. In our experiments in both the A2780 and the A2780AD, as well as the KB-3-1 and KB-V-1 Pgp$^+$ and Pgp$^-$ cell line pairs, just as the xenografts made with these cell lines, all three tumor diagnostic tracers (^{18}FDG, ^{18}F-FLT, and ^{11}C-methionine) could be well used. Jensen et al. [5] used ovarian cancer (A2780) xenografts in nude mice and they—similarly to our results—measured higher ^{18}F-FLT than ^{18}FDG uptake. On the other hand they measured approximately 50% lower SUVmean and SUVmax values compared to our results. The differences can be explained by the different experimental protocols and the biological differences between the nude and SCID mice. Ebenhan et al. [26] used KB-3-1 cervix carcinoma xenograft model (in nude mice) and found that the xenografts showed low ^{18}FDG SUV and were better visualized by ^{18}F-FLT. It is in agreement with other studies reporting that for assessing the early response to anticancer treatment ^{18}F-FLT was superior to ^{18}FDG [5]. However, other studies found higher ^{18}FDG uptake compared to ^{18}F-FLT accumulation in several xenograft models [27, 28]. In our experiments both tracers showed good visualization of the Pgp$^+$ and Pgp$^-$ tumors and the efficacy of the treatment.

^{18}FDG, the most commonly used PET radiotracer in tumor diagnostics, allows visualization of the changes in the glucose metabolic rate in tumors [3]. Since Pgp is a transport ATPase, its activity may increase the ATP demand of the cells expressing it at high level [12]. The increased energy demand of the cancer cells manifests in higher glucose metabolisms that can be measured by ^{18}FDG accumulation, but a number of factors can affect the FDG uptake in tumors [1, 3, 29, 30].

The different proliferation activity of the different tumors as well as the variance in the tumor volume suffering hypoxia may result in further differences in the ^{18}FDG uptake (Figure 5). Similarly to our results, several authors report heterogeneity in the ^{18}FDG uptake of different tumors [31, 32]. The experimental model used in our experiments provides exactly the same extracellular conditions (free glucose concentration in the blood, injected radiotracer dose, anaesthetizing procedure, etc.) since both of the Pgp$^+$ and the Pgp$^-$ tumors grow in the same mice; therefore the measured differences in the accumulation of the radiopharmacon show the intrinsic characters of the tumors.

In our experiments, we initiated the treatment of the tumors four days after the inoculation of the cells, when the gynecologic tumors were still rather small. We aimed to develop a model analogous to the clinical situation, when after removing the tumor by surgery a systemic therapy is applied to hinder the development of multidrug resistant primary or metastatic tumors.

Our results show that the above described combined treatment is an effective method for the chemotherapy of both Pgp$^+$ and Pgp$^-$ human ovarian carcinoma and epidermoid adenocarcinoma tumors growing in mice, and the efficacy of the treatment can be followed by miniPET using ^{18}FDG, ^{18}F-FLT, and ^{11}C-methionine radiotracers. In addition, ^{18}FAZA is a suitable tracer to detect the hypoxia of the tumor in xenografts. Using multitracer miniPET ^{18}FDG, ^{18}F-FLT, and ^{18}FAZA analyses also help to detect the metabolic heterogeneity of the tumors.

Abbreviations

CSA: Cyclosporine A
DOX: Doxorubicin
^{18}FAZA: [^{18}F]Fluoroazomycin-arabinofuranoside
^{18}FDG: 2-[^{18}F]Fluoro-2-deoxy-D-glucose
^{18}F-FLT: (3′-Deoxy-3′-[^{18}F]fluorothymidine)
mAb: Monoclonal antibody
MDR: Multidrug resistance
PBS: Phosphate buffered saline
PET: Positron emission tomography
Pgp: P-Glycoprotein
Pgp$^+$: P-Glycoprotein positive
Pgp$^-$: P-Glycoprotein negative.

Conflict of Interests

The authors declare that there is no conflict of interests regarding the publication of this paper.

Authors' Contribution

György Trencsényi and Teréz Márián contributed equally to this study.

Acknowledgments

This work was supported by Szodoray grant from the University of Debrecen (recipients are Z. T. Krasznai and K. Goda). The work was also supported by OTKA Grants PD75994, K72762, NK101337, NK101680, and TÁMOP-4.2.2.A-11/1KONV-2012-0023. The authors also thank Tamás Nagy and Judit P. Szabó for the technical assistance.

References

[1] R. L. Wahl, "Targeting glucose transporters for tumor imaging: "sweet" idea, "sour" result," *Journal of Nuclear Medicine*, vol. 37, no. 6, pp. 1038–1041, 1996.

[2] E. M. Rohren, T. G. Turkington, and R. E. Coleman, "Clinical applications of PET in oncology," *Radiology*, vol. 231, no. 2, pp. 305–332, 2004.

[3] S. Vallabhajosula, " ^{18}F-labeled positron emission tomographic radiopharmaceuticals in oncology: an overview of radiochemistry and mechanisms of tumor localization," *Seminars in Nuclear Medicine*, vol. 37, no. 6, pp. 400–419, 2007.

[4] J. S. Rasey, J. R. Grierson, L. W. Wiens, P. D. Kolb, and J. L. Schwartz, "Validation of FLT uptake as a measure of thymidine kinase-1 activity in A549 carcinoma cells," *Journal of Nuclear Medicine*, vol. 43, no. 9, pp. 1210–1217, 2002.

[5] M. M. Jensen, K. D. Erichsen, F. Björkling et al., "Early detection of response to experimental chemotherapeutic top216 with [^{18}F]FLT and [^{18}F]FDG PET in Human Ovary Cancer Xenografts in Mice," *PLoS ONE*, vol. 5, no. 9, Article ID e12965, 2010.

[6] P. L. Jager, W. Vaalburg, J. Pruim, E. G. E. De Vries, K.-J. Langen, and D. A. Piers, "Radiolabeled amino acids: basic aspects and clinical applications in oncology," *Journal of Nuclear Medicine*, vol. 42, no. 3, pp. 432–445, 2001.

[7] M. Piert, H. J. Machulla, M. Picchio et al., "Hypoxia-specific tumor imaging with 18F-fluoroazomycin arabinoside," *Journal of Nuclear Medicine*, vol. 46, no. 1, pp. 106–113, 2005.

[8] H. Glavinas, P. Krajcsi, J. Cserepes, and B. Sarkadi, "The role of ABC transporters in drug resistance, metabolism and toxicity.," *Current drug delivery.*, vol. 1, no. 1, pp. 27–42, 2004.

[9] K. Goda, Z. Bacsó, and G. Szabó, "Multidrug resistance through the spectacle of P-glycoprotein," *Current Cancer Drug Targets*, vol. 9, no. 3, pp. 281–297, 2009.

[10] E. B. Mechetner, B. Schott, B. S. Morse et al., "P-glycoprotein function involves conformational transitions detectable by differential immunoreactivity," *Proceedings of the National Academy of Sciences of the United States of America*, vol. 94, no. 24, pp. 12908–12913, 1997.

[11] K. Goda, F. Fenyvesi, Z. Bacsó et al., "Complete inhibition of p-glycoprotein by simultaneous treatment with a distinct class of modulators and the UIC2 monoclonal antibody," *Journal of Pharmacology and Experimental Therapeutics*, vol. 320, no. 1, pp. 81–88, 2007.

[12] Z. T. Krasznai, Á. Tóth, P. Mikecz et al., "Pgp inhibition by UIC2 antibody can be followed *in vitro* by using tumor-diagnostic radiotracers, ^{99m}Tc-MIBI and ^{18}FDG," *European Journal of Pharmaceutical Sciences*, vol. 41, no. 5, pp. 665–669, 2010.

[13] K. Kitajima, K. Murakami, S. Sakamoto, Y. Kaji, and K. Sugimura, "Present and future of FDG-PET/CT in ovarian cancer," *Annals of Nuclear Medicine*, vol. 25, no. 3, pp. 155–164, 2011.

[14] J. T. Thigpen, J. A. Blessing, P. J. DiSaia, E. Yordan, L. F. Carson, and C. Evers, "A randomized comparison of doxorubicin alone versus doxorubicin plus cyclophosphamide in the management of advanced or recurrent endometrial carcinoma: a Gynecologic Oncology Group Study," *Journal of Clinical Oncology*, vol. 12, no. 7, pp. 1408–1414, 1994.

[15] G. Balbi, S. Visconti, A. Monteverde, M.-A. Manganaro, and A. Cardone, "Liposomal doxorubicin: a phase II trial," *Acta Biomedica de l'Ateneo Parmense*, vol. 78, no. 3, pp. 210–213, 2007.

[16] N. Aide, M. Briand, P. Bohn et al., "$\alpha v\beta 3$ imaging can accurately distinguish between mature teratoma and necrosis in 18F-FDG-negative residual masses after treatment of non-seminomatous testicular cancer: a preclinical study," *European Journal of Nuclear Medicine and Molecular Imaging*, vol. 38, no. 2, pp. 323–333, 2011.

[17] K. Hamacher, H. H. Coenen, and G. Stöcklin, "Efficient stereospecific synthesis of no-carrier-added 2-[^{18}F]-fluoro-2-deoxy-D-glucose using aminopolyether supported nucleophilic substitution," *Journal of Nuclear Medicine*, vol. 27, no. 2, pp. 235–238, 1986.

[18] J. R. Grierson and A. F. Shields, "Radiosynthesis of 3′-deoxy-3′-[18F]fluorothymidine: [18F]FLT for imaging of cellular proliferation in vivo," *Nuclear Medicine and Biology*, vol. 27, no. 2, pp. 143–156, 2000.

[19] M. Mitterhauser, W. Wadsak, A. Krcal et al., "New aspects on the preparation of [^{11}C]Methionine—a simple and fast online approach without preparative HPLC," *Applied Radiation and Isotopes*, vol. 62, no. 3, pp. 441–445, 2005.

[20] I. Lajtos, M. Emri, S. A. Kis et al., "Performance evaluation and optimization of the MiniPET-II scanner," *Nuclear Instruments and Methods in Physics Research A: Accelerators, Spectrometers, Detectors and Associated Equipment*, vol. 707, no. 36, pp. 26–34, 2013.

[21] C. C. Lee, E. R. Gillies, M. E. Fox et al., "A single dose of doxorubicin-functionalized bow-tie dendrimer cures mice bearing C-26 colon carcinomas," *Proceedings of the National Academy of Sciences of the United States of America*, vol. 103, no. 45, pp. 16649–16654, 2006.

[22] F. Kratz, G. Ehling, H.-M. Kauffmann, and C. Unger, "Acute and repeat-dose toxicity studies of the (6-maleimidocaproyl)hydrazone derivative of doxorubicin (DOXO-EMCH), an albumin-binding prodrug of the anticancer agent doxorubicin," *Human and Experimental Toxicology*, vol. 26, no. 1, pp. 19–35, 2007.

[23] N. Graf, K. Herrmann, B. Numberger et al., "(^{18}F)FLT is superior to [^{18}F]FDG for predicting early response to antiproliferative treatment in high-grade lymphoma in a dose-dependent manner," *European Journal of Nuclear Medicine and Molecular Imaging*, vol. 40, no. 1, pp. 34–43, 2013.

[24] D. Kim, E. S. Lee, K. Park, I. C. Kwon, and Y. H. Bae, "Doxorubicin loaded pH-sensitive micelle: antitumoral efficacy against ovarian A2780/DOX^R tumor," *Pharmaceutical Research*, vol. 25, no. 9, pp. 2074–2082, 2008.

[25] L.-C. Ong, Y. Jin, I.-C. Song, S. Yu, K. Zhang, and P. K. H. Chow, "2-[^{18}F]-2-deoxy-D-Glucose (FDG) uptake in human tumor cells is related to the expression of GLUT-1 and hexokinase II," *Acta Radiologica*, vol. 49, no. 10, pp. 1145–1153, 2008.

[26] T. Ebenhan, M. Honer, S. M. Ametamey et al., "Comparison of [^{18}F]-Tracers in various experimental tumor models by PET imaging and identification of an early response biomarker for the novel microtubule stabilizer patupilone," *Molecular Imaging and Biology*, vol. 11, no. 5, pp. 308–321, 2009.

[27] Y.-J. Yang, J.-S. Ryu, S.-Y. Kim et al., "Use of 3′-deoxy-3′-[^{18}F]fluorothymidine PET to monitor early responses to radiation therapy in murine SCCVII tumors," *European Journal of Nuclear Medicine and Molecular Imaging*, vol. 33, no. 4, pp. 412–419, 2006.

[28] L. Brepoels, S. Stroobants, G. Verhoef, T. De Groot, L. Mortelmans, and C. De Wolf-Peeters, "18F-FDG and 18F-FLT uptake early after cyclophosphamide and mTOR inhibition in an experimental lymphoma model," *Journal of Nuclear Medicine*, vol. 50, no. 7, pp. 1102–1109, 2009.

[29] A. Breier, L. Gibalova, M. Seres, M. Barancik, and Z. Sulova, "New insight into P-Glycoprotein as a drug target," *Anti-Cancer Agents in Medicinal Chemistry*, vol. 13, no. 1, pp. 159–170, 2013.

[30] T. A. D. Smith, "Influence of chemoresistance and p53 status on fluoro-2-deoxy-d-glucose incorporation in cancer," *Nuclear Medicine and Biology*, vol. 37, no. 1, pp. 51–55, 2010.

[31] S. Chicklore, V. Goh, M. Siddique, A. Roy, P. K. Marsden, and G. J. R. Cook, "Quantifying tumour heterogeneity in ^{18}F-FDG PET/CT imaging by texture analysis," *European Journal of Nuclear Medicine and Molecular Imaging*, vol. 40, no. 1, pp. 133–140, 2013.

[32] D. Vriens, J. A. Disselhorst, W. J. G. Oyen, L.-F. De Geus-Oei, and E. P. Visser, "Quantitative assessment of heterogeneity in tumor metabolism using FDG-PET," *International Journal of Radiation Oncology Biology Physics*, vol. 82, no. 5, pp. e725–e731, 2012.

Hindawi Publishing Corporation
BioMed Research International
Volume 2014, Article ID 798474, 2 pages
http://dx.doi.org/10.1155/2014/798474

Erratum

Erratum to "Biodistribution and SPECT Imaging Study of ^{99m}Tc Labeling NGR Peptide in Nude Mice Bearing Human HepG2 Hepatoma"

Wenhui Ma, Zhe Wang, Weidong Yang, Xiaowei Ma, Fei Kang, and Jing Wang

Department of Nuclear Medicine, Xijing Hospital, Fourth Military Medical University, No. 127 West Changle Road, Xi'an, Shaanxi Province 710032, China

Correspondence should be addressed to Jing Wang; wangjing@fmmu.edu.cn

Received 4 June 2014; Accepted 7 July 2014; Published 5 August 2014

In the paper titled "*Biodistribution and SPECT imaging study of ^{99m}Tc labeling NGR peptide in nude mice bearing human HepG2 hepatoma,*" there is a mistake in the chemical structure of the NGR sequence and it is corrected in Figure 1 below. There is also a number mistake in the part of Materials and Methods (2.4. Cell Culture and Animal Model) that the HepG2 tumor model was established by subcutaneous injection of 5×10^6 HepG2 tumor cells (0.1 mL) into the right upper flanks, but not 2×10^6.

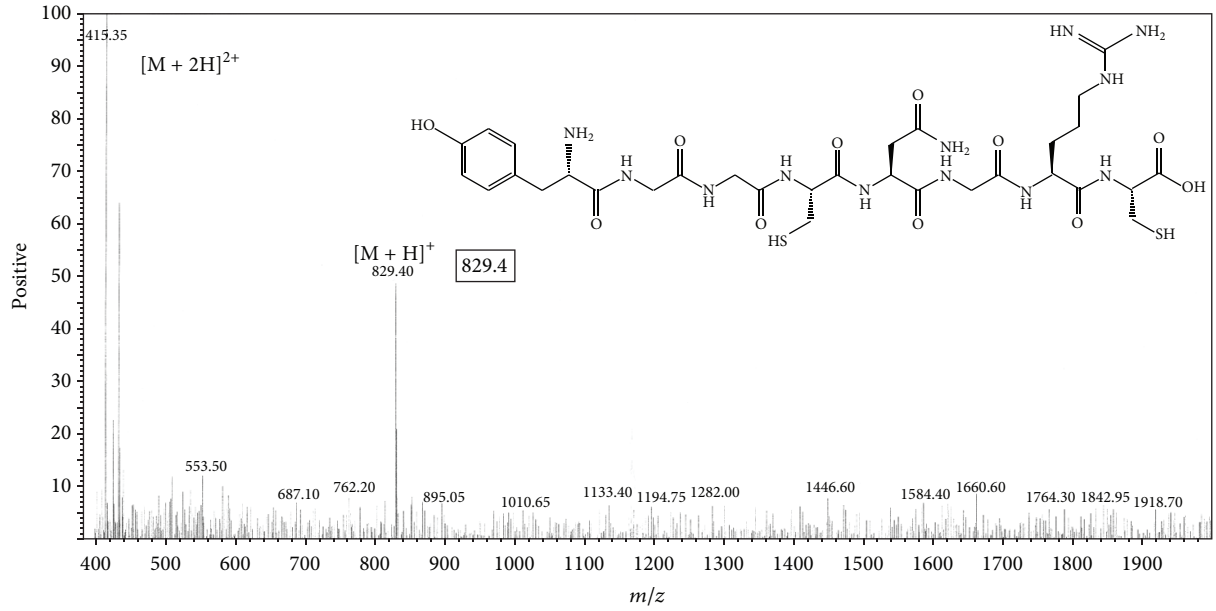

Figure 1: Chemical structure and mass result of NGR (YGGCNGRC).

Hindawi Publishing Corporation
BioMed Research International
Volume 2014, Article ID 572532, 8 pages
http://dx.doi.org/10.1155/2014/572532

Clinical Study

CEUS Helps to Rerate Small Breast Tumors of BI-RADS Category 3 and Category 4

Jian-xing Zhang,[1] Li-shan Cai,[2] Ling Chen,[1] Jiu-long Dai,[1] and Guang-hui Song[1]

[1] *Departments of Ultrasound, Second Affiliated Hospital, Guangzhou University of Traditional Chinese Medicine, Guangzhou 510120, China*
[2] *Departments of Ultrasound, First Affiliated Hospital, Guangzhou University of Traditional Chinese Medicine, Guangzhou 510405, China*

Correspondence should be addressed to Jian-xing Zhang; venant@126.com

Received 14 February 2014; Revised 29 April 2014; Accepted 1 May 2014; Published 25 May 2014

Academic Editor: Zhiyi Chen

Purpose. The primary aim of this study was to explore if classification, whether using the BI-RADS categories based on CEUS or conventional ultrasound, was conducive to the identification of benign and malignant category 3 or 4 small breast lesions. *Material and Methods*. We evaluated 30 malignant and 77 benign small breast lesions using CEUS. The range of enhancement, type of enhancement strength, intensity of enhancement, and enhancement patterns were independent factors included to assess the BI-RADS categories. *Results*. Of the nonenhanced breast lesions, 97.8% (44/45) were malignant, while, of the hyperplasic nodules, 96.8% (30/31) showed no enhancement in our study. Category changes of the lesions were made according to the features determined using CEUS. The results showed that these features could improve diagnostic sensitivity (from 70.0 to 80.0, 80.0, 90.0, and 90.0%), reduce the negative likelihood ratio (from 0.33 to 0.22, 0.25, 0.11, and 0.12), and improve the NPV (from 88.8 to 92.2, 91.2, 96.2, and 95.5%). However, this was not conducive to improve diagnostic specificity or the PPV. *Conclusion*. The vast majority of nonenhanced small breast lesions were malignant and most of the hyperplasic nodules showed no contrast enhancement. As a reference, CEUS was helpful in identifying BI-RADS category 3 or 4 small breast lesions.

1. Introduction

The American College of Radiology Breast Imaging Reporting and Data System (ACR BI-RADS) proposed ultrasound breast disease standardized diagnostic criteria in 2003 [1]. However, its low specificity has been troubling to clinicians [2, 3]. In the ACR-BI-RADS-US criteria, category 3 (less than 2 percent risk of malignancy) or category 4 (probability of cancer, ranging from 3 to 94 percent) lesions are considered different degrees of malignant breast lesions. This is especially true for hyperplastic nodules in category 3, which are considered to be uncertain ones. Such lesions do not have obvious characteristics of benign lesions, but they are still considered subjectively as category 3 lesions. There are 1-2 nonbenign characteristics of category 4 lesions, but the ACR does not provide any detailed guidance. This leads to poor interobserver consistency in classification. As one study shows [4], in some of the diagnostic category 4 subclasses, consistency is poor, especially for category 4c. This poor reproducibility reflects the highly subjective nature of this classification.

Contrast-enhanced ultrasound (CEUS) of the breast is less commonly performed than abdominal CEUS [5, 6]. In previous studies, ultrasound contrast medium was used to help differentiate between benign and malignant breast disease. However, use of this technique did not always give uniform results [7–9]. Early breast cancer detection, diagnosis, and treatment have been shown to be the key to improving the cure rate and reducing mortality [10]. On clinical exam, the current discovery rate of detection of early breast cancer in the United States is 25%, so accurate ultrasound diagnosis of early breast cancer is imperative to improve early detection; however, diagnosis of early breast cancer using ultrasound is difficult [10]. There is a higher rate of misdiagnosis and missed diagnosis of small size, nonpalpable, and atypical ultrasonographic early stage breast cancer, especially when

the maximum diameter of the lesion is ≤10 mm (cancer clinical stage belongs to T1a and T1b) [11]. The ability to diagnose early stage breast cancer when lesions are ≤10 mm would have important clinical value by improving cure rates.

There have been no published studies done on breast cancer lesions in the diameter range of 1–10 mm. On the basis of previous studies, we have summarized the characteristics of CEUS used in the detection of benign and malignant breast lesions. We have also explored the clinical value of ultrasound technology in diagnosing breast cancer at the early and malignant stages when nodules are classified as T1a or T1b and belong to BI-RADS-US category 3 or 4. At the same time, this study also explored whether the corrected BI-RADS category was appropriate in identifying breast lesions at the early and malignant stages based on CEUS.

2. Materials and Methods

2.1. Patients. Approval from the Regional Ethics Committee was obtained for this study. Written informed consent was obtained from all patients participating in this study. A total of 107 patients (each with one lesion) were evaluated from June 2011 to April 2013. All patients underwent conventional preoperative ultrasonography (US) and CEUS. The results showed that all nodules belonged to category 3 or 4 using US, and the size of the lesions ranged from 1 to 10 mm.

None of the lesions were biopsied before contrast studies were performed. The inclusion criterion was the presence of lesions on US. The exclusion criterion was contraindication to contrast agent administration. The contrast agent was not given if patients had heart disease, pulmonary or respiratory disease, or hypertension, were allergic to the contrast agent, or were pregnant or breast-feeding.

All patients underwent surgery and had a final pathologic diagnosis. Malignant lesions were found in 30 patients (age range from 31 to 71 years old and mean age was 49 years old), and 77 patients had benign lesions (age range from 25 to 64 years old and mean age was 44 years old) according to the histopathology.

2.2. Conventional and Contrast-Enhanced Imaging Protocol. GE LOGIQ E9 and LOGIQ 9 systems (GE Healthcare, USA) with a linear array transducer (LOGIQ 9 M12L or LOGIQ E9 ML6–15) were used for conventional US. A 4–9 MHz linear transducer was used for CEUS. The contrast agent was SonoVue (Bracco SpA, Milan, Italy), a lyophilized powder of phospholipid-stabilized microbubbles containing sulfur hexafluoride gas with a mean diameter of 2.5 μm. The solution was reconstituted by the addition of 5 mL of sterile saline. B-mode pulse inversion harmonic imaging was used in CEUS. Settings were as follows: mechanical index was 0.12-0.13, image depth was 3 or 4 cm, the single focus was at the bottom of the image, and the probe was stabilized manually and no pressure was exerted.

One ultrasound physician (JX Zhang with 15 years of experience in breast US) performed all US and CEUS examinations. On the US, the maximum imaging plane of the mass, which included the mass and its surrounding normal tissue (if it was possible), was selected for CEUS. After a manual bolus injection of 2.4 mL of SonoVue via a 20-gauge cannula placed in the antecubital vein, the selected plane remained unchanging during the examination and real-time imaging was recorded for up to 3 min. All static and dynamic images were stored in the ultrasound systems, and then single frames in JPEG format and movie files in digital imaging communications in medicine (DICOM) format were exported to a personal computer.

2.3. Pathological Method. A Nikon 80i upright fluorescence microscope, a Shandon Pathcentre tissue processor, a Leica 2145 rotary microtome, and a Leica ST5030 multistainer workstation were used in the pathological examination.

2.4. Image Analysis. All dynamic contrast images and conventional images were stored on the hard drive of the machine. We analyzed the CEUS-detected changes in malignant and benign lesions including contrast-enhanced range, enhanced type, intensity of enhancement, and the pattern of enhancement.

Two ultrasound physicians evaluated all ultrasonographic images without knowledge of patient clinical data, and disagreements were resolved by a third-party appraisal [6, 12].

When results of the echo strength range of the lesion size was less than 17 mm, it was regarded that the range, which was 3 mm larger than the original one, would be considered as the enlarged strength range [13] (Figure 1). When the range was less than that from US or with no enhancement, it was regarded as low-enhancement (Figure 2). In addition to these types of lesions, there were those that were regarded as having equal-enhancement.

Contrast-enhanced images were classified into three categories according to the distribution of enhanced types of the mass: (1) no enhancement, with lack of enhancement after contrast agent injection; (2) homogeneous enhancement, in which diffuse and homogeneous enhancement was apparent across the whole mass; and (3) inhomogeneous enhancement, in which enhancing areas were only in or more confined to the mass periphery; or there was part of the mass that showed homogeneous enhancement; or the mass was heterogeneously enhanced [6, 14, 15].

According to the pattern of enhancement using CEUS, masses were classified into four categories: (1) no enhancement; (2) centripetal enhancement, in which they were enhanced from edge to center; (3) centrifugal enhancement, in which they were enhanced from center to edge; and (4) atypical enhancement, in which they were not typically enhanced [6, 12, 13].

According to the intensity of enhancement using CEUS, contrast-enhanced images were classified into four categories: (1) no enhancement; (2) high-enhancement, in which the lesions were more highly enhanced than that of normal tissue; (3) low-enhancement, in which the lesions were less enhanced than that of normal tissue; and (4) equal-enhancement, in which lesions and normal tissues were equally enhanced [14, 16, 17].

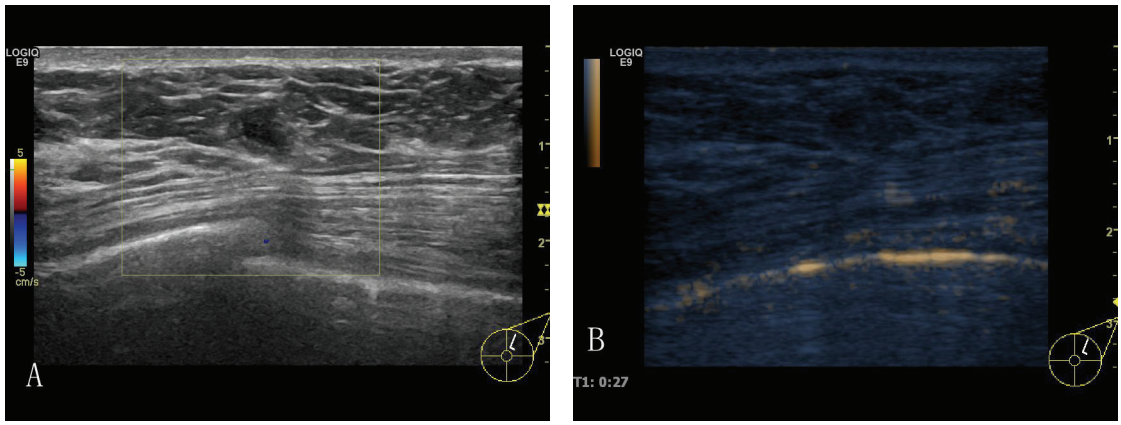

(a) (b)

Figure 1: A sonogram of a right breast from a 42-year-old woman is shown. (a) There was a solid hypoechoic nodule of 5 × 4 mm at 12-1 o'clock in the right breast, with a circumscribed margin and defined, irregular shape, with a heterogeneous internal echo and nodular posterior echo enhancement. CDFI (color Doppler flow imaging): there were no color flow signals in and surrounding the nodule. Ultrasound diagnosis: BI-RADS 4a. CEUS (b): there was no significant enhancement in and surrounding the whole of the nodule. CEUS diagnosis: BI-RADS 3. Pathology: hyperplastic disease.

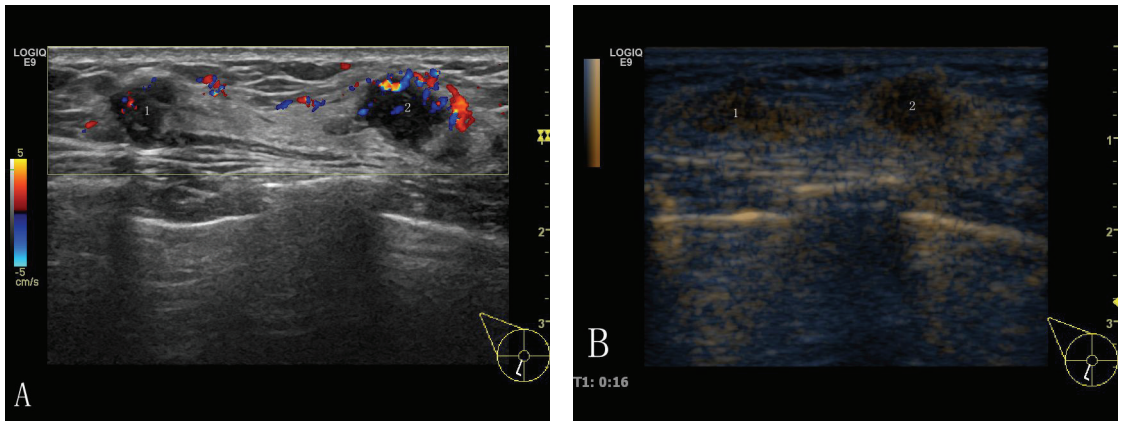

(a) (b)

Figure 2: A sonogram of a right breast from a 57-year-old woman is shown. (a) There were two solid hypoechoic lesions at 7 o'clock in the right breast (lesion 1: 6 × 5 mm and lesion 2: 9 × 7 mm), with a circumscribed margin and defined, irregular shape, with a heterogeneous internal echo and nodular posterior echo enhancement. CDFI (color Doppler flow imaging): rich color flow signals were clearly visible in the nodule and its surrounding. Ultrasound diagnosis: BI-RADS 4c. CEUS (b): in the early arterial phase, nodules within its surrounding with significantly heterogeneous concentric enhancement can be seen. The range of strengthening was greater than the range that was in US. CEUS diagnosis: BI-RADS 5. Pathology: invasive ductal breast carcinoma.

In the literature [6, 14–18], high-enhancement of the lesion, strength and heterogeneous enhancement, and peripheral radial enhancement were considered as standards of breast tumor enhancement. Lesions with the signs mentioned above were regarded as a higher classification of a malignant lesion. Lesions with low malignant-potential changes were converted into the corresponding category of low malignant-potential, which included no enhancement, homogeneous enhancement, centripetal enhancement, and low-enhancement. Others were retained in their original categories. Those have also been described in "*The clinical application guideline of CEUS*" which was proposed by the Chinese Medical Association Sonographer Branch.

2.5. Statistical Analysis. Statistical analysis was conducted using the SPSS statistical package, version 19.0 for Windows (SPSS Institute, Cary, NC, USA). According to the gold standard of pathological diagnosis, we comparatively analyzed the categories used in US with the corrected categories used in CEUS. The results of our study were evaluated on the basis of a statistical compilation and diagnostic test for statistically assessing the discriminatory power of US and CEUS.

3. Results

All 107 lesions were solid-appearing hypoechoic lesions. Thirty lesions were malignant and 77 lesions were benign on

Table 1: Changed category according to the range of enhancement in CEUS.

BI-RADS category	Changed BI-RADS category	Pathology	
		Benign ($n = 77$)	Malignant ($n = 30$)
3 ($n = 31$)	2 ($n = 25$)	25	0
	3 ($n = 5$)	5	0
	4a ($n = 1$)	1	0
4a ($n = 49$)	3 ($n = 32$)	32	0
	4a ($n = 14$)	8	6
	4b ($n = 3$)	0	3
4b ($n = 6$)	4b ($n = 5$)	3	2
	4c ($n = 1$)	1	0
4c ($n = 21$)	4c ($n = 18$)	2	16
	5 ($n = 3$)	0	3

Table 2: Changed category according to the type of enhancement in CEUS.

BI-RADS category	Changed BI-RADS category	Pathology	
		Benign ($n = 77$)	Malignant ($n = 30$)
3 ($n = 31$)	2 ($n = 23$)	23	0
	3 ($n = 6$)	6	0
	4a ($n = 2$)	2	0
4a ($n = 49$)	3 ($n = 20$)	20	0
	4a ($n = 15$)	9	6
	4b ($n = 14$)	11	3
4b ($n = 6$)	4a ($n = 2$)	2	0
	4c ($n = 4$)	2	2
4c ($n = 21$)	4c ($n = 8$)	0	8
	5 ($n = 13$)	2	11

histopathology. Malignant lesions ranged in size from 4 to 10 mm (8.73 mm standard deviation). Benign lesions ranged in size from 3 to 10 mm (7.52 mm standard deviation). Two malignant lesions and 10 benign lesions ranged in size from 3 to 5 mm. There was no significant difference in tumor size between malignant and benign lesions.

Based on US, there were 31 cases of category 3, 49 cases of category 4a, six cases of category 4b, and 21 cases of category 4c in this study. Forty-five lesions showed no obvious contrast enhancement. In those with no enhancement lesions, there were 23 cases of category 3, 21 cases of category 4a,and one case of category 4b.

3.1. Histopathological Findings. There were nineteen cases of invasive ductal carcinoma (IDC), two cases of tubular carcinoma, one case of invasive lobular carcinoma, four cases of mucinous carcinoma, two cases of ductal carcinoma *in situ* (DICS), and two cases of papillary carcinoma with minimal invasion. In the 77 cases of benign lesions, there were 19 fibroadenomas, nine intraductal papillomas, 47 hyperplastic breast lesions (one case of a hyperplastic nodule around the catheter with inflammation, 10 breast adenosis tumors, 31 hyperplastic nodules, three ductal papillary hyperplasias, and one moderate-to-severe dysplasia), one infected cyst, one postoperative scar, and one case of lipoma.

Among these 45 lesions without enhancement, 44 were benign (30 hyperplastic nodules, three breast adenosis tumors, two papillomas, five fibroadenomas, one postoperative scar, two ductal papillary hyperplasias, and one moderate-to-severe dysplasia) and one malignant case (mucinous carcinoma).

3.2. BI-RADS Regulate Category on CEUS. We modified the category of BI-RADS according to the contrast enhancement features using CEUS, which included the range of enhancement (Table 1), type of enhancement (Table 2), intensity of enhancement (Table 3), and pattern of contrast enhancement (Table 4).

Table 3: Changed category according to the intensity of enhancement in CEUS.

BI-RADS category	Changed BI-RADS category	Pathology	
		Benign ($n = 77$)	Malignant ($n = 30$)
3 ($n = 31$)	2 ($n = 25$)	25	0
	3 ($n = 1$)	1	0
	4a ($n = 5$)	5	0
4a ($n = 49$)	3 ($n = 23$)	23	0
	4a ($n = 11$)	9	2
	4b ($n = 15$)	8	7
4b ($n = 6$)	4a ($n = 4$)	3	1
	4b ($n = 1$)	1	0
	4c ($n = 1$)	0	1
4c ($n = 21$)	4b ($n = 2$)	2	0
	4c ($n = 3$)	0	3
	5 ($n = 16$)	0	16

Fifty-seven benign lesions with no enhancement or range of enhancement less than that of US modified to the low malignant-potential category as shown in Table 1 and two benign lesions and six malignant lesions with enlarged enhancement modified to the high malignant-potential category; the others were kept in their original category.

Forty-five benign lesions with no enhancement modified to the low malignant-potential category as shown in Table 2, and 17 benign lesions and 16 malignant lesions with inhomogeneous enhancement modified to the high malignant-potential category; the others were kept in their original category.

Fifty-three benign lesions with no enhancement or homogeneous enhancement modified to the low malignant-potential category as shown in Table 3, and 13 benign lesions and 24 malignant lesions with inhomogeneous enhancement modified to the high malignant-potential category; the others were kept in their original category.

Table 4: Changed category according to the pattern of contrast enhancement in CEUS.

BI-RADS category	Changed BI-RADS category	Pathology	
		Benign ($n = 77$)	Malignant ($n = 30$)
3 ($n = 31$)	2 ($n = 23$)	23	0
	3 ($n = 6$)	6	0
	4a ($n = 2$)	2	0
4a ($n = 49$)	3 ($n = 19$)	17	2
	4a ($n = 14$)	13	1
	4b ($n = 16$)	10	6
4b ($n = 6$)	4a ($n = 3$)	3	0
	4b ($n = 1$)	0	1
	4c ($n = 2$)	1	1
4c ($n = 21$)	4b ($n = 6$)	1	5
	4c ($n = 3$)	0	3
	5 ($n = 12$)	1	11

Forty-four benign lesions and seven malignant lesions with no enhancement or centrifugal enhancement modified to the low malignant-potential category as shown in Table 4, and 14 benign and 18 malignant lesions with centripetal enhancement modified to the high malignant-potential category; the others were kept in their original category.

3.3. Different Diagnosis between US and CEUS. Comparisons of the pathological diagnosis on the basis of the determined category 4b in benign and malignant breast tumor were shown in Table 5. The judgment study of benign and malignant breast lesions was shown in Table 6.

4. Discussion

Small lesions of early breast cancer are nonpalpable, especially if the size of lesion is between 1 and 10 mm (stages T1a and T1b). These lesions have no typical ultrasonographic features and there is a high rate of misdiagnosis and missed diagnosis [19]. Meanwhile, tumor sizes ≤10 mm are also difficult to diagnose and are mainly category 3 or 4 cases. If these tumors were malignant, they were still in DICS Stage or in the early stages of invasion. Early detection has a much more positive impact on the treatment, prognosis, and survival rate of breast cancer patients [20]. Early diagnosis of the disease also determines the treatment options described in the National Comprehensive Cancer Network (NCCN) guidelines. However, there are numerous differences between treatments for T1a, T1b, and other size tumors [11]. This study not only helps to clearly identify the type of lesion but also can lead to a reduction of unnecessary biopsies or reviews. At the same time, it also reduces patient suffering and improves the effectiveness and use of medical resources.

Malignant tumors of the breast have been shown to be readily visualized owing to their contrast medium staining [21–25]. This property has been exploited in contrast medium-enhanced magnetic resonance tomography, which is known, however, for its high sensitivity and low specificity in the identification of carcinomas [26, 27]. During the past decade, the introduction of sonographic microbubble contrast agents has offered an option to improve the ability of detecting the blood flow signal [28–31].

Nonenhanced ultrasound is considered to have a high specificity but a low sensitivity for breast cancer. In our study, 45 lesions showed no obvious contrast enhancement over the entire observed area. Of those cases, most of them were hyperplasic nodules and 96.8% (30/31) of hyperplasic nodules showed no enhancement, consistent with previous studies [32]. It was helpful to change the category of BI-RADS used in the diagnosis of benign and malignant lesions that was based on nonenhanced lesions using CEUS. But it must be noted that one case with no enhancement was a mucinous adenocarcinoma, which has also been reported in the literature [14].

It should be clarified that most investigators have focused their studies on the discrimination between benign and malignant masses [20, 23, 26, 30, 31, 33, 34]. We changed the category of BI-RADS that referred to enhancement features using CEUS [6, 12–18]. In this study, 25 lesions were changed from category 3 to category 2 and 32 lesions from category 4a to category 3, according to the range of enhancement determined using CEUS. All of these lesions were benign. This led to a reduction of unnecessary biopsies or reviews. It also improved the sensitivity (from 70 to 80%), accuracy (from 86.0 to 88.8), PPV (from 77.8 to 80.0%), and NPV (from 88.8 to 92.2%) and reduced the negative likelihood ratio from 0.33 to 0.22. More malignant breast lesions enlarged the range of enhancement using CEUS than using US, while more benign lesions did not [6]. It was easy to identify the range of lesions using CEUS for small lesions. This could increase accuracy of judgments in line. However, the range of enhancement was not enlarged in three malignant lesions, two mucinous carcinomas and one DCIS.

We must point out that most lesions in the modified category were based on lesions without enhancement. Changes also happened in the modified category according to the strength type of enhancement; 20 lesions were changed from category 3 to category 2, and 20 lesions from category 4a to category 3. This improved the sensitivity and reduced the negative likelihood ratio (from 0.33 to 0.25) but did not improve specificity. In these groups, heterogeneous enhancement did not appear in all malignant cases, contrary to what has been described in the literature, whereby an unbalanced spatial distribution of tumor blood vessels could lead to heterogeneous enhancement [19]. It is possible that the reason we did not see heterogeneous enhancement was that the lesions, which were <10 mm, were too small. Thus, there was no significant difference in enhancement of the strength type between benign and malignant lesions, which affected the accuracy of diagnosis using the BI-RADS categories. Another issue was that subjectivity played a large role in determining whether there was heterogeneous enhancement or not in small lesions.

Tumor angiogenesis is the development of a new vascular network essential for tumor growth and infiltration [35, 36] and is the basis for CEUS. This is closely related to the

Table 5: Ultrasound diagnosis in US and CEUS.

	US	Range of enhancement	Type of enhancement	Intensity of enhancement	Enhancement pattern
A (true- positive)	21	24	24	27	27
B (false- positive)	6	6	15	11	13
C (false- negative)	9	6	6	3	3
D (true-negative)	71	71	62	66	64

Table 6: Ultrasound diagnostic study of BI-RADS classification in US and CEUS.

	Sensitivity %	Specificity %	Positive likelihood ratio	Negative likelihood ratio	Youden index %	Accuracy %	PPV %	NPV %
BI-RADS category	70.0	92.1	8.98	0.33	0.62	86.0	77.8	88.8
Range of enhancement	80.0	92.1	10.27	0.22	0.72	88.8	80.0	92.2
Type of enhancement	80.0	80.5	4.11	0.25	0.61	80.4	61.5	91.2
Strengthening of enhancement	90.0	87.4	7.12	0.11	0.77	88.0	71.1	96.2
Enhancement pattern	90.0	83.1	5.33	0.12	0.73	85.1	67.5	95.5

PPV: positive predictive value and NPV: negative predictive value.

microvessel density (MVD) and the strength of enhancement of the tumor using CEUS, as described in the literature [37–39]. In our study, we altered the categories of the BI-RADS using CEUS. Twenty-five lesions were changed from category 3 to category 2, and 32 lesions from category 4a to category 3. Furthermore, sensitivity (from 70 to 90%), accuracy (from 86 to 88%), and NPV (from 88.8% to 96.2%) all increased, and the negative likelihood ratio decreased (from 0.33 to 0.11); however, the PPV was reduced from 8.98 to 7.12. This study shows that malignant lesions also have a richer microvascular than that of benign lesions, even in early breast cancer [36]. Therefore, the strength of enhancement was more obvious using CEUS. There were some benign inflammatory nodule merger cases. Inflammatory responses could also be accompanied by local vascular dilation, which could increase. Two papilloma cases were also high-enhancement ones. Those could interfere with the correction based on categories.

Twenty-three lesions were changed from category 3 to category 2, and 17 lesions from category 4a to category 3, according to their enhancement patterns. This also resulted in an improvement in sensitivity (from 70 to 90%) and a reduction in the rate of negative likelihood ratio (from 0.33 to 0.12); however, specificity and accuracy were worse than with the BI-RADS-US. The presence of inflammatory nodules was one of the causes of misdiagnosis, as was the size of lesions, because it was difficult to identify centrifugal or centripetal enhancement in small lesions.

5. Conclusion

CEUS in breast lesion characterization is a new type of examination that is different from US. It can provide more details on the microvasculature and hemodynamics than US. We explored the value of the categories and the correction of the BI-RADS classification determined using CEUS or US. This was conducive to the identification of benign and malignant breast lesions. Of the no enhancement lesions, 97.8% (44/45) were malignant breast lesions and 96.8% (30/31) of hyperplasic nodules showed no enhancement in our study. Those cases played an important role in the decision to implement the category changes in this study.

The results showed that these features determined using CEUS could improve diagnostic sensitivity, reduce the negative likelihood ratio, and improve the NPV; however, this was not beneficial in improving the specificity of diagnosis and PPV. It can increase the negative likelihood ratio, in which category changes were made according to the strength and range of enhancement. Many benign lesions were changed from category 3 to 2 or from category 4a to 3, according to the features determined using CEUS. These were helpful in the identification of early breast cancer and can be used as a reference.

Conflict of Interests

The authors declare that there is no conflict of interests regarding the publication of this paper.

Authors' Contribution

Jian-xing Zhang and Li-shan Cai contributed equally to this work.

References

[1] American College of Radiology, *Illustrated Breast Imaging Reporting and Data System (BIRADS) Ultrasound*, American College of Radiology, Reston, Va, USA, 2003.

[2] S. J. Kim, E. Y. Ko, J. H. Shin et al., "Application of sonographic BI-RADS To synchronous breast nodules detected in patients with breast cancer," *American Journal of Roentgenology*, vol. 191, no. 3, pp. 653–658, 2008.

[3] J. Heinig, R. Witteler, and R. Schmitz, "Accuracy of classification of breast ultrasound findings based on criteria used for BI RADS," *Ultrasound in Obstetrics & Gynecology*, vol. 32, no. 4, pp. 573–578, 2008.

[4] N. Abdullah, B. Mesurolle, M. El-Khoury, and E. Kao, "Breast imaging reporting and data system lexicon for US: interobserver agreement for assessment of breast masses," *Radiology*, vol. 252, no. 3, pp. 665–672, 2009.

[5] A. Saracco, B. K. Szabó, P. Aspelin et al., "Differentiation between benign and malignant breast tumors using kinetic features of real-time harmonic contrast-enhanced ultrasound," *Acta Radiologica*, vol. 53, no. 4, pp. 382–388, 2012.

[6] H. Liu, Y.-X. Jiang, J.-B. Liu, Q.-L. Zhu, Q. Sun, and X.-Y. Chang, "Contrast-enhanced breast ultrasonography: Imaging features with histopathologic correlation," *Journal of Ultrasound in Medicine*, vol. 28, no. 7, pp. 911–920, 2009.

[7] P. G. Sorelli, D. O. Cosgrove, W. E. Svensson et al., "Can contrast-enhanced sonography distinguish benign from malignant breast masses?" *Journal of Clinical Ultrasound*, vol. 38, no. 4, pp. 177–181, 2010.

[8] C. Balleyguier, P. Opolon, M. C. Mathieu et al., "New potential and applications of contrast-enhanced ultrasound of the breast: own investigations and review of the literature," *European Journal of Radiology*, vol. 69, no. 1, pp. 14–23, 2009.

[9] N. Caproni, F. Marchisio, A. Pecchi et al., "Contrast-enhanced ultrasound in the characterisation of breast masses: utility of quantitative analysis in comparison with MRI," *European Radiology*, vol. 20, no. 6, pp. 1384–1395, 2010.

[10] L. Jia, T. G. Jun, Z. C. Min et al., "Comparative study of light scattering ultrasound imaging and digital mammography for breast cancer diagnosis," *Chinese Journal of Radiology*, vol. 44, no. 5, pp. 470–472, 2010.

[11] National Comprehensive Cancer Network, *NCCN Clinical Practice Guidelines in Oncology*, 2013.

[12] H. Liu, Y.-X. Jiang, J.-B. Liu, Q.-L. Zhu, and Q. Sun, "Evaluation of breast lesions with contrast-enhanced ultrasound using the microvascular imaging technique: initial observations," *Breast*, vol. 17, no. 5, pp. 532–539, 2008.

[13] K. Zeggelink, E. E. Deurloo, H. Bartelink et al., "Reproducibility of the assessment of tumor extent in the breast using multiple image modalities," *Medical Physics*, vol. 30, no. 11, pp. 2919–2926, 2003.

[14] X. Wang, P. Xu, Y. Wang, and E. G. Grant, "Contrast-enhanced ultrasonographic findings of different shistopathologic types of breast cancer," *Acta Radiologica*, vol. 52, no. 3, pp. 248–255, 2011.

[15] J. Du, F.-H. Li, H. Fang, J.-G. Xia, and C.-X. Zhu, "Microvascular architecture of breast lesions: evaluation with contrast-enhanced ultrasonographic micro flow imaging," *Journal of Ultrasound in Medicine*, vol. 27, no. 6, pp. 833–842, 2008.

[16] H. Zhao, R. Xu, Q. Ouyang, L. Chen, B. Dong, and Y. Huihua, "Contrast-enhanced ultrasound is helpful in the differentiation of malignant and benign breast lesions," *European Journal of Radiology*, vol. 73, no. 2, pp. 288–293, 2010.

[17] C. Wan, J. Du, H. Fang, F. Li, and L. Wang, "Evaluation of breast lesions by contrast enhanced ultrasound: qualitative and quantitative analysis," *European Journal of Radiology*, vol. 81, no. 4, pp. e444–e450, 2012.

[18] B. Corcioni, L. Santilli, S. Quercia et al., "Contrast-enhanced US and MRI for assessing the response of breast cancer to neoadjuvant chemotherapy," *Journal of Ultrasound*, vol. 11, no. 4, pp. 143–150, 2008.

[19] J. Zhang, *Breast Ultrasound Diagnosis*, People's Medical Publishing House, 2012.

[20] A. J. Maxwell, I. M. Hanson, C. J. Sutton, J. Fitzgerald, and J. M. Pearson, "A study of breast cancers detected in the incident round of the UK NHS breast screening programme: the importance of early detection and treatment of ductal carcinoma in situ," *Breast*, vol. 10, no. 5, pp. 392–398, 2001.

[21] W. T. Yang, C. Metreweli, P. K. W. Lam, and J. Chang, "Benign and malignant breast masses and axillary nodes: evaluation with echo-enhanced color power Doppler US," *Radiology*, vol. 220, no. 3, pp. 795–802, 2001.

[22] S. Huber, M. Vesely, I. Zuna, S. Delorme, and H. Czembirek, "Fibroadenomas: computer-assisted quantitative evaluation of contrast-enhanced power Doppler features and correlation with histopatholgy," *Ultrasound in Medicine and Biology*, vol. 27, no. 1, pp. 3–11, 2001.

[23] M. Stuhrmann, R. Aronius, and M. Schietzel, "Tumor vascularity of breast lesions: potentials and limits of contrast-enhanced Doppler sonography," *American Journal of Roentgenology*, vol. 175, no. 6, pp. 1585–1589, 2000.

[24] M. H. Chaudhari, F. Forsberg, A. Voodarla et al., "Breast tumor vascularity identified by contrast enhanced ultrasound and pathology: initial results," *Ultrasonics*, vol. 38, no. 1, pp. 105–109, 2000.

[25] E. Bäz, H. Madjar, C. Reuss, M. Vetter, B. Hackelöer, and K. Holz, "The role of enhanced Doppler ultrasound in differentiation of benign vs. malignant scar lesion after breast surgery for malignancy," *Ultrasound in Obstetrics and Gynecology*, vol. 15, no. 5, pp. 377–382, 2000.

[26] L. Alamo and U. Fischer, "Contrast-enhanced color Doppler ultrasound characteristics in hypervascular breast tumors: comparison with MRI," *European Radiology*, vol. 11, no. 6, pp. 970–977, 2001.

[27] U. Aichinger, R. Schulz-Wendtland, S. Krämer, M. Lell, and W. Bautz, "Scar or recurrence—comparison of MRI and color-coded ultrasound with echo signal amplifiers," *RoFo Fortschritte auf dem Gebiet der Rontgenstrahlen und der Bildgebenden Verfahren*, vol. 174, no. 11, pp. 1395–1401, 2002.

[28] S. Huber, T. Helbich, J. Kettenbach, W. Dock, I. Zuna, and S. Delorme, "Effects of a microbubble contrast agent on breast tumors: computer- assisted quantitative assessment with color Doppler US—Early experience," *Radiology*, vol. 208, no. 2, pp. 485–489, 1998.

[29] B. B. Goldberg, J.-B. Liu, P. N. Burns, D. A. Merton, and F. Forsberg, "Galactose-based intravenous sonographic contrast agent: experimental studies," *Journal of Ultrasound in Medicine*, vol. 12, no. 8, pp. 463–470, 1993.

[30] R. P. Kedar, D. Cosgrove, V. R. McCready et al., "Microbubble contrast agent for color Doppler US: effect on breast masses. Work in progress," *Radiology*, vol. 198, no. 3, pp. 679–686, 1996.

[31] A. Özdemir, K. Kılıç, H. Özdemir et al., "Contrast-enhanced power Doppler sonography in breast lesions: effect on differential diagnosis after mammography and gray scale sonography," *Journal of Ultrasound in Medicine*, vol. 23, no. 2, pp. 183–1195, 2004.

[32] F. Caumo, G. Carbognin, A. Casarin et al., "Angiosonography in suspicious breast lesions with non-diagnostic FNAC: comparison with Power Doppler US," *Radiologia Medica*, vol. 111, no. 1, pp. 61–72, 2006.

[33] W. K. Moon, J.-G. Im, D.-Y. Noh et al., "Nonpalpable breast lesions: evaluation with power Doppler US and a microbubble contrast agent—initial experience," *Radiology*, vol. 217, no. 1, pp. 240–246, 2000.

[34] S.-H. Kook and H.-J. Kwag, "Value of contrast-enhanced power Doppler sonography using a microbubble echo-enhancing

agent in evaluation of small breast lesions," *Journal of Clinical Ultrasound*, vol. 31, no. 5, pp. 227–238, 2003.

[35] J. Folkman, "Angiogenesis in cancer, vascular, rheumatoid and other disease," *Nature Medicine*, vol. 1, no. 1, pp. 27–31, 1995.

[36] N. Weidner, J. Folkman, F. Pozza et al., "Tumor angiogenesis: a new significant and independent prognostic indicator in early-stage breast carcinoma," *Journal of the National Cancer Institute*, vol. 84, no. 24, pp. 1875–1887, 1992.

[37] N. Weidner, J. P. Semple, W. R. Welch, and J. Folkman, "Tumor angiogenesis and metastasis—correlation in invasive breast carcinoma," *The New England Journal of Medicine*, vol. 324, no. 1, pp. 1–8, 1991.

[38] N. Weidner, "Current pathologic methods for measuring intratumoral microvessel density within breast carcinoma and other solid tumors," *Breast Cancer Research and Treatment*, vol. 36, no. 2, pp. 169–180, 1995.

[39] C. F. Wan, J. Du, H. Fang et al., "Enhancement patterns and parameters of breast cancers at contrast-enhanced US: correlation with prognostic factors," *Radiology*, vol. 262, no. 2, pp. 450–459, 2012.

Hindawi Publishing Corporation
BioMed Research International
Volume 2014, Article ID 407026, 9 pages
http://dx.doi.org/10.1155/2014/407026

Clinical Study

Hypofractionated High-Dose Irradiation with Positron Emission Tomography Data for the Treatment of Glioblastoma Multiforme

Kazuhiro Miwa,[1,2] Masayuki Matsuo,[3] Shin-ichi Ogawa,[3] Jun Shinoda,[1] Yoshitaka Asano,[1] Takeshi Ito,[4] Kazutoshi Yokoyama,[4] Jitsuhiro Yamada,[4] Hirohito Yano,[5] and Toru Iwama[5]

[1] *Chubu Medical Center for Prolonged Traumatic Brain Dysfunction, Kizawa Memorial Hospital, Minokamo, Gifu 505-0034, Japan*
[2] *Department of Neurosurgery, Chubu Medical Center for Prolonged Traumatic Brain Dysfunction, 630 Shimokobi, Kobi-cho, Minokamo, Gifu 505-0034, Japan*
[3] *Department of Radiation Oncology, Kizawa Memorial Hospital, Minokamo, Gifu 505-0034, Japan*
[4] *Department of Neurosurgery, Kizawa Memorial Hospital, Minokamo, Gifu 505-0034, Japan*
[5] *Department of Neurosurgery, Gifu University Graduate School of Medicine, Gifu 501-1193, Japan*

Correspondence should be addressed to Kazuhiro Miwa; doctor.3@jasmine.ocn.ne.jp

Received 11 February 2014; Accepted 4 May 2014; Published 22 May 2014

Academic Editor: Yi-Xiang Wang

This research paper presents clinical outcomes of hypofractionated high-dose irradiation by intensity-modulated radiation therapy (Hypo-IMRT) with ^{11}C-methionine positron emission tomography (MET-PET) data for the treatment of glioblastoma multiforme (GBM). A total of 45 patients with GBM were treated with Hypo-IMRT after surgery. Gross tumor volume (GTV) was defined as the area of enhanced lesion on MRI, including MET-PET avid region; clinical target volume (CTV) was the area with 5 mm margin surrounding the GTV; planning target volume (PTV) was the area with 15 mm margin surrounding the CTV, including MET-PET moderate region. Hypo-IMRT was performed in 8 fractions; planning the dose for GTV was escalated to 68 Gy and that for CTV was escalated to 56 Gy, while keeping the dose delivered to the PTV at 40 Gy. Concomitant and adjuvant TMZ chemotherapy was administered. At a median follow-up of 18.7 months, median overall survival (OS) was 20.0 months, and median progression-free survival was 13.0 months. The 1- and 2-year OS rates were 71.2% and 26.3%, respectively. Adjuvant TMZ chemotherapy was significantly predictive of OS on multivariate analysis. Late toxicity included 7 cases of Grade 3-4 radiation necrosis. Hypo-IMRT with MET-PET data appeared to result in favorable survival outcomes for patients with GBM.

1. Introduction

Glioblastoma multiforme (GBM) is the most common primary malignancy of the adult central nervous system (CNS) and is associated with an exceptionally poor prognosis. Although radiation therapy (RT) has been shown to prolong overall survival (OS) compared to surgery alone [1], patients treated with RT typically experience disease progression within the radiation field. GBMs are infiltrative tumors that usually spread through normal brain tissue, and it is difficult to demarcate glioma-affected areas from normal brain tissue.

Recently, new methods have been developed that enable elucidation of the biologic pathways of tumors, yielding additional information about the metabolism of the tumor tissue. Functional imaging studies, such as ^{11}C-methionine positron emission tomography (MET-PET), have demonstrated increased metabolic activity due to increased amino acid transport in glioma cells compared to normal brain tissue [2]. Based on recent PET studies, we believe it would be reasonable to conduct a trial designed to evaluate the clinical outcome of RT selectively increasing the radiation dose to high-uptake area of MET-PET in patients with GBM.

Herein, we review our preliminary experience of planning and delivery of hypofractionated high-dose irradiation by intensity-modulated radiation therapy (Hypo-IMRT) with complementary use of MET-PET data. This study was

designed to measure the acute and late toxicity of patients treated with our regimen, response of GBM to this treatment, OS, and the time to disease progression after treatment.

2. Material and Methods

2.1. Patients. From April 2006 to July 2011, 45 patients with newly diagnosed GBM were enrolled. Eligibility criteria included histologically confirmed GBM, age ≥18 years, and adequate bone marrow, liver, and renal function. The extent of surgery was evaluated by three observers by viewing postoperative contrast-enhanced T1-weighted MRI images. Gross total resection of the tumor was defined as resection with no residual enhancing tumor. Exclusion criteria included multifocal or recurrent gliomas, involvement of the brainstem or posterior fossa, cerebrospinal fluid dissemination, severe concurrent disease, or prior history of RT or chemotherapy. Patients were grouped according to radiation therapy oncology group (RTOG) recursive partitioning analysis (RPA) class [3]. The institutional review board approved the study prior to patient enrollment. Informed consent was obtained from each subject after disclosing the potential risks of Hypo-IMRT and discussion of potential alternative treatments, including conventional three-dimensional conformal RT (3D-CRT). Patient characteristics are listed in Table 1.

Table 1: Patient's characteristics.

Parameter	*n* (%)
Age, years	
≥50	37 (82.2)
<50	8 (17.8)
Gender	
Male	28 (62.2)
Female	17 (37.8)
KPS score	
≥70	31 (68.9)
<70	14 (31.1)
RPA class	
III	5 (11.1)
IV	23 (51.1)
V	5 (11.1)
VI	12 (26.7)
Resection	
GTR	17 (37.8)
Others	28 (62.2)
Adjuvant TMZ chemotherapy	
Yes	33 (73.3)
No	12 (26.7)

KPS: Karnofsky performance status, RPA: recursive partitioning analysis, GTR: gross total removal, and TMZ: temozolomide.

2.1.1. Imaging: CT. CT (matrix size: 512 × 512, FOV 50 × 50 cm) was performed using a helical CT instrument (Light Speed; General Electric, Waukesha, WI). Patient heads were immobilized in a commercially available stereotactic mask, and scans were performed with a 2.5 mm slice thickness without a gap.

2.1.2. Imaging: MRI. MRI (matrix size: 256 × 256, FOV 25 × 25 cm) for radiation treatment planning was performed using a 1.5-T instrument (Light Speed; General Electric). Data were acquired using a standard head coil without rigid immobilization. An axial, three-dimensional gradient echo T1-weighted sequence with contrast medium and 2.0 mm slice thickness were acquired from the foramen magnum to the vertex, perpendicular to the main magnetic field.

2.1.3. Imaging: MET-PET. The MET-PET study was performed using a standardized procedure. All patients fasted for at least 5 h before MET-PET and were advised to eat only a light breakfast in the morning of the examination day to ensure standardized metabolic conditions. The PET scanner was an ADVANCE NXi Imaging System (General Electric Yokokawa Medical System, Hino-shi, Tokyo), which provides 35 transaxial images at 4.25 mm intervals. The crystal width is 4.0 mm (transaxial). The in-plane spatial resolution (full width at half-maximum) was 4.8 mm, and scans were performed in standard two-dimensional mode. Before emission scans were performed, a 3-minute transmission scan was performed to correct photon attenuation using a ring source containing 68 Ge. A dose of 7.0 MBq/kg of MET was injected intravenously, depending on the exam. Emission scans were acquired for 30 min, beginning 5 min after MET injection. During MET-PET data acquisition, head motion was continuously monitored using laser beams projected onto ink markers drawn over the forehead skin and corrected as necessary. Image registrations were performed with Syntegra software (Philips Medical System, Fitchburg, WI) using a combination of automatic and manual methods. Automatic registration was performed, and three observers evaluated by consensus the fusion accuracy using landmarks such as the eyeball, lacrimal glands, and lateral ventricles.

2.2. Treatment. Postoperative MRI and MET-PET were used along with the treatment-planning CT to define the radiation treatment volume. First, a simulation PET/MRI image fusion was performed for contouring. Secondly, the fusion image was positioned properly by CT scans equipped with tomotherapy (Helical TomoTherapy Hi-Art System, TomoTherapy Inc., Madison, WI). Three layered target volumes were contoured. Gross tumor volume (GTV) was the area of enhanced lesion on MRI, including MET-PET avid region; clinical target volume (CTV) was the area with 5 mm margin surrounding the GTV; planning target volume (PTV) was the area with 15 mm margin surrounding the CTV, including MET-PET moderate region (Figure 1). MET-PET avid region was defined, using a threshold value for the lesion versus normal counts of radioisotope per pixel (L/N) index of 1.7 or over. MET-PET moderate region was defined, using a threshold value for the L/N index of 1.3 or over. For primary brain tumors, both 1.3 [4] and 1.7 [5] have been used to determine the threshold value. Although we used 1.3 and 1.7 as the threshold for tumor delineation

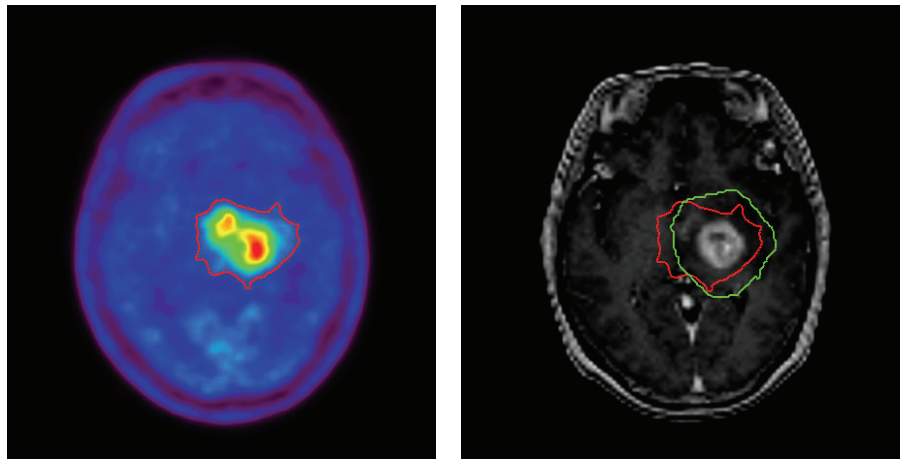

(a) (b)

Figure 1: An example of the targets planned for a Hypo-IMRT procedure. (a) ^{11}C-Methionine positron emission tomography (MET-PET). (b) Contrast-enhanced T1-weighted magnetic resonance imaging (MRI). Gross tumor volume (GTV) was the area of enhanced lesion on MRI, including MET-PET avid region. Clinical target volume (CTV) was the area with 5 mm margin surrounding the GTV. Both MET-PET moderate region (red line) and the area with 15 mm margin surrounding the CTV (green line) were included in planning target volume. The final determination of target delineation was obtained by consensus among three observers.

in this study, the final determination of MET-PET uptake region was confirmed by consensus among three observers. Hypo-IMRT was delivered using tomotherapy in 8 fractions. The dose for GTV was escalated to 68 Gy and that for CTV was escalated to 56 Gy as frequently as possible, while keeping the dose delivered to the PTV at 40 Gy. The dose was prescribed using the 95% isodose line, which covered PTV. Critical structures, including the brainstem, optic chiasm, lens, optic nerves, and cerebral cortex, were outlined, and dose-volume histograms for each structure were obtained to ensure that doses delivered to these structures were tolerable. The dose maps and dose-volume histograms of representative case are illustrated in Figure 2.

2.3. Chemotherapy. Patients received concomitant TMZ at a dose of 75 mg/m^2 per day during Hypo-IMRT, followed by adjuvant TMZ at a dose of 150–200 mg/m^2 per day for 5 days every 28 days, according to the European Organization for Research and Treatment of Cancer-National Cancer Institute of Canada regimen [6], starting 1 month after completion of RT. In the case of progression, patients were considered for second-line treatment on a case-by-case basis.

2.4. Follow-Up. Patients were assessed weekly during RT by clinical examination, complete blood count, blood chemistry, and liver enzyme tests. Regular follow-up was performed with serial neurological and radiological examinations at 1 month after completion of treatment and then every 3 months thereafter. Follow-up MRI and MET-PET were routinely conducted every 3 months or in the event of unexpected neurological worsening. When enlargement of the local lesion was observed, corticosteroid therapy was initiated and MRI was performed once a month thereafter to evaluate the efficacy of corticosteroid treatment. If the follow-up MRI revealed further enlargement of the enhanced mass, the lesion was diagnosed as "local progression," and the day on which MRI first revealed lesion enlargement was defined as the date of progression. However, in cases in which a second surgery revealed no viable tumor cells in the enhanced lesion, the diagnosis was changed to "radiation necrosis." Lesions that decreased in size during corticosteroid treatment were also defined as "radiation necrosis." "Distant failure" was defined as the appearance of a new intraparenchymal enhanced lesion distant from the original tumor site. If the new lesion arose distant from the original tumor site and was exposed to the cerebrospinal fluid (CSF) space, the lesion was defined as "CSF dissemination." Acute and late toxicities were scored according to RTOG criteria.

2.5. Statistical Analysis. Survival events were defined as death from any cause for OS and as disease progression for progression-free survival (PFS). OS and PFS were analyzed from the date of pathologic diagnosis to the date of the documented event using the Kaplan-Meier method. Tumor- and therapy-related variables were tested for a possible correlation with survival, using the log-rank test. Variables included Karnofsky performance status (KPS) (≥70 versus <70), RPA class (III, IV versus V, VI), surgery extent (gross total removal versus others), and adjuvant TMZ chemotherapy (yes versus no). The survival benefit was also evaluated by multivariate analysis using Cox's proportional hazards model.

3. Results

Patient characteristics are listed in Table 1. The median patient age was 61 years (range, 21–86 years). The average GTV was 12.11 ± 18.20 cm^3, the average CTV was 43.64 ± 35.65 cm^3, and the average PTV was 163.22 ± 100.15 cm^3.

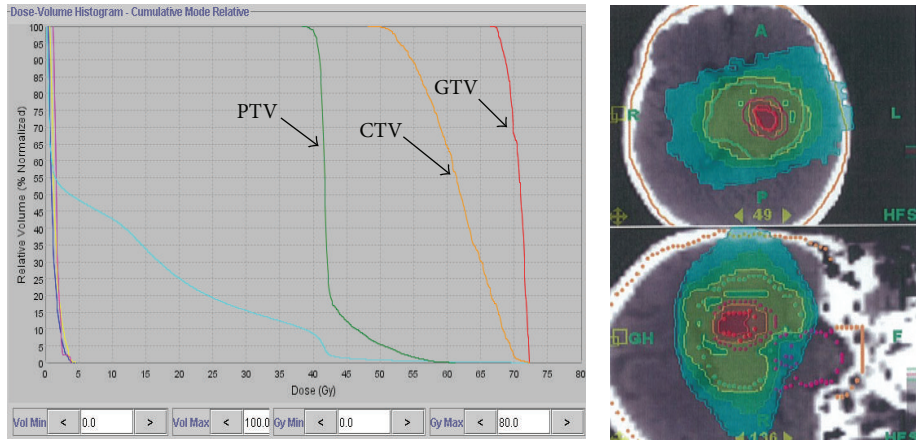

Figure 2: Dose map and dose-volume histogram of a representative case. Prescribed doses for gross tumor volume (GTV), clinical target volume (CTV), and planning target volume (PTV) were demonstrated.

Table 2: Hematologic toxicity.

Adverse event	Acute phase				Late phase			
	G 1	G 2	G 3	G 4	G 1	G 2	G 3	G 4
Neutropenia	1 (2.2)	3 (6.7)	0 (0)	0 (0)	0 (0)	3 (6.7)	1 (2.2)	0 (0)
Thrombocytopenia	0 (0)	0 (0)	0 (0)	0 (0)	0 (0)	0 (0)	0 (0)	1 (2.2)

G: grade.
Data presented as number of patients, with percentages in parentheses.

The average GTV dose was 60.38 ± 5.25 Gy, and the average CTV dose was 53.15 ± 5.45 Gy. All 45 patients completed the prescribed Hypo-IMRT with concomitant TMZ course. Overall, 12 patients (26.7%) did not receive the prescribed course of adjuvant TMZ chemotherapy for the following reasons: neutropenia ($n = 3$), patient refusal ($n = 4$), nausea/vomiting ($n = 2$), and admission to another hospital ($n = 3$).

3.1. Toxicity Assessment

Hematologic Toxicities. Hematologic toxicities are listed in Table 2. During the acute phase, Grade 1-2 neutropenia occurred in 4 patients (8.9%). During the late phase, Grade 2-3 neutropenia occurred in 4 patients (8.9%), and Grade 4 thrombocytopenia occurred in 1 patient (2.2%).

Nonhematologic Toxicities. Nonhematologic toxicities are listed in Table 3. During the acute phase, nonhematologic toxicity was minimal, and no Grade 3-4 toxicities were reported. The most common acute toxicity reported was Grade 1-2 nausea/vomiting. Late nonhematologic toxicity included 7 cases of Grade 3-4 radiation necrosis (15.6%), 1 case of Grade 3 cerebropathy (2.2%), and 2 cases of Grade 3-4 intratumoral hemorrhage (4.4%). Median time to development of symptomatic radiation necrosis from the end of Hypo-IMRT was 9.3 months (range, 3–17 months). In seven cases of Grade 3-4 radiation necrosis, the average PTV was 152.04 ± 96.14 cm^3, and the locations were one case of frontal lobe, three cases of temporal lobe, and three cases of parietal lobe. Grade 4 massive radiation necrosis required a second surgery in 2 cases (4.4%) 8 and 14 months after Hypo-IMRT. These patients are alive without disease for 13 and 11 months, respectively, after necrotomy. In 5 cases with Grade 3 radiation necrosis, initiation or increased dosage of corticosteroid therapy was required for worsening of neurological symptoms. One of these five patients died of disseminated disease 23 months after Hypo-IMRT, and the remaining four patients are alive without disease for 14, 17, 18, and 39 months after Hypo-IMRT. Although the correlation with treatment is unclear, Grade 3-4 intratumoral hemorrhage was observed 13 and 21 months after IMRT in 2 cases. The representative case of radiation necrosis was demonstrated in Figure 5.

3.2. Outcomes

Overall Survival. At a median follow-up of 18.7 months (range, 3–48 months), median OS was 20.0 months (range, 3–48 months). The 1- and 2-year OS rates were 71.2% and 26.3%, respectively (Figure 3(a)). The survival rates by KPS, RPA class, extent of surgical resection, and adjuvant TMZ chemotherapy are shown in Figures 4(a)–4(d). KPS (≥70 versus <70), extent of surgical resection (gross total removal versus others), and adjuvant TMZ chemotherapy (yes versus no) were significant predictive factors of OS as tested by univariate analysis. Multivariate analysis revealed

Table 3: Nonhematologic toxicity.

Adverse event	Acute phase				Late phase			
	G 1	G 2	G 3	G 4	G 1	G 2	G 3	G 4
Headache	3 (6.7)	0 (0)	0 (0)	0 (0)	0 (0)	0 (0)	0 (0)	0 (0)
Nausea/vomiting	2 (4.4)	2 (4.4)	0 (0)	0 (0)	0 (0)	0 (0)	0 (0)	0 (0)
Radiation necrosis	0 (0)	0 (0)	0 (0)	0 (0)	0 (0)	0 (0)	5 (11.1)	2 (4.4)
Cerebropathy	0 (0)	0 (0)	0 (0)	0 (0)	0 (0)	0 (0)	1 (2.2)	0 (0)
Hemorrhage	0 (0)	0 (0)	0 (0)	0 (0)	0 (0)	0 (0)	1 (2.2)	1 (2.2)

G: grade.
Data presented as number of patients, with percentages in parentheses.

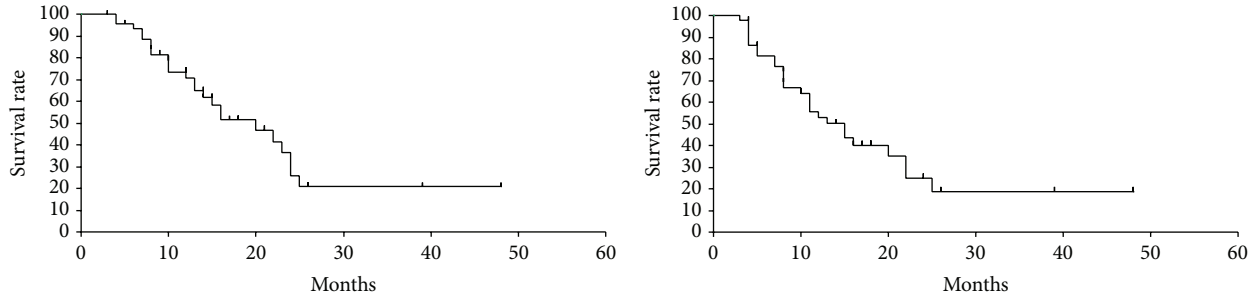

(a) Overall survival (b) Progression-free survival

Figure 3: Overall survival (a) and progression-free survival (b) for all patients. Median OS was 20.0 months, and the 1- and 2-year OS rates were 71.2% and 26.3%, respectively. Median PFS was 13.0 months, and the 1- and 2-year PFS rates were 52.6% and 20.6%, respectively.

only adjuvant TMZ chemotherapy to be a significant variable predictive of OS (Table 4).

Progression-Free Survival. Median PFS was 13.0 months (range, 3–48 months), and the 1- and 2-year PFS rates were 52.6% and 20.6%, respectively (Figure 3(b)). CSF dissemination was the most frequent failure pattern, which was observed in 17 cases (60.7% of all failures). Local progression was observed in 7 patients (25.0%), and distant failure was observed in 4 cases (14.3%). An example of a failure with CSF dissemination after Hypo-IMRT is shown in Figure 6. KPS (≥70 versus <70) was the only predictive factor for PFS as tested by univariate analysis. On multivariate analysis, none of the variables were significantly predictive of PFS (Table 5).

4. Discussion

Lately, much work has been performed on various hypofractionation regimens and dose escalation with Hypo-IMRT for GBM which revealed relatively favorable survival results [7–11], although a distinct advantage over conventional RT has not been demonstrated. However, if a very conformal treatment technique such as Hypo-IMRT can be implemented and a greater biologic dose to the infiltrating tumor is possible through hypofractionation, it could be possible to deliver a more effective therapy that may increase patient survival without increasing morbidity. To meet these requirements, the contouring of the target volume must be of critical importance in the treatment of Hypo-IMRT.

Table 4: Analysis of prognostic variables for overall survival.

Variables	Median survival (months)	Univariate analysis* *P* value	Multivariate analysis† *P* value
KPS			
≥70	23	0.0297	0.5994
<70	15		
RPA-class			
III, IV	23	0.1385	
V, VI	13		
Extent of resection			
GTR	25	0.0422	0.131
Others	13		
Adjuvant TMZ chemotherapy			
Yes	23	0.0004	0.0124
No	10		

Abbreviations as in Table 1.
Statistical analyses were performed with*log-rank test and †Cox's proportional hazards model.

PET is a newer method that can improve the visualization of molecular processes. In one study, several amino acids were radio-labeled to evaluate their potential imaging characteristics in primary brain tumors; such an analysis might be expected to elucidate mechanisms related to either amino acid metabolism or breakdown of the BBB [2]. In

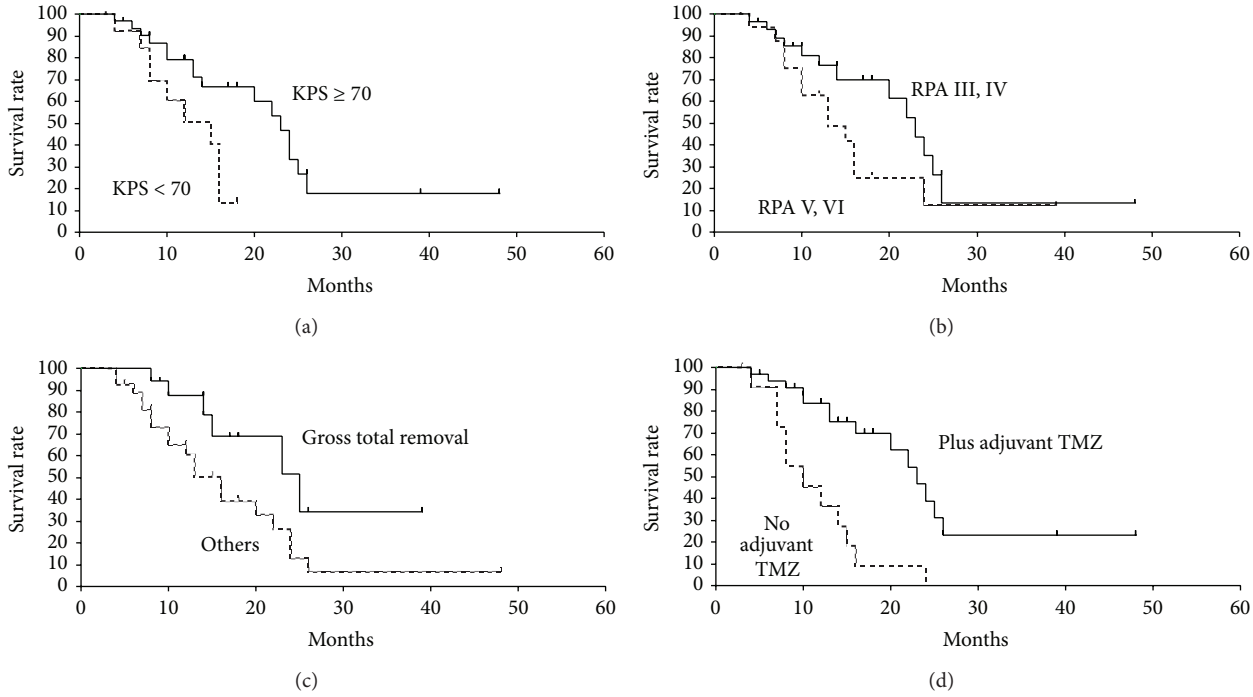

Figure 4: Overall survival rates among different subgroups by (a) Karnofsky performance status (KPS), (b) recursive partitioning analysis (RPA) subclass, (c) extent of surgical resection, and (d) adjuvant temozolomide (TMZ) chemotherapy.

Table 5: Analysis of prognostic variables for progression-free survival.

Variables	Median survival (months)	Univariate analysis* *P* value	Multivariate analysis† *P* value
KPS			
≥70	20	0.0282	0.1279
<70	8		
RPA-class			
III, IV	16	0.5895	
V, VI	11		
Extent of resection			
GTR	22	0.2004	
Others	11		
Adjuvant TMZ chemotherapy			
Yes	16	0.0548	
No	8		

Abbreviations as in Table 1.
Statistical analyses were performed with *log-rank test and †Cox's proportional hazards model.

recent PET studies, analysis of the metabolic and histologic characteristics of stereotactic biopsy specimens provided evidence that regional high MET uptake correlates with the malignant pathologic features [4, 12, 13]. In many cases of malignant glioma, the size and location of MET uptake differ considerably from the abnormalities observed on CT/MRI [14–16]. Matsuo et al. reported that MET-PET had promising potential for precisely delineating target volumes in planning radiation therapy for postoperative patients with GBM [16]. Lee et al. reported the results of a study demonstrating statistically significant correlation between the presence of increased MET-PET uptake outside the high-dose region and subsequent noncentral failure [17].

Considering the informative results of these recent trials, MET-PET might have substantial reliability as a marker of tumor biological characteristics, as well as a valuable impact on visualizing the tumor-invasive area of malignant glioma. Previously, we reported three preliminary cases of GBM treated by Hypo-IMRT with complementary use of MET-PET [18]. Herein, we report the results of prospective study to evaluate the clinical outcome of Hypo-IMRT selectively increasing the radiation dose to MET-PET uptake region (Figure 1). Consequently, we found the treatment outcomes demonstrating that median OS was 20.0 months (range, 3–48 months) and that the 1- and 2-year OS rates were 71.2% and 26.3%, respectively (Figure 3(a)). Median PFS was 13.0 months (range, 3–48 months), and the 1- and 2-year PFS rates were 52.6% and 20.6%, respectively (Figure 3(b)). Survival results of our study appeared to be favorable to published results using standard fractionation RT combined with TMZ [6]. Needless to say, direct comparisons to historical controls or to other studies should be viewed with caution; only a properly designed randomized trial can firmly establish whether the present regimen is superior to the standard treatment.

In the special feature of this study, local tumor progression occurred at a lower incidence (25.0%), suggesting

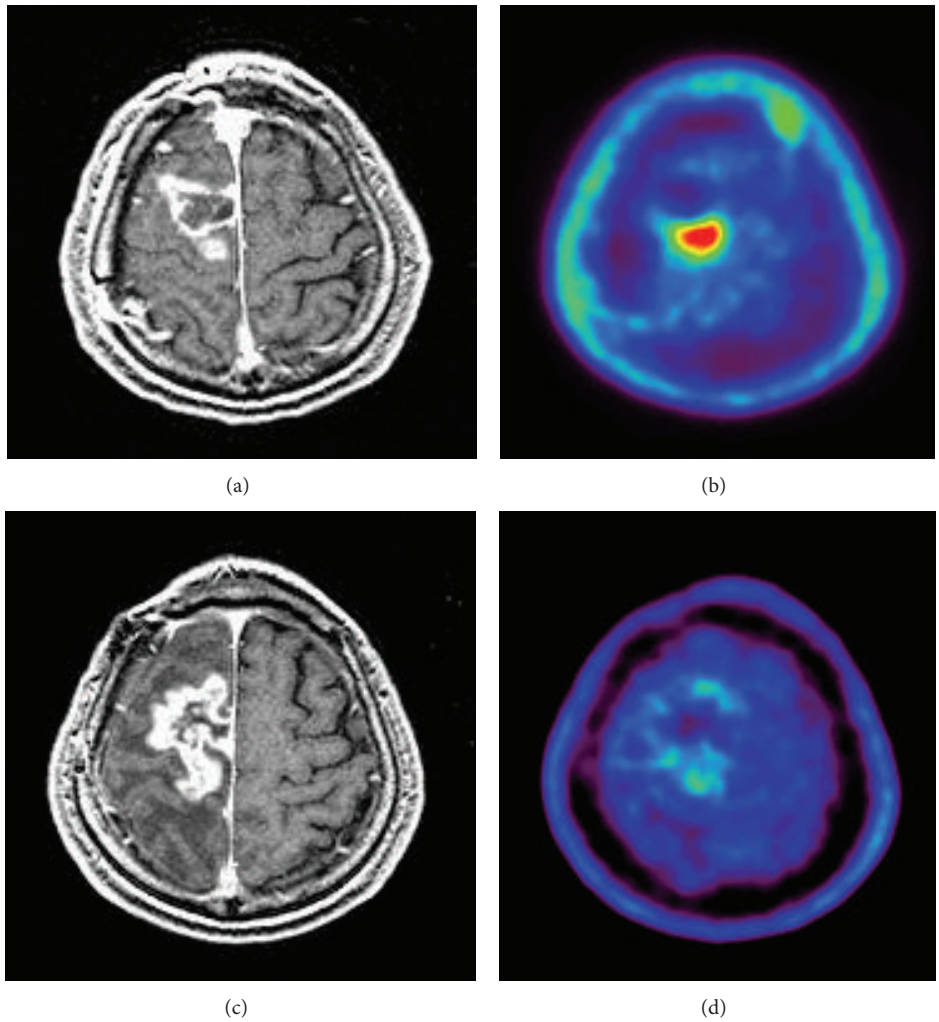

Figure 5: A 56-year-old man of GBM with symptomatic radiation necrosis. Before Hypo-IMRT, enhanced lesions were demonstrated in the right frontal lobe on T1-weighted magnetic resonance imaging (MRI) (a). ^{11}C-Methionine positron emission tomography (MET-PET) demonstrated a MET high-uptake on the region (b). 12 months after Hypo-IMRT, the enhanced lesion with perifocal edema was increased in size (c), although MET uptake decreased in the irradiated region (d). Second surgery was performed, and pathological diagnosis was defined as necrotic tissue without viable tumor cells.

that selectively increasing the radiation dose to MET-PET uptake area contributed to better local control of original tumors. Meanwhile, the most common type of failure was CSF dissemination (60.7% of all failures). It still remains difficult to prevent CSF dissemination for extended periods with our regimen, although the original lesion might be well controlled (Figure 6). For improved patient survival, prevention of CSF dissemination may be the next issue to be addressed. If new, targeted chemotherapeutic agents lead to further improvements in control of microscopic disease, radiation can be used primarily to control disease in limited regions that have the highest risk of progression, that is, where those agents are most likely to fail.

Both univariate analysis and multivariate analysis revealed a significant difference in OS between patients who did and did not receive adjuvant TMZ (Table 4). We estimated that the addition of TMZ might be particularly effective if the radiation dose to normal brain tissue was limited by better targeting. However, the impact of TMZ along with the methylation status of the O-6-methylguanine-DNA methyltransferase (MGMT) on survival was not systematically evaluated in the present study. This selection bias could not be avoided, as the patients with methylated MGMT or who were in better clinical condition were more likely to have received adjuvant TMZ chemotherapy. Nevertheless, the results of this study support our initial work and further establish the efficacy of this regimen combined with TMZ.

Late toxicity was more common with this treatment regimen than early toxicity; specifically, the most severe adverse event associated with our regimen was radiation necrosis. Overall, 5 and 2 patients experienced Grade 3 and Grade 4 radiation necrosis, respectively, and necrotomy was required in 2 patients (Figure 5). These 2 patients are alive

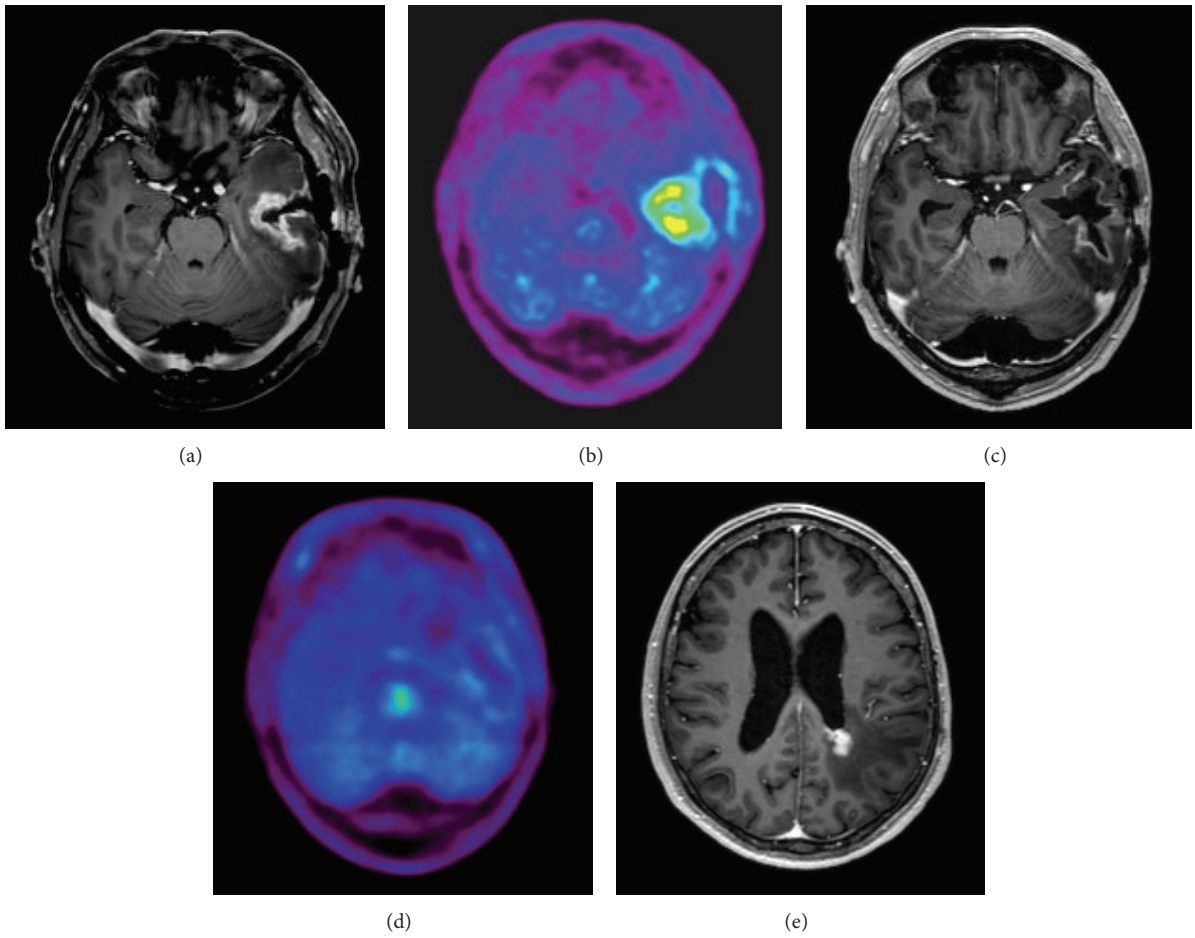

Figure 6: Representative cases of cerebrospinal fluid dissemination: 55-year-old man with GBM. Before Hypo-IMRT, an enhanced tumor was demonstrated in the left temporal lobe on T1-weighted magnetic resonance imaging (MRI) (a). ^{11}C-Methionine positron emission tomography (MET-PET) demonstrated a MET high-uptake region in the left temporal lobe (b). 20 months after Hypo-IMRT, the enhanced tumor was decreased in size (c), and the MET high-uptake region could not be detected distinctly (d), although disseminated lesion was observed around the left lateral ventricle (e).

without disease for 11 and 13 months after necrotomy. In another 5 cases with Grade 3 radiation necrosis, 4 patients are alive without disease for 14, 17, 18, and 39 months after Hypo-IMRT. Recently, the efficacy of new chemotherapeutic agents, such as bevacizumab, which are used as rescue therapies for radiation necrosis after RT, has been reported [19, 20]. It is possible that if a rescue therapy to prevent radiation necrosis was conducted on a larger scale with a sufficient number of patients, a more accurate conclusion about patient outcome could be made.

5. Conclusion

Our preliminary study demonstrated that Hypo-IMRT with complementary use of MET-PET data appeared to result in favorable survival outcomes for patients with GBM, although a properly designed randomized trial could firmly establish whether the present regimen is superior to the standard treatment.

Conflict of Interests

The authors report no conflict of interests concerning the materials or methods used in this study or the findings specified in this paper.

References

[1] M. D. Walker, S. B. Green, D. P. Byar et al., "Randomized comparisons of radiotherapy and nitrosoureas for the treatment of malignant glioma after surgery," *The New England Journal of Medicine*, vol. 303, no. 23, pp. 1323–1329, 1980.

[2] P. L. Jager, W. Vaalburg, J. Pruim, E. G. E. De Vries, K.-J. Langen, and D. A. Piers, "Radiolabeled amino acids: basic aspects and clinical applications in oncology," *Journal of Nuclear Medicine*, vol. 42, no. 3, pp. 432–445, 2001.

[3] W. J. Curran Jr., C. B. Scott, J. Horton et al., "Recursive partitioning analysis of prognostic factors in three radiation therapy oncology group malignant glioma trials," *Journal of the National Cancer Institute*, vol. 85, no. 9, pp. 704–710, 1993.

[4] L. W. Kracht, H. Miletic, S. Busch et al., "Delineation of brain tumor extent with [^{11}C]L-methionine positron emission tomography: local comparison with stereotactic histopathology," *Clinical Cancer Research*, vol. 10, no. 21, pp. 7163–7170, 2004.

[5] P. Mahasittiwat, J. Mizoe, A. Hasegawa et al., "l-[METHYL-^{11}C] methionine positron emission tomography for target delineation in malignant gliomas: impact on results of carbon ion radiotherapy," *International Journal of Radiation Oncology Biology Physics*, vol. 70, no. 2, pp. 515–522, 2008.

[6] R. Stupp, W. P. Mason, M. J. Van Den Bent et al., "Radiotherapy plus concomitant and adjuvant temozolomide for glioblastoma," *New England Journal of Medicine*, vol. 352, no. 10, pp. 987–996, 2005.

[7] T. Iuchi, K. Hatano, Y. Narita, T. Kodama, T. Yamaki, and K. Osato, "Hypofractionated high-dose irradiation for the treatment of malignant astrocytomas using simultaneous integrated boost technique by IMRT," *International Journal of Radiation Oncology Biology Physics*, vol. 64, no. 5, pp. 1317–1324, 2006.

[8] K. Sultanem, H. Patrocinio, C. Lambert et al., "The use of hypofractionated intensity-modulated irradiation in the treatment of glioblastoma multiforme: preliminary results of a prospective trial," *International Journal of Radiation Oncology Biology Physics*, vol. 58, no. 1, pp. 247–252, 2004.

[9] N. S. Floyd, S. Y. Woo, B. S. Teh et al., "Hypofractionated intensity-modulated radiotherapy for primary glioblastoma multiforme," *International Journal of Radiation Oncology Biology Physics*, vol. 58, no. 3, pp. 721–726, 2004.

[10] V. Panet-Raymond, L. Souhami, D. Roberge et al., "Accelerated hypofractionated intensity-modulated radiotherapy with concurrent and adjuvant temozolomide for patients with glioblastoma multiforme: a safety and efficacy analysis," *International Journal of Radiation Oncology Biology Physics*, vol. 73, no. 2, pp. 473–478, 2009.

[11] K. Nakamatsu, M. Suzuki, Y. Nishimura et al., "Treatment outcomes and dose-volume histogram analysis of simultaneous integrated boost method for malignant gliomas using intensity-modulated radiotherapy," *International Journal of Clinical Oncology*, vol. 13, no. 1, pp. 48–53, 2008.

[12] B. Pirotte, S. Goldman, O. Dewitte et al., "Integrated positron emission tomography and magnetic resonance imaging-guided resection of brain tumors: a report of 103 consecutive procedures," *Journal of Neurosurgery*, vol. 104, no. 2, pp. 238–253, 2006.

[13] T. Aki, N. Nakayama, S. Yonezawa et al., "Evaluation of brain tumors using dynamic (11)C-methionine-PET," *Journal of Neuro-Oncology*, vol. 109, no. 1, pp. 115–122, 2012.

[14] A. Grosu, W. A. Weber, E. Riedel et al., "L-(methyl-^{11}C) methionine positron emission tomography for target delineation in resected high-grade gliomas before radiotherapy," *International Journal of Radiation Oncology Biology Physics*, vol. 63, no. 1, pp. 64–74, 2005.

[15] K. Miwa, J. Shinoda, H. Yano et al., "Discrepancy between lesion distributions on methionine PET and MR images in patients with glioblastoma multiforme: insight from a PET and MR fusion image study," *Journal of Neurology, Neurosurgery and Psychiatry*, vol. 75, no. 10, pp. 1457–1462, 2004.

[16] M. Matsuo, K. Miwa, O. Tanaka et al., "Impact of [^{11}C]methionine positron emission tomography for target definition of glioblastoma multiforme in radiation therapy planning," *International Journal of Radiation Oncology Biology Physics*, vol. 82, no. 1, pp. 83–89, 2012.

[17] I. H. Lee, M. Piert, D. Gomez-Hassan et al., "Association of ^{11}C-Methionine PET uptake with site of failure after concurrent temozolomide and radiation for primary glioblastoma multiforme," *International Journal of Radiation Oncology Biology Physics*, vol. 73, no. 2, pp. 479–485, 2009.

[18] K. Miwa, M. Matsuo, J. Shinoda et al., "Simultaneous integrated boost technique by helical tomotherapy for the treatment of glioblastoma multiforme with ^{11}C-methionine PET: report of three cases," *Journal of Neuro-Oncology*, vol. 87, no. 3, pp. 333–339, 2008.

[19] J. Gonzalez, A. J. Kumar, C. A. Conrad, and V. A. Levin, "Effect of bevacizumab on radiation necrosis of the brain," *International Journal of Radiation Oncology Biology Physics*, vol. 67, no. 2, pp. 323–326, 2007.

[20] V. A. Levin, L. Bidaut, P. Hou et al., "Randomized double-blind placebo-controlled trial of bevacizumab therapy for radiation necrosis of the central nervous system," *International Journal of Radiation Oncology Biology Physics*, vol. 79, no. 5, pp. 1487–1495, 2011.

Hindawi Publishing Corporation
BioMed Research International
Volume 2014, Article ID 852352, 8 pages
http://dx.doi.org/10.1155/2014/852352

Research Article

The Effect of Superparamagnetic Iron Oxide with iRGD Peptide on the Labeling of Pancreatic Cancer Cells *In Vitro*: A Preliminary Study

Hou Dong Zuo,[1,2] Wei Wu Yao,[2] Tian Wu Chen,[1] Jiang Zhu,[1] Juan Juan Zhang,[1] Yu Pu,[1] Gang Liu,[1] and Xiao Ming Zhang[1]

[1] *Sichuan Key Laboratory of Medical Imaging, Department of Radiology, Affiliated Hospital of North Sichuan Medical College, Nanchong, Sichuan 637000, China*
[2] *Department of Radiology, Shanghai Jiao Tong University Affiliated Sixth People's Hospital, 600 Yishan Road, Shanghai 200233, China*

Correspondence should be addressed to Xiao Ming Zhang; cjr.zhxm@vip.163.com

Received 10 February 2014; Revised 29 April 2014; Accepted 4 May 2014; Published 19 May 2014

Academic Editor: Yi-Xiang Wang

The iRGD peptide loaded with iron oxide nanoparticles for tumor targeting and tissue penetration was developed for targeted tumor therapy and ultrasensitive MR imaging. Binding of iRGD, a tumor homing peptide, is mediated by integrins, which are widely expressed on the surface of cells. Several types of small molecular drugs and nanoparticles can be transfected into cells with the help of iRGD peptide. Thus, we postulate that SPIO nanoparticles, which have good biocompatibility, can also be transfected into cells using iRGD. Despite the many kinds of cell labeling studies that have been performed with SPIO nanoparticles and RGD peptide or its analogues, only a few have applied SPIO nanoparticles with iRGD peptide in pancreatic cancer cells. This paper reports our preliminary findings regarding the effect of iRGD peptide (CRGDK/RGPD/EC) combined with SPIO on the labeling of pancreatic cancer cells. The results suggest that SPIO with iRGD peptide can enhance the positive labeling rate of cells and the uptake of SPIO. Optimal functionalization was achieved with the appropriate concentration or concentration range of SPIO and iRGD peptide. This study describes a simple and economical protocol to label panc-1 cells using SPIO in combination with iRGD peptide and may provide a useful method to improve the sensitivity of pancreatic cancer imaging.

1. Introduction

The development of metallic or inorganic nanoparticles for disease and cancer diagnostic imaging has progressed rapidly in recent years due to their unique physical characteristics, favorable biocompatibility, and specific targeting capabilities [1–5]. Among them, superparamagnetic iron oxide (SPIO) nanoparticles have a great potential for basic and clinical application due to their several advantages, such as guided transport or distribution under an external magnetic field *in vivo* and T2-type magnetic resonance imaging contrast enhancement [3, 4, 6–10]. In particular, negative contrast agents (e.g., SPIO) for molecular imaging that decrease the T2 and T2* relaxation times of tissues and provide higher sensitivity for MRI are advantageous because they have strong contrast effects, conveniently controlled magnetic characteristics, and improved biodegradability [11]. Cationic surfaces facilitate cellular internalization [12]. Currently, there is a huge research impetus in MR diagnostic imaging to develop hybrid SPIO nanoparticles integrated with multiple imaging detection components [3, 5, 6, 8, 13]. To date, SPIOs modified or coated with dextran, polystyrene, polyethylene glycol (PEG), and polylysine (PLL) have been studied and applied [11, 13–15].

Integrins, which consist of an α and a β subunit, are a family of heterodimeric glycoprotein receptors on the cell surface which mediate and diversify biological communication involving cell adhesion and signal transduction [16]. Currently, 24 integrin subtypes have been reported [17, 18], while $\alpha v\beta 3$ integrin that is overexpressed on tumor cells is one of the most prominent receptors involved in tumor growth, invasiveness, and metastasis [16, 19–22]. The αv

integrins and neuropilin-1 are expressed on pancreatic cancer cells, including the panc-1 cell line [23–29]. In addition, $\alpha v\beta 3$ integrin can be targeted by peptides with a short amino acid sequence containing Arg-Gly-Asp (RGD) [3, 22, 30–32]. The iRGD (CRGDK/RGPD/EC) peptide is a newly identified type of tumor-penetrating peptide, which was discovered by phage display. The peptide can increase the permeability of tumor cells, mediate cellular internalization and extravasation, and enhance deep tissue penetration to improve the imaging sensitivity and therapeutic efficacy mediated by integrins and neuropilin-1 (NRP-1) receptors [3, 23, 30]. The iRGD peptide plays a part in targeting tumor cells using a similar procedure to conventional RGD peptides [3, 30]. Recently, the application of RGD peptide with SPIO has been an active focus of research. Zhang et al. [31] evaluated RGD-USPIO uptake in cultured human umbilical vein endothelial cells (HUVECs) *in vitro* by MRI.

Here, we propose and investigate a new strategy for integrin targeting and tumor diagnostic imaging based on iRGD peptide. We aim to (1) study the effect of SPIO with iRGD peptide on the labeling of pancreatic cancer cells *in vitro* and (2) find a new and useful modality for pancreatic cancer diagnostic imaging. To our knowledge, there have been no studies investigating the biophysical properties of SPIO with iRGD peptide for cellular MR imaging. Therefore, this study is novel, and previous studies suggest that it is feasible. The intracellular uptake of Fe, the viability of labeled cells, and their MRI signal intensity (SI) changes were assessed. The results suggest that our modality may be useful for alternative cell labeling and pancreatic cancer diagnostic imaging.

2. Materials and Methods

2.1. Chemicals, Reagents, and Experimental Instruments. The human pancreatic cancer cell line (panc-1) was provided by Sichuan University. The following other materials and instruments were used: iRGD peptide, SPIO (Resovist, SHU555A, SCHERING Company, Germany), polylysine, fetal bovine serum, RPMI-1640 solution, trypsin, a 3.0 T MR scanner (Discovery MR 750; GE Medical Systems, Milwaukee, WI), an inverted microscope (TS100-F), an oven (DGX-9143), and an atomic absorption spectrophotometer (AAS, SpectrAA 220FS, 12°C, 63% humidity).

2.2. The Concentration of Reagents and Solutions. The nutrient solution consisted of 85% RPMI-1640 solution and 15% fetal bovine serum. SPIO mixed solution had 840 μg iron ion per mL. The following solutions were used: 10% iRGD peptide solution, 0.5% neutral red solution, PBS buffer solution (0.1 mol/L, pH 7.4), and 0.25% trypsin. The iron ion concentration of SPIO and the PLL mixture solution was 840 μg per mL. Perl's staining solution was composed of 2% potassium ferrocyanide solution and 3% diluted hydrochloric acid mixed in an equal volume.

2.3. Cell Culture and Treatment. The human pancreatic cancer cells (1×10^6 cells/well, 9.6 cm^2 per well) were cultured for 24 hours. Then, the cells were washed with phosphate buffered saline (PBS) three times. Afterwards, the SPIO and iRGD peptide solutions were coadministered. The total solution volume was 2 mL per well. The iron ion concentrations were 8.4 μg/mL, 12.6 μg/mL, 14.7 μg/mL, 16.8 μg/mL, and 21 μg/mL. The iRGD peptide solution concentrations added were 0.25 μg/mL, 0.5 μg/mL, 0.75 μg/mL, 1.0 μg/mL, and 1.25 μg/mL, respectively. Considering the 8.4 μg/mL concentration as an example, 1980 μL, 1980 μL, 1975 μL, 1970 μL, 1965 μL, 1960 μL, and 1955 μL of nutrient culture were first added to each of the 6 wells. Next, 20 μL SPIO solution was added to each well followed by 0 μL, 0 μL, 5 μL, 10 μL, 15 μL, 20 μL, and 25 μL iRGD peptide solution, respectively. As control, SPIO-PLL was added in another well with each SPIO concentration series. Next, the cells were incubated for 24 hours. After incubation, the culture medium was removed. The adherent cells were washed with PBS three times, trypsinized, washed with PBS, and centrifuged for 5 minutes at 1000 rpm. The total number of cells (1×10^6) was determined using a counting chamber. Then, the cells were embedded in agar (1%) at room temperature for MRI examination.

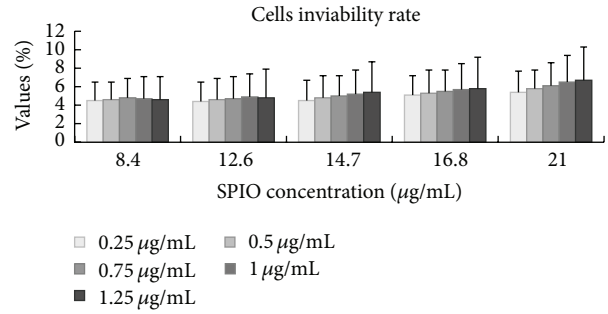

Figure 1: The rate of nonviable cells for different SPIO and iRGD peptide concentrations. As shown in the graph, trypan blue staining demonstrated that there was not a remarkable reduction in the viability of panc-1 cells after incubation with increasing concentrations of SPIO and iRGD peptide.

2.4. Cell Viability. The viability of the cells cultured under different conditions was evaluated with 0.4% trypan blue dye solution. The percentage of nonviable or dead cells was determined by counting trypan blue-positive and trypan blue-negative cells in a counting chamber. The nonviable rate was calculated. The group with the highest concentration of iRGD peptide within each iron concentration series was analyzed.

2.5. MR Sequence, Parameters, and Measurement. MR T2 relaxometry of panc-1 cells in agar was performed using a fast recovery fast spin echo T2 weighted (FRFSE-T2W) sequence with a 32-channel head coil in a 3.0 T MR scanner (slice thickness: 2 mm; interslice space: 0–0.5 mm; TR: 2800.0 ms; TE: 90.3 ms; DFOV: 18.0 × 18.0 cm; reconstruction matrix: 512 × 256). All the original images were transferred to an ADW4.4 workstation, and the best images were selected.

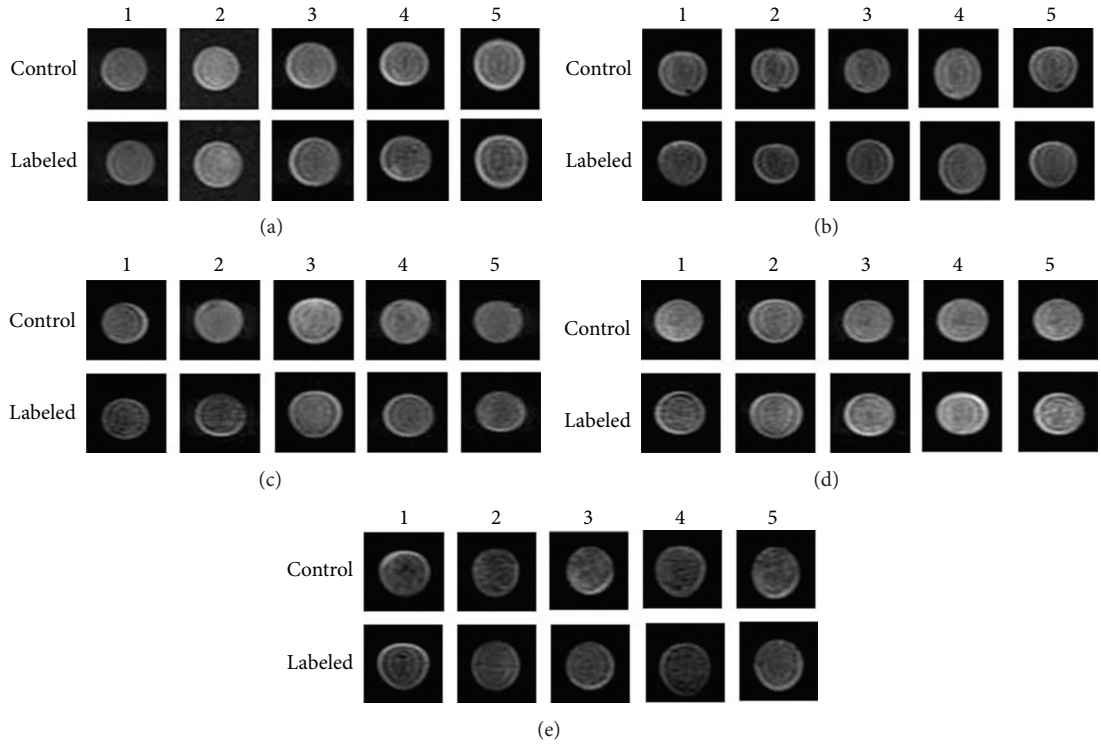

Figure 2: MR images of labeled cells in agar (1×10^6 cells) acquired using T2-weighted imaging with the FRFSE sequence. (a)–(e) indicate the iron ion concentration (from 8.4 to 21 μg/mL, resp.). The numbers 1–5 represent the iRGD peptide concentration (from 0.25 to 1.25 μg/mL, resp.).

Identification of 25 mm^2 regions of interest (ROI) was performed in triplicate, and the mean values were adopted. The signal intensity reduction value (ΔS) of every sample (including the SPIO-PLL group) relative to the control group was measured within the same SPIO concentration. The signal intensity changes ($\Delta S'$) of every sample (including the SPIO control group) were also measured relative to the PBS blank group with the same SPIO concentration to analyze the appropriate concentration of iRGD to SPIO concentration. All the data were processed and measured on the ADW4.4 workstation.

2.6. Prussian Blue Staining. For Prussian blue staining, the cells were cultivated for 24 hours in 6-well plates on glass coverslips (1×10^6 cells). After incubation, the labeled panc-1 cells were washed three times with PBS and subsequently fixed with 4% paraformaldehyde for 40 to 60 minutes. Then, the fixed cells were incubated with Perl's dye for 30 minutes and counterstained with 0.5% neutral red solution for 1 minute.

2.7. Inverted Microscope Observation and Transmission Electron Microscopy. The cells on glass coverslips were placed on slides, fixed, and then observed with an inverted microscope. The cells were routinely observed using 10x, 20x, and 40x magnification views. Photos were taken at random sites under 40x magnification. The positive labeled cells were counted under 4 magnification views (40x and 20x) randomly, and the positive labeled rate was calculated (positive labeled cell counts/total cell counts × 100%). The cells cultured with 12.6 μg/mL iron ion and 1 μg/mL iRGD peptide were selected for observation with a transmission electron microscope.

2.8. The Quantification of Iron Cell Content. After MRI scanning, the group with the best concentrations of SPIO and iRGD peptide was selected and the samples were treated with 15 mL aqua regia ($V_{HCL} : V_{HNO_3} = 3 : 1$) for the determination of the iron content by AAS.

2.9. Statistical Analysis. The continuous data were expressed as mean ± standard deviation (SD). Statistical analysis was conducted using a nonparametric Wilcoxon rank sum test. A 2-independent samples test was performed in the analysis of $\Delta S'$ and cell viability. Statistical analysis was conducted with the SPSS16.0 software package for Windows (SPSS Institute, Chicago, IL, USA). An α level of 0.05 was used.

3. Results

3.1. Evaluation of Cell Viability. Trypan blue staining did not demonstrate reduced viability of panc-1 cells after incubation with increasing concentrations of SPIO and iRGD peptide, including the SPIO and SPIO-PLL control groups. There were no significant differences among the samples. For example, for the highest concentration of iron ions (21 μg/mL) in this study, the percentages of nonviable cells for the different

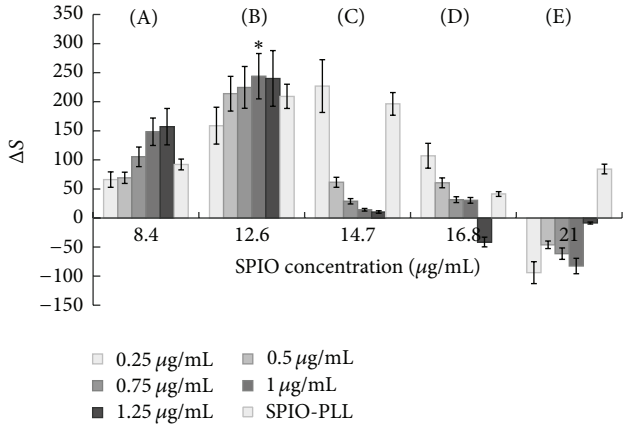

Figure 3: The evaluation of the mean signal reduction (ΔS) for different iron ion concentrations. (A)–(E) indicate 8.4–21 μg/mL iron ion concentration. The SPIO-PLL group served as the control group. *The highest ΔS value (the best concentration match of iron ions and iRGD peptide).

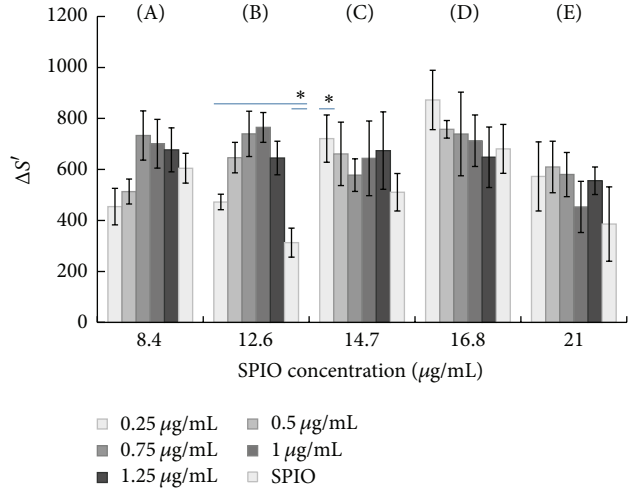

Figure 4: The evaluation of the mean signal reduction values ($\Delta S'$) for different iron concentrations. For the iron concentration of 12.6 μg/mL, a significant difference was found between the treatment and control groups ($P < 0.05$). For the iron concentration of 14.7 μg/mL, a significant difference was only found between 0.25 μg/mL iRGD and the control group. (A)–(E) indicate 8.4–21 μg/mL iron ion concentration. The SPIO group served as the control group. *$P < 0.05$.

concentrations of the iRGD peptide samples were 5.4 ± 2.5%, 5.8 ± 3.1%, 6.1 ± 3.3%, 6.5 ± 3.4%, and 6.7 ± 3.6%, respectively. These values did not differ significantly from each other (Figure 1).

3.2. In Vitro MRI Evaluation of T2-W. When the concentration of iron was 8.4 μg/mL, the signal intensity of the labeled cell samples decreased gradually with the increase in iRGD peptide concentration (Figures 2(a) and 3). The mean ΔS increased correspondingly. When the concentration reached 12.6 μg/mL, the signal intensity first decreased and then increased with increasing concentrations of iRGD peptide. Therefore, the mean ΔS first increased and then decreased. The ΔS was the highest (243.89 ± 89.1) with 1 μg/mL of iRGD peptide (Figures 2(b) and 3). When the iron concentrations were 14.7 μg/mL and 16.8 μg/mL, the signal intensity was enhanced with increasing concentration of iRGD. Consequently, the mean ΔS reduced gradually (Figures 2(c)-2(d) and 3). However, when the iron concentration was 21 μg/mL, the signal intensities for different iRGD concentrations differed from each other and were higher than those of the control group (Figures 2(e) and 3). The mean ΔS of the SPIO-PLL group was slightly lower than that of groups with the appropriate iRGD peptide concentration and iron concentrations of 12.6 and 14.7 μg/mL (Figure 3).

We also determined the appropriate concentration of iRGD peptide within the same series of iron ion concentrations. No significant difference in the mean $\Delta S'$ was found between the treatment group and control groups ($P > 0.05$) for the 8.4 μg/mL concentration of iron ions. However, when the concentration of iron ions was 12.6 μg/mL, there was a significant difference between the treatment and control groups ($P < 0.05$). Only one group (0.25 μg/mL iRGD) differed from the control group at the 14.7 μg/mL concentration of iron ions. However, no significant difference was found for the other two iron ion concentrations. Therefore, our results suggest that the appropriate concentration of iRGD peptide was 0.25–1.25 μg/mL for the 12.6 μg/mL iron ion concentration and 0.25 μg/mL for the 14.7 μg/mL of iron ion concentration (Figure 4).

3.3. Microscope Observation, Characteristics of Prussian Blue Staining, and Transmission Electron Microscopy. Cells treated with 12.6 μg/mL concentration of SPIO and a range of iRGD peptide concentrations were selected for observation. The labeled cells were diamond or oval in shape under microscopic observation when treated with iron oxide and the range of iRGD. When the cells were incubated with 1 μg/mL iRGD at an iron concentration of 12.6 μg/mL, the positive labeling rate of the treatment group was enhanced relative to the control group (Figure 6). The morphology of the cells was good. Speckled, granular, and patchy blue-stained particles were observed in the cytoplasm, cell nucleus, and cell membrane (Figure 5). The granules were mostly in the cytoplasm around the nuclei. The distribution of the intracellular Fe granules observed under transmission electron microscope is shown in Figures 5(e)-5(f).

The positive labeling rate after treatment was not different than that of the control group with 12.6 μg/mL SPIO (Figure 6). The iron content determination was confirmed by AAS analysis. The mean iron content (pg/cell) of each treatment sample with increasing concentration of iRGD peptide was 2.42 pg, 5.61 pg, 8.12 pg, 10.74 pg, and 13.20 pg, respectively, which was higher than that of the control sample (0.94 pg/cell).

4. Discussion

In the present study, the ability of SPIO combined with iRGD peptide to specifically bind to the $\alpha v\beta 3$ integrin on

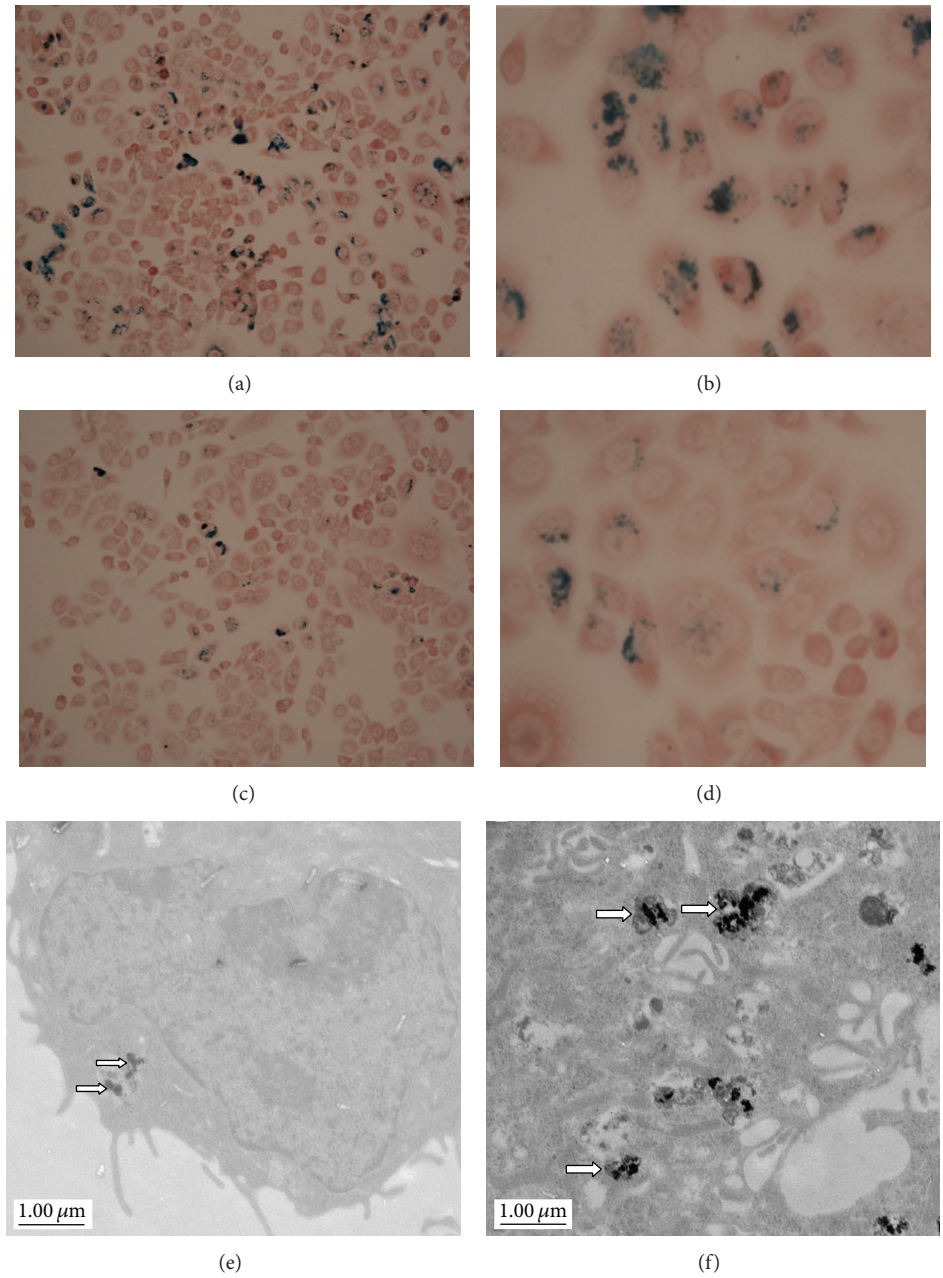

Figure 5: Prussian blue-stained and neutral red solution-counterstained panc-1 cells incubated with SPIO. (a), (b) The cells were incubated with 1 μg/mL iRGD at an iron concentration of 12.6 μg/mL ((a): 20x and (b): 40x). The cells of the control groups were incubated with SPIO without iRGD ((c): 20x and (d): 40x). Higher uptake of SPIO (blue-stained granules) with iRGD peptide compared with SPIO is clearly demonstrated (c, d). Electron microscopy of cells labeled with SPIO nanoparticles (e) and SPIO nanoparticles with iRGD peptide (f) (arrows).

tumor cells was investigated *in vitro*. In contrast to previous studies of molecular MR probes coated or modified with dextran or peptides [33, 34], we explored a novel method of coadministration of SPIO and iRGD peptide that may be useful in the enhancement of tumor imaging. Our results suggest that this method was also effective in labeling cells for MR molecular imaging.

Imaging of pancreatic cancer cells using MRI provides good spatial resolution, resulting in exquisite dynamic information and anatomical contrast, while the kinetics of SPIO distribution in tumor xenografts can be monitored with noninvasive modalities [1, 35]. In recent years, T2 and T2* sequence-mediated MR imaging with SPIO nanoparticles has become a favorable technique that may be available in the clinic. SPIO is a kind of negative contrast that can reduce T2 and T2* values and has increased sensitivity for MRI due to susceptibility effects [31]. Therefore, intracellular iron has strong T2 and T2* effects, and the high reduction in signal is related to the increase in iron oxide uptake by the cells. Human pancreatic cancer cells can be labeled with SPIO and

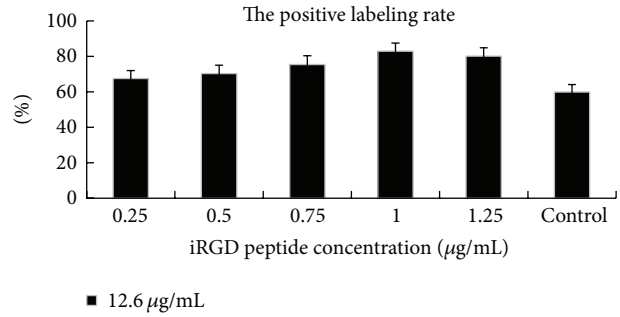

Figure 6: The evaluation of the positive labeled cells. The positive labeling rate of the control was lower than that of the iRGD treatment groups. Control denotes the control group (SPIO). The concentration of SPIO was 12.6 μg/mL.

induce tumor xenografts in nude mice after injection. Our results have demonstrated the efficient nanoparticle uptake capabilities of cells.

To optimize MR imaging *in vitro* and maximize the reliability of the results, it is important that (i) the labeling is reproducible, (ii) the function and viability of labeled cells are retained, and (iii) the process does not affect the target cells [36]. Therefore, we analyzed the cell viability at the beginning of the study through trypan blue staining with different concentrations of iron oxide and iRGD peptide and demonstrated the feasibility of our method.

Several kinds of amino acids have been used to enhance the uptake of SPIO nanoparticles, and the use of polylysine (PLL) has frequently proven to be feasible and efficient [1]. However, Kobukai et al. demonstrated that the use of PLL may be a double-edged sword; the compound can be either safe or toxic depending on the concentration used [37]. Another group suggested that PLL may trigger an inflammatory response by releasing the proinflammatory cytokine, tumor necrosis factor (TNF) [38].

Here, we investigated a new peptide (iRGD peptide) that has a similar function to PLL. The cyclic peptides containing the RGD sequence home to the $\alpha v\beta 3$ integrin specifically and have been applied widely to integrin targeting on cancer pathology, molecular imaging, and drug delivery [3, 30, 31, 34]. This kind of disulfide-based cyclic RGD peptide, called iRGD (CRGDK/RGPD/EC), can interact with both integrin and neuropilin-1 receptors to mediate cellular internalization to improve imaging sensitivity [3]. Sugahara et al. [30]. reported that iron-oxide nanoworms (16) and T7 phage extravasated and have enhanced accumulation in tumor cells upon iRGD coadministration. Therefore, we combined the tumor-penetrating peptide and contrast agents in our study. In addition, this method may also have the following additional advantages: (i) the combination does not involve SPIO surface modification, which may impair the biological characteristics or good compatibility of the particles, and (ii) the quantity or concentration of materials can easily be adjusted during the course of experiments.

In the present study, five different iron concentrations of SPIO were selected according to our previous preliminary experiment. Thorek and Tsourkas reported the appropriate iron oxide concentration as less than 50 μg/mL in nonphagocytic cells [39]. Kobukai et al. reported that there were no registered dead dendritic cells treated with SPIO nanoparticles and PLL up to the 20 μg/mL concentration threshold. Meanwhile, SPIO nanoparticles neither were toxic nor reduced the viability of the cells [37]. In our previous study, we found the appropriate iron concentration range for labeling panc-1 cells to be 21–42 μg/mL. A similar result was reported by Boutry et al. Therefore, in the present study, a concentration lower than 21 μg/mL was selected and ensured [40].

After 24 hours of incubation, differences in the SPIO uptake were found between the treatment and control groups. The control group had less pronounced signal and intracellular iron oxide content. However, with high iron concentrations (14.7–21 μg/mL), the iRGD peptide effect reduced and was even inverse. This may be explained by the fact that the $\alpha v\beta 3$ integrins were saturated or phagocytosis became the predominant mechanism of nanoparticle uptake [31]. Another possible reason is that the saturation of $\alpha v\beta 3$ integrins may inhibit phagocytosis in the presence of high iron concentrations. Our study results show that the uptake and specific binding of our iRGD and SPIO to panc-1 cells in the treatment group were higher than those in the control group, which pointed to a receptor-mediated endocytosis mechanism with the appropriate iron and iRGD exposure. These findings were confirmed by light microscopy, transmission electron microscopy (TEM), and AAS.

A few points must be addressed for better understanding of the results and for improved design of more effective molecular labeling strategies. First, the present results suggest that a small quantity of iRGD peptides can optimally label cells *in vitro*. The longitudinal tracking of pancreatic cancer cells and further investigation *in vivo* using MR will be more challenging than *in vitro* studies. However, this study can be deemed a step towards *in vivo* tracking of pancreatic cancer cells with iRGD peptide and SPIO. Further investigation in animal tumor models remains a key goal of our ongoing studies.

In conclusion, our findings demonstrate that iRGD peptide affects the uptake of iron oxide during labeling of panc-1 cells. An appropriate iRGD peptide concentration can enhance the uptake of intracellular iron. The importance of this study lies in its description of a new potential strategy for pancreatic cancer imaging.

Conflict of Interests

The authors declare that there is no conflict of interests regarding the publication of this paper.

Authors' Contribution

Hou Dong Zuo and Tian Wu Chen contributed equally to this work.

Acknowledgment

This work was supported by the National Nature Science Foundation of China Grant no. 81271643.

References

[1] S. Toki, R. A. Omary, K. Wilson et al., "A comprehensive analysis of transfection-assisted delivery of iron oxide nanoparticles to dendritic cells," *Nanomedicine*, vol. 9, no. 8, pp. 1235–1244, 2013.

[2] E. S. Lee, C. Lim, H. T. Song et al., "A nanosized delivery system of superparamagnetic iron oxide for tumor MR imaging," *International Journal of Pharmaceutics*, vol. 439, no. 1-2, pp. 342–348, 2012.

[3] K. N. Sugahara, T. Teesalu, P. P. Karmali et al., "Tissue-penetrating delivery of compounds and nanoparticles into tumors," *Cancer Cell*, vol. 16, no. 6, pp. 510–520, 2009.

[4] Z. Wang and A. Cuschieri, "Tumour cell labelling by magnetic nanoparticles with determination of intracellular iron content and spatial distribution of the intracellular iron," *International Journal of Molecular Sciences*, vol. 14, no. 5, pp. 9111–9125, 2013.

[5] X. Yang, J. J. Grailer, I. J. Rowland et al., "Multifunctional SPIO/DOX-loaded wormlike polymer vesicles for cancer therapy and MR imaging," *Biomaterials*, vol. 31, no. 34, pp. 9065–9073, 2010.

[6] H. Baraki, N. Zinne, D. Wedekind et al., "Magnetic resonance imaging of soft tissue infection with iron oxide labeled granulocytes in a rat model," *PLoS ONE*, vol. 7, no. 12, Article ID e51770, 2012.

[7] E. A. Neuwelt, P. Várallyay, A. G. Bagó et al., "Imaging of iron oxide nanoparticles by MR and light microscopy in patients with malignant brain tumours," *Neuropathology and Applied Neurobiology*, vol. 30, no. 5, pp. 456–471, 2004.

[8] J. Hu, Y. Qian, X. Wang et al., "Drug-loaded and superparamagnetic iron oxide nanoparticle surface-embedded amphiphilic block copolymer micelles for integrated chemotherapeutic drug delivery and MR imaging," *Langmuir*, vol. 28, no. 4, pp. 2073–2082, 2012.

[9] A. S. Arbab, W. Liu, and J. A. Frank, "Cellular magnetic resonance imaging: current status and future prospects," *Expert Review of Medical Devices*, vol. 3, no. 4, pp. 427–439, 2006.

[10] M. Modo, M. Hoehn, and J. W. M. Bulte, "Cellular MR imaging," *Molecular Imaging*, vol. 4, no. 3, pp. 143–164, 2005.

[11] D. Kim, K. S. Hong, and J. Song, "The present status of cell tracking methods in animal models using magnetic resonance imaging technology," *Molecules and Cells*, vol. 23, no. 2, pp. 132–137, 2007.

[12] A. Petri-Fink and H. Hofmann, "Superparamagnetic iron oxide nanoparticles (SPIONs): from synthesis to in vivo studies—a summary of the synthesis, characterization, in vitro, and in vivo investigations of SPIONs with particular focus on surface and colloidal properties," *IEEE Transactions on Nanobioscience*, vol. 6, no. 4, pp. 289–297, 2007.

[13] H. Kojima, Y. Mukai, M. Yoshikawa et al., "Simple PEG conjugation of SPIO via an Au-S bond improves its tumor targeting potency as a novel MR tumor imaging agent," *Bioconjugate Chemistry*, vol. 21, no. 6, pp. 1026–1031, 2010.

[14] X. Wang, F. Wei, A. Liu et al., "Cancer stem cell labeling using poly(L-lysine)-modified iron oxide nanoparticles," *Biomaterials*, vol. 33, no. 14, pp. 3719–3732, 2012.

[15] T. Bach-Gansmo, "Ferrimagnetic susceptibility contrast agents," *Acta Radiologica*, vol. 387, pp. 1–30, 1993.

[16] R. O. Hynes, "Integrins: versatility, modulation, and signaling in cell adhesion," *Cell*, vol. 69, no. 1, pp. 11–25, 1992.

[17] P. C. Brooks, R. A. F. Clark, and D. A. Cheresh, "Requirement of vascular integrin $\alpha(v)\beta3$ for angiogenesis," *Science*, vol. 264, no. 5158, pp. 569–571, 1994.

[18] M. Kim, C. V. Carman, and T. A. Springer, "Bidirectional transmembrane signaling by cytoplasmic domain separation in integrins," *Science*, vol. 301, no. 5640, pp. 1720–1725, 2003.

[19] H. Jin and J. Varner, "Integrins: roles in cancer development and as treatment targets," *British Journal of Cancer*, vol. 90, no. 3, pp. 561–565, 2004.

[20] J. A. Varner and D. A. Cheresh, "Tumor angiogenesis and the role of vascular cell integrin alphavbeta3," *Important Advances in Oncology*, pp. 69–87, 1996.

[21] C. C. Kumar, "Integrin $\alpha v\beta3$ as a therapeutic target for blocking tumor-induced angiogenesis," *Current Drug Targets*, vol. 4, no. 2, pp. 123–131, 2003.

[22] M. Friedlander, C. L. Theesfeld, M. Sugita et al., "Involvement of integrins alpha v beta 3 and alpha v beta 5 in ocular neovascular diseases," *Proceedings of the National Academy of Sciences of the United States of America*, vol. 93, no. 18, pp. 9764–9769, 1996.

[23] Y. Akashi, T. Oda, Y. Ohara et al., "Anticancer effects of gemcitabine are enhanced by co-administered iRGD peptide in murine pancreatic cancer models that overexpressed neuropilin-1," *British Journal of Cancer*, vol. 110, no. 6, pp. 1481–1487, 2014.

[24] M. Trajkovic-Arsic, P. Mohajerani, A. Sarantopoulos et al., "Multimodal molecular imaging of integrin $\alpha v\beta3$ for in vivo detection of pancreatic cancer," *Journal of Nuclear Medicine*, vol. 55, no. 3, pp. 446–451, 2014.

[25] S. Ji, J. Xu, B. Zhang et al., "RGD-conjugated albumin nanoparticles as a novel delivery vehicle in pancreatic cancer therapy," *Cancer Biology and Therapy*, vol. 13, no. 4, pp. 206–215, 2012.

[26] H. Sawai, Y. Okada, H. Funahashi et al., "Basement membrane proteins play an important role in the invasive processes of human pancreatic cancer cells," *Journal of Surgical Research*, vol. 144, no. 1, pp. 117–123, 2008.

[27] R. J. Weinel, A. Rosendahl, K. Neumann et al., "Expression and function of VLA-α2, -α3, -α5 and -α6-integrin receptors in pancreatic carcinoma," *International Journal of Cancer*, vol. 52, no. 5, pp. 827–833, 1992.

[28] S. E. Holloway, A. W. Beck, L. Girard et al., "Increased expression of Cyr61 (CCN1) identified in peritoneal metastases from human pancreatic cancer," *Journal of the American College of Surgeons*, vol. 200, no. 3, pp. 371–377, 2005.

[29] R. Hosotani, M. Kawaguchi, T. Masui et al., "Expression of integrin alphaVbeta3 in pancreatic carcinoma: relation to MMP-2 activation and lymph node metastasis," *Pancreas*, vol. 25, no. 2, pp. e30–e35, 2002.

[30] K. N. Sugahara, T. Teesalu, P. Prakash Karmali et al., "Coadministration of a tumor-penetrating peptide enhances the efficacy of cancer drugs," *Science*, vol. 328, no. 5981, pp. 1031–1035, 2010.

[31] C. Zhang, M. Jugold, E. C. Woenne et al., "Specific targeting of tumor angiogenesis by RGD-conjugated ultrasmall superparamagnetic iron oxide particles using a clinical 1.5-T magnetic resonance scanner," *Cancer Research*, vol. 67, no. 4, pp. 1555–1562, 2007.

[32] M. A. Dechantsreiter, E. Planker, B. Mathä et al., "N-methylated cyclic RGD peptides as highly active and selective $\alpha(v)\beta3$ integrin antagonists," *Journal of Medicinal Chemistry*, vol. 42, no. 16, pp. 3033–3040, 1999.

[33] G. Huang, C. Zhang, S. Li et al., "A novel strategy for surface modification of superparamagnetic iron oxide nanoparticles for lung cancer imaging," *Journal of Materials Chemistry*, vol. 19, no. 35, pp. 6367–6372, 2009.

[34] F. Xu, D. Lei, X. Du, C. Zhang, X. Xie, and D. Yin, "Modification of MR molecular imaging probes with cysteine-terminated peptides and their potential for in vivo tumour detection," *Contrast Media and Molecular Imaging*, vol. 6, no. 1, pp. 46–54, 2011.

[35] C. Y. Wu, Y. Pu, G. Liu et al., "MR imaging of human pancreatic cancer xenograft labeled with superparamagnetic iron oxide in nude mice," *Contrast Media & Molecular Imaging*, vol. 7, no. 1, pp. 51–58, 2012.

[36] J. A. Frank, S. A. Anderson, H. Kalsih et al., "Methods for magnetically labeling stem and other cells for detection by in vivo magnetic resonance imaging," *Cytotherapy*, vol. 6, no. 6, pp. 621–625, 2004.

[37] S. Kobukai, R. Baheza, J. G. Cobb et al., "Magnetic nanoparticles for imaging dendritic cells," *Magnetic Resonance in Medicine*, vol. 63, no. 5, pp. 1383–1390, 2010.

[38] B. L. Strand, L. Ryan, P. In't Veld et al., "Poly-L-lysine induces fibrosis on alginate microcapsules via the induction of cytokines," *Cell Transplantation*, vol. 10, no. 3, pp. 263–275, 2001.

[39] D. L. J. Thorek and A. Tsourkas, "Size, charge and concentration dependent uptake of iron oxide particles by non-phagocytic cells," *Biomaterials*, vol. 29, no. 26, pp. 3583–3590, 2008.

[40] S. Boutry, S. Brunin, I. Mahieu, S. Laurent, L. Vander Elst, and R. N. Muller, "Magnetic labeling of non-phagocytic adherent cells with iron oxide nanoparticles: a comprehensive study," *Contrast Media and Molecular Imaging*, vol. 3, no. 6, pp. 223–232, 2008.

Hindawi Publishing Corporation
BioMed Research International
Volume 2014, Article ID 618096, 6 pages
http://dx.doi.org/10.1155/2014/618096

Research Article

Biodistribution and SPECT Imaging Study of ^{99m}Tc Labeling NGR Peptide in Nude Mice Bearing Human HepG2 Hepatoma

Wenhui Ma, Zhe Wang, Weidong Yang, Xiaowei Ma, Fei Kang, and Jing Wang

Department of Nuclear Medicine, Xijing Hospital, Fourth Military Medical University, No. 127 West Changle Road, Xi'an, Shaanxi Province 710032, China

Correspondence should be addressed to Jing Wang; wangjing@fmmu.edu.cn

Received 16 December 2013; Revised 30 January 2014; Accepted 3 February 2014; Published 19 May 2014

Academic Editor: Yongdoo Choi

A peptide containing Asn-Gly-Arg(NGR) sequence was synthesized and directly labeled with ^{99m}Tc. Its radiochemical characteristics, biodistribution, and SPECT imaging were evaluated in nude mice bearing human HepG2 hepatoma. Nude mice bearing HepG2 were randomly divided into 5 groups with 5 mice in each group and injected with ~7.4 MBq ^{99m}Tc-NGR. The SPECT images were acquired in 1, 4, 8, and 12 h postinjection via caudal vein. The metabolism of tracers was determined in major organs at different time points, which demonstrated rapid, significant tumor uptake and slow tumor washout. The control group mice were blocked by coinjecting unlabelled NGR (20 mg/kg). Tumor uptake was (2.52 ± 0.83%) ID/g at 1 h, with the highest uptake of (3.26 ± 0.63%) ID/g at 8 h. In comparison, the uptake of the blocked control group was (1.65 ± 0.61%) ID/g at 1 h after injection. The SPECT static images and the tumor/muscle (T/NT) value were obtained. The highest T/NT value was 7.58 ± 1.92 at 8 h. The xenografted tumor became visible at 1 h and the clearest image of the tumor was observed at 8 h. In conclusion, ^{99m}Tc-NGR can be efficiently prepared and it exhibited good properties for the potential SPECT imaging agent of tumor.

1. Introduction

Angiogenic tumor vessels are important element for tumor growth and metastasis and the metalloexopeptidase CD13/aminopeptidase N (APN) plays a critical role in cancer angiogenesis. Peptides containing NGR have shown high efficiency in targeted cells, tissues, and new vessels with CD13 receptor overexpression [1, 2]. Moreover, in tissues that undergo angiogenesis, blood vessels also overexpress APN and proliferation of endothelial cells is well known to be an important factor in tumor angiogenesis [3, 4]. It is proved that NGR can bind with new vasculature by aminopeptidase N (CD13) and integrin $\alpha v\beta 3$, although the binding mechanisms are different. Meanwhile, CD13 receptor mediated binding to tumor vasculature is specific but not to the other CD13 rich tissues, which was proved by in vivo studies [5]. Good blood clearance was thought to favor the utilization of imaging techniques. Therefore, NGR peptide was characterized as a promising molecular imaging candidate for early diagnosis, particularly for tumor.

Many peptides containing NGR motif have been produced with excellent tumor targeted efficacy, such as tTF-NGR, NGR-hTNF, and cyclic NGR-labeled paramagnetic quantum dots (cNGR-pQDs) [6–10]. Our previous work indicated that both NGR monomer and dimer showed relatively high tumor uptake [5, 11].

In this study, a new NGR peptide was synthesized and labeled with ^{99m}Tc, then subjected to SPECT imaging of CD13 expression in a subcutaneous mouse HepG2 hepatoma xenograft model, which was proved to show positive CD13 receptor and easy formation of tumor.

2. Materials and Methods

2.1. General. All chemicals (reagent grade) were obtained from commercial suppliers and used without further purification. NGR (YGGCNGRC) was prepared by SPPS using the Fmoc method on a chlorotrityl chloride resin. $^{99m}TcO_4^-$ was produced from ^{99}Mo/^{99m}Tc generator (Beijing Atom High

Table 1: Rf values of free $^{99m}TcO_4^-$, ^{99m}Tc-colloid and ^{99m}Tc-NGR.

Rf value	Free $^{99m}TcO_4^-$	^{99m}Tc-colloid	^{99m}Tc-NGR
Acetone	0.9~1.0	0.0	0.0
Vethanol : Vammonia water : Vwater = 2 : 1 : 5	0.9~1.0	0.0	0.7~0.8

Tech, China). Water was purified using a Milli-Q ultrapure water system from Millipore (Milford, USA), followed by passing through a Chelex 100 resin before bioconjugation and radiolabeling. Radio-TLC was performed on silica gel-coated plastic sheets (Polygram SIL G, Macherey-Nagel) with acetone and Vethanol : Vammonia water : Vwater = 2 : 1 : 5 as the eluents. The plates were read with Bioscan Mini-scan (USA) and Allchhrom Plus software. The semipreparative high-performance liquid chromatography (HPLC, Aglint, Canada) was employed for peptide analysis. NGR-containing peptide was prepared by solid phase peptide synthesis (SPPS) using the Fmoc strategy on chlorotrityl chloride resins as previously reported [12]. Mass spectra were used to confirm the identity of the products. Mass spectra were obtained on a Q-Tof premier-UPLC system equipped with an electrospray interface (ESI; Waters, USA) or a Thermo Electron Finnigan LTQ mass spectrometer equipped with an electrospray ionization source (Thermo Scientific, USA).

2.2. Radiolabelling and Formulation. The fresh $^{99m}TcO_4^-$ solution (37–74 MBq) was added into a solution of NGR peptide (15~20 μg peptide per mCi $^{99m}TcO_4^-$) with 200 μg stannous chloride dissolved in 1 M HCl (5 μg/μL) and 20 μL of 0.2 M NaAc/HAc buffer (pH = 4.2) solution. The mixture was incubated at room temperature for 30 min. The $^{99m}TcO_4^-$-containing solution was filtered over a 0.2 μm syringe filter (Acrodisc, PALL, USA) and then passed through a 0.2 μm Millipore filter into a sterile vial for use.

2.3. In Vitro Stability. The stability of ^{99m}Tc-labeled NGR peptide in PBS and mouse serum at 37°C was studied at 1, 3, 6, and 12 h. Then the percentage of parent tracer was determined by radio-TLC (Table 1).

2.4. Cell Culture and Animal Model. HepG2 cells were grown in high glucose DMEM culture medium. All cell lines were cultured in medium supplemented with 10% (v/v) fetal bovine serum (Gibco, USA), 1% mycillin, and 1% Glutamine (Beyotime, China) at 37°C in a humidified atmosphere with 5% CO_2. Using female BALB/c nude mice (4–6 weeks of age), HepG2 tumor model was established by subcutaneous injection of 2×10^6 HepG2 tumor cells (0.1 mL) into the right upper flanks. When the tumor volume reached 0.8~1.0 cm in diameter (2-3 weeks after inoculation), the tumor-bearing mice were used for SPECT imaging and biodistribution studies. All animal studies were approved by Clinical Center at the FMMU.

2.5. Cell Uptake Study. HepG2 cells were seeded into 48-well plates at a density of 2×10^5 cells per well 24 h prior to the experiment. HepG2 cells were then incubated with ^{99m}Tc-labeled NGR peptides (~370 kBq/well) at 37°C for 15, 30, 60, 120, and 240 min. After incubation, tumor cells were washed three times with ice cold PBS and harvested by trypsinization with 0.25% trypsin/0.02% EDTA (Hyclone, USA). Cell suspensions were collected and measured in a gamma counter (Zhida, Shannxi, China). Cell uptake data was presented as percentage of total input radioactivity added to the culture medium after decay correction. Experiments were performed twice with triplicate wells.

2.6. Cell Binding Assay. In vitro CD13 receptor binding affinity and specificity of ^{99m}Tc-NGR were assessed via competitive cell binding assay. The best-fit 50% inhibitory concentration (IC_{50}) values for the HepG2 cells were calculated by fitting the data with nonlinear regression using Graph-Pad Prism5.0 (Graph-Pad Software, San Diego, CA, USA).

2.7. SPECT Imaging. HepG2 tumor-bearing animals were imaged in supine position with a one-head SPECT MPR (GE, USA) equipped with a pinhole collimator. About 7.4 MBq of ^{99m}Tc-labeled NGR peptide was intravenously injected into each mouse under intraperitoneal injection of sodium pentobarbital at a dose of 45.0 mg/kg. Static SPECT images were acquired at 1, 4, 8, and 12 h pi. The acquisition count limit was set at 200 k.

2.8. Biodistribution Studies. Nude mice bearing human HepG2 hepatoma were randomly divided into 5 groups and injected with ~7.4 MBq of ^{99m}Tc-NGR with or without excess unlabelled NGR peptide (20 mg/kg). After injection of the tracer, mice were sacrificed and dissected. The radioactivity in the HepG2 tumor, major organs, and muscle were collected and weighed wet with tubes (%ID/g). Mean uptake (%ID/g) for a group of animals was calculated with standard deviations. Values were expressed as mean ± SD (n = 5/group).

3. Results

3.1. Chemistry and Radiochemistry. NGR peptide was well prepared (Figure 1). The analytical HPLC and mass spectroscopy were used to confirm the identity of the products. The mass spectroscopy data and chemical structures for NGR were represented below (Figure 1). The electrospray ionization mass spectra of NGR were determined to be m/z = 829.40 ($[M+H]^+$). After purification, the specific activity of ^{99m}Tc-labeled tracers was determined to be about

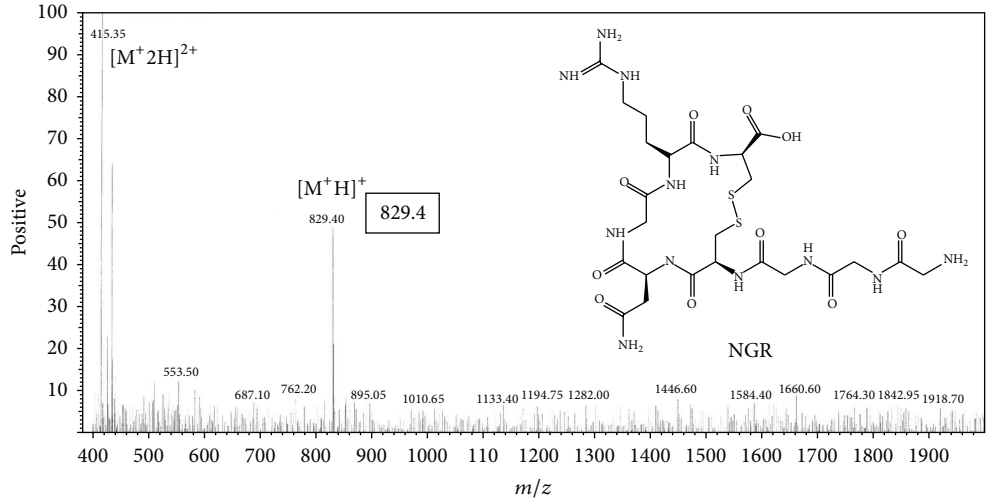

Figure 1: Chemical structure and mass result of NGR (YGGCNGRC).

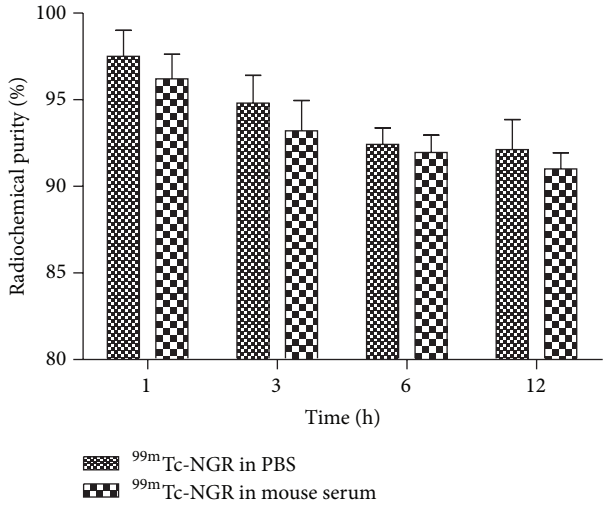

Figure 2: Stability of ^{99m}Tc-NGR peptide in PBS (pH = 7.4) and mouse serum at 37°C for 1, 3, 6, and 12 h. Its radiochemical purity was >98%. 92% of ^{99m}Tc-NGR peptide almost remained intact in PBS and mouse serum after 12 h of incubation.

3.08~6.17 MBq/nmol. The labeling yield of the product was 95 ± 0.35% and the radiochemical purity was greater than 98%. The in vitro stability of ^{99m}Tc-NGR in PBS (pH 7.4) at 37°C was shown in Figure 2. After 12 h of incubation, more than 92% of ^{99m}Tc-NGR peptide remained intact in mice serum.

3.2. Cell Uptake. Cell uptake study revealed that ^{99m}Tc-NGR bound to HepG2 tumor cells directly. During the first 15 min, about 0.49 ± 0.05% of ^{99m}Tc-NGR uptake in HepG2 cells were determined. After 2 h incubation, the peptide uptake in HepG2 cells reached the maximum of 1.52 ± 0.13% (Figure 3(a)). About 1.35 ± 0.27% of ^{99m}Tc-NGR were still associated with HepG2 cells after 4 h incubation.

3.3. Cell Binding Assay. Ligand-receptor binding affinities of ^{99m}Tc-NGR to CD13 were determined by a competitive cell-binding assay. ^{99m}Tc-NGR inhibited the binding of NGR peptide to HepG2 cells in a concentration-dependent manner (Figure 3(b)). The IC_{50} values for ^{99m}Tc-NGR were calculated to be 287 ± 34 nmol/L.

3.4. SPECT Imaging. The tumor-targeting efficacy of ^{99m}Tc-NGR probe in HepG2 tumor-bearing nude mice was evaluated by static SPECT scans at different time points after injection. Representative decay-corrected images are shown in Figure 4. The HepG2 tumors were clearly visualized with good tumor-to-background contrast for the tracer. Overall, ^{99m}Tc-NGR provided better image quality with the same amount of injected activity.

3.5. Biodistribution Studies. Tissue distribution data for ^{99m}Tc-NGR in mice bearing HepG2 hepatoma tumors are given as percentage administered activity per gram of tissue (%ID/g) in Table 2 and Figure 5. The in vivo biodistribution of with and without coinjection of nonradiolabeled NGR peptide (20 mg/kg of mouse body weight) was examined in HepG2 tumor-bearing mice. For ^{99m}Tc-NGR, the tumor uptake was determined to be 2.52 ± 0.83, 3.03 ± 0.71, 3.26 ± 0.63, and 2.81 ± 0.25% ID/g at 1, 4, 8, and 12 h, respectively. ^{99m}Tc-NGR exhibited 7.93 ± 2.13% ID/g kidney uptake and 4.07 ± 0.76% ID/g liver uptake at 1 h pi. The nonspecific uptake in the muscle was at a very low level. ^{99m}Tc-NGR exhibited high tumor uptake at the early time point (Figure 5), indicating the specific binding and relatively longer circulation time.

A decrease of radioactivity was observed in all dissected tissues and organs similar to SPECT imaging results in blocking group (Table 2), with the change of tumor uptake being the most significant reducing markedly from 2.52 ± 0.83% ID/g whereas the presence of nonlabeled NGR peptide significantly reduced to 1.65 ± 0.61% ID/g at 1 h after

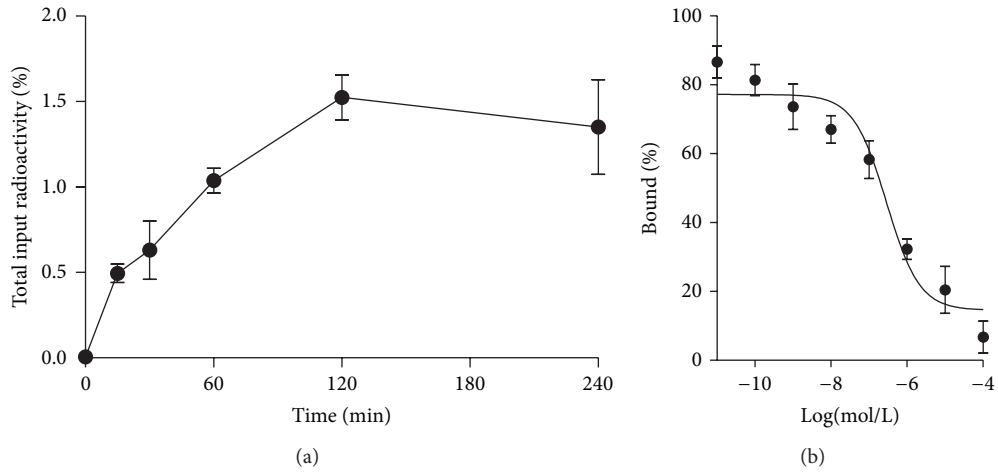

Figure 3: In vitro cell uptake assay and cell-binding assay of HepG2 human hepatoma cells. (a) Cell uptake assay of ^{99m}Tc-NGR (n = 3, mean ± SD). The background readings are reflected at time 0. (b) Cell binding assay of ^{99m}Tc-NGR on CD13 receptor of HepG2 cells (n = 3, mean ± SD).

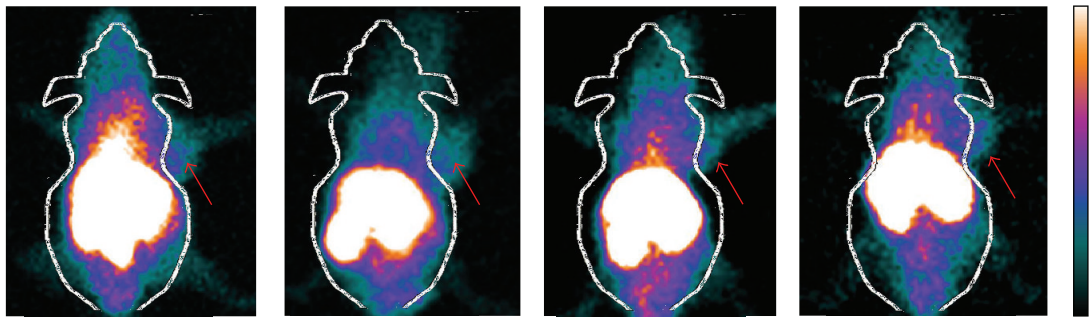

Figure 4: Representative decay-corrected whole-body SPECT images of mice bearing HepG2 tumors on right front flank after intravenous administration of ^{99m}Tc-NGR (~7.4 MBq) SPECT images of nude mice bearing HepG2 tumor at 1, 4, 8, and 12 h pi (tumors are indicated by red arrows).

Table 2: Biodistribution data (%ID/g) of ^{99m}Tc-NGR in HepG2 hepatoma tumor-bearing nude mice at 1, 4, 8, and 12 h postinjection (n = 5, mean ± SD).

	1 h	4 h	8 h	12 h	Blocking (1 h)
Blood	3.82 ± 0.41	1.75 ± 0.39	0.98 ± 0.22	0.75 ± 0.31	2.56 ± 0.34
Heart	3.74 ± 0.54	2.26 ± 0.33	1.15 ± 0.32	1.07 ± 0.25	2.73 ± 0.29
Lung	2.52 ± 0.83	2.13 ± 0.44	1.86 ± 0.38	1.21 ± 0.31	2.04 ± 0.28
Liver	4.07 ± 0.76	3.85 ± 0.73	3.44 ± 0.52	3.26 ± 0.47	3.27 ± 0.16
Kidney	7.93 ± 2.13	7.03 ± 0.95	6.21 ± 0.43	5.96 ± 0.41	5.03 ± 0.97
Spleen	2.37 ± 0.43	2.09 ± 0.60	1.88 ± 0.42	1.72 ± 0.37	1.89 ± 0.22
Stomach	3.07 ± 0.56	2.20 ± 0.26	1.61 ± 0.39	1.56 ± 0.32	3.41 ± 0.31
Intestine	2.65 ± 1.06	2.18 ± 0.96	1.93 ± 0.22	1.60 ± 0.27	2.40 ± 0.59
Muscle	0.53 ± 0.33	0.46 ± 0.11	0.43 ± 0.14	0.39 ± 0.22	0.48 ± 0.27
Tumor	2.52 ± 0.83	3.03 ± 0.71	3.26 ± 0.63	2.81 ± 0.25	1.65 ± 0.61
Tumor-to-normal tissue uptake ratio at 1 h postinjection					
			T/M	4.75 ± 0.91	
			T/L	0.62 ± 0.33	
			T/K	0.32 ± 0.15	

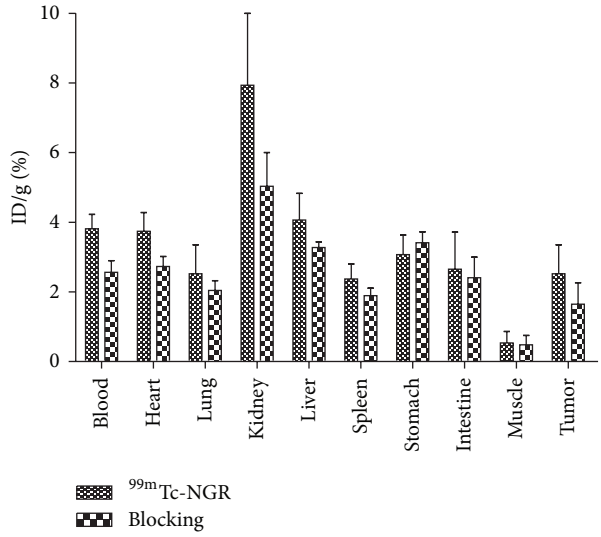

Figure 5: Biodistribution of ^{99m}Tc-NGR (~7.4 MBq) in athymic nude mice bearing HepG2 tumor with or without NGR (20 mg/kg) at 1 h (n = 5, mean ± SD).

injection. For ^{99m}Tc-NGR nonblocking group, 4.07 ± 0.76% ID/g in liver and 7.93 ± 2.13% ID/g in kidney were decreased to 3.27 ± 0.16% ID/g and 5.03 ± 0.97% ID/g by blocking, respectively.

4. Discussion

In this study, we synthesized a novel NGR peptide and investigated its biological targeting specificity, which turned out to be a promising tumor molecular imaging probe for clinical practice.

^{99m}Tc has favorable chemical and physical properties and can be produced from the generator directly [11]. CD13 receptor is an attractive biological target, which has been found to be overexpressed on newly formed neovasculature and on a wide range of tumor cells types. The high radiochemical purity of the radiotracer (>98%) stimulated further analysis encompassing in vitro and in vivo evaluation, without the time consuming steps of purification and drying of the compound. The ^{99m}Tc-labeled tracer also showed good stability (Figure 2) and affinity (Figure 3). The results showed that imaging acquisition after injection within 12 h is enough for detecting tumor clearly. The labeling process in this study is so convenient that the probe is practical in future clinical imaging.

The development of radiolabeled peptides for diagnostic and therapeutic applications has expanded exponentially in the last decades [8, 13, 14]. Peptide-based radiopharmaceuticals can be produced easily and inexpensively and have many favorable properties, including fast clearance, rapid tissue penetration, and low antigenicity [6, 9, 15–17]. In this study, the cysteine beside NGR motif formed a cyclic via a disulfide linkage and the direct labeling method resulted in a very stable product. At the meantime, breaking the disulfide linkage in the NGR-containing peptide during the directly labeling process may explain the slightly lower binding affinity compared with our previous results [18]. Otherwise, the extra three glycines were added to protect the core motif NGR and may increase peptide half-life and stability [19]. Meanwhile, the liver and kidney uptake was obviously reduced compared with previous study, which may also be caused by adding glycine [18].

SPECT scans of ^{99m}Tc-NGR in nude mice bearing HepG2 hepatoma showed notable uptake in tumor and dominant renal and hepatic clearance. But the unspecific binding on the other tissues was decreasing and the tumor to nontumor ratio was consequently increasing. The receptor specificity of ^{99m}Tc-NGR was further confirmed by effective inhibition of tumor uptake in the presence of excess nonlabeled NGR peptide in biodistribution study (Table 1). Although the ^{99m}Tc-NGR uptake in liver and gastrointestinal tract was lower than previous results, the practice in detecting tumor and metastases in the abdominal area is inapplicable. Since the excretion of the probe was mainly renal, fast blood depuration should be another favorable feature.

In brief, our data demonstrated that synthesizing novel ^{99m}Tc-NGR was a promising synthetic strategy for SPECT imaging in terms of in vitro and in vivo properties. Our future work will continually focus on more optimal approach to reduce liver and gastrointestinal tract uptake by modifying the peptide structure and keep the specificity binding. Additionally, a thorough comparison between various NGR peptides is warranted to screen the better radiotracers.

5. Conclusion

NGR peptide was successfully labeled with the generator-produced ^{99m}Tc for SPECT imaging of tumor CD13 receptor. ^{99m}Tc-NGR exhibited good properties in terms of binding affinity, cellular uptake, tumor uptake and retention, and pharmacokinetics. ^{99m}Tc-NGR peptide is a potential SPECT agent for imaging and early diagnosis of tumor.

Conflict of Interests

The authors declare that there is no conflict of interests regarding the publication of this paper.

Authors' Contribution

Wenhui Ma and Zhe Wang contributed equally to this work.

Acknowledgments

This work was supported by the Key Program of National Natural Science Foundation of China (Grant no. 81230033), the Major State Basic Research Development Program (Grant no. 2011CB707704), The Major Instrument of National Natural Science Foundation Research Project (Grant no. 81227901), the Major Program of National Natural Science Foundation of China (Grant no. 81090270), the General Program of National Natural Science Foundation of China

(Grant no. 81371594), and the International Cooperation Program of Xijing Hospital (Grant no. XJZT13G02).

References

[1] X. Wang, Y. Wang, X. Chen, J. Wang, X. Zhang, and Q. Zhang, "NGR-modified micelles enhance their interaction with CD13-overexpressing tumor and endothelial cells," *Journal of Controlled Release*, vol. 139, no. 1, pp. 56–62, 2009.

[2] B.-J. Zhao, X.-Y. Ke, Y. Huang et al., "The antiangiogenic efficacy of NGR-modified PEG-DSPE micelles containing paclitaxel (NGR-M-PTX) for the treatment of glioma in rats," *Journal of Drug Targeting*, vol. 19, no. 5, pp. 382–390, 2011.

[3] S. V. Bhagwat, J. Lahdenranta, R. Giordano, W. Arap, R. Pasqualini, and L. H. Shapiro, "CD13/APN is activated by angiogenic signals and is essential for capillary tube formation," *Blood*, vol. 97, no. 3, pp. 652–659, 2001.

[4] A. H. Negussie, J. L. Miller, G. Reddy, S. K. Drake, B. J. Wood, and M. R. Dreher, "Synthesis and in vitro evaluation of cyclic NGR peptide targeted thermally sensitive liposome," *Journal of Controlled Release*, vol. 143, no. 2, pp. 265–273, 2010.

[5] K. Chen, W. Ma, G. Li et al., "Synthesis and evaluation of ^{64}Cu-labeled monomeric and dimeric NGR peptides for MicroPET imaging of CD13 receptor expression," *Molecular Pharmacology*, vol. 10, no. 1, pp. 417–427, 2013.

[6] W. Arap, R. Pasqualini, and E. Ruoslahti, "Cancer treatment by targeted drug delivery to tumor vasculature in a mouse model," *Science*, vol. 279, no. 5349, pp. 377–380, 1998.

[7] F. Curnis, G. Arrigoni, A. Sacchi et al., "Differential binding of drugs containing the NGR motif to CD13 isoforms in tumor vessels, epithelia, and myeloid cells," *Cancer Research*, vol. 62, no. 3, pp. 867–874, 2002.

[8] I. Dijkgraaf, C.-B. Yim, G. M. Franssen et al., "PET imaging of $\alpha v\beta 3$ integrin expression in tumours with68Ga-labelled mono-, di- and tetrameric RGD peptides," *European Journal of Nuclear Medicine and Molecular Imaging*, vol. 38, no. 1, pp. 128–137, 2011.

[9] J. Meng, Z. Yan, X. Xue et al., "High-yield expression, purification and characterization of tumor-targeted IFN-α2a," *Cytotherapy*, vol. 9, no. 1, pp. 60–68, 2007.

[10] Y.-S. Yang, X. Zhang, Z. Xiong, and X. Chen, "Comparative in vitro and in vivo evaluation of two ^{64}Cu-labeled bombesin analogs in a mouse model of human prostate adenocarcinoma," *Nuclear Medicine and Biology*, vol. 33, no. 3, pp. 371–380, 2006.

[11] Z. Wang, W. Ma, J. Wang et al., "Imaging and therapy of hSSTR2-transfected tumors using radiolabeled somatostatin analogs," *Tumor Biology*, vol. 34, no. 4, pp. 2451–2457, 2013.

[12] L. Adar, Y. Shamay, G. Journo, and A. David, "Pro-apoptotic peptide-polymer conjugates to induce mitochondrial-dependent cell death," *Polymers for Advanced Technologies*, vol. 22, no. 1, pp. 199–208, 2011.

[13] K. Chen, X. Sun, G. Niu et al., "Evaluation of ^{64}Cu labeled GX1: a phage display peptide probe for PET imaging of tumor vasculature," *Molecular Imaging and Biology*, vol. 14, no. 1, pp. 96–105, 2012.

[14] Y. Wu, X. Zhang, Z. Xiong et al., "microPET imaging of glioma integrin $\alpha v\beta 3$ expression using ^{64}Cu-labeled tetrameric RGD peptide," *Journal of Nuclear Medicine*, vol. 46, no. 10, pp. 1707–1718, 2005.

[15] M. W. Ndinguri, R. Solipuram, R. P. Gambrell, S. Aggarwal, and R. P. Hammer, "Peptide targeting of platinum anti-cancer drugs," *Bioconjugate Chemistry*, vol. 20, no. 10, pp. 1869–1878, 2009.

[16] A. Corti, M. Giovannini, C. Belli, and E. Villa, "Immunomodulatory agents with antivascular activity in the treatment of non-small cell lung cancer: focus on TLR9 agonists, IMiDs and NGR-TNF," *Journal of Oncology*, vol. 2010, Article ID 732680, 8 pages, 2010.

[17] K. Chen and P. S. Conti, "Target-specific delivery of peptide-based probes for PET imaging," *Advanced Drug Delivery Reviews*, vol. 62, no. 11, pp. 1005–1022, 2010.

[18] W. Ma, F. Kang, Z. Wang et al., "^{99m}Tc-labeled monomeric and dimeric NGR peptides for SPECT imaging of CD13 receptor in tumor-bearing mice," *Amino Acids*, vol. 44, no. 5, pp. 1337–1345, 2013.

[19] K. N. Samli, M. J. McGuire, C. B. Newgard, S. A. Johnston, and K. C. Brown, "Peptide-mediated targeting of the islets of Langerhans," *Diabetes*, vol. 54, no. 7, pp. 2103–2108, 2005.

Hindawi Publishing Corporation
BioMed Research International
Volume 2014, Article ID 587806, 7 pages
http://dx.doi.org/10.1155/2014/587806

Clinical Study

Time-Intensity Curve Parameters in Rectal Cancer Measured Using Endorectal Ultrasonography with Sterile Coupling Gels Filling the Rectum: Correlations with Tumor Angiogenesis and Clinicopathological Features

Yong Wang,[1] Lin Li,[1] Yi-Xiang J. Wang,[2] Ning-Yi Cui,[1] Shuang-Mei Zou,[3] Chun-Wu Zhou,[1] and Yu-Xin Jiang[4]

[1] *Department of Diagnostic Imaging, Cancer Hospital & Institute, Peking Union Medical College and Chinese Academy of Medical Sciences, Beijing 100021, China*
[2] *Department of Imaging and Interventional Radiology, Prince of Wales Hospital, The Chinese University of Hong Kong, Shatin, NT, Hong Kong*
[3] *Department of Pathology, Cancer Hospital & Institute, Peking Union Medical College and Chinese Academy of Medical Sciences, Beijing 100021, China*
[4] *Department of Diagnostic Ultrasound, Peking Union Medical College Hospital, Peking Union Medical College and Chinese Academy of Medical Sciences, Beijing 100730, China*

Correspondence should be addressed to Chun-Wu Zhou; drzhouchunwu@163.com and Yu-Xin Jiang; yuxinjiangxh@hotmail.com

Received 25 January 2014; Accepted 20 April 2014; Published 13 May 2014

Academic Editor: Zhiyi Chen

The primary aim of this study was to investigate the relationship between contrast-enhanced ultrasonography (CEUS) imaging parameters and clinicopathological features of rectal carcinoma and assess their potential as new radiological prognostic predictors. A total of 66 rectal carcinoma patients were analyzed with the time-intensity curve of CEUS. The parameter arrival time (AT), time to peak enhancement (TTP), wash-in time (WIT), enhanced intensity (EI), and ascending slope (AS) were measured. Microvessel density (MVD) was evaluated by immunohistochemical staining of surgical specimens. All findings were analysed prospectively and correlated with tumor staging, histological grading, and MVD. The mean values of AT, TTP, WIT, EI, and AS value of the rectal carcinoma were 10.84 ± 3.28 s, 20.61 ± 5.52 s, 9.78 ± 2.83 s, 28.68 ± 4.67 dB, and 3.20 ± 1.10, respectively. A positive linear correlation was found between the EI and MVD in rectal carcinoma ($r = 0.295$, $P = 0.016$), and there was a significant difference for EI among histological grading ($r = -0.264$, $P = 0.007$). EI decreased as T stage increased with a trend of association noted ($P = 0.096$). EI of contrast enhanced endorectal ultrasonography provides noninvasive biomarker of tumor angiogenesis in rectal cancer. CEUS data have the potential to predict patient prognosis.

1. Introduction

It is well known that rectal cancer is an important contributor to cancer mortality and morbidity [1]. Angiogenesis, which involves sprouting of endothelial cells to form new vessels and supplying nutriments and oxygen for the tumor cells, is essential for tumor formation, growth, and dissemination [2]. Microvessel density measured by immunofluorescent analysis is used to evaluate tumor angiogenesis activity as standard method, but it is invasive and depending on experience of operators [3, 4]. Noninvasive imaging modalities such as dynamic contrast enhanced magnetic resonance (DCE-MR) [5], perfusion computed tomography [6], and contrast enhanced ultrasound (CEUS) are applied to observe tumor vascularity. Ultrasound is low cost and convenient and no radiation is associated. The second generation of ultrasound contrast agents consists of microbubbles remaining strictly intravascular, leading to CEUS becoming a promising indirect method of evaluating blood flow within functional vessel [7, 8]. Meanwhile, the analysis of time intensity curve (TIC)

makes it possible to assess tumor vascularity quantitatively [9].

Recent studies have demonstrated that CEUS perfusion parameters are closely correlated with tumor vascularity in several types of malignancies, such as hepatocellular carcinoma, pancreatic carcinoma, prostate cancer, breast tumors, and gastric carcinoma [10–13]; however, there is limited experience in using CEUS to assess tumor vascularity in rectal cancer. Zhuang et al. [14] demonstrated positive linear correlation between TIC parameters by CEUS and MVD in colorectal tumor, but only two rectal cases were concluded in the study. The value of TIC parameters in assessing tumor vascularity in rectal cancer remained to be investigated.

Some researchers also explored the relationship between DCE-MRI perfusion parameters and prognostic factors in rectal cancer, but results have been conflicting. Oberholzer et al. [15] reported that DCE-MRI parameter correlated with the N category and k21 with the occurrence of distant metastases; Hong et al. [16] reported that Erise was correlated with N stage, and Tp was correlated with histologic grade, while Kim et al. [4] found no correlation between any DCE-MRI perfusion parameters and TN stage. Till now, there have been few reported studies on relationship between CEUS perfusion parameters and prognostic factors in rectal cancer.

Therefore, the purpose of this study was to investigate the correlation of time-intensity curve (TIC) parameters with microvessel density in rectal cancer and we also evaluate the relationship between TIC parameters, MVD, and the standard prognostic variables (tumor stage, lymphatic metastasis, distant metastasis, and histologic grade) to explore the diagnostic value in tumor vascularity and prognostic value of TIC parameters in rectal cancer.

2. Materials and Methods

2.1. Patients. A total of 66 patients with rectal cancer who underwent endorectal ultrasound (ERUS) and CEUS examinations were involved. All patients had undergone surgery within 1 week after CEUS in our hospital between December 2009 and June 2013. None had undergone radiation or chemotherapy before surgery. Patients with rectal mass who had not been referred for ERUS and CEUS examinations or in whom surgery was not undertaken within one week were not included in this study. ERUS and CEUS examinations were approved by the Hospital Ethics Committee. Each patient was consent informed. All of the patients had solitary lesions. The diagnoses for all 66 lesions were confirmed by surgery and pathology.

2.2. ERUS. All ERUS examinations were performed using a Philips iU22 unit (Philips, Bothell, WA, USA). An end-fire type endorectal probe (C5-9 sec) was utilized. Patients stayed in the left lateral decubitus position, prepared with enemas to remove all air, stool, and mucus from the rectum. Instead of the standard water-balloon filling technique, we developed a novel technique in our previous study, where the coupling gel was injected into the rectum directly [17]. The amount of gel used was usually 100–150 mL, depending on filling degree of the rectum, which was to ensure the five layers of the bowel wall and the tumor can be clearly seen. The gel helped the US probe to pass through the tumoral stenosis of rectum, minimized compression and distortion of the lesion, and improved visualization of the rectal wall and tumor. The tumors were evaluated for their size and depth of invasion, echo pattern, and internal vascularity as well as the localization of the rectal wall layers that were disrupted by the tumor.

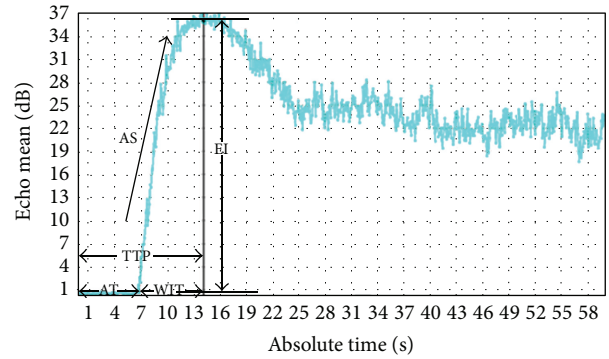

Figure 1: Time-intensity curve (TIC) from region of interest (ROI) within the tumor and the ultrasound TIC parameters. Arrival time (AT), time to peak enhancement (TTP), wash-in time (WIT), enhanced intensity (EI), and ascending slope (AS).

2.3. CEUS. CEUS examination was performed after the ERUS examination. The mechanical index was 0.08–0.11. 2.4 mL contrast agent SonoVue (Bracco, Italy) which was administrated through a forearm vein in bolus through a 20-gauge intravenous cannula within 1 to 2 seconds, followed by a flush of 5 mL of 0.9% normal saline solution. The contrast agent wash in and wash out were recorded for 60 seconds. By using Q lab software (version 5; Philips Medical Systems, Bothell, WA, USA) on the workstation; the region of interest (ROI) of every lesion was manually drawn in the most enhanced region within the tumor on contrast ultrasonographic images and the ROI area was set to 25 mm^2. The time-intensity curve was reconstructed for each ROI and then arrival time (AT), time to peak enhancement (TTP), wash-in time (WIT), enhanced intensity (EI), and ascending slope (AS) were obtained. The AT was defined as the time from injection until the enhancement. The TTP was defined as the interval from injection to the peak of the time-intensity curve. The WIT was defined as interval from beginning of enhancement to the peak of the enhancement. The EI was defined as peak intensity minus baseline intensity. The AS was defined as the slope rate of ascending curve (Figure 1). All contrast-enhanced ultrasound data were analyzed by two experienced radiologists who were blinded to all clinical and pathological information.

2.4. Histopathological Analysis. Histological sections were reviewed by one experienced pathologist without knowledge of the results of the ultrasound findings. The description of the gross specimen and 4 μm thick haematoxylin and eosin-stained histological sections were reviewed. Morphologic

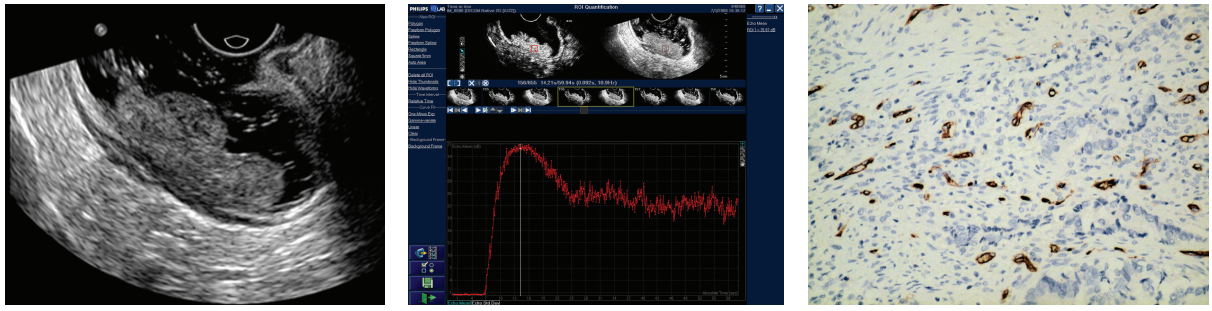

(a) (b) (c)

Figure 2: Images of poorly differentiated rectal adenocarcinoma with T2 stage. (a) Endorectal ultrasonography showed that an irregular hypoechoic lesion invaded muscularis propria. (b) Time-intensity curve was obtained from ROI with EI = 36.83 dB, AT = 6.87 s, TTP = 14.57 s, WIT = 7.70 s, and AS = 4.78. (c) Representative photomicrographs of Immunohistochemical CD34 staining in the same tumor (200x magnification) showed microvasculature in brown and poorly differentiated rectal adenocarcinoma. The MVD value is 43.

prognostic factors including TNM stage and histologic grade were identified according to the World Health Organization classification. Rectal adenocarcinoma are graded by the proportion of fully formed glands seen in microscopic slides and classified as well-differentiated, moderately differentiated, and poorly differentiated. Well differentiated adenocarcinoma shows >95% gland formation. Moderately differentiated adenocarcinoma shows 50–95% gland formation. Poorly differentiated adenocarcinoma is mostly solid with <50% gland formation. To determine MVD, the tissues obtained from the most representative paraffin blocks were mounted on poly-L-lysine-coated slides for immunostaining. The CD34 antibody (Dako, Glostrup, Denmark) was used to label the vascular endothelium cytoplasm. The five most vascularized areas ("hot spot") with the highest number of microvessel profiles were chosen subjectively from each tumor section by examination under a low power lens (100x magnification); the total number of microvessels labelled with the CD34 antibody was counted for each area under a high power lens (200x magnification). The mean value of the microvessel number was the MVD value of the tumor [18].

2.5. Statistical Analysis. All analyses were performed with SPSS version 20 for Windows personal computers (SPSS Inc., Chicago, IL, USA). All data were described as means (SD). Two-tailed P values less than 0.05 were considered to indicate a significant difference. Bivariate Pearson correlation analysis was performed to investigate the correlation between CEUS parameters with MVD values and clinicopathologic features.

3. Results

A total of 66 patients were included in the study. The age of the patients ranged from 37 to 71 years (mean 55.8 years), with 46 male and 20 female patients. Following the total mesorectal excision (TME) principle, all 66 patients underwent standard rectal cancer resection, including Mile's and Dixon's operations.

3.1. Time-Intensity Curve Analysis of Rectal Cancer. All of the time intensity curve showed similar enhancement pattern. After the administration of contrast agent, signal intensity increased linearly with time and then reached a plateau then decreased gradually (Figures 2(b), 3(b), and 4(b)). Arriving time ranged 4.35–19.47 sec (10.84 ± 3.28); time to peak enhancement ranged 10.49–34.43 sec (20.61 ± 5.52); wash-in time ranged 4.61–16.69 sec (9.78 ± 2.83); enhanced intensity ranged 18.34–36.83 dB (28.68 ± 4.67). Ascending slope ranged 1.44–6.51 (3.20 ± 1.10).

Table 1: Correlations of CEUS time-intensity curve parameters with MVD.

CEUS parameters	MVD Count	
	Correlation coefficient	P
Arrival time, s	−0.167	0.179
Time to peak enhancement, s	−0.068	0.586
Wash-in time, s	0.025	0.840
Enhanced intensity, dB	**0.295**	**0.016**
Ascending slope	0.071	0.570

CEUS: contrast enhanced ultrasound.
MVD: microvascular density.
Statistical method: bivariate Pearson correlation analysis.

3.2. CEUS Perfusion Parameters and MVD Count. The correlations of CEUS parameters with MVD count are shown in Table 1. The MVD count ranged from 5 to 78 vessels/mm^2 (26.63 ± 15.23) (Figures 2(c), 3(c), and 4(c)). The enhanced intensity was positively correlated with MVD count (r = 0.295, P = 0.016) (Figure 5). No statistic differences were found in MVD count with other CEUS parameters (the arriving time, time to peak, ascending slope, and wash-in time) (P = 0.179–0.840).

3.3. CEUS Parameters and Clinicopathologic Features. All of the 66 lesions were rectal adenocarcinoma. The median diameter for all tumors was 2.5 cm (range 1.8–4.0 cm). Histopathological tumor staging was determined to be T1 in 10, T2 in 12, T3 in 34, (Figures 2(a), 3(a) and 4(a)). and T4 in 10 patients, and N0 in 40 patients, N1 in 10 patients, N2 in 16 patients. 9 patients had hepatic metastases

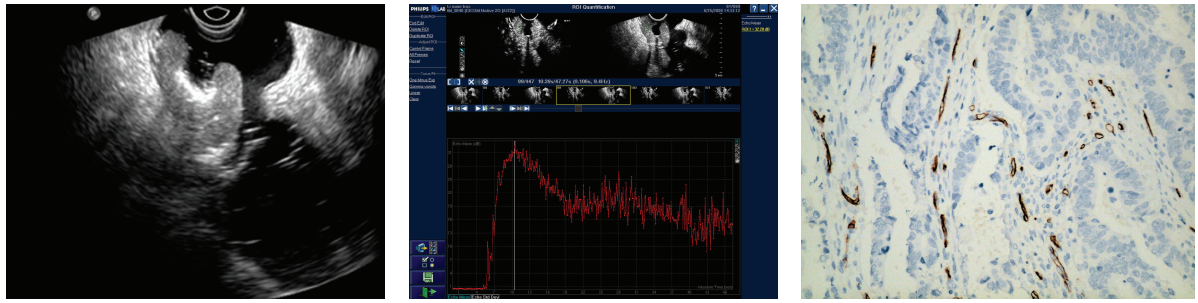

(a) (b) (c)

Figure 3: Images of moderately differentiated rectal adenocarcinoma with T3 stage. (a) Endorectal ultrasonography showed an irregular hypoechoic lesion proceeded beyond the muscularis propria and serosa and perirectal fat. (b) Time-intensity curve was obtained from ROI with EI = 29.61 dB, AT = 5.83 s, TTP = 10.49 s, WIT = 4.66 s, and AS = 6.35. (c) Representative photomicrographs of Immunohistochemical CD34 staining in the same tumor (200x magnification) showed microvasculature in brown and moderately differentiated rectal adenocarcinoma. The MVD value is 24.

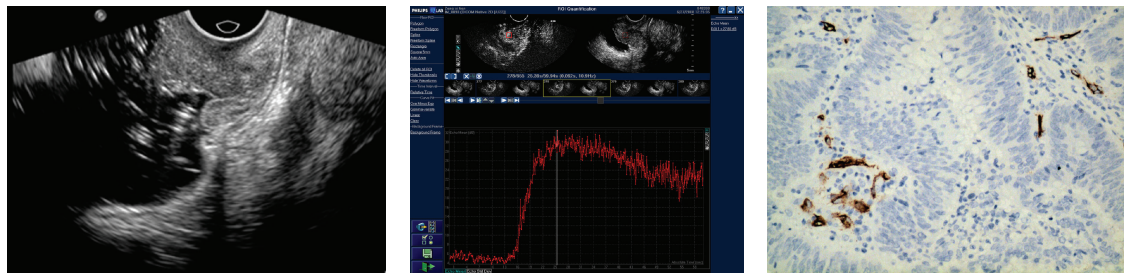

(a) (b) (c)

Figure 4: Images of well differentiated rectal adenocarcinoma with T1 stage. (a) Endorectal ultrasonography showed that an irregular hypoechoic lesion invaded both the mucosa and submucosa layer. (b) Time-intensity curve was obtained from ROI with EI = 25.21 dB, AT = 13.01 s, TTP = 25.12 s, WIT = 12.11 s, and AS = 2.08. (c) Representative photomicrographs of Immunohistochemical CD34 staining in the same tumor (200x magnification) showed microvasculature in brown and well differentiated rectal adenocarcinoma. The MVD value is 16.

proved in enhanced CT follow-up. The tumors were well-differentiated in 12, moderately-differentiated in 36, and poorly-differentiated in 18 patients. The correlations of CEUS parameters with TNM stage and histologic grade were shown in Table 2. The enhanced intensity was negatively correlated with histologic grade ($r = -0.264$, $P = 0.007$) (Figure 6); poorly differentiated tumors showed higher enhanced intensity compared with well differentiated lesions. It was that noted EI decreased as T stage increased ($P = 0.096$). A trend of association was noted though statistical significance was not reached.

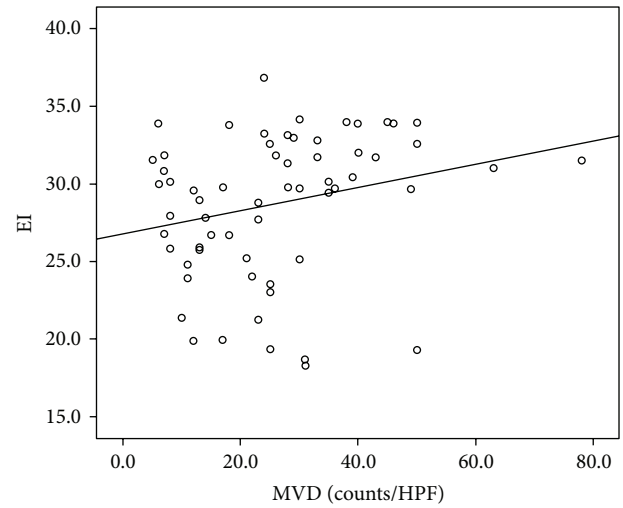

Figure 5: Scatter plots show positive correlations between MVD and EI ($r = 0.295$, $P = 0.016$).

4. Discussion

Angiogenesis is a prerequisite factor for tumor growth and metastatic dissemination, and might be indicative for prognosis and treatment option [19–21]. Nowadays, the standard method used for quantitative evaluation of angiogenesis is immunofluorescent analysis of intratumoral microvessel density (MVD), which quantifies the number of vessels per unit volume [22]. However, this method is limited by its following disadvantages. Firstly, tissue samples have to be obtained via invasive biopsy procedures. Secondly, tissue samples only represent a certain area within the tumor. Thirdly, tissue must be obtained repeatedly to monitor changes in tumor angiogenesis. Fourthly, the results are not immediately available for the clinician [23].

Table 2: Correlations of CEUS time-intensity curve parameters with histologic grade and TNM stage.

CEUS parameter	Histologic grade		T stage		N stage		Metastasis	
	Correlation coefficient	P	Correlation coefficient	P	Correlation coefficient	P	Correlation coefficient	P
Arrival time, s	0.104	0.287	0.037	0.696	−0.058	0.554	0.022	0.830
Time to peak enhancement, s	0.085	0.332	0.085	0.373	−0.021	0.829	0.058	0.569
Wash-in time, s	0.001	0.995	0.073	0.441	−0.024	0.804	0.018	0.859
Enhanced intensity, dB	**−0.264**	**0.007**	−0.158	**0.096**	−0.026	0.789	−0.018	0.859
Ascending slope	−0.116	0.232	−0.143	0.131	−0.008	0.934	−0.001	0.993

CEUS: contrast enhanced ultrasound.
Statistical method: bivariate Pearson correlation analysis.

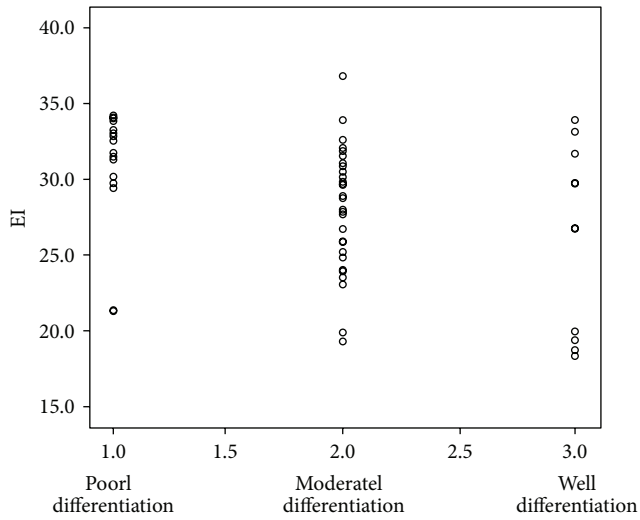

Figure 6: Scatter plots show negative correlations between histologic grade and EI ($r = -0.264$, $P = 0.007$).

Contrast-enhanced ultrasonography (CEUS) is a well accepted and widely available imaging modality in recent years [24–26], because it has overcome the limitations of conventional ultrasonography and created a significant opportunity for visualization of the microcirculation [27]. The second-generation contrast agents (e.g., SonoVue) combined with a low-mechanical index ultrasonographic technique based on nonlinear acoustic effects on interactions with microbubbles make the microbubbles more stable and durable and therefore can facilitate continuous and dynamic observation for a specific period and research of the perfusion of tumor vessels [10]. Furthermore, gray scale CEUS is thought to maximize contrast and spatial resolution, and the diameter of second-generation contrast agent microbubble is only about several micrometers, thereby leading the evolution of CEUS from vascular imaging to imaging of perfused tissue at the microvascular level [27]. Following injection, the bubbles circulate throughout the vascular space and constrictively confined in the microvasculature, which is different from enhanced CT or MR. From time-intensity curve, fractional vascular volume, and flow velocity, relative perfusion rate can be obtained.

Zhuang et al. [14] assessed angiogenesis of colorectal tumor using double contrast enhanced ultrasound (DCEUS). In our experience, contrast-enhanced transabdominal ultrasound is useful in depicting colon cancer, but is not suitable for rectal cancer. In this study, we adapted ERUS for diagnosis of rectal cancer and introduced a novel gels-filling technique. Instead of using a water bath around the probe, the new technique improves the visualization of the rectal cancer and contrast enhanced endorectal ultrasound is less affected by attenuation of the enhancement with depth compared with transabdominal sonography [17].

Recently, increasing positive results regarding the correlation of CEUS parameters with MVD in various cancers have been reported in literatures [10, 13, 28–30]. Although CEUS TIC parameters were investigated in many other malignancies, there are only few studies dealing with CEUS in rectal cancer. Our study showed a positive correlation between enhanced intensity and MVD ($r = 0.295$, $P = 0.016$). Image intensity is proportional to the concentration of bubbles in the vasculature and thus blood flow; increased enhanced intensity showed a tendency toward stronger enhancement and greater perfusion flow, thus correspondent with increased MVD count. We found no association between other CEUS parameters and MVD; this is might be because AT, TTP, WIT, and ascending slope are time-dependent parameters, represented the enhanced speed of the tumor, which might related to spatial distribution of clutter, vascular uneven thickness, distorting, and arteriovenous fistula formation happened in neoangiogenesis, but not number of microvessels. Our findings were very similar to that obtained reported in previous literatures [11, 12, 14]. Therefore, our study suggests that EI could be used for noninvasive estimation of tumor angiogenesis in rectal cancer.

TNM stage and histologic grade are important prognostic factors in rectal cancer. With development of new modalities, additional prognostic indicator for more clinic information may be provided. Some researchers explored the relationship between DCE-MRI perfusion parameters and prognostic factors in rectal cancer, and results were not conclusive. Lollert and Hong reported that DCE-MRI parameters correlated significantly with the N category [31, 32]; Tuncbilek and Hong reported Erise was correlated with N stage, and steepest slope, maximal enhancement, and time to peak were correlated with

histologic grade, respectively [32, 33]. On the other hand, Kim found no correlation between any dynamic contrast-enhanced MRI perfusion parameters and TN stage [34]. In our study, enhanced intensity negatively correlated with histologic grade ($r = -0.295$, $P = 0.007$), and none of other parameters correlated with TNM stage and histologic grade. Some research also found significant correlation between MVD and histologic grade of various type of tumors [35–37], suggesting that increased MVD, signifying angiogenesis, is accompanied with higher grade of tumor. Differences in vascularization between well and poorly differentiated tumors might reflect the stromal reaction, interaction of the tumor cells with environments (matrix components, enzymes, and growth factors), and a balance between positive and negative angiogenesis regulators. The process and interaction between tumor cells, endothelial cells, and stroma during tumor progression are very dynamic and determined the tumor growth. At the later stages of tumor progression the angiogenesis was stimulated and tumor cell presented with more aggressive biological behavior. Poorly differentiated tumor cells indicated rapid cell division and thus connote a worse prognosis than well-differentiated tumors [38, 39]. A trend of negative association was seen between EI and T stage. It may suggest that tumor perfusion differed with T staging, but other confounding factors could also contribute to T staging in addition to angiogenesis. The value of CEUS perfusion parameters in indicating prognosis remains to be further investigated.

5. Conclusion

In conclusion, enhanced intensity of contrast enhanced endorectal ultrasonography provides noninvasive biomarker of tumor angiogenesis in rectal cancer. CEUS data have the potential to predict patient prognosis.

Study Limitations

Our study has some limitations. Firstly, the most enhanced region within the tumor from ultrasonography images was drawn as ROI, which might not be correspondent to the hot spot in the histopathological analysis precisely. Secondly, the record time of 60 seconds in CEUS examination was relatively short to include later wash-out phase of perfusion. Thirdly, we did not observe reoccurrence free survival and overall survival rates with a long-term follow-up.

Conflict of Interests

The authors declare that there is no conflict of interests regarding the publication of this paper.

Authors' Contribution

Yong Wang and Lin Li contributed equally to this work as first authors. Chun-Wu Zhou and Yu-Xin Jiang contributed equally to this work as corresponding authors.

Acknowledgments

The authors like to thank Professor Wen Chen, biostatistician at Department of Cancer Epidemiology, Professor Xiao-Li Feng and Jian-Ming Ying, pathologist at Department of Pathology, Cancer Hospital, Peking Union Medical College, Chinese Academy of Medical Sciences. This study was supported by Beijing Municipal Science & Technology Commission no. Z131107002213016 and Beijing Hope Run Special Fund of China Cancer Research Foundation (CCRF) no. LC2013A04 and The Personnel Department of the People's Republic of China Funds Preferred Activities of Science and Technology Project Funding.

References

[1] D. M. Muzny, M. N. Bainbridge, K. Chang et al., "Comprehensive molecular characterization of human colon and rectal cancer," *Nature*, vol. 487, pp. 330–337, 2012.

[2] R. Bendardaf, A. Buhmeida, M. Hilska et al., "VEGF-1 expression in colorectal cancer is associated with disease localization, stage, and long-term disease-specific survival," *Anticancer Research B*, vol. 28, no. 6, pp. 3865–3870, 2008.

[3] S. Dighe, H. Blake, N. Jeyadevan et al., "Perfusion CT vascular parameters do not correlate with immunohistochemically derived microvessel density count in colorectal tumors," *Radiology*, vol. 268, no. 2, 2013.

[4] Kim, Y. -E, J. S. Lim et al., "Perfusion parameters of dynamic contrast-enhanced magnetic resonance imaging in patients with rectal cancer: correlation with microvascular density and vascular endothelial growth factor expression," *Korean Journal of Radiology*, vol. 14, no. 6, pp. 878–885, 2013.

[5] S. J. Ahn, C. S. An, W. S. Koom, H.-T. Song, and J.-S. Suh, "Correlations of 3T DCE-MRI quantitative parameters with microvessel density in a human-colorectal-cancer xenograft mouse model," *Korean Journal of Radiology*, vol. 12, no. 6, pp. 722–730, 2011.

[6] V. Goh, S. Halligan, F. Daley, D. M. Wellsted, T. Guenther, and C. I. Bartram, "Colorectal tumor vascularity: quantitative assessment with multidetector CT-Do tumor perfusion measurements reflect angiogenesis?" *Radiology*, vol. 249, no. 2, pp. 510–517, 2008.

[7] M. Nishida, K. Koito, N. Hirokawa, M. Hori, T. Satoh, and M. Hareyama, "Does contrast-enhanced ultrasound reveal tumor angiogenesis in pancreatic ductal carcinoma? A pospective study," *Ultrasound in Medicine and Biology*, vol. 35, no. 2, pp. 175–185, 2009.

[8] T. Samdani and J. Garcia-Aguilar, "Imaging in rectal cancer: magnetic resonance imaging versus endorectal ultrasonography," *Surgical Oncology Clinics of North America*, vol. 23, no. 1, pp. 59–77, 2014.

[9] J. Wang, F. Lv, X. Fei et al., "Study on the characteristics of contrast-enhanced ultrasound and its utility in assessing the microvessel density in ovarian tumors or tumor-like lesions," *International Journal of Biological Sciences*, vol. 7, no. 5, pp. 600–606, 2011.

[10] Z. Wang, J. Tang, L. An et al., "Contrast-enhanced ultrasonography for assessment of tumor vascularity in hepatocellular carcinoma," *Journal of Ultrasound in Medicine*, vol. 26, no. 6, pp. 757–762, 2007.

[11] J. Jiang, Y. Chen, Y. Zhu, X. Yao, and J. Qi, "Contrast-enhanced ultrasonography for the detection and characterization of prostate cancer: correlation with microvessel density and Gleason score," *Clinical Radiology*, vol. 66, no. 8, pp. 732–737, 2011.

[12] J. Du, F.-H. Li, H. Fang, J.-G. Xia, and C.-X. Zhu, "Correlation of real-time gray scale contrast-enhanced ultrasonography with microvessel density and vascular endothelial growth factor expression for assessment of angiogenesis in breast lesions," *Journal of Ultrasound in Medicine*, vol. 27, no. 6, pp. 821–831, 2008.

[13] L. Shiyan, H. Pintong, W. Zongmin et al., "The relationship between enhanced intensity and microvessel density of gastric carcinoma using double contrast-enhanced ultrasonography," *Ultrasound in Medicine and Biology*, vol. 35, no. 7, pp. 1086–1091, 2009.

[14] H. Zhuang, Z. G. Yang, H. J. Chen, Y. L. Peng, and L. Li, "Time—intensity curve parameters in colorectal tumours measured using double contrast—enhanced ultrasound: correlations with tumour angiogenesis," *Colorectal Disease*, vol. 14, no. 2, pp. 181–187, 2012.

[15] K. Oberholzer, M. Menig, A. Kreft et al., "Rectal cancer: mucinous carcinoma on magnetic resonance imaging indicates poor response to neoadjuvant chemoradiation," *International Journal of Radiation Oncology Biology Physics*, vol. 82, no. 2, pp. 842–848, 2012.

[16] Hong, H. -S, S. H. Kim et al., "Correlations of dynamic contrast-enhanced magnetic resonance imaging with morphologic, angiogenic, and molecular prognostic factors in rectal cancer," *Yonsei Medical Journal*, vol. 54, no. 1, pp. 123–130, 2013.

[17] Y. Wang, C.-W. Zhou, Y.-Z. Hao et al., "Improvement in T-staging of rectal carcinoma: using a novel endorectal ultrasonography technique with sterile coupling gel filling the rectum," *Ultrasound in Medicine — Biology*, vol. 38, no. 4, pp. 574–579, 2012.

[18] M. Claudon, D. Cosgrove, T. Albrecht et al., "Guidelines and good clinical practice recommendations for contrast enhanced ultrasound (CEUS)—update 2008," *Ultraschall in der Medizin*, vol. 29, no. 1, pp. 28–44, 2008.

[19] L. Hiatky, C. Tsionou, P. Hahnfeldt, and C. N. Coleman, "Mammary fibroblasts may influence breast tumor angiogenesis via hypoxia-induced vascular endothelial growth factor up-regulation and protein expression," *Cancer Research*, vol. 54, no. 23, pp. 6083–6086, 1994.

[20] L. Holmgren, M. S. O'Reilly, and J. Folkman, "Dormancy of micrometastases: balanced proliferation and apoptosis in the presence of angiogenesis suppression," *Nature Medicine*, vol. 1, no. 2, pp. 149–153, 1995.

[21] M. S. O'Reilly, L. Holmgren, Y. Shing et al., "Angiostatin: a novel angiogenesis inhibitor that mediates the suppression of metastases by a Lewis lung carcinoma," *Cell*, vol. 79, no. 2, pp. 315–328, 1994.

[22] N. Weidner, "Current pathologic methods for measuring intratumoral microvessel density within breast carcinoma and other solid tumors," *Breast Cancer Research and Treatment*, vol. 36, no. 2, pp. 169–180, 1995.

[23] S. Ohlerth, M. Wergin, C. R. Bley et al., "Correlation of quantified contrast-enhanced power Doppler ultrasonography with immunofluorescent analysis of microvessel density in spontaneous canine tumours," *Veterinary Journal*, vol. 183, no. 1, pp. 58–62, 2010.

[24] S. G. Zheng, H. X. Xu, and L. N. Liu, "Management of hepatocellular carcinoma: the role of contrast-enhanced ultrasound," *World Journal of Radiology*, vol. 6, no. 1, pp. 7–14, 2014.

[25] L. N. Liu, H. X. Xu, M. D. Lu et al., "Contrast-enhanced ultrasound in the diagnosis of gallbladder diseases: a multi-center experience," *PLoS ONE*, vol. 7, no. 10, Article ID e48371, 2012.

[26] H. X. Xu, M. D. Lu, L. N. Liu et al., "Discrimination between neoplastic and non-neoplastic lesions in cirrhotic liver using contrast-enhanced ultrasound," *The British Journal of Radiology*, vol. 85, no. 1018, pp. 1376–1384, 2012.

[27] A. Klauser, J. Demharter, A. de Marchi et al., "Contrast enhanced gray-scale sonography in assessment of joint vascularity in rheumatoid arthritis: results from the IACUS study group," *European Radiology*, vol. 15, no. 12, pp. 2404–2410, 2005.

[28] Y. Xia, Y. X. Jiang, Q. Dai, Y. Xiao, K. Lv, and L. Wang, "Contrast-enhanced ultrasound of hepatocellular carcinoma: correlation of washout time and angiogenesis," *Clinical Hemorheology and Microcirculation*, vol. 48, no. 4, pp. 265–273, 2011.

[29] E. Yildiz, S. Ayan, F. Goze, G. Gokce, and E. Y. Gultekin, "Relation of microvessel density with microvascular invasion, metastasis and prognosis in renal cell carcinoma," *BJU International*, vol. 101, no. 6, pp. 758–764, 2008.

[30] C. F. Wan, J. Du, H. Fang, F. H. Li, J. S. Zhu, and Q. Liu, "Enhancement patterns and parameters of breast cancers at contrast-enhanced US: correlation with prognostic factors," *Radiology*, vol. 262, no. 2, pp. 450–459, 2012.

[31] E. Assenat, S. Thézenas, E. Samalin et al., "The value of endoscopic rectal ultrasound in predicting the lateral clearance and outcome in patients with lower-third rectal adenocarcinoma," *Endoscopy*, vol. 39, no. 4, pp. 309–313, 2007.

[32] S. R. Hamilton and L. A. Aaltonen, *Pathology and Genetics of Tumours of the Digestive System*, IARC press, Lyon, France, 2000.

[33] H. Ju, D. Xu, D. Li, G. Chen, and G. Shao, "Comparison between endoluminal ultrasonography and spiral computerized tomography for the preoperative local staging of rectal carcinoma," *Bioscience trends*, vol. 3, no. 2, pp. 73–76, 2009.

[34] S. A. Badger, P. B. Devlin, P. J. D. Neilly, and R. Gilliland, "Preoperative staging of rectal carcinoma by endorectal ultrasound: is there a learning curve?" *International Journal of Colorectal Disease*, vol. 22, no. 10, pp. 1261–1268, 2007.

[35] I. Chebib, M. T. Shabani-Rad, M. S. Chow, J. Zhang, and Z.-H. Gao, "Microvessel density and clinicopathologic characteristics in hepatocellular carcinoma with and without cirrhosis," *Biomarker Insights*, vol. 2, article 59, 2007.

[36] N. Kavantzas, H. Paraskevakou, S. Tseleni-Balafouta et al., "Association between microvessel density and histologic grade in renal cell carcinomas," *Pathology and Oncology Research*, vol. 13, no. 2, pp. 145–148, 2007.

[37] H. Deniz, M. Karakök, F. YagcI, and M. E. Güldür, "Evaluation of relationship between HIF-1α immunoreactivity and stage, grade, angiogenic profile and proliferative index in bladder urothelial carcinomas," *International Urology and Nephrology*, vol. 42, no. 1, pp. 103–107, 2010.

[38] S. R. Harris and U. P. Thorgeirsson, "Tumor angiogenesis: biology and therapeutic prospects," *In Vivo*, vol. 12, no. 6, pp. 563–570, 1998.

[39] S.-Y. Sung, C.-L. Hsieh, D. Wu, L. W. K. Chung, and P. A. S. Johnstone, "Tumor microenvironment promotes cancer progression, metastasis, and therapeutic resistance," *Current Problems in Cancer*, vol. 31, no. 2, pp. 36–100, 2007.

Hindawi Publishing Corporation
BioMed Research International
Volume 2014, Article ID 872984, 12 pages
http://dx.doi.org/10.1155/2014/872984

Review Article

New Progress in Angiogenesis Therapy of Cardiovascular Disease by Ultrasound Targeted Microbubble Destruction

Yang-Ying Liao,[1] Zhi-Yi Chen,[1] Yi-Xiang Wang,[2] Yan Lin,[1] Feng Yang,[1] and Qiu-Lan Zhou[1]

[1] *Laboratory of Ultrasound Molecular Imaging, Department of Ultrasound Medicine, The Third Affiliated Hospital of Guangzhou Medical University, Guangzhou 510150, China*
[2] *Department of Imaging and Interventional Radiology, Prince of Wales Hospital, The Chinese University of Hong Kong, Shatin, New Territories, Hong Kong*

Correspondence should be addressed to Zhi-Yi Chen; winchen@vip.126.com

Received 13 February 2014; Accepted 26 March 2014; Published 12 May 2014

Academic Editor: Yongdoo Choi

Angiogenesis plays a vital part in the pathogenesis and treatment of cardiovascular disease and has become one of the hotspots that are being discussed in the past decades. At present, the promising angiogenesis therapies are gene therapy and stem cell therapy. Besides, a series of studies have shown that the ultrasound targeted microbubble destruction (UTMD) was a novel gene delivery system, due to its advantages of noninvasiveness, low immunogenicity and toxicity, repeatability and temporal and spatial target specificity; UTMD has also been used for angiogenesis therapy of cardiovascular disease. In this review, we mainly discuss the combination of UTMD and gene therapy or stem cell therapy which is applied in angiogenesis therapy in recent researches, and outline the future challenges and good prospects of these approaches.

1. Introduction

Angiogenesis is a complex blood vessel formation process, involving a variety of angiogenic growth factors synergistic effect. Angiogenesis is divided into two types (physiological and pathological), and the latter always leads to many diseases, such as cardiovascular disease, tumor, and inflammation. Therapeutic angiogenesis, which can improve blood flow, revascularization, and myocardial function, has proved to be one of the most promising therapies for cardiovascular disease. Furthermore, therapeutic angiogenesis has been mainly used for the treatment of ischemic diseases (such as ischemic heart disease). Owing to the disadvantage of invasiveness, limited drug diffusion or lack of selectivity towards targeted tissues, previous drug, or surgical treatment cannot meet the demands of patients and doctors any longer. At the moment, an emerging technique, UTMD, has been proposed for a noninvasive and targeting specific approach in angiogenesis therapy of cardiovascular disease. UTMD refers to that microbubble is exposed to ultrasound (US); on a certain condition, it will be gradually or suddenly activated and/or collapsed. It maybe creates a series of biological effects, including local tissue damage, transient membrane permeability improvement, and extravasation, which are going to facilitate the targeted genes or drugs entering into the tissue or cell of interest [1–4]. UTMD technique has an advantage over other gene delivery methods, mainly reflecting in (1) high safety (being low toxicity and immunogenicity compared with viral vectors and getting rid of threatening ionizing radiation), (2) high cost effectiveness and broad availability (compared with other imaging modalities, a high cost effectiveness makes it more acceptable to be used in clinical application), (3) noninvasiveness and repeatability (microbubbles being always administered intravascularly which makes it possible for repeated applications), and (4) high tissue specificity [5, 6] (drugs or targeted genes being selectively delivered to the only region of interest, rather than nontargeted position). In a word, there are so many advantages that make UTMD a good alternative in angiogenesis therapy of cardiovascular disease.

2. The Proposed Mechanism of UTMD

UTMD stands for a technique that molecular bioactive substance or therapeutic gene, injected or incorporated into microbubble in blood circulation, can be eventually released into the targeted tissue or organ under the action of ultrasound. The biological effects produced by ultrasound are used to facilitate gene transfection into targeted tissues or cells; thus, the purpose of targeted therapy is successfully achieved [7]. The commonly used microbubbles, being about 1–10 μm in diameter, can smoothly go through the capillaries, but cannot reach targeted tissue through endothelial gap. Consequently, UTMD mediated gene therapy is mainly based on the biological effects which were produced by the interaction among ultrasound, cell membrane, and endothelial cells. Ultrasound can promote gene-loaded microbubbles local accumulation in lesions, and the biological effects of ultrasound can improve the permeability of the blood vessels and cell membrane, promoting gene exosmosis to targeted lesion and improving the therapeutic effect. These biological effects mainly include the cavitation effect and sonoporation effect. Cavitation effect refers to the cavitation nucleus that is existing in the liquid, after ultrasound exposure, and can produce the dynamic processes mainly including oscillation, collapse, expansion, and contraction [8]. Microbubble can be used as a kind of man-made cavitation nuclei. After injection of microbubble, the concentration of cavitation nucleus in the blood will be increased, which maybe reduces the cavitation threshold, finally enhancing the ultrasonic cavitation effect. Cavitation effect can be divided into instantaneous cavitation and steady-state cavitation. It is generally believed that ultrasound cavitation effect is produced by the following three different mechanisms [9], including (1) producing transient pores on vascular endothelial cell surface to promote macromolecular absorption into the cells; (2) destroying the integrity of the vascular endothelium to make large molecules transfer through the intercellular transfer; and (3) stimulating cell endocytosis function to enhance the intracellular delivery [10]. Sonoporation is described as the phenomenon of forming temporary small holes on cell membrane after ultrasound exposure, which can promote the uptake of extracellular substance into the cell [11, 12]. Numerous studies have showed that sonoporation effect was related to microstreaming, microjet, and shock wave, especially the inertial cavitation, after ultrasound exposure. Moreover, sonoporation has long been regarded as the main mechanism of improving delivery efficiency and it is necessary to optimize sonoporation protocols to obtain a higher transfection rate [13]. In fact, the precise and underlying mechanism of UTMD mediated gene transport in vivo has not been very clear. However, based on what we have known at present, UTMD can be well applied to angiogenic therapy. With the aid of the proposed mechanism of UTMD (such as cavitation effect and sonoporation effect), targeted genes or stem cells can be delivered to ischemic myocardium to promote angiogenesis and restore flow perfusion (Figure 1). Along with the development of mechanism, UTMD technology will play a more and more important role in angiogenesis therapy.

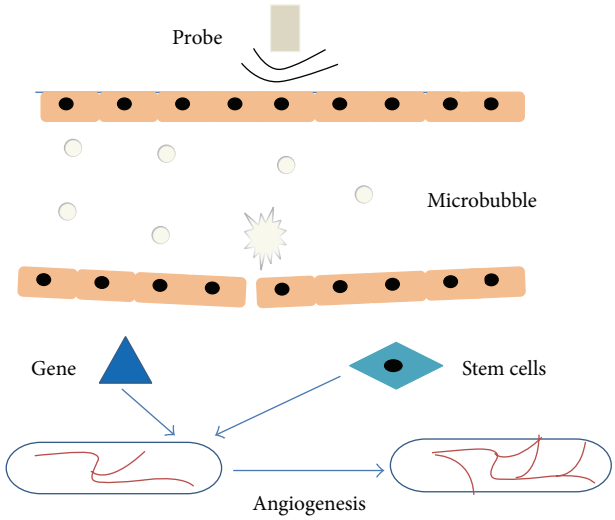

Figure 1: Schematic illustration of UTMD inducing angiogenesis therapy. With the aid of UTMD, targeted genes or stem cells can be delivered to ischemic tissue or organ to promote angiogenesis and increase flow perfusion.

3. Gene Therapy

With the rapid development of molecular biology techniques, gene therapy is developing as a novel and promising angiogenesis therapy. Among the researches of gene therapy for cardiovascular diseases, the ischemic heart model is more commonly used. Although the basic research on gene therapy showed the tempting prospects, the results in most of the clinical trial did not achieve the goal of effective treatments, mainly due to the low gene transfection rate and lack of safety [14]. For this reason, there is a great need for designing a safe, efficient, and noninvasive gene delivery approach, which has become a crucial problem to be solved in the gene therapy research. Some researchers began to focus on the safe and noninvasive ultrasound and microbubble. Microbubbles, firstly only developed for clinical diagnostic applications, are now well admitted as nonviral vectors for gene therapy [15]. When they were exposed to ultrasound, microbubbles could strengthen the cavitation effect and facilitate targeted gene delivery [16]. To date, UTMD has been explored as an innovative gene delivery strategy and attracted the attention of many researchers [17]. During the last decade, many efforts and studies have focused on exploring the feasibility of UTMD in angiogenesis therapy and demonstrated that UTMD was a safe and effective targeted transfection strategy for angiogenesis therapy in myocardial ischemia and limb ischemia animal models. The following research was a typical example. In hind-limb ischemia mouse models, Chappell et al. [18] prepared nanoparticles which associated with the gene encoding fibroblast growth factor-2 and injected them into the mouse adductor muscles in the presence of 1 MHz ultrasound. Two weeks later, they observed arteriolar caliber and density were apparently improved in fibroblast growth factor-2 treated group.

3.1. Growth Factors Gene Therapy. There are an increasing number of genes for therapeutic angiogenesis, although what are commonly used are still proangiogenic growth factors, mainly including vascular endothelial growth factor (VEGF), fibroblast growth factor (FGF), hepatocyte growth factor (HGF), and angiogenin (Ang). Proangiogenic growth factors, endogenous or exogenous, can markedly promote angiogenesis with the aid of UTMD.

3.1.1. VEGF Gene Therapy. In mammal animals, the VEGF family has five isoforms, including VEGF-A, VEGF-B, VEGF-C, VEGF-D, and placental growth factor [19]. VEGF is necessary throughout the angiogenic process involving vascular endothelial cell migration, infarct size improvement, and apoptosis inhibition. Recent studies show that an increased VEGF expression can promote angiogenic response, under the mechanical effect of UTMD. Taken together, previous studies showed that via increasing the expression of VEGF, the gene therapy could significantly promote angiogenesis and improve cardiac function after myocardial damage [20]. Kobulnik et al. [21] compared the $VEGF_{165}$ gene transfection rate via two delivery methods, ultrasound mediated (UM) of intravenous injection and intramuscular (IM) injection. At 14, 17, 21 and 28 days and 8 weeks following iliac artery ligation, microvascular blood volume (MBV) and microvascular blood flow (MBF) and total transfection efficiency were examined and measured to monitor and evaluate the efficiency of therapeutic angiogenesis. Their results showed that the UM delivery had an advantage over IM delivery in improvement of MBV and MBF, in spite of a lower gene transfection efficiency. This superiority may be related to a wider diffusion and distribution of transgene which was more beneficial to promoting angiogenesis (Figure 2).

Similarly, Leong-Poi et al. [22] conducted a study which was associating ultrasound with microbubbles loaded plasmid DNA encoding the $VEGF_{165}$ in the setting of serious peripheral arterial disease. The results showed that the $VEGF_{165}$/GFP-treated group could significantly enhance the tissue blood perfusion as showed in contrast-enhanced ultrasound (CEU) imaging and remarkably enhance the microvascular density compared with control groups (Figure 3). In this study, the recovery in skeletal muscle perfusion was highly related to the increased noncapillary blood volume, with perfusion peaking at 14 days after transfection. Therefore, they also verified that the UTMD technique held great promise in gene therapy for ischemic disease.

In an animal model of postcoronary artery ligation, Fujii et al. [23] incubated perflutren lipid microbubbles with empty plasmid, plasmid DNA encoding VEGF, stem cell factor (SCF), or GFP. The formative mixture was intravenously administered into the heart which was exposed to Acuson sequoia C256 system (New York, Siemens Medical Solutions Inc) under the ultrasound irradiation (8 MHz, 1.6 mechanical index, 20 min irradiation time, and 500 ms time interval). Two weeks later, they found that GFP was expressed in the infarcted heart, meaning the success of gene transfection. Additionally, vascular density, left ventricular myocardial perfusion, and myocardial function were both observably improved compared with the control group, due to a much higher expression of VEGF and SCF (Figure 4). In consequence, it is hypothesized that the UTMD provides an effective and noninvasive method for delivering targeted gene after myocardial infarction.

3.1.2. FGF Gene Therapy. Asahara et al. [24] were first to demonstrate that FGF gene could facilitate angiogenesis and enhance tissue blood perfusion in a rabbit model of limb ischemia. The major and typical FGF family members, FGF-1 (also called aFGF) and FGF-2 (also called bFGF), are the most commonly used in research. Negishi and his colleagues [25] have delivered the bFGF plasmid DNA and bubble liposomes (BL) into the adductor muscle of the hind-limb ischemia model in the presence of a low intensity of ultrasound exposure. Compared to other treatment groups, a highly efficient gene transfection, the increase of capillary vessels, and quick recovery of the blood flow were observed in the BL with US exposure treatment groups. In this study, UTMD technique was proved to be an effective, noninvasive, and nonviral method in angiogenesis therapy of various ischemic diseases (such as ischemic heart disease). Based on that intramuscular injection could make gene transfection colocalize in the region of the administration site in the previous studies, subsequently, they expanded the previous study for a further step. Therefore, with the aid of US, plasmid DNA, and BLs were systemically administrated into hind-limb ischemia area in the experiment. They found that this method could obtain a more effective and efficient gene transfection and was more suitable for gene therapy of ischemic diseases (such as myocardial infarction) [26]. In a rat model of ischemic myocardium, Zhao et al. [27] elucidated the feasibility of targeting delivery of heparin modified microbubbles (HMB) carrying aFGF into ischemic myocardium with the help of UTMD technique. A remarkably promotion of myocardial vessel neogenesis, which was proved by M-mode echocardiography, contributed to remarkable enhancement of regional and global cardiac functions. As shown in hematoxylin and eosin staining of acute myocardial infarction, ischemic myocardium was significantly improved in aFGF-HMB + US treatment group, being consistent with cardiac function results. This study suggested that cavitation induced by ultrasound and HMB could accelerate FGF gene therapy of ischemic myocardium.

3.1.3. HGF Gene Therapy. Previous studies have shown that HGF played an important part in cell growth and motility and angiogenesis process. Therefore, it may be a better candidate gene for angiogenesis therapy [28]. In a rabbit ischemia model, HGF gene therapy has been firstly proven to effectively promote gene transfection, with the help of UTMD [29]. In 2011 [30] and 2012 [31], Yuan et al. demonstrated that the combinations of an angiogenic gene and UTMD technique could enhance the expression efficiency of the delivered gene. As a consequence, it was identified as a useful angiogenic gene therapy of ischemic heart disease. Along the same line, they had a deeper and further research. In the experiment, they tested the therapeutic effect of combining UTMD with plasmid DNA encoding the HGF in treatment of myocardial infarction. They found that HGF + MB + US

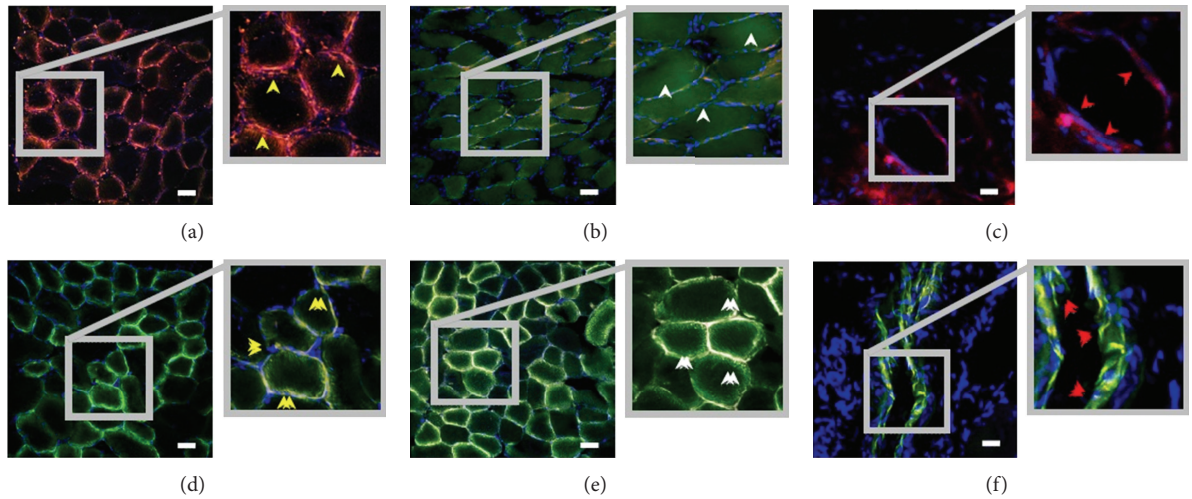

Figure 2: Representative immunofluorescent staining of IM-therapy ((a)–(c)) and UM-therapy ((d)–(f)) ischemic hind-limb muscle, at 17 days following iliac artery ligation, CD31 staining (red); TO-PRO-3-nuclei staining (blue); colocalization of GFP and red CD31 staining (yellow). Within IM-therapy groups: (a) areas without discernable GFP signal (yellow arrows), (b) regions with strong GFP signal (white arrows), and (c) arterioles with little GFP signal (red arrows). In comparison, in UM-therapy groups, a wider diffuse of GFP signal was distributed in (d) both capillaries endothelial (yellow arrows), (e) the adjacent areas (white arrows), and (f) small- to medium-sized arterioles (red arrows). Scale bar = 50 μm. Adapted from [21].

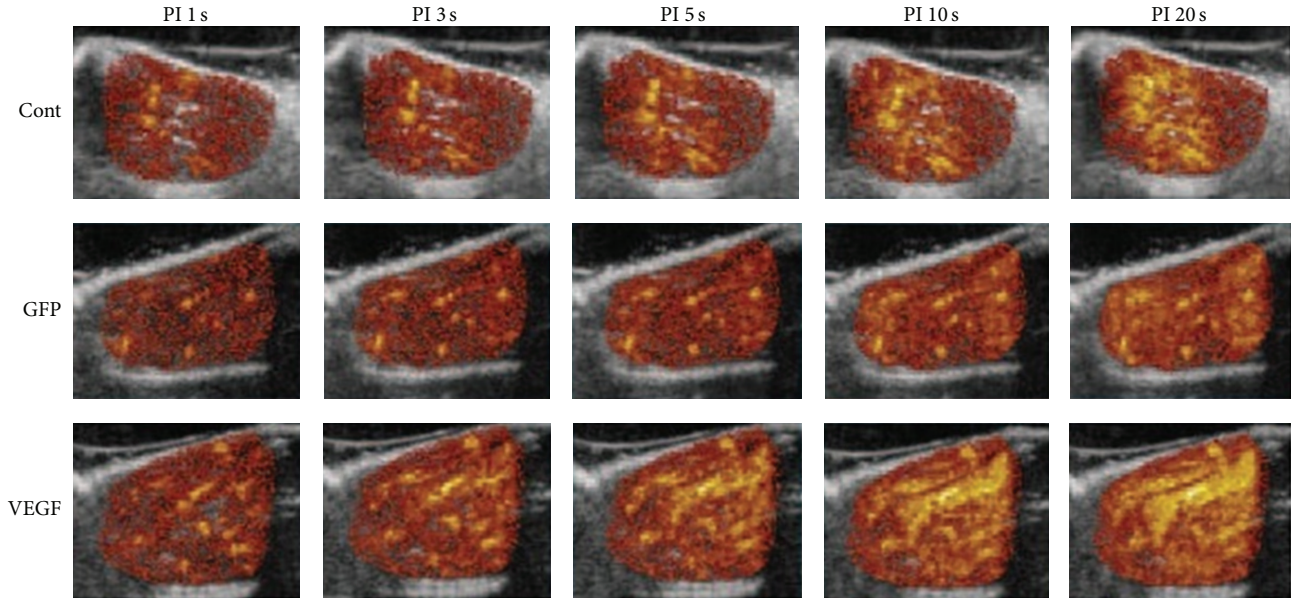

Figure 3: CEU perfusion images of ischemic skeletal muscle were performed at 4 weeks after ligation, showing the corresponding pulsing intervals (PI) versus signal intensity from the animals in the 3 treatment groups. There was a stronger and faster contrast enhancement in VEGF treatment group. Adapted from [22].

treatment group could significantly reduce the infarct size and left ventricle weight, along with augmenting microvessel density, which was consistent with their previous research results [32]. In addition, Zhou et al. [33] have reported that after the UTMD-induced gene delivery, the expression of HGF gene was significantly improved while only a negligible impact on cell viability was observed. At the same time, it could also improve angiogenesis, blood flow, and fibrosis in myocardial ischemia. Therefore, it was identified as a novel and promising gene therapy of cardiovascular disease.

3.1.4. Ang Gene Therapy. Ang is one of much concern cytokines that promote angiogenesis, with its family members mainly including Ang1, Ang2, Ang3, and Ang4. Ang1 and its receptor Tie2 are most widely studied and Ang1/Tie2 system has an effect on angiogenesis in the late stage, predominantly

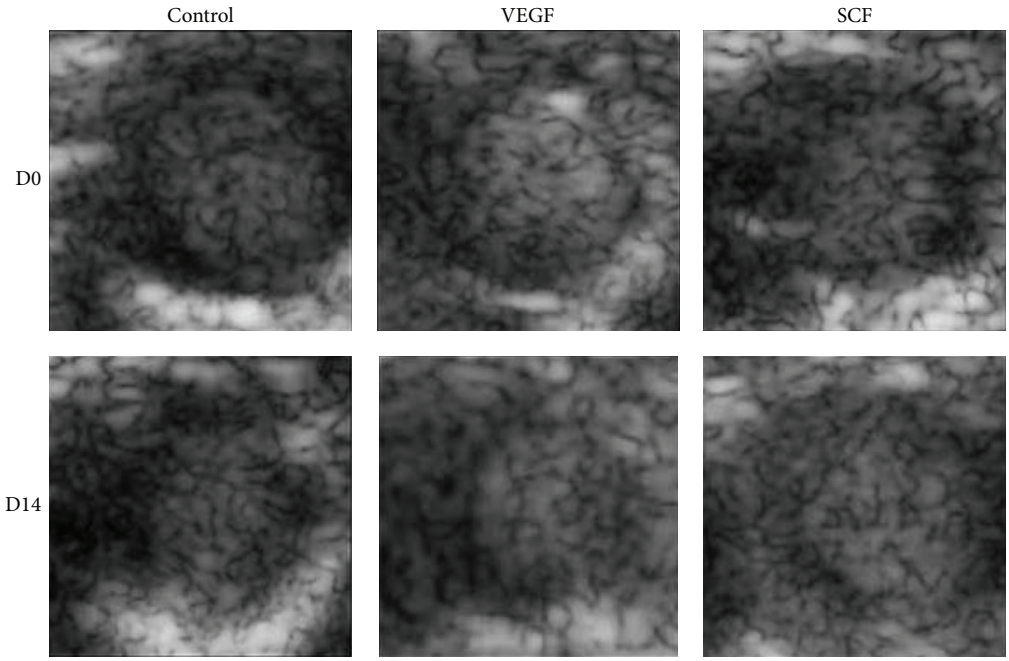

Figure 4: Representative images obtained by myocardial contrast echocardiography performed before (D0) and 14 days (D14) after UTMD mediated empty plasmid (in control group), VEGF, or SCF gene transfection in coronary artery ligation mice. Compared to the control group, blood flow volume was greatly improved in both VEGF and SCF treatment groups. Adapted from [23].

accelerating endothelial cell migration and maintaining his survival. Previous studies have proved that UTMD can significantly improve transfection efficiency of Ang-1 gene both in vitro and in vivo, suggesting that this transfection strategy can be used for angiogenic therapy. Furthermore, in order to enhance the hAng-1 gene transfection efficiency, Zhou et al. [34] explored and tested some transfection parameters (such as FBS, the cell suspension, and adherent mode), no longer limited to ultrasound irradiation parameters in previous studies. The obtained optimized transfection parameters lay the foundation of future research of UTMD assisted angiogenic gene therapy of cardiovascular disease. Meanwhile, they pointed out that we should not blindly pursue the maximal gene transfection rate, while ignoring the cell or tissue damage.

3.2. Other Gene Therapies. Except for common angiogenic growth factors, an increasing amount of genes have been studied the potentiality for treatment of cardiovascular disease. Taking the protein kinase Akt as an example; previous studies have showed that Akt could protect heart from damage and restore cardiac function. Therefore, Akt also was regarded as a therapeutic target for gene therapy of cardiovascular disease. Taking into consideration the low transfection rate of the commercially available Definity microbubble; Sun et al. [35] used a cationic microbubble, which has the ability to bear more plasmid DNA, to transfer the Akt targeted gene to the animal model of ischemic myocardium. The measured data showed that the combination of UTMD and Akt therapeutic gene had a bright future in angiogenesis therapy. Moreover, Li et al. [36] also tested the feasibility and safety of exogenous Akt1 gene delivery under the condition of UTMD in the myocardium of new-born gender rats. When several ultrasound parameters were simultaneously optimized, it was possible to improve the efficiency of gene transfection and only produce a minor side reaction. Their study suggested the method of UTMD-assisted exogenous Akt1 gene transfection had a chance to be applied to gene therapy of cardiovascular disease.

Additionally, previous study indicated that thymosin beta 4 (TB4) played an important role in facilitating cardiac neovascularization, promoting cell proliferation and differentiation, and maintaining myocardial function following the adult heart ischemic damage [37]. In order to avoid other nontargeted organs affected and obtain a higher and longer targeted gene transfection, Chen et al. [38] combined the piggybac transposon-mediated gene-delivery system with UTMD technique in an experimental study. In their study, they systemically administrated exogenous TB4 gene and then dealt with them under the UTMD. Results showed that adult resident cardiac progenitor cells were induced to proliferate and form three major cardiac lineages. In addition, the treatment groups could dramatically augment coronary artery and capillary density, indicating generating angiogenesis and arteriogenesis (Figure 5). Based on the above results, it is considered as that the therapeutic method could be used for angiogenesis therapy.

3.3. Multigene Therapy. Angiogenesis is a complex blood vessel formation process, involving a variety of angiogenic growth factors synergistic effect, and it finally comes into being mature vascular beds. Successful therapeutic angiogenesis should be able to enhance their treatment effects as well as alleviate the undesirable impact by complementary

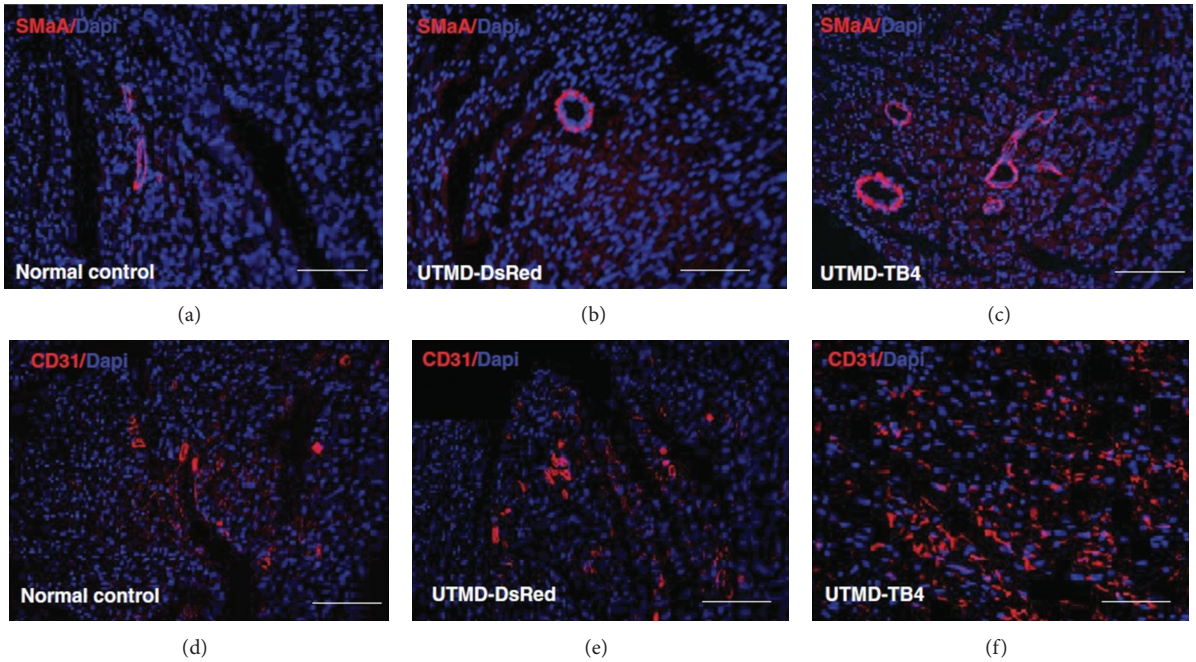

Figure 5: Representative microscopic images of angiogenesis after UTMD mediated TB4 treatment (scale bar = 150 mm). ((a)–(c)) The top panels are stained antibodies against smooth muscle a-actin (SMaA) (red) and nucleus (blue). Groups from left to right are, respectively, normal control, DsRed control, and UTMD-TB4 treated. An increase in SMaA was observed in the UTMD-TB4 treatment group, being consistent with coronary arteriogenesis response. ((d)–(f)) The middle panels are similar except the antibody is against CD31. Adapted from [38].

effects of several angiogenic growth factors. Some researches on combinations of several growth factors have been explored in animal models of coronary artery disease and peripheral arterial disease. With the aid of viral vectors, a combination gene therapy of VEGF early and Angiopoietin-1 (Ang-1) has been demonstrated that it could promote angiogenesis, facilitate cardiomyocyte proliferation, and decrease apoptosis and ventricular remodeling [39, 40]. Smith et al. [41] designed a similar experiment with the aid of UTMD. In a rat model of chronic hind-limb ischemia, delivering VEGF early and Ang-1 5 min later was performed under the UTMD. VEGF with Ang-1 late delivery groups could increase and/or sustain vessel density, blood flow, and flow reserve, along with enhancing pericyte coverage at 8 weeks after ligation (Figure 6). They also came up with that it was of great importance to imitate the timeline of endogenous gene expression in order to promote angiogenesis.

3.4. Assessment of the Efficacy of Gene Therapy. Gene therapy of angiogenesis has turned out to be a promising method in preclinical studies; however, the therapeutic effect in clinical trials has not reached the target that was expected initially. Therefore, it is necessary to exploit new means to monitor and evaluate the efficacy of gene therapy of angiogenesis. For example, CEU and targeted microbubbles was one of the approaches. What is important, the noninvasive technique not only can detect the safety of some novel therapeutic methods before they get into clinical application, but also can evaluate the treatment effect and guide the next step therapy. The feasibility of this approach was firstly demonstrated by Leong-Poi et al. [42]. In a model of chronic hind-limb ischemia rat, the treated group was injected FGF-2 via intramuscular after iliac artery ligation. They observed and assessed blood flow (by CEU perfusion imaging) and oxygen tension (by phosphor quenching) at 0, 4, 7, 14, or 28 days after ligation. They observed that the signal generated by Integrin $\alpha V\beta 3$-targeted microbubble was markedly augmented at 4 days after ligation in FGF-2 treated group, coinciding with a greater angiogenic response (Figure 7). Therefore, they draw a conclusion that CEU and targeted microbubbles could assess gene therapy of angiogenesis. Meanwhile, CEU imaging can provide more information about the pathophysiology of angiogenesis, and it will greatly promote the development of angiogenesis therapy. Therefore, we should take full advantage of this technique in the future, not only in the preclinical but also in clinical trials.

4. Stem Cell-Based Therapies

Stem cells have been proved an alternative angiogenesis therapy approach of cardiovascular diseases (such as peripheral vascular disease and myocardial infarction disease). Bone marrow cell (BMC) is a typical example. In a systematic review, the treatment effect of migrated adult BMC was critically evaluated by meta-analysis, after follow-up of the patients who suffered from ischemic heart disease. It came to a conclusion that the therapeutic benefits were considerable and positive, and this therapeutic method has a prospect on ischemic heart disease [43]. However, the low transplantation efficiency and poor survivability of migrated cells

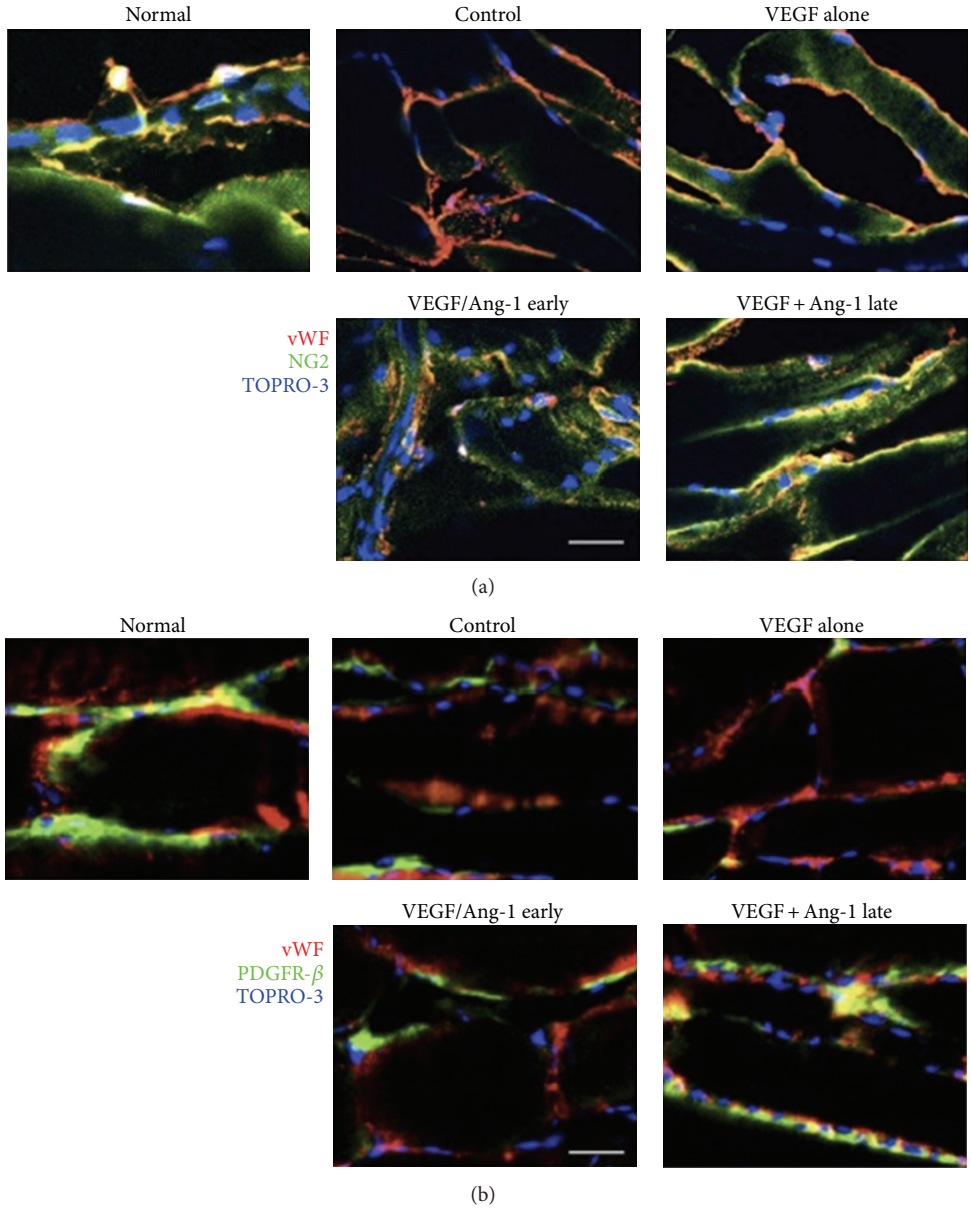

Figure 6: Representative images of pericyte coverage from nonischemic and schematic adductor muscle in respective therapy group at 8 weeks after ligation, von willebrand factor (vWF)-endothelial cells (red), and TOPRO-3-nuclei (blue). (a) NG2-pericyte coverage, (green). Scale bar = 100 μm. (b) Platelet-derived growth factor receptor (PDGFR)-beta-pericyte coverage, (green). Scale bar = 20 μm, colocalization of vWF and either NG2 or PDGFR-beta (yellow). There were the greatest pericytes expressing NG-2 (a) and PDGFR-beta (b) in VEGF + Ang-1 late groups. Adapted from [41].

were the major limiting factors in the development and application of stem cell-based therapy [44]. Hence, it is very necessary to improve the poor engraftment rate. Currently, ultrasound and microbubble can also be regarded as a novel and promising gene delivery methods for facilitating drug, gene, and stem cells targeted transportation [45]. Due to spatially and temporally targeting tissues, noninvasive UTMD technology can make sure that stem cell can be selectively delivered into area of interest. Studies have proved the combination of UTMD and stem cell treatment could strengthen the efficacy of transplantation and was a promising method in angiogenesis therapy of cardiovascular disease. In a rat model of ischemic hind-limb, Imada et al. [46] demonstrated that the combination of UTMD and bone marrow mononuclear cells (BMMNCs) method could facilitate angiogenesis and arteriogenesis response. They observed that BMMNCs were transplanted and attached to the endothelium via electron microscopy. In addition, as showed in angiography, newly formed collateral vessels were obviously enhanced in Bubble + US + BMMNC i.v. group, on postoperative day 28 (Figure 8). Therefore, the method of combination of UTMD and BMMNCs maybe has potential applications in myocardial infarction disease treatment.

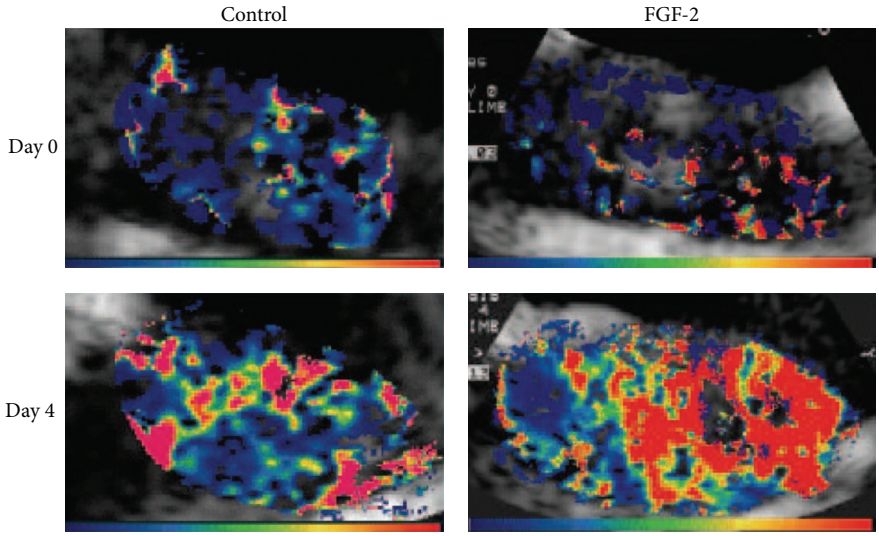

Figure 7: Representative color-coded CEU images reflecting retention fraction of Integrin $\alpha V\beta 3$-targeted microbubbles in control and ischemic proximal hind-limb adductor muscles from untreated and FGF-2-treated rats after ligation (Day 0) and at day 4 after ligation (Day 4). Color scales appear at bottom. Adapted from [42].

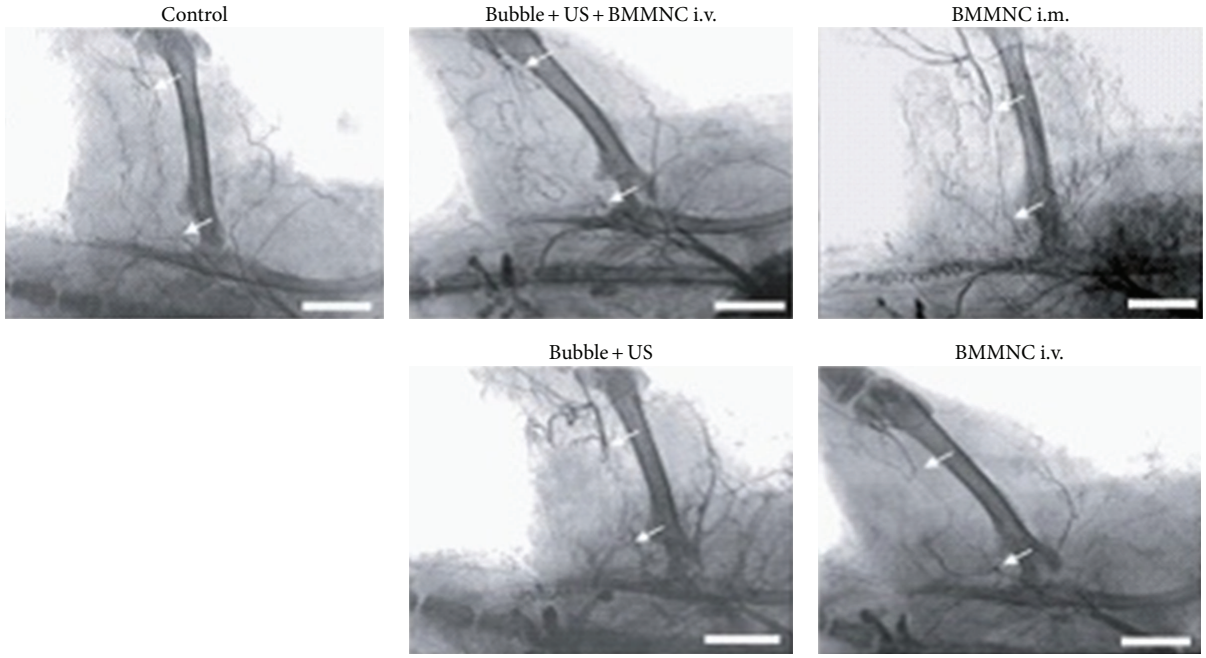

Figure 8: Compared with the BMMNC i.v. Group, the collateral vessel formation in the Bubble + US + BMMNC i.v. and BMMNC i.m. Groups were very obvious, respectively, enhancing 4.2 ± 0.2-fold and 4.3 ± 0.2-fold; the Bubble + US Group was 1.8 ± 0.1-fold, being much less than Bubble + US + BMMNC i.v. Group; Control Group was an equal degree. Adapted from [46].

While they are applied to imaging, microbubbles also can be used as a nonviral vector for inducing stem cell homing [47]. The mechanism of UTMD in promoting stem cell transplantation is possible to be related to sonoporation. The mechanical effect of UTMD could improve myocardial permeability to markedly enhance mesenchymal stem cells (MSC) transplantation to the ischemic myocardium. In addition, with the aid of UTMD, the damaged heart or blood vessels can be stimulated to secrete many kinds of cytokines (such as VCAM-1). Finally, it can accelerate stem cells or progenitor cells attachment and homing, promote angiogenesis, and repair the damaged heart cells [47]. The

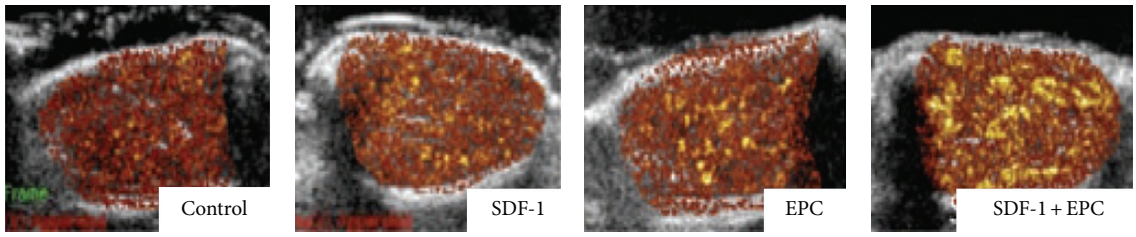

Figure 9: At 2 weeks after iliac artery ligation, all groups were performed on CEU. Above color-coded CEU perfusion images showed ischemic hind-limb muscle blood flow, indicating CEU signal from microbubbles was strongest for combination of SDF-1 and EPC-treated ischemic muscle. Adapted from [50].

Table 1: Summary of experimental studies of UTMD mediated stem cell therapy of angiogenesis.

Author	Candidate stem cell	Animal model	Main finds and results
Tong et al. [57]	BMSCs	Myocardial infarction (rat)	have no effect on the proliferation or apoptosis of MSCs; more efficiently migrate MSCs; a much higher expression of CXCR4, SDF-1 and VEGF; markedly improve the cardiac function and capillary density
Ling et al. [58]	MSCs	Myocardial infarction (mongrel dogs)	markedly improve myocardial perfusion; significantly improve heart function and the wall motion score index; markedly enhance MSC transplantation
Xu et al. [47]	MSC	Myocardial infarction (New Zealand rabbits)	markedly improve the cardiac function; much more capillaries; increase the expression of adhesion molecule and VEGF; enhance the myocardial permeability of microvessel; significantly decrease the area of cardiac fibrosis
Song et al. [59]	BMSC	Myocardial infarction (rabbits)	improve the efficacy of cardiac cell therapy; improve cardiac function in infarcted heart; strengthen the collateral circulation
Kuliszewski et al. [50]	EPC	Chronic hind-limb ischemia (rats)	targeted delivery to the vascular endothelium; greater local engraftment of EPCs; the most obvious improvement in tissue perfusion and capillary density
Ghanem et al. [60]	MSC	After acute myocardial infarction (female wistar rats)	enhance endothelial cell targeting adhesion; augment myocardial engraftment of MSCs
Zhong et al. [61]	MSC	Ischemic myocardium (mongrel dogs)	a much higher expression of various cytokines; provoke inflammatory response and minor myocardial injure; markedly enhance MSCs transplantation to the ischemic myocardium.

※Mesenchymal stem cells (MSCs), endothelial progenitor cells (EPCs), and bone marrow mesenchymal stem cells (BMSCs).

recent researches of the combination of commonly used stem cells and UTMD in therapeutic angiogenesis are showed in the Table 1.

5. Genetically Modified Stem Cell Therapy

Stem cell therapy is identified as a promising and useful treatment method for regenerative medicine. However, the limited proliferation and poor survivability of migrated cells impede their development and application. Recent literatures have reported that genetic modification of stem cells methods could enhance the therapy efficacy in cardiovascular disease. Meanwhile, it came to a conclusion that the stem cell-based gene therapy could overcome the weakness of each other and make both better by complementary of two methods [48]. In previous studies, microbubbles usually served as a nonviral vector to deliver drugs or genes into targeted tissues and cells. Recently, microbubbles have begun to be applied to inducing stem cell-based gene therapy. Otani et al. [49] have reported that UTMD could markedly increase the efficiency of delivering migrated stem cells (MSC and adipose tissue-derived stromal cells) which were genetically modified by small interfering RNA. Despite that this new method maybe produces cell damage, it is better than a viral technique-assistance in the past. Therefore, they came to a conclusion that the novel method had therapeutic potential for cardiovascular diseases in the future. Based on their previous research results, Kuliszewski et al. [50] hypothesized that UTMD in combination with stromal cell-derived factor-1 (SDF-1) had the ability to promote the homing and recruitment of delivered EPCs into chronically ischemic tissue, which proved neovascularization response. In a rat model of hind-limb ischemia, they intravenously administered microbubbles bearing SDF-1 plasmid DNA and exogenous EPCs into the ischemic tissue with the aid of UTMD. At 14 days after delivery, blood perfusion and vascular density in chronically ischemic area were significantly enhanced in the combination of SDF-1 and EPCs treatment group (Figure 9).

6. Summary and Prospect

Overall, UTMD mediated gene therapy and stem cell therapy have emerged as novel methods to enhance angiogenesis. So as to get the best curative effect based on UTMD, future studies should go on to explore the UTMD technique to both obtain maximal transfection efficiency and minimal side effect. Here are some questions that are worthy of attention and further research.

6.1. Security. Ultrasound was applied into medical treatment since 1930s. Later, the safety of ultrasound in therapeutic application has been also a problem worthy of concern and a complicated research at the same time. A large number of works have reported that the application of ultrasound and microbubbles could cause adverse bioeffects (such as a negative chronotropic effect [51] and renal tissue damage [52]). Most of the current studies of UTMD technology are only in the preclinical stage (either in vitro or in small animal models), and there is still much room for development in the future. Taking into account the security concerns, future research should focus on large animals to continue to repeatedly identify the possible human adverse events before clinical trials begin.

6.2. Transfection Efficiency. In the previous research, some investigators have demonstrated that UTMD technique appears to be feasible as a noninvasive and effective approach for angiogenesis therapy. However, there are still many influential factors that limit its application in the clinical treatment. Transfection efficiency is one of very important factors. At present, many researchers have studied the transfection parameters (such as microbubble concentration and composition, the ultrasonic intensity, duty cycle, plasmid DNA concentration, and DNA phosphate ratio) which can dramatically affect the transfection efficiency [34, 53, 54]. And they found that a higher transfection efficiency and a lower cell death could be simultaneously obtained by means of optimizing parameters [55]. Numerous studies have proved that microbubbles could increase the gene transfection efficiency [54, 56]. When microbubbles were exposed to ultrasound irradiation, it would produce a temporary increase of cell membrane permeability, thus promoting gene transfection into the target tissue. However, if the microbubbles concentration is too high or too low, it will be unfavorable for gene transfection. Only under a moderate microbubbles concentration, can be achieved a higher gene transfection, not causing serious cell or tissue damage at the same time. In the future, it is of necessity to explore and build novel microbubbles which will be more beneficial to improve gene transfection.

In the process of UTMD induced gene transfection, with the transfection rate increasing, it is likely to result in a decreased cell viability. For this reason, we should choose the appropriate level of ultrasonic radiation intensity, exposure time, and concentration of microbubbles in future researches. Under such conditions, it is possible to achieve a higher transfection efficiency, as well as ensure a lower cell or tissue damage. There are still many deficiencies in the current research work. What needs to be done in the future is to continue to systematically study and explore the optimization of transfection parameters, laying the theoretical foundation for more effective gene therapy.

Moreover, it is necessary to promote collaboration between UTMD technology and other transfection methods. Believing that with further collaboration among stem cell transplant experts, ultrasound engineers, and cardiovascular biologists, there will be developing more innovative and more mature methods for angiogenesis therapy of cardiovascular disease.

Conflict of Interests

The authors declare no conflict of interests regarding the publication of this paper.

Acknowledgments

This work was supported by National Natural Science Foundation of China (no. 81371572), Research Fund of Doctoral Program of Universities (no. 20124401120002), Sixth Special Project of China Postdoctoral Science Foundation (no. 2013T60826), China Postdoctoral Science Foundation (no. 2011M501375), Research Project of Guangzhou Technology Bureau (no. 12C22021645), Research Project of Science and Technology Guangdong Province (no. 2012B050300026), Research Project of Science and Technology Liwan District (no. 20124414124), and Natural Science Foundation of Guangdong Province (no. S2012040006593).

References

[1] A. P. Sarvazyan, O. V. Rudenko, and W. L. Nyborg, "Biomedical applications of radiation force of ultrasound: historical roots and physical basis," *Ultrasound in Medicine and Biology*, vol. 36, no. 9, pp. 1379–1394, 2010.

[2] S. Horie, Y. Watanabe, R. Chen, S. Mori, Y. Matsumura, and T. Kodama, "Development of localized gene delivery using a dual-intensity ultrasound system in the bladder," *Ultrasound in Medicine and Biology*, vol. 36, no. 11, pp. 1867–1875, 2010.

[3] D. A. B. Smith, S. S. Vaidya, J. A. Kopechek et al., "Ultrasound-triggered release of recombinant tissue-type plasminogen activator from echogenic liposomes," *Ultrasound in Medicine and Biology*, vol. 36, no. 1, pp. 145–157, 2010.

[4] C. S. Yoon and J. H. Park, "Ultrasound-mediated gene delivery," *Expert Opinion on Drug Delivery*, vol. 7, no. 3, pp. 321–330, 2010.

[5] R. Bekeredjian, S. Chen, P. A. Frenkel, P. A. Grayburn, and R. V. Shohet, "Ultrasound-targeted microbubble destruction can repeatedly direct highly specific plasmid expression to the heart," *Circulation*, vol. 108, no. 8, pp. 1022–1026, 2003.

[6] S. T. Laing and D. D. McPherson, "Cardiovascular therapeutic uses of targeted ultrasound contrast agents," *Cardiovascular Research*, vol. 83, no. 4, pp. 626–635, 2009.

[7] L. J. M. Juffermans, A. van Dijk, C. A. M. Jongenelen et al., "Ultrasound and microbubble-induced intra- and intercellular bioeffects in primary endothelial cells," *Ultrasound in Medicine and Biology*, vol. 35, no. 11, pp. 1917–1927, 2009.

[8] J. Park, Z. Fan, R. E. Kumon, M. E. H. El-Sayed, and C. X. Deng, "Modulation of intracellular Ca^{2+} concentration in brain

microvascular endothelial cells in vitro by acoustic cavitation," *Ultrasound in Medicine and Biology*, vol. 36, no. 7, pp. 1176–1187, 2010.

[9] Y. H. Chuang, P. W. Cheng, and P. C. Li, "Combining radiation force with cavitation for enhanced sonothrombolysis," *IEEE Transactions on Ultrasonics, Ferroelectrics and Frequency Control*, vol. 60, no. 1, pp. 97–104, 2013.

[10] B. D. M. Meijering, L. J. M. Juffermans, A. Van Wamel et al., "Ultrasound and microbubble-targeted delivery of macromolecules is regulated by induction of endocytosis and pore formation," *Circulation Research*, vol. 104, no. 5, pp. 679–687, 2009.

[11] H. Yu and L. Xu, "Cell experimental studies on sonoporation: state of the art and remaining problems," *Journal of Controlled Release*, vol. 174, pp. 151–160, 2014.

[12] L. Reslan, J.-L. Mestas, S. Herveau, J.-C. Béra, and C. Dumontet, "Transfection of cells in suspension by ultrasound cavitation," *Journal of Controlled Release*, vol. 142, no. 2, pp. 251–258, 2010.

[13] A. Delalande, S. Kotopoulis, M. Postema, P. Midoux, and C. Pichon, "Sonoporation: mechanistic insights and ongoing challenges for gene transfer," *Gene*, vol. 525, no. 2, pp. 191–199, 2013.

[14] D. Pezzoli, R. Chiesa, L. De Nardo, and G. Candiani, "We still have a long way to go to effectively deliver genes!," *Journal of Applied Biomaterials & Functional Materials*, vol. 10, no. 2, pp. 82–91, 2012.

[15] X. Guo and L. Huang, "Recent advances in nonviral vectors for gene delivery," *Accounts of Chemical Research*, vol. 45, no. 7, pp. 971–979, 2012.

[16] N. A. Geis, H. A. Katus, and R. Bekeredjian, "Microbubbles as a vehicle for gene and drug delivery: current clinical implications and future perspectives," *Current Pharmaceutical Design*, vol. 18, no. 15, pp. 2166–2183, 2012.

[17] Z. Y. Chen, F. Yang, Y. Lin et al., "New development and application of ultrasound targeted microbubble destruction in gene therapy and drug delivery," *Current Gene Therapy*, vol. 13, no. 4, pp. 250–274, 2013.

[18] J. C. Chappell, J. Song, C. W. Burke, A. L. Klibanov, and R. J. Price, "Targeted delivery of nanopartides bearing fibroblast growth factor-2 by ultrasonic microbubble destruction for therapeutic arteriogenesis," *Small*, vol. 4, no. 10, pp. 1769–1777, 2008.

[19] S. Rey and G. L. Semenza, "Hypoxia-inducible factor-1-dependent mechanisms of vascularization and vascular remodelling," *Cardiovascular Research*, vol. 86, no. 2, pp. 236–242, 2010.

[20] C. A. Johnson, R. J. Miller, and W. D. O'Brien, "Ultrasound contrast agents affect the angiogenic response," *Journal of Ultrasound in Medicine*, vol. 30, no. 7, pp. 933–941, 2011.

[21] J. Kobulnik, M. A. Kuliszewski, D. J. Stewart, J. R. Lindner, and H. Leong-Poi, "Comparison of gene delivery techniques for therapeutic angiogenesis. Ultrasound-mediated destruction of carrier microbubbles versus direct intramuscular injection," *Journal of the American College of Cardiology*, vol. 54, no. 18, pp. 1735–1742, 2009.

[22] H. Leong-Poi, M. A. Kuliszewski, M. Lekas et al., "Therapeutic arteriogenesis by ultrasound-mediated VEGF165 plasmid gene delivery to chronically ischemic skeletal muscle," *Circulation Research*, vol. 101, no. 3, pp. 295–303, 2007.

[23] H. Fujii, Z. Sun, S.-H. Li et al., "Ultrasound-targeted gene delivery induces angiogenesis after a myocardial infarction in mice," *JACC: Cardiovascular Imaging*, vol. 2, no. 7, pp. 869–879, 2009.

[24] T. Asahara, C. Bauters, L. P. Zheng et al., "Synergistic effect of vascular endothelial growth factor and basic fibroblast growth factor on angiogenesis in vivo," *Circulation*, vol. 92, no. 9, pp. 365–371, 1995.

[25] Y. Negishi, K. Matsuo, Y. Endo-Takahashi et al., "Delivery of an angiogenic gene into ischemic muscle by novel bubble liposomes followed by ultrasound exposure," *Pharmaceutical Research*, vol. 28, no. 4, pp. 712–719, 2011.

[26] Y. Negishi, Y. Endo-Takahashi, Y. Matsuki et al., "Systemic delivery systems of angiogenic gene by novel bubble liposomes containing cationic lipid and ultrasound exposure," *Molecular Pharmaceutics*, vol. 9, no. 6, pp. 1834–1840, 2012.

[27] Y. Z. Zhao, C. T. Lu, X. K. Li et al., "Improving the cardio protective effect of aFGF in ischemic myocardium with ultrasound-mediated cavitation of heparin," *Journal of Drug Targeting*, vol. 20, no. 7, pp. 623–631, 2012.

[28] R. Morishita, S. Nakamura, S.-I. Hayashi et al., "Therapeutic angiogenesis induced by human recombinant hepatocyte growth factor in rabbit hind limb ischemia model as cytokine supplement therapy," *Hypertension*, vol. 33, no. 6, pp. 1379–1384, 1999.

[29] Y. Taniyama, K. Tachibana, K. Hiraoka et al., "Development of safe and efficient novel nonviral gene transfer using ultrasound: enhancement of transfection efficiency of naked plasmid DNA in skeletal muscle," *Gene Therapy*, vol. 9, no. 6, pp. 372–380, 2002.

[30] Q.-Y. Yuan, J. Huang, B.-C. Chu, X.-S. Li, and L.-Y. Si, "A visible, targeted high-efficiency gene delivery and transfection strategy," *BMC Biotechnology*, vol. 11, article 56, 2011.

[31] Q. Y. Yuan, Z. W. Zhu, Z. Wang et al., "A novel method of augmenting gene expression and angiogenesis in the normal and ischemic canine myocardium," *Heart Vessels*, vol. 27, no. 3, pp. 316–326, 2012.

[32] Q.-Y. Yuan, J. Huang, B.-C. Chu, X.-J. Li, X.-S. Li, and L.-Y. Si, "A targeted high-efficiency angiogenesis strategy as therapy for myocardial infarction," *Life Sciences*, vol. 90, no. 17-18, pp. 695–702, 2012.

[33] Z. Zhou, P. Zhang, J. Ren et al., "Synergistic effects of ultrasound-targeted microbubble destruction and TAT peptide on gene transfection: an experimental study in vitro and in vivo," *Journal of Controlled Release*, vol. 170, no. 3, pp. 437–444, 2013.

[34] Q. Zhou, J. L. Chen, Q. Chen et al., "Optimization of transfection parameters for ultrasound/SonoVue microbubble-mediated hAng-1 gene delivery in vitro," *Molecular Medicine Reports*, vol. 6, no. 6, pp. 1460–1464, 2012.

[35] L. Sun, C. W. Huang, J. Wu et al., "The use of cationic microbubbles to improve ultrasound-targeted gene delivery to the ischemic myocardium," *Biomaterials*, vol. 34, no. 8, pp. 2107–2116, 2013.

[36] D. Y. Li, X. Y. Jiang, T. D. Xu, J. T. Song, H. Zhu, and Y. Y. Luo, "The anti-apoptotic effect of transgenic Akt1 gene on cultured new-born rats cardiomyocytes mediated by ultrasound/microbubbles destruction," *Frontier and Future Development of Information Technology in Medicine and Education*, vol. 269, pp. 1–9, 2014.

[37] N. Smart, C. A. Risebro, J. E. Clark et al., "Thymosin $\beta 4$ facilitates epicardial neovascularization of the injured adult heart," *Annals of the New York Academy of Sciences*, vol. 1194, pp. 97–104, 2010.

[38] S. Chen, M. Shimoda, J. Chen, and P. A. Grayburn, "Stimulation of adult resident cardiac progenitor cells by durable myocardial expression of thymosin beta 4 with ultrasound-targeted microbubble delivery," *Gene Therapy*, vol. 20, no. 2, pp. 225–233, 2013.

[39] Z. Tao, B. Chen, X. Tan et al., "Coexpression of VEGF and angiopoietin-1 promotes angiogenesis and cardiomyocyte proliferation reduces apoptosis in porcine myocardial infarction (MI) heart," *Proceedings of the National Academy of Sciences of the United States of America*, vol. 108, no. 5, pp. 2064–2069, 2011.

[40] S. M. Samuel, Y. Akita, D. Paul et al., "Coadministration of adenoviral vascular endothelial growth factor and angiopoietin-1 enhances vascularization and reduces ventricular remodeling in the infarcted myocardium of type 1 diabetic rats," *Diabetes*, vol. 59, no. 1, pp. 51–60, 2010.

[41] A. H. Smith, M. A. Kuliszewski, C. Liao, D. Rudenko, D. J. Stewart, and H. Leong-Poi, "Sustained improvement in perfusion and flow reserve after temporally separated delivery of vascular endothelial growth factor and angiopoietin-1 plasmid deoxyribonucleic acid," *Journal of the American College of Cardiology*, vol. 59, no. 14, pp. 1320–1328, 2012.

[42] H. Leong-Poi, J. Christiansen, P. Heppner et al., "Assessment of endogenous and therapeutic arteriogenesis by contrast ultrasound molecular imaging of integrin expression," *Circulation*, vol. 111, no. 24, pp. 3248–3254, 2005.

[43] V. Jeevanantham, M. Butler, A. Saad, A. Abdel-Latif, E. K. Zuba-Surma, and B. Dawn, "Adult bone marrow cell therapy improves survival and induces long-term improvement in cardiac parameters: a systematic review and meta-analysis," *Circulation*, vol. 126, no. 5, pp. 551–568, 2012.

[44] P. Lipiec, M. Krzemińska-Pakuła, M. Plewka et al., "Impact of intracoronary injection of mononuclear bone marrow cells in acute myocardial infarction on left ventricular perfusion and function: a 6-month follow-up gated 99mTc-MIBI single-photon emission computed tomography study," *European Journal of Nuclear Medicine and Molecular Imaging*, vol. 36, no. 4, pp. 587–593, 2009.

[45] F. Kiessling, S. Fokong, P. Koczera, W. Lederle, and T. Lammers, "Ultrasound microbubbles for molecular diagnosis, therapy, and theranostics," *Journal of Nuclear Medicine*, vol. 53, no. 3, pp. 345–348, 2012.

[46] T. Imada, T. Tatsumi, Y. Mori et al., "Targeted delivery of bone marrow mononuclear cells by ultrasound destruction of microbubbles induces both angiogenesis and arteriogenesis response," *Arteriosclerosis, Thrombosis, and Vascular Biology*, vol. 25, no. 10, pp. 2128–2134, 2005.

[47] Y.-L. Xu, Y.-H. Gao, Z. Liu et al., "Myocardium-targeted transplantation of mesenchymal stem cells by diagnostic ultrasound-mediated microbubble destruction improves cardiac function in myocardial infarction of New Zealand rabbits," *International Journal of Cardiology*, vol. 138, no. 2, pp. 182–195, 2010.

[48] H. K. Haider, A. Mustafa, Y. Feng, and M. Ashraf, "Genetic modification of stem cells for improved therapy of the infarcted myocardium," *Molecular Pharmaceutics*, vol. 8, no. 5, pp. 1446–1457, 2011.

[49] K. Otani, K. Yamahara, S. Ohnishi, H. Obata, S. Kitamura, and N. Nagaya, "Nonviral delivery of siRNA into mesenchymal stem cells by a combination of ultrasound and microbubbles," *Journal of Controlled Release*, vol. 133, no. 2, pp. 146–153, 2009.

[50] M. A. Kuliszewski, J. Kobulnik, J. R. Lindner, D. J. Stewart, and H. Leong-Poi, "Vascular gene transfer of SDF-1 promotes endothelial progenitor cell engraftment and enhances angiogenesis in ischemic muscle," *Molecular Therapy*, vol. 19, no. 5, pp. 895–902, 2011.

[51] D. L. Miller, C. Dou, and R. C. Wiggins, "Contrast-enhanced diagnostic ultrasound causes renal tissue damage in a porcine model," *Journal of Ultrasound in Medicine*, vol. 29, no. 10, pp. 1391–1401, 2010.

[52] E. B. Buiochi, R. J. Miller, E. Hartman et al., "Transthoracic cardiac ultrasonic stimulation induces a negative chronotropic effect," *IEEE Transactions on Ultrasonics, Ferroelectrics, and Frequency Control*, vol. 59, no. 12, pp. 2655–2661, 2012.

[53] C. B. Zhang, H. L. Cao, Q. Li et al., "Enhancement effect of ultrasound-induced microbubble cavitation on branched polyethylenimine-mediated VEGF(165) transfection with varied N/P ratio," *Ultrasound in Medicine & Biology*, vol. 39, no. 1, pp. 161–171, 2013.

[54] Z.-Y. Chen, X.-F. Sun, J.-Q. Liu et al., "Augmentation of transgenic expression by ultrasound-mediated liposome microbubble destruction," *Molecular Medicine Reports*, vol. 5, no. 4, pp. 964–970, 2012.

[55] Q.-Q. Zhao, J.-L. Chen, T.-F. Lv et al., "N/P ratio significantly influences the transfection efficiency and cytotoxicity of a polyethylenimine/chitosan/DNA complex," *Biological and Pharmaceutical Bulletin*, vol. 32, no. 4, pp. 706–710, 2009.

[56] Y.-C. Chen, L.-P. Jiang, N.-X. Liu, Z.-H. Wang, K. Hong, and Q.-P. Zhang, "P85, Optison microbubbles and ultrasound cooperate in mediating plasmid DNA transfection in mouse skeletal muscles in vivo," *Ultrasonics Sonochemistry*, vol. 18, no. 2, pp. 513–519, 2011.

[57] J. Tong, J. Ding, X. Shen et al., "Mesenchymal stem cell transplantation enhancement in myocardial infarction rat model under ultrasound combined with nitric oxide microbubbles," *PLoS ONE*, vol. 8, no. 11, Article ID e80186, 2013.

[58] Z. Y. Ling, S. Y. Shu, S. G. Zhong et al., "Ultrasound targeted microbubble destruction promotes angiogenesis and heart function by inducing myocardial microenvironment change," *Ultrasound in Medicine & Biology*, vol. 39, no. 11, pp. 2001–2010, 2013.

[59] X. Song, H. Zhu, L. Jin et al., "Ultrasound-mediated microbubble destruction enhances the efficacy of bone marrow mesenchymal stem cell transplantation and cardiac function," *Clinical and Experimental Pharmacology and Physiology*, vol. 36, no. 3, pp. 267–271, 2009.

[60] A. Ghanem, C. Steingen, F. Brenig et al., "Focused ultrasound-induced stimulation of microbubbles augments site-targeted engraftment of mesenchymal stem cells after acute myocardial infarction," *Journal of Molecular and Cellular Cardiology*, vol. 47, no. 3, pp. 411–418, 2009.

[61] S. Zhong, S. Shu, Z. Wang et al., "Enhanced homing of mesenchymal stem cells to the ischemic myocardium by ultrasound-targeted microbubble destruction," *Ultrasonics*, vol. 52, no. 2, pp. 281–286, 2012.

Hindawi Publishing Corporation
BioMed Research International
Volume 2014, Article ID 901642, 7 pages
http://dx.doi.org/10.1155/2014/901642

Research Article

Acoustic Radiation Force Impulse Elastography for Efficacy Evaluation after Hepatocellular Carcinoma Radiofrequency Ablation: A Comparative Study with Contrast-Enhanced Ultrasound

Xiaohong Xu,[1,2] Liangping Luo,[1] Jiexin Chen,[2] Jiexin Wang,[2] Honglian Zhou,[2] Mingyi Li,[2] Zhanqiang Jin,[2] Nianping Chen,[2] Huilai Miao,[2] Manzhou Lin,[2] Wei Dai,[2] Anil T. Ahuja,[3] and Yi-Xiang J. Wang[3]

[1] *The First Affiliated Hospital of Jinan University, Guangzhou 510632, China*
[2] *The Affiliated Hospital of Guangdong Medical College, Zhanjiang 524001, China*
[3] *Department of Imaging & Interventional Radiology, Prince of Wales Hospital, The Chinese University of Hong Kong, Shatin, N.T., Hong Kong*

Correspondence should be addressed to Liangping Luo; tluolp@jnu.edu.cn and Yi-Xiang J. Wang; yixiang_wang@cuhk.edu.hk

Received 19 March 2014; Revised 18 April 2014; Accepted 20 April 2014; Published 6 May 2014

Academic Editor: Zhiyi Chen

Aim. To explore acoustic radiation force impulse (ARFI) elastography in assessing residual tumors of hepatocellular carcinoma (HCC) after radiofrequency ablation (RFA). *Materials and Methods*. There were 83 HCC lesions among 72 patients. All patients were examined with ARFI, contrast enhanced ultrasound (CEUS), and CT or MRI. Tumor brightness on virtual touch tissue imaging (VTI) and shear wave velocity (SWV) were assessed before and approximately one month after RFA. *Results*. There were 14 residual tumors after RFA. VTI showed that all the tumors were darker after RFA. VTI was not able to distinguish the ablated lesions and the residual tumors. 13 residual tumor lesions were detected by CEUS. All completely ablated nodules had SWV demonstration of x.xx., while with those residual nodules, 6 tumors had x.xx measurement and 8 tumors had measurable SWV. nine lesions with residual tumors occurred in cirrhosis subjects and 5 lesions with residual tumors occurred in fibrosis subjects; there was no residual tumor in the normal liver subjects. *Conclusion*. VTI technique cannot demonstrate residual tumor post RFA. While SWV measurement of less than x.xx is likely associated with residual tumors, measurement of less than x.xx cannot exclude residual tumors. Liver cirrhosis is associated with decreased chance of a complete ablation.

1. Introduction

Primary hepatocellular carcinoma (HCC) is one of the most common malignancies. Although surgery demonstrates highest possibility for curing HCC, only 20–30% patients have opportunities of surgical treatment because HCC often occurs on the basis of hepatitis and liver cirrhosis and presents with multifocal lesion [1–3]. Recently radiofrequency ablation (RFA) is developed as one of the popular techniques for tumor ablation [2]. Using resistive ionic heating through electrodes, it can lead to coagulation necrosis of tumor. This technique is commonly used clinically because it is highly effective, minimally invasive, and requires fewer sessions [2]. Several randomized clinical trials have also confirmed that for small HCC, treatment efficacy of thermal ablation is comparable to that of surgical resection [3–5]. However, after RFA residual tumor may still exist [2]. The evaluation of treatment efficacy after percutaneous ablation therapy for HCC is essential for the determination of subsequent treatment and follow-up strategy. Dynamic contrast-enhanced CT and MRI are the standard techniques to evaluate the clinical effectiveness of RFA [6, 7]. Contrast-enhanced Ultrasound (CEUS) is also used to evaluate treatment efficacy after ablation therapy. The agreement between

CEUS and contrast-enhanced CT, as well as MRI, has been reported to be good [8].

Acoustic radiation force impulse (ARFI) imaging is a new ultrasound-based diagnostic technique that, evaluating the wave propagation speed, allows the assessment of tissue stiffness [9]. ARFI does not need external compression so the operator dependency is reduced. By short-duration acoustic radiation forces (less than 1 ms), ARFI generates localized displacements in a selected region of interest (ROI) identified on a conventional B-mode image. Depending on the interactions with the transducer, the generated wave scan provides qualitative (imaging) or quantitative (wave velocity values, measured in m/s) responses, by virtual touch tissue imaging (VTI) and virtual touch tissue quantification (VTQ) techniques, respectively (Siemens, Erlangen, Germany) [9]. VTI image is based on the degree of lightness and darkness in the regions of interest for different tissue elasticity coded display of hardness, with the more light color indicating the more soft tissue, the darker color the more hard tissue. VTQ is based on the conventional two-dimensional sonogram with a longitudinal wave emitted by the probe, resulting in a horizontal elastic shear wave propagation in tissue and detect the shear wave velocity to provide information on tissue stiffness, with the more hard tissue showing faster shear wave velocity. There are a number of studies using ARFI in differentiating cancer from benign disease [9–12]. However, few studies on using ARFI techniques to assess the outcome of RFA treatment in liver carcinoma have been reported [13]. In this prospective study, we aimed to investigate whether ARFI could be one alternative technique of CEUS to assess RFA outcomes in HCC.

2. Materials and Methods

2.1. Patients. The prospective study was carried out during May 2010 and December 2011. It was approved by the local research ethics committee and informed consent was obtained for each subjects. RFA was performed on 186 consecutive HCC patients; all of them had histopathological confirmation and did not have surgery indication or willingness. Patients included in this study had a tumor diameter equaling or less than 3 cm and the number of masses was ≤2. Exclusion criteria included: (1) patients could not hold their breathing; (2) the distance between lesion and skin greater than 8.0 cm; (3) lesions close to heart and big vessels such as aorta and inferior vena cava; (4) lesions close to dome of diaphragm (within a distance of approximately 5 cm) and lesions obscured by gas in intestine. 83 HCC masses in 72 patients satisfied the above inclusion and exclusion criteria. Of these patients, 61 patients showed single HCC mass, 8 patients had two HCC masses, and 3 patients had one recurred HCC mass after RFA. HCC patients with comorbidities of liver fibrosis (≤stage F3) due to hepatitis B or C and liver cirrhosis (stage F4) accounted for 83.3% (60/72) of the sample size.

2.2. Acoustic Radiation Force Impulse Method. The ultrasound system was Siemens Acuson S2000 with color Doppler ultrasonography and 4C1 convex array probe operating at the frequency of 2.0~4.0 MHz. This system was equipped with ARFI imaging and contrast enhanced-imaging pulse sequence. Conventional gray scale ultrasound was performed to show the lesions before and after the RFA. VTI was initiated with appropriate adjustments of sampling frame size, until the ablation lesion and parts of the surrounding liver parenchyma were covered. The lesion sites were divided into three categories based on their brightness, being high-echo (softer), iso-echo (similar echo-intensity as the surrounding liver parenchyma), and low-echo (harder). After VTI images acquisition and storage, VTQ technology was initiated which involves the selection of an anatomic region to be interrogated for elastic properties with the use of an ROI cursor by placing a "measuring box" of 10 mm long and 5 mm wide. The ROI was included entirely within the lesion, excluding all vessels and biliary structures. The shear waves were detected by sonographic detection pulses and the numeric values of the shear wave velocity (SWV, m/s) were calculated and displayed on the monitor. For liver parenchyma and pre-RFA measurement lesion, seven measurements were carried out on each lesion with sampling frame distributed evenly in the lesion. The highest value and lowest value were discarded; the average of the remaining 5 values was taken as the measurement for the lesion [14, 15]. For post-RFA measurement, at least 7 measurements were attempted and the sampling frame evenly covered the tumor. When measurements were out of the tolerable range of the system for shear wave velocity calculation, the shear wave velocity was displayed with "x.xx" [12, 13]. If the system displays "x.xx m/s", according to the literature, a value of 9 m/s was used after the exclusion of cystic changes in the lesion [12]. Our previous experiences suggest that any post-RFA measurement with value lower than 9 m/s would suggest viable tissue, and therefore residue tumor [16].

2.3. Contrast-Enhanced Ultrasound. Ultrasound contrast agent (SonoVue, Bracco, Italy) was a freeze-dried powder formulation of sulfur hexafluoride phospholipid. Before use, 5 mL saline solution was mixed with the powder into a homogeneous suspension by oscillation. 2.4 mL of this contrast agent was injected through the elbow superficial vein by a rapid bolus followed by 5 mL saline flush, then a built-in timer started ultrasound scanning. With the entering of CEUS status, acoustic output power, focus and gain were adjusted, and the mechanical index was set to 0.05 using a low mechanical index gray-scale continuous real-time ultrasound scanning technology. Real-time continuous observation of the lesion contrast perfusion and echo intensity were carried out. If the arterial phase perfusion of contrast agent was required again for the ablation assessment, the second contrast injection was made 15 min later than the initial injection. Dynamic contrast-enhanced ultrasound movies and single-frame still images were recorded and then reviewed.

2.4. Contrast-Enhanced CT or MRI. Tissue surrounding the RF ablated surrounding may have the short term inflammatory edema. Contrast-enhanced CT or MRI evaluation of liver was performed approximately one month after the

ablation so that inflammatory edema subdued (Figure 1). Siemens Somatom Sensation 64-slice spiral CT or GE Signa HD 1.5T magnetic resonance imaging system were used for examinations.

2.5. Radiofrequency Ablation Treatment. Patients were treated with RFA using the Cool-tip RF System (Radionics, Burlington, Massachusetts, USA) with 0–200 W of power and 480 kHz of frequency, and at cold cycling and RF pulse transmission mode. Ultrasound was performed to determine the suitable puncture track, followed by local anesthesia and RF electrode was advanced into the tumor interior. The intended ablation area covers the entire tumor and extended 1.0 cm beyond the border. Treatment started after confirming the correct location of the RF electrode. The treatment lasted 12 min each time.

2.6. RAF Efficacy Evaluation. Conventional ultrasound, ARFI, CEUS, contrast-enhanced CT, or MRI were read, respectively, by one experienced sonographer and one radiologist blinded to patient history, and the lesion size or ablation size measurement was performed. Lesion ablation measurement was performed at the same standard section for conventional B mode ultrasound, CEUS, enhanced CT, or MRI. For residual lesion assessment, if both the interior and peripheral parts of the primary tumor showed no enhancement, the post-treatment results of "complete ablation" was established. If radiologic evaluation showed the post-ablation lesion had interior or rim enhancement at arterial phase with portal phase subsiding, then the diagnosis of "partial residual tumor" was established.

Statistical analysis was performed using software SPSS (version 12.0 for Windows; SPSS, Chicago, Ill). Mann Whitney U test was used for comparison between the groups. One-way analysis of variance (ANOVA) and linear trend test was used in comparing SWV and ablation size in liver cirrhosis, liver fibrosis, and normal liver parenchyma subjects.

Reexamination of routine ultrasound, CEUS, ARFI, and contrast-enhanced CT or MRI was performed in about 20~30 days after RFA (Figure 1). Enhanced CT or MRI manifestations was regarded as reference standard for assessing residual tumor after RFA. Biopsy was performed for residual tumors when detected by post-RFA imaging.

3. Results

Prior to RFA procedure, on VTI images 25 tumors out of 83 (30.1%) were in the high-echo group, 17 tumors (20.5%) fell into the iso-echo group, and 41 tumors (49.4%) were in low-echo group. All tumors displayed low-echo after the RFA (Figures 2 and 3). The lesion size was 2.39 ± 0.47 mm with B mode US measurement, while was 3.03 ± 0.53 mm with VTI measurement ($P < 0.05$). Lesion size measurement from CEUS was 2.93 ± 0.51 mm ($P > 0.05$ versus VTI measurement). B mode measurement underestimated the lesion area (Figure 3), while ARFI-VTI measurement had good agreement with CEUS.

Among the 83 tumor lesions, after RFA there were 14 lesions had residual tumors detected by CT or MRI (Table 1). VTI was not able to detect residual tumors. Out of the 14 residual tumor lesions, 13 were detected by CEUS (Figure 4), and CEUS missed one lesion with residual tumor. CEUS reported two false positive residual tumors which was negative on CT or MRI, and confirmed to be negative by biopsy. Compared with those had completed ablation, the 14 tumors with residual nodule had no difference in lesion size, both before and after RFA procedure, and also there was no tumor SWV difference before RFA procedure (Table 2). All the completely ablated nodules had a SWV demonstration of x.xx. While with those residual nodules, 6 (42.9%) had x.xx measurement, and 8 (57.1%) had measurable SWV (3.08 ± 0.59 m/s).

When the 83 tumors were divided into three groups based on whether the patients had normal parenchyma ($n = 12$, 14.5%), liver fibrosis ($n = 44$, 53.0%), or liver cirrhosis ($n = 27$, 35.5%), the liver parenchyma SWV showed a value of 1.52 ± 0.412 (m/s), 2.13 ± 0.42 (m/s), 2.71 ± 0.44 (m/s), respectively, representing a significant increasing trend ($P < 0.05$); while the ablation size showed a value of 4.17 ± 0.74 (cm), 4.16 ± 0.60 (cm), and 4.07 ± 0.50 (cm), respectively, representing a significant decreasing trend ($P < 0.05$). 9 lesions with residual tumor occurred in liver cirrhosis subjects (9/27, 33.3%), 5 lesions with residual tumor occurred in liver fibrosis subjects (5/44, 11.4%), while there was no residual tumor in the normal liver parenchyma subjects (0/12). Therefore there was an increased possibility of residual tumor associated with increasing liver parenchyma stiffness.

4. Discussion

Local therapies, especially percutaneous ablation therapies, have gained increasing attention in treatment for liver cancer because of their advantages such as mini-invasiveness, easy manipulation, repeatability, and cost-effectiveness. RFA technique employs ultrasound, CT, or other imaging techniques to guide an electrode needle to be inserted into the interior of tumors, and it causes local lesions tissue temperature to arise, resulting in localized tumor lesion hyperthermia and coagulation necrosis [2]. Ultrasound-guided RFA is particularly widespread for HCC treatment [11]. A potential eradicative RFA should include the entire tumor plus a 5–10 mm peritumoral safety margin in an ideal sphere of necrosis, whereas an area of coagulation smaller than expected may lead to local recurrence [17]. In clinical practice, many factors (i.e., probe gauge, tip length, temperature achieved, heating duration, heat-sink effect of nearby blood vessels, and incomplete fusion of RFA lesions between prongs of expandable electrodes or surgical clips near the tumor) may alter this ideal geometrical shape producing an irregularly sized, distorted, or incomplete area of necrosis. It has been reported that conventional RFA devices with a single electrode or deployed electrode arrays with a thermal diameter of 3–4 cm provide a complete ablation rate of more than 90% for small tumors, but yield lower rates of 53–61% for medium-sized tumors (diameter 3.1–5 cm) and 20–45% for larger tumors

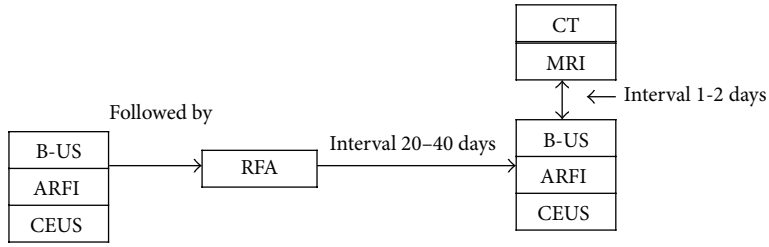

Figure 1: A flow diagram of the imaging and radiofrequency ablation (RFA) schedule.

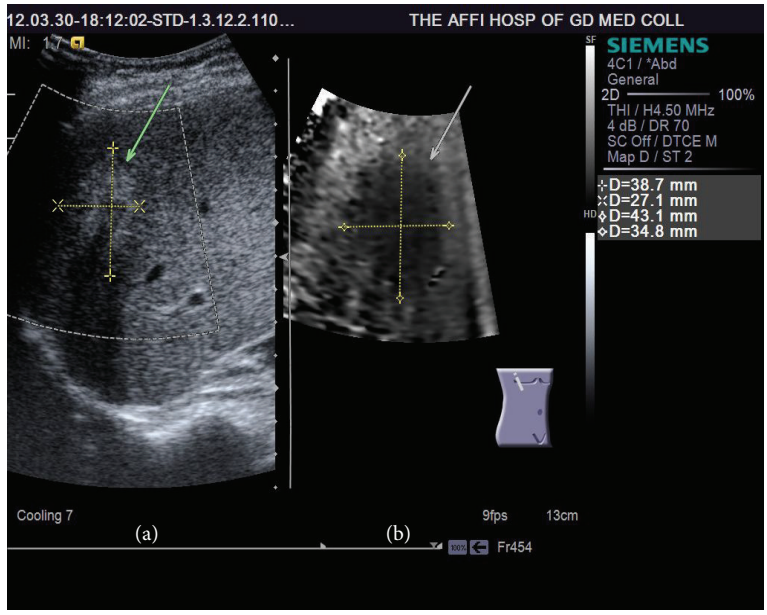

Figure 2: 2D conventional US (a) and virtual touch tissue imaging (VTI, b). Tumor mass after RFA is remarkably darker (stiffer) than adjacent hepatic parenchyma on VTI. The ablated size of VTI (34.8 mm × 43.1 mm) is larger than that of 2D conventional US (27.1 mm × 38.7 mm).

(>5 cm) [17]. To correctly judge the location and extent of necrosis after RFA is a key evaluation for treatment effect, and it is directly related to prognosis of the patient.

Enhanced CT and MRI are often used as the reference diagnostic standard for post RF ablation efficacy evaluation. Enhanced CT and MRI determine whether RFA ablated completely the tumor or there are residual tumors based on whether the tumor is enhanced, that is, to use whether the contrast agent enters the tumor as a criterion. No enhancement means that the ablation is complete, with the pathological basis that when coagulation necrosis occurs there is no blood supply to the tumor, and therefore without contrast agent entering the tumor. By using ultrasound contrast agents and contrast specific imaging techniques, CEUS is able to depict the micro and macrocirculation in the liver and the treated lesion, thus allowing assessment of the treatment efficacy for HCC after percutaneous ablation therapy in a similar fashion with CECT or CEMRI [10, 18–21]. Different to CT or MRI contrast agents, ultrasound contrast agents do not diffuse into the intercellular space, and as such they reflect the blood supply of liver tumors by observing blood microcirculation characteristics. CEUS, similar to CECT or CEMRI, also follows the guideline of the modified Response Evaluation Criteria in Solid Tumor (mRECIST) [22]. In this guideline, viable HCC is defined as uptake of contrast agent in the arterial phase of CEUS; while complete response is defined as disappearance of any intratumoral arterial enhancement in HCC lesions [22, 23]. Researches showed CEUS in the assessment of RF ablation of liver cancer have the similar accuracy as contrast enhanced CT or MRI [24, 25].

VTI and VTQ are used to obtain tissue elasticity image and elasticity value, respectively. After RF ablation tissue stiffness in the necrotic areas is different from the surrounding normal tissues. By detecting the change of tissue hardness ARFI is used to determine the extent of inactivation of tumor. Among the 83 lesions, we carefully compared the 14 residual tumors with the 69 tumors had a complete ablation. The VTI display was all black, that is, overall hardness of the ablated zone being higher than the surrounding liver parenchyma. As the previous report by Kwon et al. [13], all the tumors appeared dark color after RFA treatment. This is likely due to that the RF ablated site was comprised of hard lesions that showed coagulative necrosis and fibrotic scarring [13]. This study shows that VTI imaging could estimate the tumor lesion area accurately, being consistent with the values

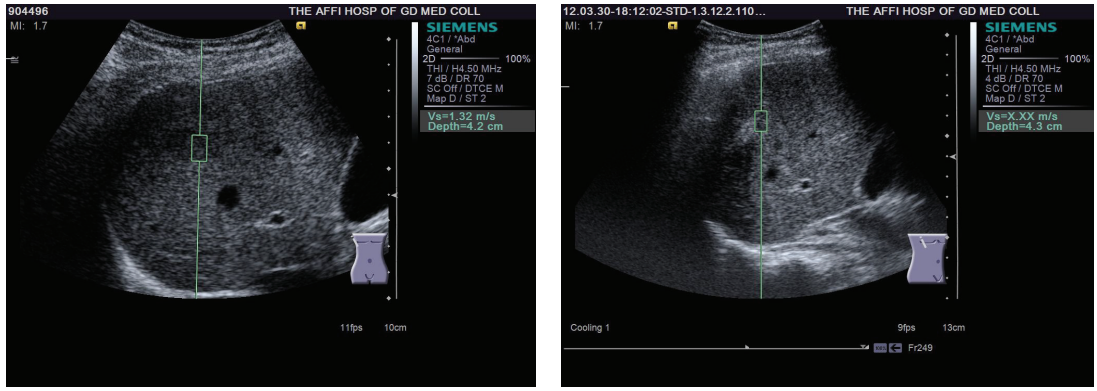

(a) (b)

Figure 3: Virtual touch tissue quantification (VTQ) before (a) and after (b) RFA. Before RFA the shear wave velocity of this tumor is 1.32 m/s, while after RFA the shear wave velocity in the ablated area shows x.xx m/s (i.e. out of the range of the measurable values).

Table 1: ARFI measurements of 14 residual tumors.

Sex	Age	Comorbidity	Tumor size* B-mode	Tumor size* VTI	Tumor size* CEUS	SWV** after RFA	RFA size* VTI
M	62	Cirrhosis	2.72	2.89	2.81	x.xx	3.78
M	72	Fibrosis	1.91	2.22	2	x.xx	3.3
M	50	Fibrosis	2.22	2.51	2.5	3.15	3.14
M	72	Cirrhosis	1.58	3.02	2.82	3.97	3.66
M	55	Cirrhosis	2.5	3.52	3.33	3.78	4.24
F	74	Fibrosis	1.98	3	3	2.57	3.63
M	64	Cirrhosis	2.31	3	3	x.xx	3.7
M	73	Fibrosis	2.6	3.13	3	3.12	4.12
M	65	Cirrhosis	3	3.82	3.71	2.47	4.58
F	71	Fibrosis	3	3.61	3.46	2.38	4.26
M	60	Cirrhosis	1.72	2	2	3.21	3.69
M	61	Cirrhosis	2.38	2.92	2.87	x.xx	4.51
M	59	Cirrhosis	3	3.65	3.54	x.xx	4.23
F	54	Cirrhosis	2.6	3.14	3	x.xx	4.6

M: male; F: female; ARFI: acoustic radiation force impulse; HCC: hepatocellular carcinoma; SWV: shear wave velocity; RFA: radiofrequency ablation; VTI: virtual touch tissue imaging; *unit in cm; **unit in m/sec.

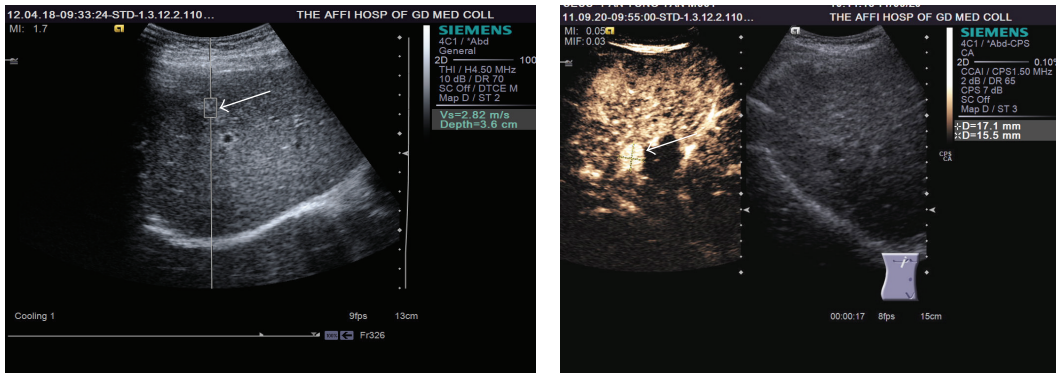

(a) (b)

Figure 4: (a): Virtual touch tissue quantification (VTQ) in a HCC residual tumor area (arrow) after RFA with a shear wave velocity of 2.82 m/s. (b): CEUS image of the same residual tumor. Left part of lesion with residual tumor (arrow) shows enhancement after contrast injection whereas contrast perfusion cannot be observed in the completely ablated area. The border between residual tumor area and complete ablation area can be displayed clearly by CEUS.

Table 2: The ARFI results comparison between the 14 residual tumors and 69 complete ablated sites.

	n	VTI before RFA size (cm)	VTI after RFA size (cm)	Tumors site before RFA SWV (m/s)	Liver parenchyma tissue SWV (m/s)
Completely ablated tumors	69	$2.93 \pm 0.56^{\S}$	$4.19 \pm 0.63^{\S}$	$2.45 \pm 0.54^{\S}$	$2.01 \pm 0.55^{*}$
Lesions with residual tumor	14	$3.03 \pm 0.53^{\S}$	$3.91 \pm 0.46^{\S}$	$2.31 \pm 0.57^{\S}$	$2.65 \pm 0.45^{*}$

§Indicates no significant difference between the two groups ($P > 0.05$).
*Indicates significant difference between the two groups ($P < 0.05$).

from CEUS, and show a larger measurement than those obtained from the conventional B mode ultrasound. It has been previously reported that CEUS shows larger HCC size than conventional US measurement [26].

Our study suggested VTI could not distinguish between tumor residuals and complete ablation. This is consistent with results reported by Fahey et al. [27]. Kwon et al. [13] reported completely ablated lesion had VTQ value of x.xx. The 62/83 (74.7%) completely ablated lesions in our study agreed with Kwon et al's report, all showing x.xx measurement. With the 14 residual tumor lesions, 6 residual lesions also had a VTQ value of x.xx, another 8 lesions demonstrated measurable values. It is possible that the measurable SWV value may be partially due to the sampling frame of ROI being relatively large and may sample both residual tumor and necrotic tissues. Our results suggest that a post-RFA VTQ of measurable elasticity values indicates residual tumors, while a x.xx measurement cannot guarantee a complete ablation.

Our study demonstrated that liver cirrhosis was associated with decreased chance of a complete ablation of HCC. With the normal liver parenchyma, liver fibrosis, or cirrhosis, the ablation sizes were 4.17 ± 0.74 (cm), 4.16 ± 0.60 (cm), and 4.07 ± 0.50 (cm), respectively, representing a significant decreasing trend. 9 residual tumors occurred in liver cirrhosis subjects (9/27, 33.3%), 5 residual tumors occurred in liver fibrosis subjects (5/44, 11.4%), while there was no residual tumor in the normal liver parenchyma subjects (0/12). In a recent study by Kang et al. [17], the correlation between RFA extent and hepatic parenchymal SWV was evaluated. It was shown that a highly significant negative correlation between parenchymal mean SWV and RFA extent. The results showed the higher the parenchymal SWV, which indicates hepatic fibrosis, the smaller the RFA extent, which indicates decreasing RFA efficacy. Therefore the parenchymal SWV measured by ARFI is an important parameter in the prediction of RFA treatment extent. Kang et al. suggested if the peritumoral SWV is higher than the cut-off value 2.41, multiple session of RFA may be needed to ablate the tumor with free safe margin [17].

There are a number of limitations for the current study. The major weak point of this study is that the measured stiffness on ARFI imaging was not correlated with real stiffness determined by histopathological examination. Patients with limitations of ARFI application were excluded from the study, such as those tumors located too deep (>8 cm). Additionally, we did not link the ARFI or CEUS results to the survival data. Out of the 14 residual tumor lesions, CEUS missed one lesion with residual tumor and reported two false positive residual tumors. These results suggested CEUS was slightly inferior in assessing residual tumor after RFA than contrast enhanced CT/MRI. This result has been recently reported by Zheng et al. [18]. Hyperenhancement in the arterial phase of CEUS lasts only few seconds so CEUS has no enough time to scrutinize the whole lesion. As a consequence, CEUS may miss some residual tumor tissue that declines from hyper to iso or hypoenhancement [18].

In conclusion, our study suggested that while VTI technique shows accurate lesion size estimation, it cannot reliably demonstrate residual tumors post RFA. All fully ablated tumors have VTQ measurement of x.xx, but VTQ results of x.xx in the ablated lesion cannot exclude residual tumor. ARFI cannot replace CEUS or CT/MRI for residual tumor assessment. Our study further confirms liver cirrhosis is associated with decreased RFA efficacy for HCC.

Conflict of Interests

The authors declare that there is no conflict of interests regarding the publication of this paper.

References

[1] K. Y. Tam, K. C.-F. Leung, and Y.-X. J. Wang, "Chemoembolization agents for cancer treatment," *European Journal of Pharmaceutical Sciences*, vol. 44, no. 1-2, pp. 1–10, 2011.

[2] S. McDermott and D. A. Gervais, "Radiofrequency ablation of liver tumors," *Seminars in Interventional Radiology*, vol. 30, no. 1, pp. 49–55, 2013.

[3] J. Bruix and M. Sherman, "Management of hepatocellular carcinoma: an update," *Hepatology*, vol. 53, no. 3, pp. 1020–1022, 2011.

[4] T. Livraghi, F. Meloni, M. di Stasi et al., "Sustained complete response and complications rates after radiofrequency ablation of very early hepatocellular carcinoma in cirrhosis: is resection still the treatment of choice?" *Hepatology*, vol. 47, no. 1, pp. 82–89, 2008.

[5] L. Tiong and G. J. Maddern, "Systematic review and meta-analysis of survival and disease recurrence after radiofrequency ablation for hepatocellular carcinoma," *British Journal of Surgery*, vol. 98, no. 9, pp. 1210–1224, 2011.

[6] J. Wu, W. Yang, S. Yin et al., "Role of contrast-enhanced ultrasonography in percutaneous radiofrequency ablation of liver metastases and efficacy evaluation," *Chinese Journal of Cancer Research*, vol. 25, no. 2, pp. 143–154, 2013.

[7] W. He, W. Wang, P. Zhou et al., "Enhanced ablation of high intensity focused ultrasound with microbubbles: an experimental study on rabbit hepatic VX2 tumors," *CardioVascular and Interventional Radiology*, vol. 34, no. 5, pp. 1050–1057, 2011.

[8] M. Westwood, M. Joore, J. Grutters et al., "Contrast-enhanced ultrasound using SonoVue (sulphur hexafluoride microbubbles) compared with contrast-enhanced computed tomography and contrast-enhanced magnetic resonance imaging for the characterisation of focal liver lesions and detection of liver metastases: a systematic review and cost-effectiveness analysis," *Health Technology Assessment*, vol. 17, no. 16, pp. 1–243, 2013.

[9] M. D'Onofrio, S. Crosara, R. de Robertis et al., "Acoustic radiation force impulse of the liver," *World Journal of Gastroenterology*, vol. 19, no. 30, pp. 4841–4849, 2013.

[10] V. Salvatore and L. Bolondi, "Clinical impact of ultrasound-related techniques on the diagnosis of focal liver lesions," *Liver Cancer*, vol. 1, no. 3-4, pp. 238–246, 2012.

[11] L. Mearini, "High intensity focused ultrasound, liver disease and bridging therapy," *World Journal of Gastroenterology*, vol. 19, no. 43, pp. 7494–7499, 2013.

[12] A. Gallotti, M. D'Onofrio, and R. P. Mucelli, "Acoustic Radiation Force Impulse (ARFI) technique in ultrasound with Virtual Touch tissue quantification of the upper abdomen," *La Radiologia Medica*, vol. 115, no. 6, pp. 889–897, 2010.

[13] H.-J. Kwon, M.-J. Kang, J.-H. Cho et al., "Acoustic radiation force impulse elastography for hepatocellular carcinoma-associated radiofrequency ablation," *World Journal of Gastroenterology*, vol. 17, no. 14, pp. 1874–1878, 2011.

[14] Y. F. Zhang, H. X. Xu, He et al., "Virtual touch tissue quantification of acoustic radiation force impulse: a new ultrasound elastic imaging in the diagnosis of thyroid nodules," *PLoS ONE*, vol. 7, Article ID e49094, 2012.

[15] L.-H. Guo, H.-X. Xu, H.-J. Fu, A. Peng, Y.-F. Zhang, and L. N. Liu, "Acoustic radiation force impulse imaging for noninvasive evaluation of renal parenchyma elasticity: preliminary findings," *PLoS ONE*, vol. 8, Article ID e68925, 2013.

[16] J. Chen, X. Xu, H. Xu, and H. Zhou, "Visualization of radiofrequency ablation treated lesions on bovine liver ex vivo using acoustic radiation force impulse elastography," *Journal of Clinical Ultrasound in Medicine*, vol. 15, pp. 145–148, 2013 (Chinese).

[17] J. Kang, H. Kwon, J. Cho et al., "Comparative study of shear wave velocities using acoustic radiation force impulse technology in hepatocellular carcinoma: the extent of radiofrequency ablation," *Gut Liver*, vol. 6, no. 3, pp. 362–367, 2012.

[18] S.-G. Zheng, H.-X. Xu, M.-D. Lu et al., "Role of contrast-enhanced ultrasound in follow-up assessment after ablation for hepatocellular carcinoma," *World Journal of Gastroenterology*, vol. 19, no. 6, pp. 855–865, 2013.

[19] H.-X. Xu, M.-D. Lu, X.-H. Xie et al., "Treatment response evaluation with three-dimensional contrast-enhanced ultrasound for liver cancer after local therapies," *European Journal of Radiology*, vol. 76, no. 1, pp. 81–88, 2010.

[20] S.-G. Zheng, H.-X. Xu, and L.-N. Liu, "Management of hepatocellular carcinoma: the role of contrast-enhanced ultrasound," *World Journal of Radiology*, vol. 6, no. 1, pp. 7–14, 2014.

[21] L. Romanini, M. Passamonti, L. Aiani et al., "Economic assessment of contrast-enhanced ultrasonography for evaluation of focal liver lesions: a multicentre Italian experience," *European Radiology Supplement*, vol. 17, no. 6, pp. 99–106, 2007.

[22] R. Lencioni and J. M. Llovet, "Modified recist (mRECIST) assessment for hepatocellular carcinoma," *Seminars in Liver Disease*, vol. 30, no. 1, pp. 52–60, 2010.

[23] A. Forner, C. Ayuso, M. Varela et al., "Evaluation of tumor response after locoregional therapies in hepatocellular carcinoma: are response evaluation criteria in solid tumors reliable?" *Cancer*, vol. 115, no. 3, pp. 616–623, 2009.

[24] C. K. Kim, D. Choi, H. K. Lim et al., "Therapeutic response assessment of percutaneous radiofrequency ablation for hepatocellular carcinoma: utility of contrast-enhanced agent detection imaging," *European Journal of Radiology*, vol. 56, no. 1, pp. 66–73, 2005.

[25] P. Ricci, V. Cantisani, F. Drudi et al., "Is contrast-enhanced US alternative to spiral CT in the assessment of treatment outcome of radiofrequency ablation in hepatocellular carcinoma?" *Ultraschall in der Medizin*, vol. 30, no. 3, pp. 252–258, 2009.

[26] M. H. Chen, W. Yang, K. Yan et al., "The role of contrast-enhanced ultrasound in planning treatment protocols for hepatocellular carcinoma before radiofrequency ablation," *Clinical Radiology*, vol. 62, no. 8, pp. 752–760, 2007.

[27] B. J. Fahey, R. C. Nelson, D. P. Bradway, S. J. Hsu, D. M. Dumont, and G. E. Trahey, "In vivo visualization of abdominal malignancies with acoustic radiation force elastography," *Physics in Medicine and Biology*, vol. 53, no. 1, pp. 279–293, 2008.

Hindawi Publishing Corporation
BioMed Research International
Volume 2014, Article ID 218578, 9 pages
http://dx.doi.org/10.1155/2014/218578

Research Article

Early Monitoring Antiangiogenesis Treatment Response of Sunitinib in U87MG Tumor Xenograft by ^{18}F-FLT MicroPET/CT Imaging

Xiao Bao,[1,2,3] Ming-Wei Wang,[1,2,3] Yong-Ping Zhang,[1,2,3] and Ying-Jian Zhang[1,2,3]

[1] *Department of Nuclear Medicine, Fudan University Shanghai Cancer Center, Shanghai 200032, China*
[2] *Department of Oncology, Shanghai Medical College, Fudan University, Shanghai 200032, China*
[3] *Center for Biomedical Imaging, Fudan University, Shanghai 200032, China*

Correspondence should be addressed to Ying-Jian Zhang; yjzhang111@aliyun.com

Received 13 February 2014; Accepted 19 March 2014; Published 9 April 2014

Academic Editor: Sophie Laurent

Aim. It was aimed to monitor early treatment response of Sunitinib in U87MG models mimicking glioblastoma multiforme by longitudinal ^{18}F-FLT microPET/CT imaging in this study. *Methods*. U87MG tumor mice were intragastrically injected with Sunitinib at a dose of 80 mg/kg for consecutive 7 days. ^{18}F-FLT microPET/CT scans were acquired on days 0, 1, 3, 7, and 13 after therapy. Tumor sizes and body weight were measured. Tumor samples were collected for immunohistochemical analysis of proliferation and microvessel density (MVD) with anti-Ki67 and anti-CD31, respectively. *Results*. The uptake ratios of tumor to the contralateral muscle (T/M) of ^{18}F-FLT in the Sunitinib group decreased from baseline to day 3 ($T/M_0 = 2.98 \pm 0.33$; $T/M_3 = 2.23 \pm 0.36$; $P < 0.001$), reached the bottom on day 7 ($T/M_7 = 1.96 \pm 0.35$; $P < 0.001$), and then recovered on day 13. The T/M of ^{18}F-FLT uptake in the control group remained around 3.0. There was no difference for the tumor size between both groups until day 11. ^{18}F-FLT uptakes of tumor were correlated with Ki67 staining index and MVD. *Conclusion*. Early therapy response to Sunitinib could be predicted via ^{18}F-FLT PET, which will contribute to monitoring antiangiogenesis treatment.

1. Introduction

Angiogenesis is a fundamental physiological process to form new blood vessel to support cancer growth and development by providing nutrients and oxygen. It occurs for almost all solid tumors such as glioblastoma (GBM) and thus antiangiogenesis therapeutics are increasingly applied to treat various cancers. GBM is the most aggressive primary malignant brain tumor in humans with a 5-year survival rate under 5% and median overall survival of only 12–14 months [1]. GBM features rich vascularization due to the high expression of various proangiogenic factors, which makes antiangiogenesis as an attractively newly emerging targeted therapy strategy of GBM, although the standard treatments of GBM are still surgical operation, radiotherapy, and chemotherapy at present [2]. For instance, vascular endothelial growth factor inhibitor, bevacizumab, has been the sole antiangiogenesis targeted therapeutic licensed by the FDA for use in GBM [3]. In order to discover more effective anticancer agents, multitargeted tyrosine kinase inhibitors (TKIs), such as Sunitinib, are being under clinical investigations owing to their antitumor capabilities via the pathways of antiangiogenesis as well as antiproliferation [4]. Sunitinib as antiangiogenic therapeutic has already been used to treat renal carcinoma, gastrointestinal stromal tumors, lung cancer, and other solid tumors [5, 6]; however, it showed controversial value in primary or recurrent GBM therapy [7–9]. Moreover, antiangiogenic treatment faces currently some other challenges, such as low objective response rate and a huge economic burden of the high price [4, 10]. Since TKIs are predominant cytostatic therapeutics rather than cytotoxic therapeutics, decrease in tumor size caused by TKIs therapy might take 3–6 months or might not always occur [11, 12]. As results, conventional methods relying on tumor size changes, that is, response evaluation criteria in solid tumors (RECIST) is insufficient and even inappropriate for the response evaluation by monitoring the variation of tumor size after targeted therapies. Notably and importantly, size-based treatment evaluation is unable

to discriminate residual viable tumor tissue from fibrosis. In contrast, molecular imaging by PET/CT with specific functional probes can visualize and evaluate biological and metabolic activity status of tumor cells [13]. So far, ^{18}F-FDG PET/CT as the core role of PET response evaluation criteria in solid tumors (PERCIST) has been successfully used for monitoring early response of cytotoxic chemotherapy. However, it showed some limitations for ^{18}F-FDG PET/CT to follow the therapy efficacy of antiangiogenesis due to the nonspecific uptake in benign tissues [14–16]. Therefore, it is in great demand to develop an alternative molecular imaging method using suitable PET probes for the early effective therapy evaluation of targeted treatment.

Beyond ^{18}F-FDG, 3′-deoxy-3′-^{18}F-fluorothymidine (^{18}F-FLT) is another widely used PET molecular imaging probe in preclinical and clinical studies and has presented its superiority to predict early therapeutic response of cancers due to its unique cell uptake mechanism involved in DNA synthesis pathway via thymidine kinase-1. ^{18}F-FLT is a radiolabeled nucleoside analogue and is generally used to image cell proliferation by PET/CT for tumor detection and grade. Moreover, previous studies had already shown that ^{18}F-FLT PET/CT played a clinically useful role for predicting treatment response of cytotoxic chemotherapy and radiotherapy [17–20]. However, ^{18}F-FLT PET/CT as response biomarker for cytostatic therapeutics of antiangiogenesis has not been fully proved and is still without universal understanding according to current publications [14, 15]. Consequently, more efforts are needed to further confirm the potential of ^{18}F-FLT PET/CT in monitoring early response to antiangiogenic agents [21]. In the current study, we proposed to investigate the feasibility of ^{18}F-FLT PET/CT to monitor early treatment response of antiangiogenesis via Sunitinib in a xenograft U87MG tumor model mimicking GBM.

2. Materials and Methods

2.1. Cell Lines and Tumor Models. The human glioblastoma multiforme cell line U87MG was purchased from Cell Bank, Shanghai Institutes for Biological Sciences, Chinese Academy of Sciences, and grown in DMEM medium (Gibco) supplemented with 10% fetal bovine serum and 1% penicillin/streptomycin (P/S) under a humidified 5% CO_2 atmosphere at 37°C. The cells were collected by trypsinization with 0.25% trypsin/EDTA. Female athymic Balb/c nude mice (4–6 weeks) were obtained from Department of Laboratory Animal Science, Fudan University, and allowed to acclimatize for one week in the animal facility before any intervention was initiated. The U87MG tumor model was generated by subcutaneous injection of 5×10^6 tumor cells in the right shoulders of the mice. Caliper measurements of perpendicular axes of the tumor were performed to follow up tumor growth. The mice weight was also measured. The treatment was initiated when the tumor reached a diameter between 8.0 and 12.0 mm (3-4 weeks after inoculation).

2.2. Experimental Design. Table 1 demonstrated the experimental design in this study. Mice were randomized into two major groups: the imaging group ($n = 10$) and the immunohistochemical (IHC) staining group ($n = 27$). The main purpose of using additional group mice for the IHC staining was to ensure the accuracy of the data in IHC group and not disrupt the consistency in the imaging group. Each major group was then divided into Sunitinib treatment group and control group. The treatment group was intragastrically administrated with Sunitinib (Dalian Melone Pharmaceutical Co., Ltd.) at a dose of 80 mg/kg for consecutive 7 days while the control group received oral administration of vehicle alone. Sunitinib was suspended in carboxymethylcellulose (CMC) solution (CMC 5%, NaCl 1.8%, Tween 80 0.4%, and benzyl alcohol 0.9% in distillated water). The imaging group was scanned with ^{18}F-FLT microPET/CT on days 0, 1, 3, 7, and 13 after therapy initiation. Mice in the IHC staining group were sacrificed on corresponding imaging time points for IHC analysis. There were up to 3 mice sacrificed in Sunitinib and control groups, respectively, on each time point. Tumor dimensions and mice body weight were measured every other day to follow up tumor growth. The tumor volume was calculated from the following formula: tumor volume = $a \times (b^2)/2$, where a and b represent the tumor length and width, respectively.

Table 1: Experimental design for longitudinal ^{18}F-FLT microPET/CT imaging of Sunitinib treatment efficacy.

Parameter	Day								
	0	1	2	3	4	5	6	7	13
^{18}F-FLT									
Sunitinib	√	+ √	+	+ √	+	+	+	+ √	√
Control	√	+ √	+	+ √	+	+	+	+ √	√
Histology									
Sunitinib	×	+ ×	+	+ ×	+	+	+	+ ×	×
Control	×	+ ×	+	+ ×	+	+	+	+ ×	×

√: microPET/CT; +: vehicle or Sunitinib treatment; ×: tumor sampling.

2.3. MicroPET/CT Imaging. MicroPET/CT scans and image analysis were performed using an Inveon microPET/CT (Siemens Medical Solution). Each U87MG tumor-bearing mouse was injected with 11.1 MBq (300 μCi) of ^{18}F-FLT via tail vein. Ten-minute static scans were acquired at 1.0 h after injection and animals were maintained under isoflurane anesthesia during scanning period. The images were reconstructed using three-dimensional ordered-subset expectation maximization (OSEM3D)/maximum algorithm. For each microPET/CT scan, 4.0 mm diameter spherical regions of interest (ROIs) were drawn over both the tumor and the contralateral muscle on decay-corrected images using Inveon Research Workplace to obtain percentage injected dose per gram (%ID/g) and standardized uptake values (SUV). The highest uptake point of entire tumor was included in ROI and no necrosis area was allowed. The mean %ID/g (%ID/g_{mean}), maximal %ID/g (%ID/g_{max}), mean SUV (SUV_{mean}), and maximal SUV (SUV_{max}) were measured. Additionally, the ratio of %ID/g_{max} of tumor to the contralateral muscle (T/M) was calculated.

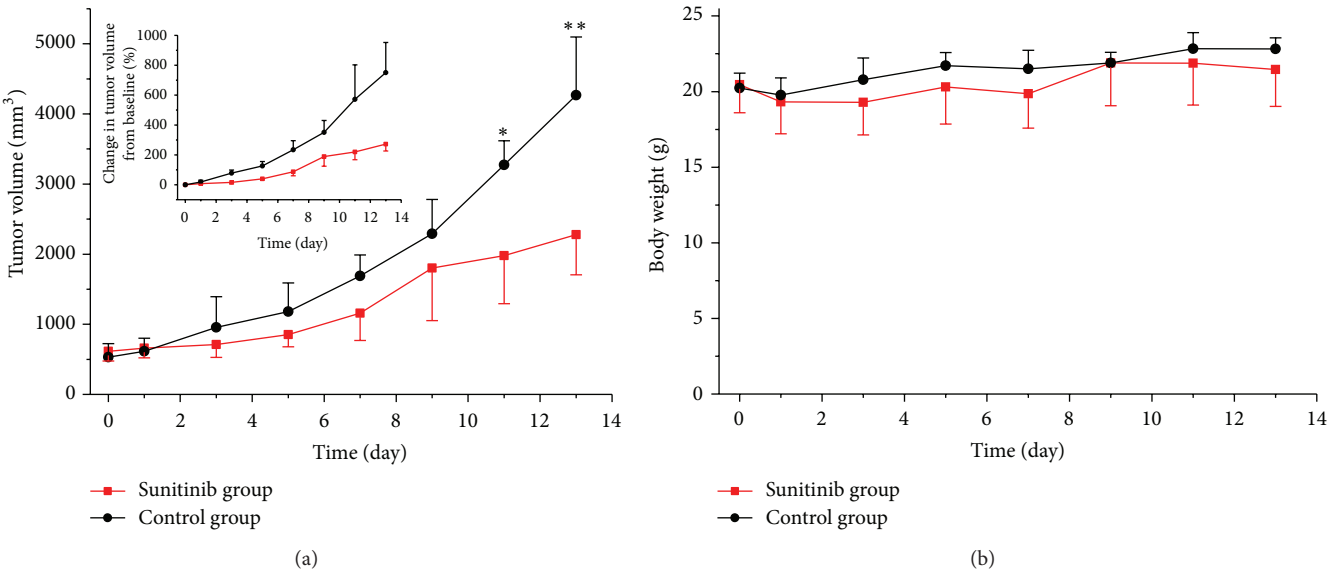

Figure 1: Antitumor activity of Sunitinib in U87MG xenografts. (a) Tumor volume or $(V - V_0)/V_0$ of U87MG tumor-bearing mice treated with vehicle or Sunitinib. There was significant difference for the tumor size between the Sunitinib group and control group after day 11 ($P = 0.015$). (b) Body weight of U87MG tumor-bearing mice treated with vehicle or Sunitinib. There was no difference for the mice weight between the Sunitinib group and control group. $^*P < 0.05$ and $^{**}P < 0.01$.

2.4. Immunohistochemistry and Histology. On days 0, 1, 3, 7, and 13 after therapy initiation, in order to minish the sampling error of IHC staining, three U87MG tumor-bearing mice in each group were sacrificed and tumor samples were collected to fix in 10% formalin neutral buffer solution for paraffin embedding. Paraffin-embedded tissues were cut into 4 μm sections and stained with mouse anti-human Ki67 antibody (1 : 100, Abcam) and rat anti-mouse anti-CD31 (Abcam). Endogenous peroxidase activity was blocked with 3% H_2O_2 for 15 min. Antigen retrieval was performed by boiling the sections for 10 min in citrate buffer (pH 6.0) and cooling at room temperature, followed by blocking with 10% normal goat serum for 1.0 h. The sections were incubated with optimal dilutions of anti-Ki67 and anti-CD31 overnight at 4°C, and then $Ki67^+$ cells and $CD31^+$ areas were detected with horseradish peroxidase- (HRP-) conjugated anti-mouse/rat secondary antibodies using an EnViSion Detection kit (Gene Tech Co., Ltd., Shanghai, China). After washing with PBS three times for 5.0 min each time, the immune complexes were visualized using a Peroxidase Substrate DAB kit (Gene Tech Co., Ltd., Shanghai, China) according to the manufacturer's instructions. Finally, the slices were counterstained with hematoxylin and dehydrated. $Ki67^+$ cells and $CD31^+$ areas were counted on 4 randomly selected visual fields per section of each sample under high power.

2.5. Immunohistochemistry Analysis. Adobe Photoshop CS5 software was used to assess the total number of Ki67-positive cells and CD31-positive vessels. The Ki67 staining index (SI) was defined as the percentage of positive nuclei in relation to the total number of nuclei. CD31-positive vessels counting method was modified from the protocol described by Weidner et al. [22]. Microvessel density (MVD) was assessed by light microscopy in areas containing the highest numbers of CD31-positive vessels per area (neovascular "hot spots") [22]. All stained endothelial cells or cell clusters were counted as one microvessel. When two or more positive foci seemed to belong to a single continuous vessel, they were counted as one microvessel. Vessel lumens were not essential. For each section, individual microvessel counts were made on four randomly high-powered fields at 200x magnification. MVD count was defined as the average of the vessel numbers on the 4 fields.

2.6. Statistical Analysis. Quantitative data were presented as mean ± SD. One way analysis of variance was used to compare groups of two by SPSS 16.0. P values <0.05 were considered statistically significant.

3. Results

3.1. Sunitinib Treatment Inhibited U87MG Tumor Growth. As expected, intragastrical administration of consecutive 7 doses of Sunitinib (80 mg/kg) led to a delay in tumor volume. A time-related increase in tumor volume was observed in the control group (Figure 1(a)), in which the average percentage of tumor volume increases, expressed as $(V - V_0)/V_0$, were 18.5 ± 12.2%, 77.9 ± 20.8%, 234.6 ± 60.6%, and 750.6 ± 201.9% on days 1, 3, 7, and 13, respectively. As a comparison, Sunitinib treatment resulted in lower $(V - V_0)/V_0$ of 7.6 ± 4.2%, 15.9 ± 9.1%, 87.0 ± 26.7%, and 272.1 ± 45.9% on days 1, 3, 7, and 13, respectively. There was significant difference for the tumor size between the Sunitinib group and control group after day 11 ($P < 0.05$). In the treated mice, average percentage of tumor volume increase on day 9, $(V - V_0)/V_0 = 188.8 \pm 64.8\%$, was slightly above the trend line, which may be attributed to the

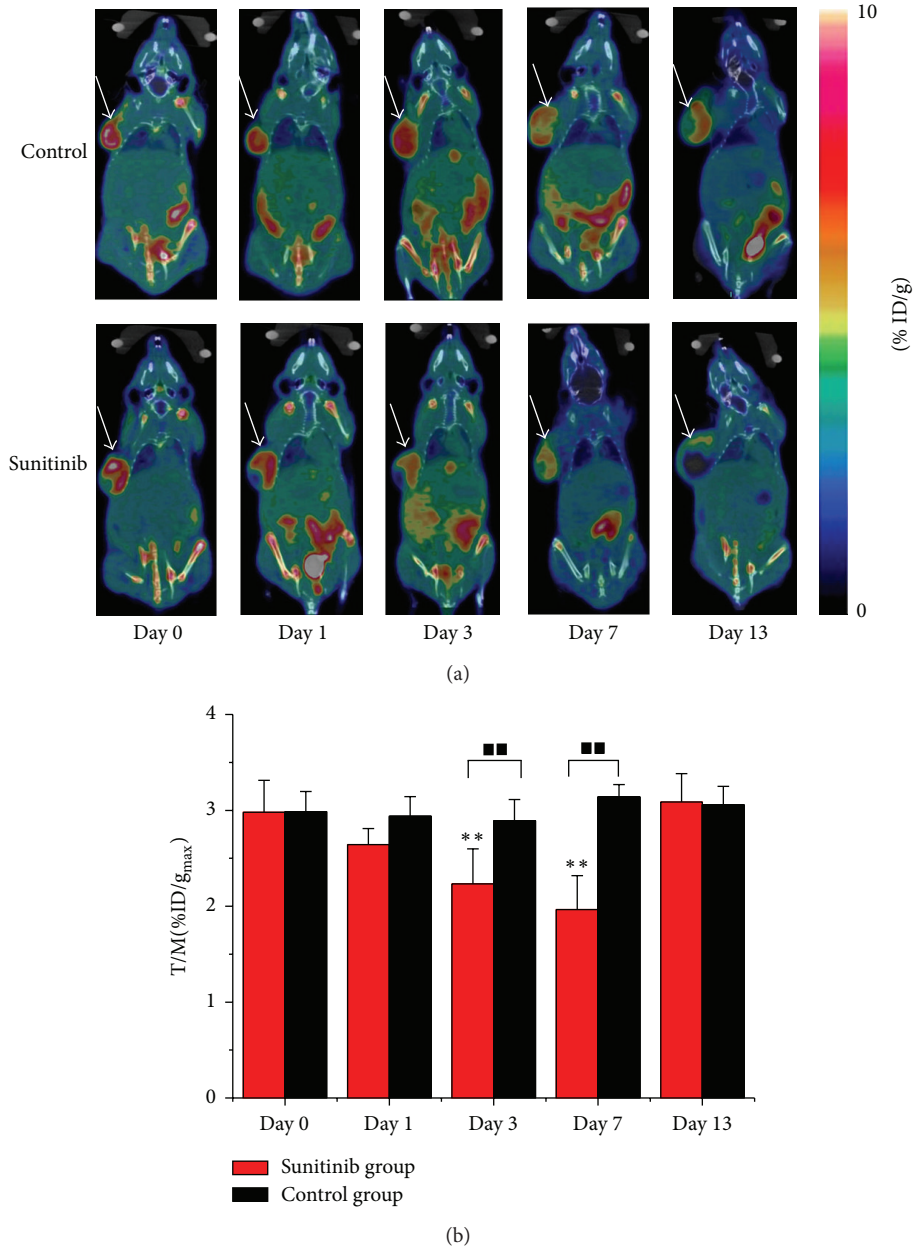

Figure 2: ^{18}F-FLT microPET/CT imaging of U87MG tumor-bearing mice. (a) Representative decay-corrected whole-body coronal microPET/CT images at 1.0 h after intravenous injection of ^{18}F-FLT (11.1 MBq per mouse) on days 0, 1, 3, 7, and 13 after treatment was initiated. (b) The ratios of %ID/g_{max} of tumor to the contralateral muscle (T/M) in the Sunitinib and control groups based on quantitative ROIs analysis from ^{18}F-FLT microPET/CT on days 0, 1, 3, 7, and 13 after treatment. The tumors are indicated by *arrows*. $^{**}P < 0.01$, within the Sunitinib group, compared to day 0. $^{\blacksquare\blacksquare}P < 0.01$, between the Sunitinib group and the control group.

rebound phenomenon that resulted from the sudden stop of Sunitinib (picture inset in Figure 1(a)). This change was also observed in a previous report [23, 24]. Mice body weight was measured as an indicator of the toxic side effects of Sunitinib. As shown in Figure 1(b), no significant body weight loss was observed during the treatment period at the dosage 80 mg/kg of Sunitinib used in this study.

3.2. Sunitinib Treatment Inhibited Tumor Cell Proliferation. Static microPET/CT scans (Figure 2(a)) at 1.0 h after injection of ^{18}F-FLT were acquired on days 0 (baseline), 1, 3, 7, and 13. Figure 2(b) described the ratios of %ID/g_{max} of tumor to the contralateral muscle (T/M) of ^{18}F-FLT in the Sunitinib and control groups. After Sunitinib treatment, the U87MG tumor uptake of ^{18}F-FLT decreased from baseline to day 3 ($T/M_0 = 2.98 \pm 0.33$, $T/M_3 = 2.23 \pm 0.36$, $P < 0.001$), rapidly reaching the bottom on day 7 when therapy stopped ($T/M_7 = 1.96 \pm 0.35$, $P < 0.001$), which represented a decrease of up to 34%. On day 13, 6 days after the withdrawal of treatment, ^{18}F-FLT uptake recovered ($T/M_{13} = 3.09 \pm 0.29$).

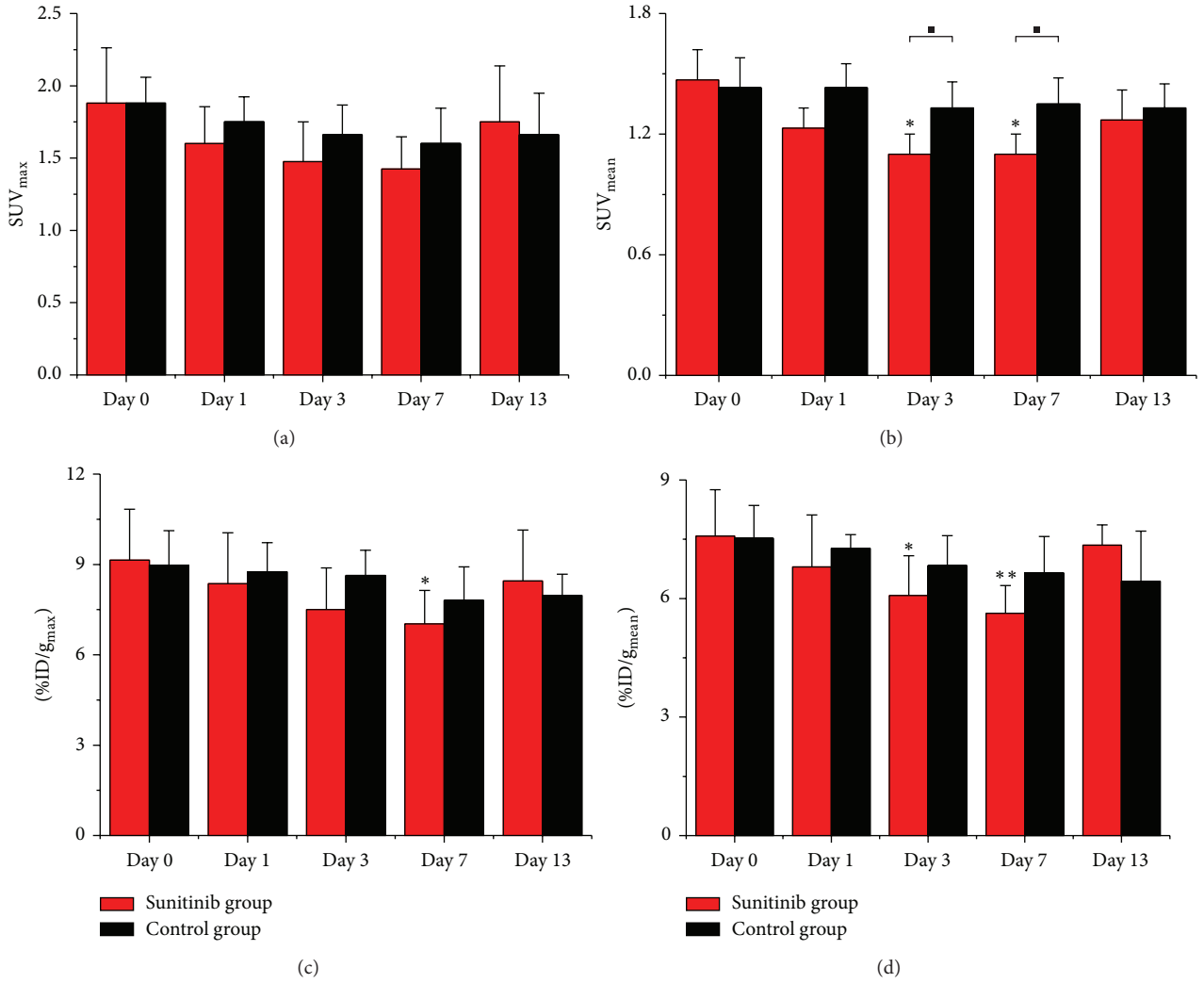

Figure 3: Quantitative ROIs analysis of tumor uptake from ^{18}F-FLT microPET/CT. ((a) SUV$_{max}$, (b) SUV$_{mean}$, (c) %ID/g$_{max}$, and (d) %ID/g$_{mean}$) $^{*}P < 0.05$ and $^{**}P < 0.01$, within the Sunitinib group, compared to day 0. $^{\blacksquare}P < 0.05$, between the Sunitinib group and the control group.

Compared to the drastic fluctuations in the Sunitinib group, T/M of ^{18}F-FLT uptake in the control group remained around 3.0 throughout the two-week study. Significant differences between the treatment group and the vehicle group were observed on days 3 and 7, where both of P values were less than 0.001.

3.3. SUV$_{mean}$, SUV$_{max}$, %ID/g$_{mean}$, and %ID/g$_{max}$. In this study, we compared 5 different parameters (SUV$_{mean}$, SUV$_{max}$, %ID/g$_{mean}$, %ID/g$_{max}$, and T/M) to choose out the most suitable evaluation criterion. No significant differences were observed between the Sunitinib group and the control group for SUV$_{max}$, %ID/g$_{mean}$, and %ID/g$_{max}$, whereas only for SUV$_{mean}$ this was observed on days 3 and 7. Within the Sunitinib group, decreases in SUV$_{mean}$ and %ID/g$_{mean}$ showed statistical differences on days 3 and 7, compared to the baseline (day 0), while decreases in %ID/g$_{max}$ only revealed significant differences on day 3 (Figures 3(a)–3(d)).

3.4. Immunohistochemistry and Histology. Figure 4 shows representative tumor sections of haematoxylin and eosin (H&E), CD31, and Ki-67 staining for the control and Sunitinib groups on days 0, 1, 3, 7, and 13 after therapy. CD31-positive staining was broadly observed in all untreated tumor sections, which demonstrated relatively abundant microvessel density (MVD). After Sunitinib treatment, the MVD level in tumor sections decreased remarkably, which indicated effective antiangiogenic activity of the drug. The MVD level lowered to 36.33 ± 3.64% on day 1 after therapy, compared with that of the vehicle group (61.88 ± 0.16, $P = 0.003$) and continuously declined until day 7 ($P < 0.001$) (Figure 4(e)). The Ki-67 SI showed a remarkable decrease after the initiation of treatment, which was the most pronounced one on day 3 compared with that for the control tumors ($P = 0.005$). On day 13, the Ki-67 SI returned yet to be still less than the baseline level. The untreated tumors remained with a relatively high proliferation rate with Ki67

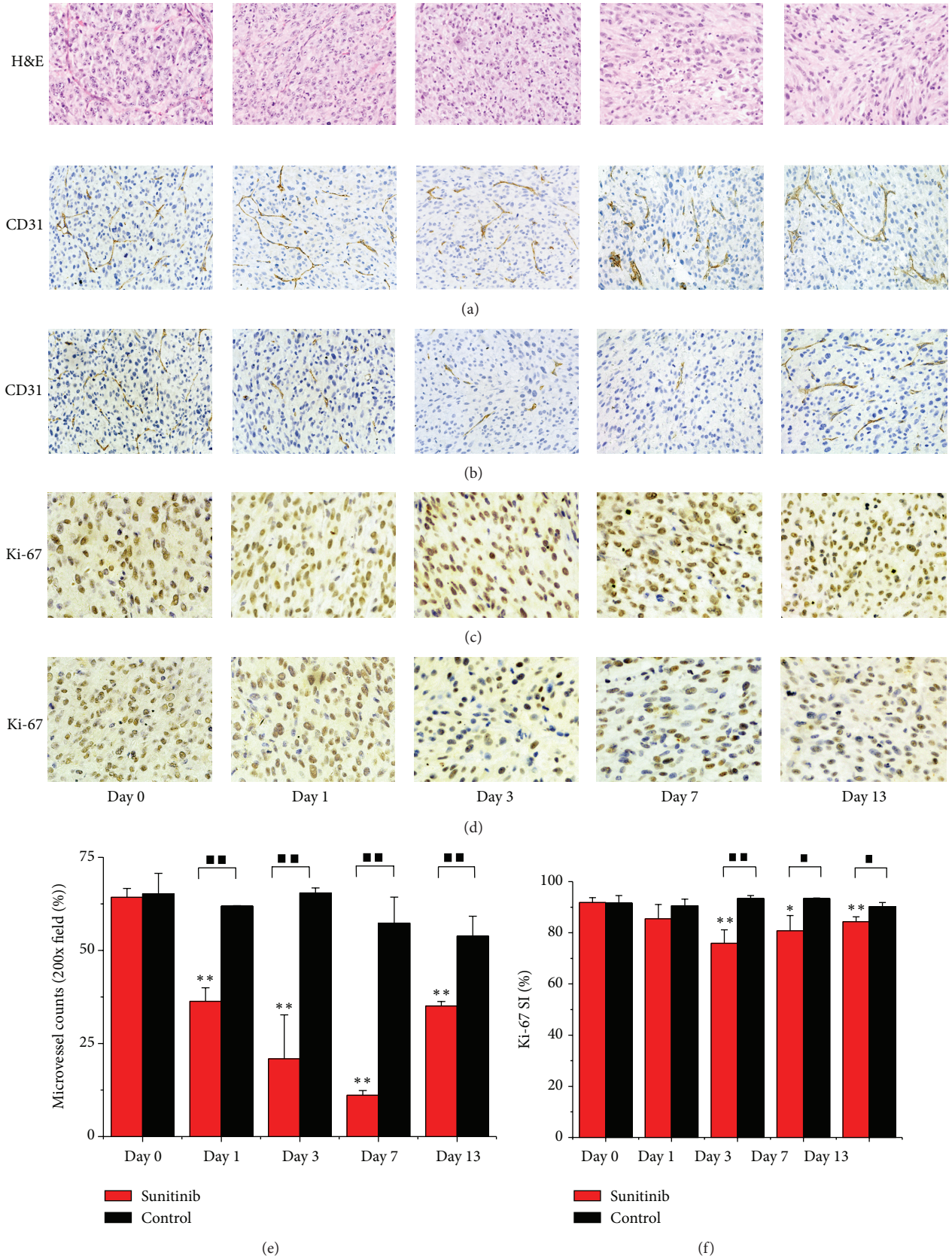

Figure 4: Continued.

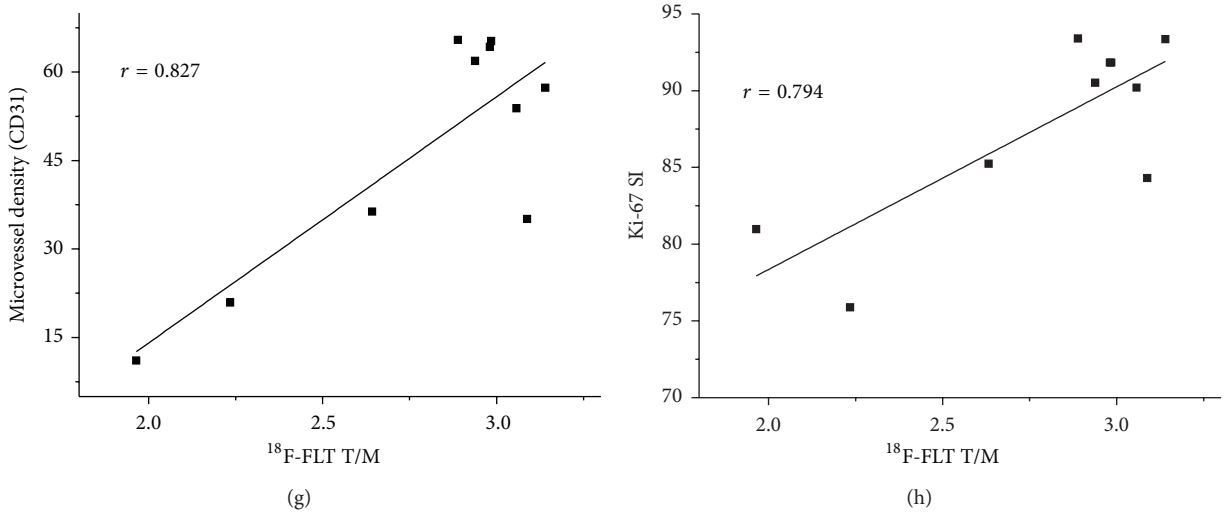

Figure 4: Immunohistochemical and histologic analysis of tumor sections about CD31, Ki67, and H&E on days 0, 1, 3, 7, and 13 after therapy. Top line showed H&E staining in the Sunitinib group. CD31 staining in the Sunitinib group revealed effective antiangiogenic activity from day 1 to day 7 ((a) control, (b) Sunitinib, and 40 × 10, (e)). Ki67 showed a remarkable decrease after the initiation of treatment, which was the most pronounced one on day 3 compared with that for the control tumors ((c) control, (d) Sunitinib, and 40 × 10, (f)). T/M of ^{18}F-FLT uptakes of tumor in the treatment group were correlated well with the quantitative data of MVD (g) and Ki67 SI (h). $^{*}P < 0.05$ and $^{**}P < 0.01$, within the Sunitinib group, compared to day 0. $^{\blacksquare}P < 0.05$ and $^{\blacksquare\blacksquare}P < 0.01$, between the Sunitinib group and the control group.

SI of more than 90% (Figure 4(f)). T/M of ^{18}F-FLT uptakes were correlated well with the quantitative data of MVD and Ki-67 SI (Figures 4(g)-4(h)).

4. Discussion

Angiogenesis, the formation of new blood vessels, has been proved to be critical in the growth and invasiveness of solid tumors, which makes antiangiogenesis become the widely used targeted therapy of cancer up to today [25]. Antiangiogenic agents include tyrosine kinase inhibitors (TKI) like Sunitinib and vascular endothelial growth factor- (VEGF-) targeted antibody Bevacizumab. Sunitinib is a multitargeted TKI which results in VEGF signaling blockade to suppress cancer cell growth. Thus, compared with the conventional cytotoxic agents, TKI may provide a more tolerable cytostatic therapy against solid tumors with diverse histology, either as monotherapy or in combination with radiation and/or additional chemotherapy [26]. Various TKI agents, such as SU11248 (Sunitinib), Bevacizumab, and GW786034 (Pazopanib), have been approved by FDA for clinical applications [27–30]. Single-agent TKIs have low objective rates of response, which are usually less than 50% in the selected patients [10, 31]. Therefore, noninvasive visualization and quantification of antitumor and antiangiogenesis potency would be of importance for patient selection, dosage optimization, and dose intervals of compounds in this category [16]. Herein, we aimed to monitor antiangiogenic treatment response of Sunitinib in U87MG tumor xenografts mimicking GBM by dynamic ^{18}F-FLT microPET/CT imaging in this study.

Our longitudinal study proved the value of quantitative ^{18}F-FLT PET/CT imaging in monitoring early response to the antiangiogenic therapy (ATT) of Sunitinib in U87MG tumor xenografts. In the Sunitinib treatment group, the ratio of %ID/g_{max} of tumor to the contralateral muscle (T/M) of ^{18}F-FLT decreased by 25% on day 3 and by 34% on day 7, whereas T/M in the control group remained around the baseline level throughout the study. It was beyond our expectation that another 4 parameters (SUV_{max}, SUV_{mean}, %ID/g_{mean}, and %ID/g_{max}) had not shown statistical value in this study. They were often used to evaluate therapy response in previous studies and gave rise to controversial results [14–16, 23], because they as single measured values (SUV_{mean}, SUV_{max}, %ID/g_{mean}, and %ID/g_{max}) could be influenced by various factors such as individual difference among mice, change of physical state, operation errors, and therapeutic intervention, even to the utmost extent avoiding the impact of those factors. It might remind us that the parameters beyond SUV and %ID/g could be of benefit to response evaluation. Significant difference for the tumor size between the Sunitinib group and control group was observed until day 11 according to the traditional RECIST. Quantitative ^{18}F-FLT PET/CT imaging can not only reflect the status of tumor cell proliferation but also distinguish residual viable tumor tissue from fibrosis [13]. For example, Figure 2(a) showed a large necrosis area without ^{18}F-FLT uptake in Sunitinib-treated tumors on day 13. Although tumor sizes in untreated group were larger than that in Sunitinib-treated group, it yet displayed uniform tumor uptake of ^{18}F-FLT without remarkable necrosis area, which further illustrated the ATT effects of Sunitinib. This was also validated by the decrease of Ki67 SI and MVD after therapy initiation.

There have been several reports about the use of various PET tracers to predict ATT efficacy of TKIs in solid tumors [16, 23, 32, 33]. For example, Battle et al. used ^{18}F-Fluciclatide

to detect the therapeutic response after a 2-week dosing regimen (60 mg/kg) of Sunitinib in U87MG tumors [23]. They found that the uptake level of ^{18}F-Fluciclatide in tumor sites from the Sunitinib-treated group immediately decreased on day 2, and a level of MVD expression was observed on day 13 significantly lower than that in control animals. However, ^{18}F-Fluciclatide as a new PET biomarker is without easy accessibility at present and another limitation of their study was not to compare longitudinal MVD level due to the lack of histopathologic data from tumor samples at early time points. Morrison et al. applied ^{18}F-AH111585 to monitor ZD4190 therapy response of Calu-6 nonsmall cell lung tumor xenografts [32]. A significant decrease (31.8%) in ^{18}F-AH111585 uptake was discovered, which proved that ^{18}F-labeled RGD tracer could noninvasively monitor the antiangiogenic effect of ZD41190. Yang et al. established MDA-MB-435 breast cancer xenografts and evaluated the early response to ZD4190 by ^{18}F-FDG, ^{18}F-FLT, and ^{18}F-FPPRGD2 [16]. In ZD4190-treated tumors, the uptake of ^{18}F-FLT decreased by 8.1% on day 1 and by 21% on day 3, which was confirmed by Ki67 SI. However, ^{18}F-FDG uptake in tumors with or without treatment showed no significant difference, even increasing slightly in ZD4190-treated tumors on day 3. The uptake of ^{18}F-FDG in inflammatory cells may lead to an overestimation of the viable tumor cells. In contrast, ^{18}F-FLT uptake would be less disturbed by the inflammatory response because inflammatory cells have only minor proliferation tendency [34]. They found that ^{18}F-FPPRGD2 PET/CT imaging showed lower background and higher tumor/muscle ratio compared with ^{18}F-FLT imaging, and the magnitude of the changes in tumor uptake of ^{18}F-FPPRGD2 was also higher than that of ^{18}F-FLT. As a result, they considered that ^{18}F-FPPRGD2 would be superior to ^{18}F-FLT as a PET probe for predicting the early response of tumor to ZD4190. Nevertheless, ^{18}F-FPPRGD2 has not been put into the clinical application due to its complicated synthesis steps and relatively low radiochemical yield. ^{18}F-Fluciclatide and ^{18}F-AH111585 faced also the same kind of limitations as those of ^{18}F-FPPRGD2 under current conditions. Therefore, ^{18}F-FLT, a well-established PET molecular imaging probe, was selected to monitor treatment response of Sunitinib in U87MG xenografts in our study. At last, our results proved the great potential value of ^{18}F-FLT PET/CT imaging protocol for monitoring the early response of Sunitinib.

5. Conclusions

We investigated the feasibility of longitudinal ^{18}F-FLT PET/CT to monitor the early response of antiangiogenesis therapy of Sunitinib in U87MG xenografts. This protocol could be easily translated into clinical trials and make contribution to treatment plan of antiangiogenesis treatment in the future.

Abbreviations

GBM: Glioblastoma multiforme
ATT: Antiangiogenic therapy
TKIs: Tyrosine kinase inhibitors
RECIST: Response evaluation criteria in solid tumors
PERCIST: PET response evaluation criteria in solid tumors
VEGF: Vascular endothelial growth factor
MVD: Microvessel density
SPSS: Statistical package for the social science.

Conflict of Interests

The authors declare that there is no conflict of interests related to this work.

Authors' Contribution

Xiao Bao and Ming-Wei Wang contributed equally to this paper.

Acknowledgment

This study was partly supported by National Natural Science Foundation of China (Grants no. 11275050 and no. 30700188).

References

[1] J. de Groot and V. Milano, "Improving the prognosis for patients with glioblastoma: the rationale for targeting Src," *Journal of Neuro-Oncology*, vol. 95, no. 2, pp. 151–163, 2009.

[2] E. R. Gerstner and T. T. Batchelor, "Antiangiogenic therapy for glioblastoma," *Cancer Journal*, vol. 18, no. 1, pp. 45–50, 2012.

[3] M. A. Jarzabek, K. J. Sweeney, R. L. Evans et al., "Molecular imaging in the development of a novel treatment paradigm for glioblastoma (GBM): an integrated multidisciplinary commentary," *Drug Discovery Today*, vol. 18, no. 21-22, pp. 1052–1066, 2013.

[4] C. Sessa, A. Guibal, G. Del Conte, and C. Rüegg, "Biomarkers of angiogenesis for the development of antiangiogenic therapies in oncology: tools or decorations?" *Nature Clinical Practice Oncology*, vol. 5, no. 7, pp. 378–391, 2008.

[5] M. Ayala-Ramirez, C. N. Chougnet, M. A. Habra et al., "Treatment with sunitinib for patients with progressive metastatic pheochromocytomas and sympathetic paragangliomas," *The Journal of Clinical Endocrinology and Metabolism*, vol. 97, no. 11, pp. 4040–4050, 2012.

[6] G. Liu, R. Jeraj, M. Vanderhoek et al., "Pharmacodynamic study using FLT PET/CT in patients with renal cell cancer and other solid malignancies treated with sunitinib malate," *Clinical Cancer Research*, vol. 17, no. 24, pp. 7634–7644, 2011.

[7] P. M. Costa, A. L. Cardoso, C. Nóbrega et al., "MicroRNA-21 silencing enhances the cytotoxic effect of the antiangiogenic drug sunitinib in glioblastoma," *Human Molecular Genetics*, vol. 22, no. 5, pp. 904–918, 2013.

[8] M. Hutterer, M. Nowosielski, J. Haybaeck et al., "A single-arm phase II Austrian/German multicenter trial on continuous daily sunitinib in primary glioblastoma at first recurrence (SURGE 01-07)," *Neuro-Oncology*, vol. 16, no. 1, pp. 92–102, 2012.

[9] A. Sanchez, D. Tripathy, X. Yin, J. Luo, J. M. Martinez, and P. Grammas, "Sunitinib enhances neuronal survival in vitro

via NF-kappaB-mediated signaling and expression of cyclooxygenase-2 and inducible nitric oxide synthase," *Journal of Neuroinflammation*, vol. 10, article 93, 2013.

[10] H. van Cruijsen, A. van der Veldt, and K. Hoekman, "Tyrosine kinase inhibitors of VEGF receptors: clinical issues and remaining questions," *Frontiers in Bioscience*, vol. 14, no. 6, pp. 2248–2268, 2009.

[11] R. L. Wahl, H. Jacene, Y. Kasamon, and M. A. Lodge, "From RECIST to PERCIST: evolving considerations for PET response criteria in solid tumors," *Journal of Nuclear Medicine*, vol. 50, supplement S2, no. 1, pp. 122–150, 2009.

[12] S. D. Curran, A. U. Muellner, and L. H. Schwartz, "Imaging response assessment in oncology," *Cancer Imaging*, vol. 6, pp. S126–S130, 2006.

[13] W. A. Weber, "Use of PET for monitoring cancer therapy and for predicting outcome," *Journal of Nuclear Medicine*, vol. 46, no. 6, pp. 983–995, 2005.

[14] M. Yang, H. Gao, X. Sun et al., "Multiplexed PET probes for imaging breast cancer early response to VEGF121/rGel treatment," *Molecular Pharmaceutics*, vol. 8, no. 2, pp. 621–628, 2011.

[15] J. L. Goggi, R. Bejot, S. S. Moonshi, and K. K. Bhakoo, "Stratification of ^{18}F-labeled PET imaging agents for the assessment of antiangiogenic therapy responses in tumors," *Journal of Nuclear Medicine*, vol. 54, no. 9, pp. 1630–1636, 2013.

[16] M. Yang, H. Gao, Y. Yan et al., "PET imaging of early response to the tyrosine kinase inhibitor ZD4190," *European Journal of Nuclear Medicine and Molecular Imaging*, vol. 38, no. 7, pp. 1237–1247, 2011.

[17] N. Graf, K. Herrmann, B. Numberger et al., "[^{18}F]FLT is superior to [^{18}F]FDG for predicting early response to antiproliferative treatment in high-grade lymphoma in a dose-dependent manner," *European Journal of Nuclear Medicine and Molecular Imaging*, vol. 40, no. 1, pp. 34–43, 2013.

[18] H. Dittmann, B. Dohmen, R. Kehlbach et al., "Early changes in [^{18}F]FLT uptake after chemotherapy: an experimental study," *European Journal of Nuclear Medicine*, vol. 29, no. 11, pp. 1462–1469, 2002.

[19] A. J. de Langen, B. Klabbers, M. Lubberink et al., "Reproducibility of quantitative ^{18}F-3′-deoxy-3′-fluorothymidine measurements using positron emission tomography," *European Journal of Nuclear Medicine and Molecular Imaging*, vol. 36, no. 3, pp. 389–395, 2009.

[20] M. Perumal, E. A. Stronach, H. Gabra, and E. O. Aboagye, "Evaluation of 2-deoxy-2-[^{18}F]fluoro-D-glucose- and 3′-deoxy-3′-[^{18}F]fluorothymidine-positron emission tomography as biomarkers of therapy response in platinum-resistant ovarian cancer," *Molecular Imaging and Biology*, vol. 14, no. 6, pp. 735–761, 2012.

[21] M. H. Michalski and X. Chen, "Molecular imaging in cancer treatment," *European Journal of Nuclear Medicine and Molecular Imaging*, vol. 38, no. 2, pp. 358–377, 2011.

[22] N. Weidner, P. R. Carroll, J. Flax, W. Blumenfeld, and J. Folkman, "Tumor angiogenesis correlates with metastasis in invasive prostate carcinoma," *The American Journal of Pathology*, vol. 143, no. 2, pp. 401–409, 1993.

[23] M. R. Battle, J. L. Goggi, L. Allen, J. Barnett, and M. S. Morrison, "Monitoring tumor response to antiangiogenic sunitinib therapy with ^{18}F-fluciclatide, an ^{18}F-labeled αVβ3-integrin and αVβ3-integrin imaging agent," *Journal of Nuclear Medicine*, vol. 52, no. 3, pp. 424–430, 2011.

[24] J. M. L. Ebos and R. S. Kerbel, "Antiangiogenic therapy: impact on invasion, disease progression, and metastasis," *Nature Reviews Clinical Oncology*, vol. 8, no. 4, pp. 210–221, 2011.

[25] N. Ferrara, "VEGF and the quest for tumour angiogenesis factors," *Nature Reviews Cancer*, vol. 2, no. 10, pp. 795–803, 2002.

[26] S. R. Wedge, D. J. Ogilvie, M. Dukes et al., "ZD4190: an orally active inhibitor of vascular endothelial growth factor signaling with broad-spectrum antitumor efficacy," *Cancer Research*, vol. 60, no. 4, pp. 970–975, 2000.

[27] U. Lassen, M. Sorensen, T. B. Gaziel, B. Hasselbalch, and H. S. Poulsen, "Phase II study of bevacizumab and temsirolimus combination therapy for recurrent glioblastoma multiforme," *Anticancer Research*, vol. 33, no. 4, pp. 1657–1660, 2013.

[28] T. J. Semrad, C. Eddings, M. P. Dutia, S. Christensen, and P. N. Lara Jr., "Phase I study of the combination of temsirolimus and pazopanib in advanced solid tumors," *Anticancer Drugs*, vol. 24, no. 6, pp. 636–640, 2013.

[29] S. J. Park, J. L. Lee, I. Park et al., "Comparative efficacy of sunitinib versus sorafenib as first-line treatment for patients with metastatic renal cell carcinoma," *Chemotherapy*, vol. 58, no. 6, pp. 468–474, 2013.

[30] B. Neyns, J. Sadones, C. Chaskis et al., "Phase II study of sunitinib malate in patients with recurrent high-grade glioma," *Journal of Neuro-Oncology*, vol. 103, no. 3, pp. 491–501, 2011.

[31] R. J. Motzer, T. E. Hutson, P. Tomczak et al., "Overall survival and updated results for sunitinib compared with interferon alfa in patients with metastatic renal cell carcinoma," *Journal of Clinical Oncology*, vol. 27, no. 22, pp. 3584–3590, 2009.

[32] M. S. Morrison, S.-A. Ricketts, J. Barnett, A. Cuthbertson, J. Tessier, and S. R. Wedge, "Use of a novel Arg-Gly-Asp radioligand, ^{18}F-AH111585, to determine changes in tumor vascularity after antitumor therapy," *Journal of Nuclear Medicine*, vol. 50, no. 1, pp. 116–122, 2009.

[33] R. T. Ullrich, T. Zander, B. Neumaier et al., "Early detection of Erlotinib treatment response in NSCLC by 3′-deoxy-3′-[^{18}F]-fluoro-L-thymidine ([^{18}F]FLT) positron emission tomography (PET)," *PLoS ONE*, vol. 3, no. 12, Article ID e3908, 2008.

[34] A. van Waarde, D. C. P. Cobben, A. J. H. Suurmeijer et al., "Selectivity of ^{18}F-FLT and ^{18}F-FDG for differentiating tumor from inflammation in a rodent model," *Journal of Nuclear Medicine*, vol. 45, no. 4, pp. 695–700, 2004.